



Publicly Accessible Penn Dissertations

1-1-2016

Tensile Mechanics of the Knee Meniscus in the Context of Cracks: Failure and Fracture Mechanisms, Strain Concentrations, and the Effect of Specimen Shape

John Mark Peloquin

University of Pennsylvania, john.peloquin@gmail.com

Follow this and additional works at: <http://repository.upenn.edu/edissertations>



Part of the [Biomechanics Commons](#), and the [Biomedical Commons](#)

Recommended Citation

Peloquin, John Mark, "Tensile Mechanics of the Knee Meniscus in the Context of Cracks: Failure and Fracture Mechanisms, Strain Concentrations, and the Effect of Specimen Shape" (2016). *Publicly Accessible Penn Dissertations*. 1938.
<http://repository.upenn.edu/edissertations/1938>

This paper is posted at ScholarlyCommons. <http://repository.upenn.edu/edissertations/1938>
For more information, please contact libraryrepository@pobox.upenn.edu.

Tensile Mechanics of the Knee Meniscus in the Context of Cracks: Failure and Fracture Mechanisms, Strain Concentrations, and the Effect of Specimen Shape

Abstract

Knee meniscus tears (cracks) are a major cause of knee dysfunction and osteoarthritis, but little is known about how they grow or what effects they have on meniscus mechanics. The objective of this work was to investigate the mechanics and failure of crack-free and cracked meniscus in uniaxial tension, with specific attention to failure mechanisms (fracture and bulk rupture) and local strain concentrations. A finite element model was used to find a test configuration likely to cause fracture and crack propagation. Center cracks with a 45° crack–fiber angle were selected for producing large fiber stresses, and 90° edge cracks were selected for producing large inter-fiber shear stresses. The circumferential and radial tensile mechanics of the meniscus were quantified using ex vivo tensile testing. A fiber recruitment model was fitted to the test data, and a method was developed to quantify the inflection (yield) point and modulus based on the shape of the stress–strain curve. Comparison of tensile test specimen shapes showed that an expanded tab specimen shape produces more rapid and complete fiber recruitment, lesser yield strain, and greater peak stress (strength) than rectangle specimens, and, likely, dogbone specimens.

Mechanical effects of meniscus cracks were quantified by comparing cracked and crack-free specimens in circumferential and radial tension. The cracks did not cause a decrease in peak stress, indicating fracture did not occur. However, significantly greater longitudinal strain and shear strain was found near the crack tip for circumferential tension specimens. In radial tension specimens, all strain field components were greater near the crack tip. Failure tended to proceed along fascicle boundaries. Circumferential specimens failed by widespread interdigitating fiber pull-out, which also caused crack deflection. Radial specimens failed by necking and fiber rotation. These data demonstrate the remarkable fracture toughness of the meniscus, but increased near-tip strain may cause sub-failure damage and dysfunction. These results provide functional targets for interventions to repair or regenerate the meniscus.

Degree Type

Dissertation

Degree Name

Doctor of Philosophy (PhD)

Graduate Group

Bioengineering

First Advisor

Dawn M. Elliott

Keywords

failure, finite element analysis, fracture, knee meniscus, meniscus tear, tensile testing

Subject Categories

Biomechanics | Biomedical

TENSILE MECHANICS OF THE KNEE MENISCUS IN THE CONTEXT OF CRACKS:
FAILURE AND FRACTURE MECHANISMS, STRAIN CONCENTRATIONS, AND THE
EFFECT OF SPECIMEN SHAPE

John M. Peloquin

A DISSERTATION

in

Bioengineering

Presented to the Faculties of the University of Pennsylvania

In Partial Fulfillment of the Requirements for the Degree of Doctor of Philosophy

2016

Supervisor of Dissertation

Dawn M. Elliott, Professor of Biomedical Engineering, University of Delaware

Graduate Group Chairperson

Jason Burdick, Professor of Bioengineering

Dissertation Committee

Louis J. Soslowky, Committee Chair, Professor of Orthopaedic Surgery and Bioengineering

Beth A. Winkelstein, Professor of Bioengineering

Vivek B. Shenoy, Professor of Materials Science and Engineering

Michael H. Santare, Professor of Mechanical Engineering, University of Delaware

ACKNOWLEDGMENT

First and foremost, I would like to thank Dr. Dawn Elliott for being my PhD advisor. I have greatly enjoyed my time in her lab, and am particularly appreciative of the flexibility and freedom she allows her students to pursue their research interests and goals. Her genuineness and sagacity has made working on my PhD a pleasure. Dr. Robert Mauck and Dr. Lou Soslowsky also provided me important training and opportunities early in my PhD, for which I am grateful. Spencer Szczesny provided valuable mentorship to me as a more senior student during the first several years of my PhD. Julia Pezick and Pranita Muralidhar provided considerable help with the sample preparation and mechanical testing involved in this dissertation.

I especially thank my parents for their constant support in all my endeavors.

Before I started my PhD, Dr. Lara Estroff gave me my first opportunity to do scientific research. Dr. Cynthia Reinhart-King shortly thereafter provided me my first opportunity to complete an independent research project and to publish a first-author paper. My experiences in their labs are what made me decide to pursue a PhD.

Finally, many other unnamed people have helped me along the way. I appreciate all their efforts on my behalf.

ABSTRACT

TENSILE MECHANICS OF THE KNEE MENISCUS IN THE CONTEXT OF CRACKS:
FAILURE AND FRACTURE MECHANISMS, STRAIN CONCENTRATIONS, AND THE
EFFECT OF SPECIMEN SHAPE

John M. Peloquin

Dawn M. Elliott

Knee meniscus tears (cracks) are a major cause of knee dysfunction and osteoarthritis, but little is known about how they grow or what effects they have on meniscus mechanics. The objective of this work was to investigate the mechanics and failure of crack-free and cracked meniscus in uniaxial tension, with specific attention to failure mechanisms (fracture and bulk rupture) and local strain concentrations. A finite element model was used to find a test configuration likely to cause fracture and crack propagation. Center cracks with a 45° crack-fiber angle were selected for producing large fiber stresses, and 90° edge cracks were selected for producing large inter-fiber shear stresses. The circumferential and radial tensile mechanics of the meniscus were quantified using *ex vivo* tensile testing. A fiber recruitment model was fitted to the test data, and a method was developed to quantify the inflection (yield) point and modulus based on the shape of the stress-strain curve. Comparison of tensile test specimen shapes showed that an expanded tab specimen shape produces more rapid and complete fiber recruitment, lesser

yield strain, and greater peak stress (strength) than rectangle specimens, and, likely, dogbone specimens.

Mechanical effects of meniscus cracks were quantified by comparing cracked and crack-free specimens in circumferential and radial tension. The cracks did not cause a decrease in peak stress, indicating fracture did not occur. However, significantly greater longitudinal strain and shear strain was found near the crack tip for circumferential tension specimens. In radial tension specimens, all strain field components were greater near the crack tip. Failure tended to proceed along fascicle boundaries. Circumferential specimens failed by widespread interdigitating fiber pull-out, which also caused crack deflection. Radial specimens failed by necking and fiber rotation. These data demonstrate the remarkable fracture toughness of the meniscus, but increased near-tip strain may cause sub-failure damage and dysfunction. These results provide functional targets for interventions to repair or regenerate the meniscus.

TABLE OF CONTENTS

List of Tables	viii
List of Figures	ix
1 Introduction	1
2 Background	8
2.1 Meniscus structure	8
2.2 Mechanical function of meniscus	11
2.3 Mechanical testing of the meniscus	16
2.4 Fracture testing of fibrous soft tissue	17
2.5 Epidemiology of meniscus tears	21
2.6 Mechanical models for meniscus	24
3 A comparison of stress in cracked fibrous tissue specimens with varied crack location, loading, and orientation using finite element analysis	28
3.1 Introduction	28
3.2 Materials and methods	30
3.2.1 Specimen geometry and loading	30
3.2.2 Crack-fiber angle	31
3.2.3 Mesh construction	32
3.2.4 Constitutive model and material properties	32
3.2.5 Stress components	33
3.2.6 Fracture risk analysis	34
3.3 Results	35
3.3.1 Stress fields	35
3.3.2 Relative stress concentration severity	38
3.3.3 Element size sensitivity	39
3.4 Discussion	40
3.4.1 Implications for physical crack extension testing	40
3.4.2 Crack blunting and plastic deformation	42
3.4.3 Calculation of crack tip stresses and mesh sensitivity	43
3.4.4 Limitations	44
3.5 Conclusion	45

4	Quantification of meniscus tensile mechanics and selection of specimen shape	46
4.1	Introduction	46
4.2	Methods	51
4.2.1	Specimen preparation and tensile test protocol	51
4.2.2	Specimen characteristics and specimen exclusion	55
4.2.3	Data analysis	58
4.2.4	Fiber recruitment model	60
4.2.5	Statistics and inference	62
4.3	Results	62
4.3.1	Stress–strain curves, yield, and rupture	62
4.3.2	Effect of specimen shape on mechanical properties	64
4.3.3	Strain fields	66
4.4	Discussion	68
4.4.1	Overview	68
4.4.2	Fiber recruitment model and stress–strain nonlinearity	69
4.4.3	Yield point	70
4.4.4	Radial specimens and tie fibers	72
4.4.5	Comparison with prior work	72
4.4.6	Rupture location	74
4.4.7	Strain field inhomogeneity, grip effects, and damage	77
4.4.8	Choice of specimen shape	78
4.4.9	Choice of strain measurement	82
4.5	Conclusion	83
5	Uniaxial tensile testing of cracked meniscus and its failure mechanisms	88
5.1	Introduction	88
5.2	Methods	92
5.2.1	Specimen preparation	92
5.2.2	Tensile test protocol	94
5.2.3	Stress and strain data processing	97
5.2.4	Statistics and inference	98
5.3	Results	99
5.3.1	Effects of cracks on stress–strain curves and strain fields	99
5.3.2	Qualitative rupture patterns and crack behavior	102
5.3.3	Rupture location	105
5.4	Discussion	105
5.4.1	No fracture observed	105
5.4.2	Fracture test configurations	107
5.4.3	Crack-induced changes in radial specimen yield stress and tangent modulus	108
5.4.4	Morphology of ruptures and functional failure	109
5.4.5	Significance of increased strain near the crack tip	110
5.4.6	Permanent deformation	111

5.4.7	Comparison of meniscus failure to that of other tissues	112
5.4.8	Differences between loading axes	113
5.4.9	Potential for fracture in vivo	115
5.5	Conclusion	117
6	Conclusion and future directions	128
6.1	Summary	128
6.2	Path forward for studying crack propagation in meniscus	132
6.3	Role of meniscus fascicle structure and anisotropy	136
6.4	Boundary conditions and grips	140
6.5	Discriminating between fracture and bulk rupture	142
6.6	Adjustment of test geometry to promote crack propagation and fracture	145
6.7	Identifying mechanical and structural mechanisms of failure	148
6.8	Improvements to protocol efficiency	153
6.9	Conclusion	155
APPENDIX A	Endpoints for tests used to study the effect of specimen shape	159
APPENDIX B	Choice of Vic-2D parameters	176
B.1	Introduction	176
B.2	Subset size sensitivity analysis	178
B.2.1	Subset size analysis setup	178
B.2.2	Effect of subset size on strain field appearance	179
B.2.3	Effect of subset size on point tracking	181
B.2.4	Effect of subset size on aggregate strain field statistics	181
B.2.5	Subset size and image scale	182
B.2.6	Choice of subset size	183
B.3	Filter size sensitivity analysis	183
B.3.1	Filter size analysis setup	183
B.3.2	Effect of filter size	184
B.3.3	Choice of filter size	185
APPENDIX C	Endpoints for tests used to study the effect of cracks	200
	Bibliography	220

LIST OF TABLES

4.1	Mechanical parameters compared between circumferential ET specimens tested in air and PBS. There was no significant difference with respect to any parameter and the 95% confidence intervals for potential differences are small.	55
4.2	Specimen counts by rupture type, test axis, and specimen shape before and after excluding invalid ruptures and duplicate specimens from the same meniscus. .	56
4.3	Fiber recruitment model and stress–strain results by loading direction and specimen shape.	66
4.4	Comparison of current and prior circumferential uniaxial tensile tests. Values are listed for the center region (anterior-posterior axis) unless otherwise indicated.	75
4.5	Comparison of current and prior radial uniaxial tensile tests. Values are listed for the center region (anterior-posterior axis) unless otherwise indicated. . . .	76
5.1	Specimen counts for cracked and control specimens in each test group.	92
5.2	Specimen dimensions (mean \pm sd)	95
5.3	Specimen counts by rupture type	96
5.4	Statistics for comparison of near-tip strain to away-from tip strain at 70% of peak stress. Values are mean \pm s.d. (across tests). The p value is from a paired Welch t-test.	101
A.1	Test endpoints for specimens reported in Chapter 4.	159
B.1	Image scale	182
C.1	Test endpoints for specimens reported in Chapter 5.	200

LIST OF FIGURES

2.1	Bovine medial and lateral menisci viewed from the anterior–superior direction. The medial meniscus is on the left; the lateral meniscus is on the right. Black arrows mark the anterior and posterior horns of the meniscus, where it attaches to the bone. The gray arrow marks where the medial meniscus is attached to the medial collateral ligament. The medial meniscus is also attached to the joint capsule along its rim. The joint capsule has been mostly removed in this photo, although some remnants are visible along the rim of the medial meniscus. In humans, the posterior lateral meniscus attachment attaches to the tibia rather than the femur.	9
2.2	Typical meniscus tear morphologies (O’Keefe et al. 2013). Complex and horizontal tears are thought of as degenerative and longitudinal, bucket handle, radial, and oblique tears are thought of as resulting from acute injury. Complex tears are more broad than illustrated, similar to an amalgamation of several other tears. Bucket-handle tears and longitudinal tears may also be called circumferential tears. Nomenclature varies slightly between publications.	25
3.1	Test configurations. Three configurations were compared: center crack biaxial (CCB), center crack uniaxial (CCU), and single edge notch (SENT). Each is illustrated here for a crack perpendicular to the fibers. The crack angle was varied in each case.	31
3.2	Quantification of crack tip stress. (a) Stress was sampled along a line (in the reference configuration) extending from the crack tip to the edge of the mesh. (b) To find the stress at the crack tip, the stress profile was fit with an exponential function and extrapolated to 0 mm distance. This example shows the fit for the 45° CCB case with 50 μm elements.	35
3.3	Fiber-parallel stress fields. (a) 45° CCB, (b) 45° CCU, (c) 45° SENT, (d) 90° CCB, (e) 90° CCU, and (e) 90° SENT. Each panel shows a 3.2 mm tall subregion of the specimen.	36
3.4	Fiber-perpendicular stress fields. (a) 45° CCB, (b) 45° CCU, (c) 45° SENT, (d) 90° CCB, (e) 90° CCU, and (e) 90° SENT. Each panel shows a 3.2 mm tall subregion of the specimen.	37
3.5	Fiber shear stress fields. (a) 45° CCB, (b) 45° CCU, (c) 45° SENT, (d) 90° CCB, (e) 90° CCU, and (e) 90° SENT. In panels a and b, asterisks mark locations with stress magnitudes similar to the crack tip stress, yet distant from the crack tip. Each panel shows a 3.2 mm tall subregion of the specimen.	37

3.6	Fiber-parallel stress calculated by the stress profile fitting method. Center-cracked specimens with acutely angled cracks have greater fiber stress compared to edge-cracked specimens. 0° = crack parallel to fiber axis; 90° = crack perpendicular to fiber axis.	38
3.7	Maximum element-wise stress for (a) fiber-parallel stress, (b) fiber-perpendicular stress, and (c) fiber shear stress components. For fiber stress, Figure 3.6 uses a more robust metric. The 15° CCB and CCU cases are excluded from panels b and c because these cases nearly inverted some elements near the crack tip (shown in Figure S3), producing spurious values for fiber-perpendicular stress and fiber shear stress. The 0° CCU case has approximately zero fiber-perpendicular stress and fiber shear stress, so it is not shown in panels b or c. 0° = crack parallel to fiber axis; 90° = crack perpendicular to fiber axis.	39
3.8	Effect of mesh element size on crack tip fiber stress. Each panel plots data from specimens with the indicated crack-fiber angle. For all acutely oriented cracks, smaller elements caused increases in stress. Specimens with a crack-fiber angle of 90° are much less sensitive to mesh size. Since specimens with cracks 0° to the fibers have no fiber stress concentration, they are insensitive to mesh size. 0° = crack parallel to fiber axis; 90° = crack perpendicular to fiber axis.	40
4.1	Meniscus specimen shapes used in this study and their dissection locations. The specimen and meniscus outlines are printed at 1:2 scale. The specimen outlines match the median dimensions used in this study. The gray shaded regions of the specimen were clamped by the grips. The dashed lines schematically illustrate the curved path of the meniscus' fibers.	52
4.2	Mean and standard deviation of yield and peak points for circumferential ET specimens by test environment. The stress–strain response of specimens tested in air and PBS did not differ with respect to these points or any other measured parameter (see Table 4.1 for other parameters).	55
4.3	Classification scheme for types of specimen rupture. Circumferential specimens (A) ruptured in two more ways than radial specimens (B). Gripped region failures and longitudinal splits were considered invalid and excluded from mechanical analysis.	57
4.4	A representative stress–strain curve for circumferential ET specimens with the fiber recruitment range (the 0.025 and 0.975 quantiles of λ_c), mean fiber recruitment stretch ($\bar{\lambda}_c$), yield point, and peak point marked. The lower plot shows the point-wise tangent modulus curve (the first derivative of the stress–strain curve), the first local maximum of which was identified as the yield point. Both plots share the same x-axis.	59
4.5	Stress–strain curves for circumferential and radial specimens by rupture type and specimen shape. The yield and peak stress points are marked.	63

4.6	Fiber modulus (k_f) was strongly correlated with tangent modulus at yield (r [95% CI] = 0.77–0.94 by Pearson correlation). The solid blue line and shaded region is the best-fit line and its 95% confidence interval. The dotted black line illustrates a 1:1 relationship (slope = 1, intercept = 0).	64
4.7	Fiber recruitment model and stress–strain results for circumferentially stretched expanded tab (ET), rectangle (R), and dogbone (DB) specimens. Significant differences between specimen shapes are marked with a bar and asterisk. The ET specimens showed differences indicating more complete and rapid fiber recruitment.	84
4.8	Stress–strain results for radially stretched rectangle (R) and dogbone (DB) specimens. There were no significant differences between specimen shapes.	85
4.9	Representative longitudinal strain (E_{xx}) fields at yield for circumferentially loaded specimens. In subfigure C, the dashed outline over the dogbone’s strain field indicates the “loaded region”, which has potential grip-to-grip fiber continuity. The flared margins outside this outline are the “shielded region”, which has no grip-to-grip continuous fibers and exhibits less longitudinal strain than the loaded region. Color scales are truncated at the 0.05 and 0.95 quantiles. The scale bars are 5 mm long.	85
4.10	Representative (A) shear strain (E_{xy}) and (B) transverse strain (E_{yy}) field at yield for circumferential specimens with (C) the corresponding camera image of the specimen. An ET specimen is shown. The bands in the E_{xy} field qualitatively match the fascicle boundaries visible in the camera image. The color scales are truncated at the 0.05 and 0.95 quantiles. The scale bars are 5 mm long.	86
4.11	Representative plot of longitudinal strain (E_{xx}) in a DB specimen measured optically (y-axis) and by grip displacement (x-axis). The median optical strain in the central region (the “loaded region”), which has grip-to-grip fiber continuity, is much greater than in the flared ends of the specimen (the “shielded region”), which contain severed fibers. See Figure 4.9C for a diagram of these regions. The line of 1:1 correspondence between optical and grip strain is marked by a solid black line. Optical strain is approximately linearly correlated with grip strain up to and a little past the yield point.	86
4.12	Representative longitudinal (E_{xx}), shear (E_{xy}), and transverse (E_{yy}) strain fields for radially stretched DB specimens at yield. The strain fields for radially stretched R specimens are similar. The scale bars are 5 mm long.	86
4.13	Optical longitudinal strain 0.05/0.95 inter-quantile range (red shaded region) compared with grip strain (solid black line). The optical strain range broadens in proportion to the applied grip strain. This is a representative example; in other cases, the optical strain range may broaden nonlinearly. The plot shows data up to the peak point.	87

5.1	Specimen schematics. (a) Anatomic origin of specimens with respect to the whole meniscus. This example shows a lateral meniscus. The narrow circumferential specimens are cut so that they have the same width and come from the same region as the uncracked width in a normal specimen with a 90° edge crack. (b) Specimen shapes for each of this study’s analysis groups (circumferential 90° edge crack, circumferential 45° center crack, and radial 90° center crack) and their corresponding crack-free controls. The narrow specimens are used as controls for the 90° edge crack specimens so that they have similar cross-sectional area and come from the same region.	118
5.2	Near-tip and away-from-tip regions defined for identifying possible near-tip strain concentrations. Both regions extended 0.5 mm to the left and right of the crack. The near-tip region extended 0.5 mm from the crack tip. All other tissue in the 1 mm wide band extending from the crack tip was assigned to the away-from-tip region.	118
5.3	Comparison of stress–strain curve parameters between circumferentially stretched cracked specimens and their corresponding controls. The boxplots follow Tukey’s style.	119
5.4	Comparison of stress–strain curve parameters between radially stretched cracked specimens and their corresponding controls. The boxplots follow Tukey’s style. * indicates $p < 0.05$, no crack vs. 90° edge.	120
5.5	Stress–strain curves for circumferential 90° edge crack and 45° center crack specimens and their controls.	121
5.6	Stress–strain curves for radial 90° edge crack specimens and their controls. . .	121
5.7	Optical strain compared pairwise between near-tip and away-from tip regions. * indicates $p < 0.05$, paired near-tip vs. away-from-tip.	122
5.8	Optical strain near and away from the crack tip. Solid or dashed line = median; shaded band = 0.16 and 0.84 quantiles; blue = away from tip; red = near tip. The yield strain and peak strain for the tests shown in each plot are marked with vertical dashed lines. The plotted values were computed from the pooled median strain values for each region for each test.	123
5.9	Representative strain fields for cracked specimens in each analysis group loaded to 70% of peak stress.	124
5.10	Representative example of circumferential specimen rupture (bracketed by arrows). Ruptures were consistently broad, spanning ~5 mm of specimen length and were bridged by fascicles and smaller fibers.	125
5.11	Example of near-crack-tip rupture (bracketed by arrows) and crack tip opening in a circumferential 90° edge crack specimen.	125
5.12	Representative example of rupture (arrows) in a circumferential 45° center crack specimen.	126
5.13	An unusual z-shaped rupture (arrows) in a circumferential 45° center crack specimen.	126

5.14	Example of crack growth (bracketed by arrows) in a radial 90° edge crack specimen.	127
5.15	Example of rupture (bracketed by arrows) in a radial 90° edge crack specimen by necking and simultaneous rupture across the entire uncracked width. This failure mode is in contrast to crack growth.	127
B.1	An example of an erroneous image correlation. Points from the lower left are misclassified as displacing to the lower center, resulting in a displacement field that folds over itself, making it non-diffeomorphic.	178
B.2	The circumferential specimens used in the Vic-2D sensitivity analysis, shown immediately prior to rupture. The black square illustrates the size of a 55 px subset. The top specimen here is also the top specimen in the subsequent strain field figures. Top: Circumferential specimen 1. Bottom: Circumferential specimen 2.	186
B.3	The radial specimens used in the Vic-2D sensitivity analysis, shown immediately prior to rupture. The black square illustrates the size of a 55 px subset. The top specimen here is also the top specimen in the subsequent strain field figures. Top: Radial specimen 1. Bottom: Radial specimen 2.	187
B.4	Effect of Vic-2D subset size on the longitudinal (E_{xx}) strain field for circumferential specimens. Top: Circumferential specimen 1. Bottom: Circumferential specimen 2. Circumferential specimen 2 has no strain field for the 9 px subset size because too many points were lost in the digital image correlation.	188
B.5	Effect of Vic-2D subset size on the shear (E_{xy}) strain field for circumferential specimens. Top: Circumferential specimen 1. Bottom: Circumferential specimen 2. Circumferential specimen 2 has no strain field for the 9 px subset size because too many points were lost in the digital image correlation.	189
B.6	Effect of Vic-2D subset size on the transverse (E_{yy}) strain field for circumferential specimens. Top: Circumferential specimen 1. Bottom: Circumferential specimen 2. Circumferential specimen 2 has no strain field for the 9 px subset size because too many points were lost in the digital image correlation.	190
B.7	Effect of Vic-2D subset size on the longitudinal (E_{xx}) strain field for radial specimens. Top: Radial specimen 1. Bottom: Radial specimen 2.	191
B.8	Effect of Vic-2D subset size on the shear (E_{xy}) strain field for radial specimens. Top: Radial specimen 1. Bottom: Radial specimen 2.	192
B.9	Effect of Vic-2D subset size on the transverse (E_{yy}) strain field for radial specimens. Top: Radial specimen 1. Bottom: Radial specimen 2.	193
B.10	Effect of subset size on median strain (solid line) and 0.05 and 0.95 quantiles (dashed lines) for circumferential specimens.	194
B.11	Effect of subset size on median strain (solid line) and 0.05 and 0.95 quantiles (dashed lines) for radial specimens.	195
B.12	Effect of filter size on the strain field for circumferential specimen 1.	196
B.13	Effect of filter size on the strain field for circumferential specimen 2.	197
B.14	Effect of filter size on the strain field for radial specimen 1.	198

B.15 Effect of filter size on the strain field for radial specimen 2. 199

CHAPTER 1: INTRODUCTION

Tears in the knee meniscus cause symptoms such as joint locking, pain, and instability. Perhaps more importantly, by altering knee mechanics, meniscus tears lead to degenerative changes in the knee's articular cartilage and hence osteoarthritis. Preventing tears or treating them (via repair or regeneration) before they can cause osteoarthritis is therefore beneficial. However, many tears in the meniscus heal poorly, especially tears in the inner, avascular region. Symptomatic tears that are judged to have a poor prognosis for healing, or do not heal after attempted repair, must be treated by meniscectomy (partial or complete removal of the meniscus). Meniscectomy greatly changes articular cartilage loading and so also causes osteoarthritis; it is preferably avoided. Asymptomatic tears may therefore be better left untreated if it can be determined that they will not propagate.

Despite the functional impairment and disease caused by meniscus tears and the consequences of treating tears by meniscectomy, very little is known about meniscus tear mechanics. There is scant ability to quantitatively predict the impact of a tear on the meniscus' function or whether a tear will propagate, and hence scant ability to determine if a tear requires treatment. Quantification of meniscus tears' mechanical effects and the conditions necessary for tear propagation would be a significant asset to clinical decision-making and development of reparative or regenerative treatments.

A key question related to meniscus tear propagation is whether meniscus fails by fracture

or bulk rupture. The two processes have different effects and require different approaches to predict failure. The dichotomy is not exclusive; the meniscus may fail by fracture in some conditions and bulk rupture in others. Failure by fracture occurs when a crack or crack-like defect causes a stress concentration. (Subsequent discussion of meniscus tears from a fracture perspective will refer to them as cracks.) For a crack, the stress concentration is at the crack's tip. The stress concentration causes local failure, causing the crack to propagate. This moves the stress concentration to fresh material, which fails in turn. The crack propagates across the entire tissue in this manner. Failure by fracture is in contrast to failure by bulk rupture, in which the entire tissue cross-section yields and fails together and there is no decrease in strength due to migration of a zone of local failure. Due to the stress concentration, fracture occurs at lesser nominal stress than bulk rupture. Predicting meniscus crack growth therefore requires that these mechanisms be distinguished and quantified.

Although cracks grow in the meniscus in vivo, crack growth does not necessarily occur by fracture. Fracture always involves a growing crack, but the reverse is not true. Bulk failure can create both failure with a crack-like appearance and failure that is diffuse and not crack-like. The meniscus definitely develops in vivo failures that have a crack-like appearance, but whether these failures are created by fracture or bulk rupture is unknown.

In addition to fracture and crack-like bulk failure, failure without apparent crack growth constitute a third category for investigation. This category is particularly interesting because a crack that is asymptomatic, does not impair the meniscus' mechanical function, and will not grow is benign and, from a clinical perspective, is as functional as an intact meniscus. Leaving

the native meniscus in place when possible is best for long term joint health, and a benign crack permits this. Correctly deciding whether a cracked meniscus can be safely left in place requires identification of the applicable mechanisms of failure, namely fracture and/or bulk rupture, and quantification of the relevant failure criteria.

It is currently unknown whether a cracked meniscus fails by fracture or bulk rupture, or whether the crack will grow for a given loading condition. Tensile loading of pre-cracked specimens is the standard *ex vivo* test protocol for investigating crack behavior in fibrous soft tissues. Tests using this approach in fibrous tissues other than the meniscus predominantly produced bulk failure without crack growth, even with an initial crack created prior to testing. Fracture and crack propagation cannot be quantified mechanically without a test protocol that produces these kinds of failure. No tensile fracture tests have yet been done for meniscus. The present work is designed to address this knowledge gap.

The overall objective of this work was to investigate meniscus mechanics and failure in the context of meniscus cracks, with specific attention to failure mechanisms (fracture and bulk rupture) and strain concentrations. To support this goal, key nonlinear mechanical properties of the meniscus were quantified in uniaxial tension for both crack-free and cracked specimens and several experimental issues regarding stress–strain curve quantification, rupture location, and specimen shape were examined. Since the meniscus bears both circumferential and radial tension *in vivo*, and the predominantly circumferential alignment of its collagen fiber bundles (fascicles) causes significant mechanical anisotropy, tensile properties were quantified in both the circumferential and radial directions. To quantify sub-failure meniscus mechanics, a fiber

recruitment model was developed and fit to circumferential tensile test data and methods were developed to quantify the yield point (stress–strain curve inflection point). To ensure physiologically representative loading of collagen fibers in the tensile tests, expanded tab, dogbone, and rectangle specimen shapes were compared to identify the shape that best produced secure gripping and loading of the collagen fibers. In order to select crack configurations likely to be relevant to crack propagation and fracture, finite element analysis (FEA) was used to compare candidate test cases. The cases producing the greatest crack-associated stress were selected for physical ex vivo testing. The goal of identifying failure mechanisms in cracked meniscus specimens, determining whether cracks cause strain concentrations, and determining whether cracks grow in the selected test configurations was achieved by comparing the behavior of cracked specimens to crack-free controls using the selected crack configurations and specimen shapes.

The objective of identifying a test condition that was likely to produce fracture in fibrocartilaginous tissue such as the meniscus is addressed by the work in Chapter 3. The approach was to use FEA to simulate crack-associated stress concentrations in several test configurations that could be used for subsequent fracture studies. Biaxial and uniaxial tests were examined with varied crack position (edge vs. center) and crack orientation (0° to 90° relative to the prevailing collagen fiber direction; 15° increments), mimicking an assortment of in vivo tear types associated with acute injury. Due to the anisotropic collagen arrangement and mechanical properties of the meniscus, it was hypothesized that varying the crack angle would produce large changes in the crack-associated stress concentration. The predicted stress fields were post-processed to obtain the stress components in the fiber direction, perpendicular to the fiber direction, and

in inter-fiber shear. For each stress component, the test configurations were ranked according to the severity of the crack tip stress and the configuration producing the greatest stress was considered to have the greatest potential for fracture.

The objective of quantifying the nonlinear mechanical properties of the meniscus in uniaxial tension and addressing experimental issues regarding stress–strain curve quantification, rupture location, and specimen shape is addressed by the work in Chapter 4. Since the meniscus bears multiaxial loads in vivo—axial compression combined with in-plane circumferential and radial tension—and is anisotropic, tensile tests were done in both the circumferential and radial directions. The pre-yield stress–strain curve in circumferential tension was quantified using a structural model based on the concept of sequential fiber recruitment. The fiber recruitment model was intended to support structural interpretation of meniscus stress–strain nonlinearity. The stress–strain curve was also parameterized using non-model parameters, including (for the first time in meniscus) the inflection point (yield point). An algorithm was developed to quantify the inflection point based on how the yield point is reported for other fibrous soft tissues. This procedure for quantifying the inflection point also provided a modulus measurement that does not depend on identification of a linear region in the nonlinear stress–strain curve. This stress–strain quantification is an important step forward for study of the meniscus and the methods are transferable to other fibrous soft tissues.

The comparison of specimen shapes was prompted by the observation of grip slip, grip line rupture, and unloaded regions in preliminary testing. To find a test configuration that securely grips the meniscus' fibers and minimizes grip-induced stress concentrations, stress–strain

statistics and failure patterns were compared between rectangular, dogbone, and expanded tab shapes. The expanded tab specimen is a very infrequently used asymmetric shape with large tabs for gripping. The tabs follow the arc of the meniscus' fibers, allowing more fibers to enter the gripped area. It was hypothesized that the expanded tab would increase the number of loaded fibers and hence increase measured stiffness and strength.

The overall objective of investigating failure mechanisms and strain concentrations in cracked meniscus specimens is addressed by work presented in Chapter 5, which applies the results from Chapters 3 and 4. As in Chapter 4, both circumferential and radial specimens were tested, as both axes are subject to tensile loading *in vivo*. Tensile properties are particularly important for study of cracks because one of the major ways a crack can grow is under tension perpendicular to the crack, which causes crack opening and hence crack growth. The circumferential alignment of collagen fascicles in the meniscus means that cracks growing circumferentially (under radial tension) propagate between fascicles, whereas cracks growing radially (under circumferential tension) propagate across fascicles. Different loading directions and crack directions were therefore expected to produce different behavior. The peak stress of the cracked specimens was compared to uncracked controls. If the hypothesis that cracked specimens fail by fracture was true, they would fail at lesser stress. Test configurations were selected based on the FEA predictions made in Chapter 3 regarding which test configurations were most likely to produce fracture. The cracked specimen configurations employed represented *in vivo* tears of the radial, oblique, and circumferential or bucket-handle types, which are considered to generally be caused by acute (traumatic) injury rather than progressive degeneration. Specimen shapes were

selected based on the results from Chapter 4. Expanded tab specimens were used for circumferential tensile tests, and rectangle specimens were used for radial tensile tests. Full-specimen strain fields were obtained via digital image correlation and used to establish the presence or absence of crack-tip associated strain concentrations. Strain concentrations such as these, if present, could cause damage and functional impairment even if the crack doesn't propagate.

The meniscus mechanics quantified in this study are useful for several purposes. Quantifying meniscus crack mechanics—whether cracks grow by fracture or bulk rupture, whether they promote potentially injurious sub-failure strain and stress concentrations, and the loads necessary to produce these outcomes—is a necessary step towards being able to determine whether an in vivo crack requires treatment or whether it is benign. The mechanical model and stress–strain parameters measured in this study for both crack-free and cracked meniscus are useful as functional targets for meniscus replacements or repair procedures. These parameters, and the procedures developed to measure them, may also be used in future research to compare disease states and develop diagnostic markers. Mechanical studies such as the present work are a key step towards improved, evidence-based treatment of meniscus cracks.

CHAPTER 2: BACKGROUND

2.1 Meniscus structure

The medial and lateral menisci are lunar-shaped chunks of fibrocartilage positioned on either side of the knee between the femoral condyles and the tibial plateau (Figure 2.1). The lateral meniscus has more of a C-shape and is broader than the medial meniscus. The meniscus cross-section is wedge-shaped. The superior side is steeply sloped so as to cup the femoral head; the inferior side is flatter to match the tibial plateau geometry. The medial meniscus is attached to the tibial plateau at each of its ends; it is also attached to the medial collateral ligament and the joint capsule along its outer rim. The lateral meniscus is attached to the tibial plateau at each of its ends. (The posterior and anterior attachments are sometimes called the roots.) The menisci are otherwise free to move about inside the knee. The lateral meniscus's lesser number of attachments makes it more mobile than the medial meniscus.

The meniscus is predominantly made of collagen I (Lento and Akuthota 2000). The total amount of proteoglycan in meniscus is < 1% wet weight (Kelly et al. 1990). The outer meniscus is mostly collagen I, with small amounts of decorin, biglycan, collagen III, collagen V, and collagen VI (Cheung 1987; Roughley and White 1992). The outer meniscus is vascularized; the inner meniscus is not (Arnoczky and Warren 1982). The inner meniscus contains large amounts of both collagen I and II and has more aggregating proteoglycans than the outer meniscus (Che-

ung 1987). Nerve fibers are present in the outer meniscus, but not in the inner meniscus (Fox et al. 2015; Makris et al. 2011). Meniscus composition (in terms of sulfated glycosaminoglycan, water, and hydroxyproline content) is the same for lateral and medial human menisci (Kelly et al. 1990). Composition is also constant across the posterior/center/anterior regions.

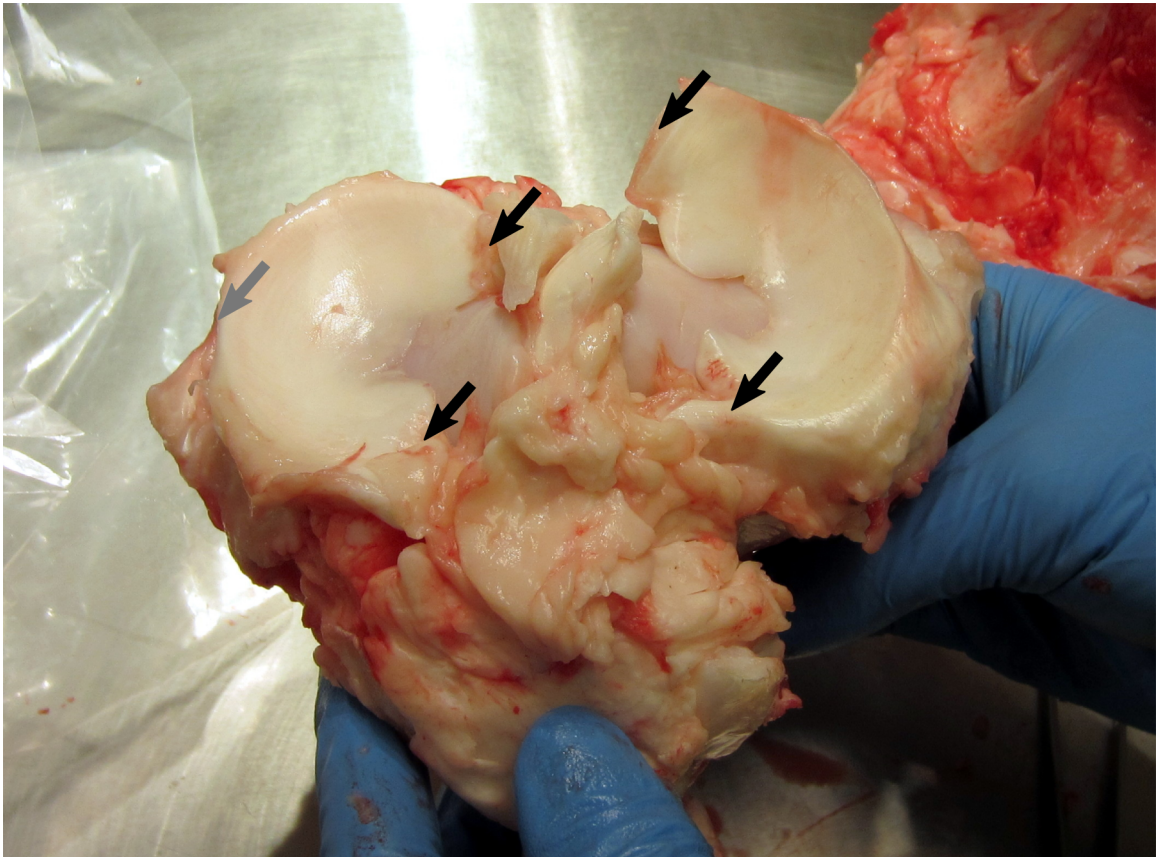


Figure 2.1: Bovine medial and lateral menisci viewed from the anterior–superior direction. The medial meniscus is on the left; the lateral meniscus is on the right. Black arrows mark the anterior and posterior horns of the meniscus, where it attaches to the bone. The gray arrow marks where the medial meniscus is attached to the medial collateral ligament. The medial meniscus is also attached to the joint capsule along its rim. The joint capsule has been mostly removed in this photo, although some remnants are visible along the rim of the medial meniscus. In humans, the posterior lateral meniscus attachment attaches to the tibia rather than the femur.

The meniscus is made of a large number of collagen fascicles that collectively follow a path arcing along the meniscus from one tibial attachment to the other (Bullough et al. 1970). Each

fascicle is 50 μm to 500 μm in diameter (Andrews et al. 2013; Petersen and Tillmann 1998; Sweigart and Athanasiou 2005; Kelly et al. 1990). The fascicles are in turn made of 5 μm to 10 μm diameter fibril bundles (Rattner et al. 2011). Cells associate with fibril bundles of this size, and cell processes extend between cells on the same fibril bundle and to cells on adjacent fibril bundles (Hellio Le Graverand et al. 2001). The fibrils that make up the fibril bundles are 100 nm to 150 nm in diameter (Sweigart and Athanasiou 2005; Petersen and Tillmann 1998). Nomenclature has not been standardized; fascicles are sometimes called fiber bundles. The meaning of “fiber” is generally context-dependent, and fibril is sometimes used as a synonym for fiber. In the present work, the hierarchy of 100 μm to 500 μm diameter fascicle \rightarrow 5 μm to 10 μm fibril bundle \rightarrow 100 nm to 150 nm fibril will be used, with fiber adopting its nonspecific meaning as referring to a threadlike structure.

The fiber architecture of the meniscus varies with depth. The surface of the meniscus is covered with a network of thin fibrils with diameter ~ 35 nm (Petersen and Tillmann 1998). These fibrils are oriented randomly. The layer is about 10 μm thick. Beneath the surface fibril network there is a layer of 20 μm to 50 μm wide fibril ribbons. This layer is 150 μm to 200 μm thick, and is 20 μm to 30 μm thicker near the outer rim than the inner rim. In the outer regions, the fibril ribbons are mostly radial, whereas in the inner regions there are two crisscrossing fiber populations slightly off-axis from the circumferential direction. In the mid-radial region, most of the fibril ribbons follow the circumferentially oriented crisscrossing pattern. Near the tibial insertions the architecture is different—most of these fibril ribbons are radial, even near the inner edge. The central layer, which comprises the bulk of the meniscus, contains the circumferential

fascicles described in the previous paragraph.

Woven throughout the circumferential fascicles are radial tie fiber sheets that arborize through the fascicles in a branching, netlike pattern (Andrews et al. 2014). Tie fibers also run vertically, connecting the superficial zone fibers with the radially oriented tie fibers. Some tie fiber sheets envelop blood vessels and their associated glycosaminoglycan-rich matrix. The radial tie fiber sheets are 0.1 mm to 0.5 mm thick and, like the circumferential fascicles, comprised of 5 to 10 μm fibril bundles. Unlike the circumferential fascicles, tie fibers contain elastin fibrils interspersed throughout their interior (Rattner et al. 2011).

2.2 Mechanical function of meniscus

Healthy meniscus distributes load from the femoral head across the tibial plateau, absorbs shock, lubricates its contact surface with the articular cartilage, and is a secondary knee stabilizer. The relatively low compressive stiffness and low permeability of meniscus makes it a more efficient shock absorber than articular cartilage (Kelly et al. 1990). Shock absorption in knees without menisci is 20% less than in knees with menisci (Voloshin and Wosk 1983). The meniscus supports 50% of the knee load in extension (Ahmed and Burke 1983). This fraction increases to 90% at 90° of flexion.

Meniscus tears have mechanical consequences in terms of both primary symptoms and creating mechanical dysfunction that is thought to in turn cause osteoarthritis. More than half of patients with meniscal tears have mechanical symptoms and recurrent effusions (Corea et al. 1994). Meniscus tears or damage-induced laxity may reduce hoop stress and impair fluid pres-

surization, thereby increasing the friction coefficient between the meniscus and the articular cartilage (Baro et al. 2012). Increased friction leads to further tissue degradation and promotes osteoarthritis. Radial tears transecting 90% of the meniscus increase contact pressure on the articular cartilage (Bedi et al. 2010). However, radial tears transecting $\leq 60\%$ of the meniscus do not change the location or magnitude of peak knee contact pressure in ex vivo tests with simulated gait. However, partial meniscectomy had a more severe effect, so it may be beneficial to preserve a partially torn meniscus. In FEA of the knee, Mononen et al. (2013) found substantial stress concentrations at the tips of tears that transected $2/3$ of the meniscus width, but no corresponding increase in articular cartilage stresses. The material model was a mixture of viscoelastic cartilage fibers and neo-Hookean poroelastic matrix. A 2 cm peripheral tear of the posteromedial meniscus horn qualitatively increased peak local contact stress on the articular cartilage (Baratz et al. 1986). In an ex vivo study using a thin pressure sensor, horizontal tears caused a small increase in peak tibial cartilage contact pressure and a small decrease in contact area (Arno et al. 2015). Feucht et al. (2015), in the context of anterior cruciate ligament (ACL) injury combined with meniscus tears, describe incomplete longitudinal tears or complete stable longitudinal tears as having minor consequences. They consider root tears, complete radial tears, and bucket handle tears to have major biomechanical consequences and require repair.

Meniscus tears are not necessarily loaded with large opening forces. A sharp longitudinal crack in human meniscus does not produce measurable distraction pressures on an intra-crack pressure transducer when the knee is compressed and moved (Richards et al. 2008). In static ex vivo testing, a suture across a vertical longitudinal tear 25 mm long in the lateral meniscus

remains unloaded in compression, and is loaded only 0.5 N to 4.1 N under combined compression, flexion, and rotation (Stärke et al. 2009). The authors of both studies suggest that shear stress may be more relevant than tear opening stress to meniscus tear propagation.

Symptomatic tears are often treated with meniscectomy, in which part or all of the meniscus is removed. Repair (such as with sutures), allograft transplants, or synthetic implants are the other options (Rodkey et al. 1999; Vrancken et al. 2013; Rongen et al. 2015; Elsner et al. 2010; Bulgheroni et al. 2015; Waterman et al. 2016; Shelbourne and Dersam 2004; Toman et al. 2009). Meniscus allograft transplant does not prevent damage to articular cartilage or osteoarthritis, but does reduce the extent of damage compared to meniscectomy (Rongen et al. 2015). Meniscectomy leads to worse clinical outcomes than meniscus repair, but meniscus repair has a greater reoperation rate (Paxton et al. 2011). The posterior horn is difficult to repair and so is more often treated with meniscectomy (McDermott and Amis 2006). The outer (peripheral) meniscus, which is vascularized, can heal without intervention, but the inner, avascular meniscus typically fails to heal (Arnoczky and Warren 1983).

Meniscectomy has severe consequences for knee mechanics. In one study, partial meniscectomy was found to reduce contact area (the load-bearing area on the articular cartilage) by ~10% and increase peak local contact stress (again, on the articular cartilage) by ~60% (Baratz et al. 1986). In another study, loss of 16–34% of the meniscus (basically, the entire inner meniscus) was found to increase contact stress by ~350% (Seedhom and Hargreaves 1979). Partial meniscectomy for radial tears was predicted by FEA to increase contact pressure (~50%), maximum principal strain (~20%) and stress (~40%), and pore pressure (~40%) in the articular cartilage

(Mononen et al. 2013). Another simulation of meniscectomized knees using FEA (using a linear elastic model) shows a doubling of compressive stress on the tibial cartilage with a 25% meniscectomy, tripling with 50% meniscectomy, and increasing by a factor of 6 with 75% meniscectomy (Atmaca et al. 2013). Total meniscectomy decreases contact area by about 75%, increases energy dissipation in cyclic loading of the joint (at 0° flexion), increases axial joint stiffness by 2-fold, and increases cartilage contact stress by 2 to 3-fold (Kurosawa et al. 1980; Baratz et al. 1986; Lee et al. 2006). Kettelkamp and Jacobs (1972) and Fukubayashi and Kurosawa (1980) also report greatly increased articular cartilage contact stress after removal of the medial meniscus. In a sheep model, meniscectomy was found to change the distribution of strains in the articular cartilage, creating a distribution with larger low-strain and high-strain regions, and smaller medium-strain regions, compared with strain patterns in a normal knee (Song et al. 2014). Removing the medial meniscus, combined with ACL section, allows greater increases in anterior displacement under ex vivo anterior-posterior loading (Levy et al. 1982). Resection of $\geq 50\%$ of the medial meniscus leads to AP laxity, but resection of 22% of the meniscus does not (Arno et al. 2013). Medial meniscectomy increases ACL graft forces by 33–50% (Papageorgiou et al. 2001). Overall, meniscectomy concentrates loads on the articular cartilage and destabilizes the knee, increasing stress and promoting damage.

Considering the severe over-stress and over-strain produced by meniscectomy, it is not surprising that it increases the risk of osteoarthritis (Petty and Lubowitz 2011; Magnussen et al. 2009; Shelbourne and Gray 2000). Lateral meniscectomy is associated with greater osteoarthritis risk than medial meniscectomy (Magnussen et al. 2009; Øiestad et al. 2009). Meniscectomy

in a rabbit model leads to changes in the magnitude and distribution of subchondral bone mineral density (Anetzberger et al. 2014). Fibrillation of the tibial cartilage started at 8 weeks post meniscectomy and progressed to complete erosion (with exposed bone) at 24 weeks post meniscectomy.

Physiologic loads are not precisely known for the meniscus, but the joint-scale motion and loading has been fairly well studied. Knee joint forces reach loads of 2–4 body weights during walking, and up to 8 body weights during running (Lento and Akuthota 2000). Force peaks last on the order of 0.1 s for walking, ascending and descending a ramp, and ascending and descending stairs (Morrison 1969). Limb loading rates during stair climbing are about 3.5 BW/s (Oliveira Silva et al. 2015). Knee joint contact forces have been predicted by static optimization for standing, walking, and running (Miller et al. 2015). The load peaks when walking and running were 0.2 s in duration (ascending and descending) Flexion/extension moments, varus/valgus moments, and internal/external rotation moments have been measured for running, sidestepping, and crossover cutting (Besier et al. 2001). Sidestepping and crossover cutting generate much greater varus/valgus and internal/external rotation moments than normal running (Besier et al. 2001).

Physiologic loading is sufficiently complicated that interpreting its effect on the meniscus requires some sort of simulation, usually FEA. Linear elastic FEA of meniscus suggests physiologic strains of about 0.04 (Aspden 1985). Chia and Hull (2008) used FEA with a compressive strain rate of 0.32 s^{-1} to represent walking. Mononen et al. (2015) have applied boundary conditions measured from gait studies to meniscus FEA with a fiber-reinforced poroviscoelastic

model. Validation revealed some issues, but the combination of this up-to-date model with gait data is an important step forward in meniscus FEA.

2.3 Mechanical testing of the meniscus

Tensile properties of the meniscus are reviewed and tabulated in Section 4.4.5, so only studies involving other loading modalities or variation of mechanical properties with other factors (such as meniscal region) are described here. The tensile modulus of the meniscus does not vary appreciably with circumferential position. Although Fithian et al. (1990) found that the anterior meniscus had greater modulus, Tissakht and Ahmed (1995) and Lechner et al. (2000) found no effect for circumferential position. These studies were of human medial meniscus. Lechner et al. (2000) had good statistical power, so there is good evidence for a lack of circumferential variation. The modulus of human medial meniscus in circumferential tension has also been reported to be insensitive to radial position (Lechner et al. 2000). However, Kelly et al. (1990), also testing in circumferential tension, found that the inner third of bovine meniscus is less stiff than the outer meniscus. Depth-dependent changes in modulus have also been reported. Whipple et al. (1985) found that the surface layer had equal stiffness in both radial and circumferential directions in uniaxial tension, but the deep slices were much stiffer in the circumferential direction than in the radial. The transition from surface in-plane isotropy to central anisotropy makes sense given that the surface layer is made of fibers with an isotropic in-plane dispersion, whereas the deep zone is made predominantly of circumferential fascicles.

Abraham et al. (2011) tested meniscal attachments in transverse uniaxial tension, compar-

ing the performance of several constitutive models: Neo-Hookean, Mooney-Rivlin, and Ogden. The Mooney-Rivlin model produced the best fit, although the Ogden model was similar. The authors also tested meniscal attachments in longitudinal tension, adding a fiber stress term similar to Quapp and Weiss (1998). Meniscus root (attachment region) strength has also been measured by Ellman et al. (2014), who showed that posterior medial, posterior lateral, and anterior medial roots were stronger in the native state than when sectioned as if for surgical reattachment. This decrease in strength after surgical sectioning was attributed to removal of the peripheral material surrounding the most dense part of the meniscus root.

Specimen thickness has been reported to cause variations in the tensile modulus of human meniscus specimens cut in the circumferential-axial plane and tested in the circumferential direction (Lechner et al. 2000). The modulus ranged from 120 ± 50 MPa for 0.5 mm thick specimens to 50 ± 70 MPa for 3 mm thick specimens.

2.4 Fracture testing of fibrous soft tissue

Cracks and other structural defects in materials can create stress concentrations, causing local failure and growth of the defect at loads that would be safe were the defect not present. This mode of failure is called fracture. The region of material in which the stress concentration causes local failure, and hence crack growth, is called the process zone (Taylor 2007). The process zone may be surrounded by a larger region called the plastic zone in which plastic deformation or damage occurs. Plasticity and damage dissipate energy, so a larger plastic zone tends to inhibit crack growth. A specimen with no crack fails when the stress exceeds the material strength. This

is called bulk rupture. When a crack is present, the specimen may fail either by bulk rupture or fracture, depending on its strength, resistance to fracture, and the applied load.

The driving force for fracture can be measured in terms of stress concentration magnitude or in terms of energy release per unit of crack extension. In an isotropic linear elastic material, stress near the tip of a sharp crack is proportional to $1/\sqrt{\text{distance from the tip}}$. The constant of proportionality includes the stress intensity factor K , which varies in proportion to $\sqrt{\text{crack length}}$. A longer crack thus produces a more severe stress concentration. Different modes of crack propagation are quantified with different stress intensity factors. The most commonly examined mode is tensile crack opening (mode I; K_I). In-plane shear is mode II (with K_{II}) and out-of-plane shear is mode III (with K_{III}). The fracture toughness is the critical stress intensity above which crack growth occurs. Some (short) cracks may never produce a large enough K to cause fracture before the material strength is exceeded and bulk rupture occurs.

Since fibrous soft tissue is mechanically nonlinear and anisotropic, energy-based approaches to quantifying fracture are often easier to implement than stress-based approaches. A strain energy release rate for a unit crack extension can be calculated or measured for a particular crack and loading. If the strain energy release rate exceeds the crack resistance of the material, the crack will grow.

Measurement of the strain energy release rate can be done by measuring the strain energy of repeated loading cycles. For two cycles with crack growth in between, the difference in strain energy between the cycles divided by the newly created crack area gives the strain energy release

rate (Taylor et al. 2012). Viscoelasticity and other energy dissipation mechanisms intrinsic to tissue complicate this measurement, but it is still possible (Oyen-Tiesma and Cook 2001; Koop and Lewis 2003). Viscoelastic energy dissipation throughout the entire tissue is distinct from the dissipative mechanisms operating local to the crack in the plastic zone. Measurement of the strain energy release rate from a single loading cycle is in principle possible, but must explicitly account for additional sources of energy storage, such as deformation of the tissue strips used for gripping (Rivlin and Thomas 1953).

Fracture tests of the meniscus, or tests of cracked meniscus specimens, have not been previously performed. In practice, whether fibrous soft tissue will fail is usually predicted using its strength (Kim 2000; Qasim et al. 2012; Qasim et al. 2014). Dropped masses have been used to create ACL rupture and meniscus tear in rabbits, both ex vivo and in vivo, but this requires a 1100 N impact load with a velocity at impact of ~ 3.8 m/s (Isaac et al. 2010; Isaac et al. 2008). The study was intended to produce an injury model (at which it succeeded), not measure mechanics. Roeddecker et al. (1994) performed trouser tear tests of meniscus scar 6 weeks after longitudinal crack introduction in a rabbit model and measured the tearing energy. The tearing energy was slightly lower near the tear tip compared to a contralateral control, suggesting accumulation of damage or insufficient healing. Interestingly, the energy required to create a full 11 mm tear was greater in the torn-and-healed group than the control. The trouser tear technique was also used by Sonoda et al. (2000) to measure the effect of hyaluronan treatment. The tearing energy measurements are not necessarily measures of fracture (any tear has an associated tearing energy regardless of the mechanism of failure), but with additional theoretical development

this approach could be used to predict the occurrence of fracture or its lack.

Cartilage is somewhat similar to the meniscus in structure and function, and its crack growth and fracture properties have also been studied. Overload of meniscus explants (0.5 unconfined compression strain applied at 1 s^{-1}) results in no structural damage (although some cell death occurs near the surface) (Kisiday et al. 2010). When the procedure is applied to cartilage, however, $10 \text{ }\mu\text{m}$ surface fissures were produced in 55% of specimens. Furthermore, compression testing of cartilage specimens with 1 mm long cracks was found to reduce the compressive strength to half that of uncracked specimens (Flachsmann et al. 2006). These data suggest that articular cartilage—at least, superficial zone articular cartilage—is more vulnerable to fracture than meniscus (fibrocartilage).

The limited available fracture data for other fibrocartilage tissues besides the meniscus also support the idea that articular cartilage is more brittle than fibrocartilage. The minimum process zone size in superficial articular cartilage is estimated to be in the $4 \text{ }\mu\text{m}$ to $50 \text{ }\mu\text{m}$ range (Taylor et al. 2012; Chin-Purcell and Lewis 1996), although it should be noted that a second study's data indicates a process zone size $> 0.1 \text{ mm}$ (Stok and Oloyede 2007; Taylor et al. 2012). (The process zone is the region near a crack tip that fails due to the crack-associated stress concentration and so propagates the crack in fracture.) Small process zones imply that little energy is required to propagate the crack; in other words, the material is more brittle. The temporomandibular joint disc, which is similar to the meniscus in both structure and function, is estimated to have a process zone size $> 1.8 \text{ mm}$ (Taylor et al. 2012; Koombua et al. 2006), suggesting a much greater toughness than the articular cartilage. On the other hand, the articular

cartilage data is inconsistent and the temporomandibular joint disc data only provides a lower limit, so firm conclusions are not possible.

2.5 Epidemiology of meniscus tears

Many types of tears occur in the meniscus. Major tear types are shown in Figure 2.2. Tear position is classified by dividing the meniscus into 3 circumferential segments (anterior, middle, posterior) and 4 radial segments (meniscosynovial junction, outer third, middle third, inner third) (Cooper et al. 1990). Different tear phenotypes (combinations of tear type, tear position, and which meniscus is torn) are associated with different etiologies. Broadly speaking, meniscus tear etiology falls into two groups: (1) acute tears, which are associated with a specific overload event/injury and are common in younger people and (2) degenerative tears, which are not associated with a specific injury.

Meniscus injury and meniscus-related surgeries are very common. Arthroscopic treatment of meniscus injuries comprised 10–20% of all surgeries in the U.S. in 1990 (Greis et al. 2002). Meniscus tears are associated with three causes in roughly equal proportion: (non-professional) sports-related injury, injuries unrelated to sports, and no identifiable cause (Drosos and Pozo 2004). A third of non-sporting injuries are sustained rising from or descending to a squatting position. In young people, meniscal injury is accompanied by a snapping or popping sensation (Wagemakers et al. 2008). Horizontal cleavage, flap, and complex tears are considered degenerative because they are more common in older patients (age > 40 years) who cannot recall a specific injury event (Drosos and Pozo 2004). Simple longitudinal tears and bucket handle

tears (which may have the “handle” torn into two pieces) are considered acute/traumatic. Longitudinal tears and bucket-handle tears typically occur in people aged 20–30 year in the middle and posterior sections of the meniscus (Lento and Akuthota 2000; Oberlander and Pryde 1994; Hardin et al. 1992). Shear stress has been hypothesized to be important in the formation of vertical and horizontal tears (Smillie 1978). The prevalence of meniscal tears increases with age, from ~25% per knee at age 50–59 years to ~45% at age 70–90 years (Englund et al. 2008). Drosos and Pozo (2004) have proposed that degenerative changes prior to 20 years of age diminish the elasticity of the meniscus and increase its susceptibility to injury.

The medial meniscus is more vulnerable to injury than the lateral meniscus because it is attached to the medial collateral ligament and so has less mobility (Lento and Akuthota 2000). Medial meniscus tears are 2–5 times as common as lateral meniscus tears (Campbell et al. 2001; Englund et al. 2008; Burk et al. 1988). The prevalence of lateral meniscus tears increases for sport-related meniscus tears, but is still less than the prevalence of medial meniscus tears (Drosos and Pozo 2004). In the sagittal plane, the medial tibial plateau is concave up (McDermott 2006). This could promote crushing and tearing of the medial meniscus.

Meniscus tears are considered to be a cause of osteoarthritis (Cohen et al. 2007; Englund et al. 2008). In individuals with risk factors for osteoarthritis (age 45–55 years), 64% had meniscus lesions and 79% had cartilage lesions (Laberge et al. 2012). Meniscus tears (as identified in 1.5T MRI) are much more common in people with radiographic evidence of osteoarthritis (an osteophyte or worse) than in those without (60% vs. 25%) (Englund et al. 2008). In patients with advanced knee osteoarthritis, the most common type of meniscal abnormality was a hy-

perthrophied displaced tear (Jung et al. 2010). Meniscus injury is a risk factor for developing osteoarthritis after ACL injury (Øiestad et al. 2009). At least part of the correlation between meniscus tears and osteoarthritis is probably mediated by tears being treated by meniscectomy, with meniscectomy being the proximal cause of ensuing osteoarthritis.

Meniscus tears can also adversely affect knee structures other than the articular cartilage, such as the ACL (Arnold et al. 1979). Conversely, injuries to the ACL make meniscus injury more likely (Bellabarba et al. 1997). In ACL-deficient knees, the medial meniscus load increases by 50–200%, depending on knee flexion (Allen et al. 2000; Papageorgiou et al. 2001). More than one third of meniscus tears are associated with an ACL injury (Poehling et al. 1990), and about one third of knees with ACL injury also have meniscus tears, mostly of the medial meniscus (Warren and Marshall 1978). Patients with ACL tears due to a jumping injury are more likely to have meniscus tears than patients with a non-jumping injury (Paul et al. 2003).

Optimal management of meniscus tears is uncertain. Surgeons tend to consistently agree on the treatment of meniscus tears (Dunn et al. 2004). However, it is still difficult to definitively say whether any given tear can be left untreated (Duchman et al. 2015). There is concern about tear-induced joint instability or post-surgical rehabilitation causing tear extension (Lento and Akuthota 2000). At least some incomplete tears appear to be stable and best left untreated. Longitudinal partial-thickness tears, stable (< 5 mm long) full-thickness peripheral tears, and short (< 5 mm long) radial tears may not require surgical repair (Lento and Akuthota 2000). Calling a tear stable means that the tear doesn't affect the local rigidity of the meniscus upon (arthroscopic) manipulation. Definitions do vary; Duchman et al. (2015) define a stable tear

as one that cannot be moved into the intercondylar notch, and say there is little consistency in definitions between studies. Treatment for incomplete longitudinal tears and complete stable longitudinal tears is considered to not be required (Feucht et al. 2015; Pujol and Beaufils 2009; Fitzgibbons and Shelbourne 1995). Root tears, complete radial tears, and bucket handle tears, however, are mechanically relevant and should be repaired as soon as feasible (Feucht et al. 2015; LaPrade et al. 2014; Forkel et al. 2014; Ode et al. 2012; Schillhammer et al. 2012; Kluczynski et al. 2013). A rule of thumb is that any medial meniscus vertical lesion ≥ 10 mm long that is associated with ACL tear requires repair (Seil et al. 2009). These judgment calls are not especially accurate. Considering specifically tears discovered during ACL repair, 4–22% of untreated lateral meniscus tears undergo subsequent reoperation in a 6-year followup, as do 10–66% of untreated medial tears (Duchman et al. 2015; Pujol and Beaufils 2009). Lateral meniscus tears tend to scar and heal better than medial meniscus tears if left in situ (Seil et al. 2009). Medial meniscus tears tend to produce secondary tears if left in situ. Overall, the behavior of tears is not predictable at this time, and judgment calls are made based on accumulated experience rather than mechanical or biological rationale.

2.6 Mechanical models for meniscus

Modeling of the meniscus began with linear elastic models, and these are still used in some studies (Mononen et al. 2013; Aspden 1985; Peña et al. 2005; Mononen et al. 2013). The meniscus has anisotropic properties due to its anisotropic fiber organization. Anisotropy is often dealt with by using a transversely isotropic model or an orthotropic model. However,

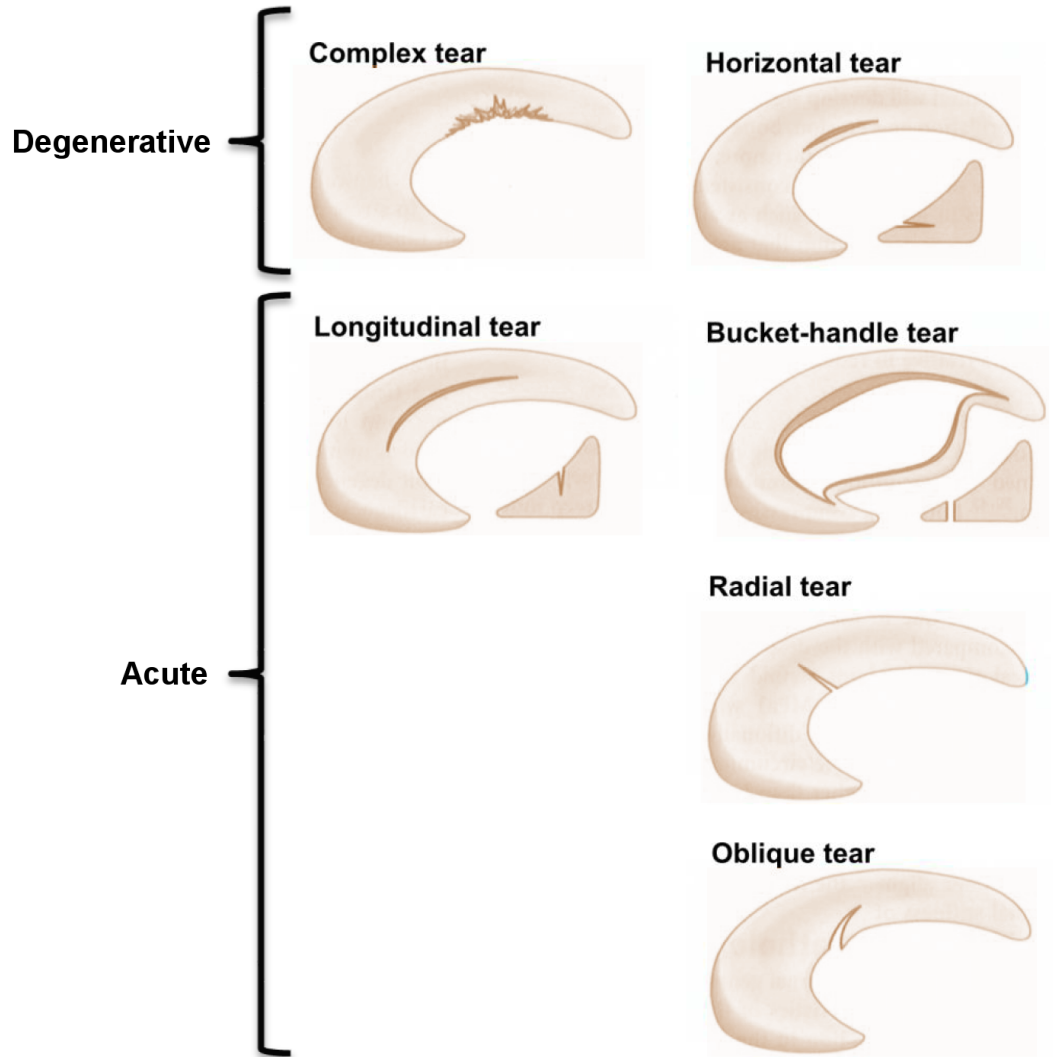


Figure 2.2: Typical meniscus tear morphologies (O’Keefe et al. 2013). Complex and horizontal tears are thought of as degenerative and longitudinal, bucket handle, radial, and oblique tears are thought of as resulting from acute injury. Complex tears are more broad than illustrated, similar to an amalgamation of several other tears. Bucket-handle tears and longitudinal tears may also be called circumferential tears. Nomenclature varies slightly between publications.

the meniscus is nonlinear. Its stress–strain curve has a low-stiffness toe region, followed by a strain-stiffening regime, an inflection point (which is matched with the yield point in Chapter 4), a strain-softening region, and ultimately the peak point. The nonlinear mechanics of the meniscus have been modeled using an exponential or a piecewise quadratic and linear formulation (Stabile et al. 2010; Mow et al. 2005; Upton et al. 2006; Párraga Quiroga et al. 2014; Tissakht and Ahmed 1995). Tissakht and Ahmed (1995) used a piecewise polynomial fit with a quadratic equation for the toe region and a linear equation for the linear region. Wren and Carter (1998) used a composite model containing both a fiber and matrix phase, with each phase failing at a specified strain. The model included uncrimping and fiber reorientation. The predictions of this model were compared to data from Proctor et al. (1989) and showed a qualitatively good match. This model by Wren and Carter (1998) is particularly interesting because it predicts a jagged descending profile for the post-peak stress–strain curve, which qualitatively matches experiments (for example, refer to Figure 4.5). Biphasic models have also been used to represent the mechanical effects of intra-meniscal fluid flow and hydrostatic pressurization (Párraga Quiroga et al. 2014; Spilker et al. 1992). Spilker et al. (1992) represented the solid phase as a linear elastic material. Párraga Quiroga et al. (2014) used a combination of a nonlinear isotropic matrix term and two exponential fiber terms (one directional, one quasi-isotropic) for the solid phase. The collagen fibers are sometimes modeled as a viscoelastic material, for instance using the standard linear solid model (Párraga Quiroga et al. 2014). A recent model by Mononen et al. (2015) combines a viscoelastic fibril network term with a neo-Hookean porohyperelastic matrix. However, the fibril network term was an isotropic homogenization over 13 fibril directions

(Wilson et al. 2004). Not all of these models have been fit to data or validated, and much work remains to be done. Only the model by (Wren and Carter 1998) represents damage or failure.

CHAPTER 3: A COMPARISON OF STRESS IN CRACKED FIBROUS TISSUE SPECIMENS WITH VARIED CRACK LOCATION, LOADING, AND ORIENTATION USING FINITE ELEMENT ANALYSIS

3.1 Introduction

Cracks in fibrocartilage are a common pathology with potentially severe consequences. Meniscus cracks cause pain, compromise knee motion and, most importantly, promote osteoarthritis (Englund et al. 2012; Bedi et al. 2010; Mononen et al. 2013; Maffulli et al. 2010; Berthiaume et al. 2005; Lento and Akuthota 2000; Lohmander et al. 2007). Overload of the knee meniscus, such as in sport-related injuries, can create cracks (Isaac et al. 2010; Drosos and Pozo 2004; Fox et al. 2015; Snoeker et al. 2013). In the intervertebral disc annulus fibrosus, cracks (i.e., tears) occur as the disc degenerates, causing pain or mechanical disruption (Osti et al. 1992; Vernon-Roberts et al. 2007; Haughton et al. 2000; Lee et al. 2004; Peng et al. 2005; Videman and Nurminen 2004). Furthermore, cracks in avascular fibrocartilage have poor healing potential (Arnoczky and Warren 1983).

Cracks can grow quickly, so the future risk posed by a given crack is not necessarily obvious. A crack creates a stress concentration at its tip that facilitates local failure and thus crack extension (fracture) (Anderson 2005). Even a small, asymptomatic crack may consequently be cause for concern. However, the mechanisms and mechanical loading conditions required for crack extension in fibrocartilage (and other fibrous soft tissues) are still largely unknown.

It has proven very difficult to produce crack extension in ex vivo mechanical testing. Only a few publications report fracture toughness for fibrous soft tissue (Purslow 1985; Stok and Oloyede 2007; Chin-Purcell and Lewis 1996; Oyen-Tiesma and Cook 2001; Koombua et al. 2006; Beatty et al. 2008; Wu et al. 2006b). Taylor's review of these studies indicated that most did not actually produce fracture (Taylor et al. 2012). Von Forell et al. noted a lack of crack extension in their fracture tests of Achilles tendon and anterior longitudinal spine ligament (Von Forell et al. 2014). Although fracture is not necessarily a relevant failure mode for all fibrous tissues (Taylor et al. 2012), cracks in fibrocartilage clearly do grow in vivo.

The absence of crack extension in most experiments may be caused by loading conditions that do not sufficiently represent in vivo conditions. The fracture tests cited above were all done using edge-cracked specimens in uniaxial tension, with the crack perpendicular to the edge of the specimen. In contrast, in vivo cracks (1) are often situated in the middle of the tissue, (2) are loaded multiaxially, and (3) come in a variety of orientations (Shieh et al. 2013; Swenson and Harner 1995; Osti et al. 1992; Kawamura et al. 2003; McNally and Adams 1992; Yoder et al. 2014).

The objective of this study was to identify candidate test configurations that are likely to produce crack extension. This information will be used to plan future experiments. Finite element analysis (FEA) was used to compare specimens with varying (1) crack location (center vs. edge), (2) loading (uniaxial vs. biaxial), and (3) crack-fiber angle. The likelihood of fracture was compared using the magnitude of the crack-induced stress concentration. Greater stress was interpreted as greater fracture risk. Since fibrous tissue has multiple failure mechanisms,

including fiber rupture, matrix rupture, and fiber sliding, fracture risk was evaluated separately for fiber-parallel, fiber-perpendicular, and fiber shear stress.

We hypothesized that at least one of the test configurations would have a greater stress concentration (a greater risk of fracture) than uniaxially loaded edge crack specimens. Our results partially supported this hypothesis. Center crack specimens with oblique crack-fiber angles produced greater fiber-parallel stress, and thus a greater likelihood of fiber rupture, than edge crack specimens. Edge crack specimens instead produced greater fiber-perpendicular stress (matrix rupture) and fiber shear stress (fiber sliding).

3.2 Materials and methods

3.2.1 Specimen geometry and loading

The finite element specimen geometry was a 1 mm thick plate, which was meant to represent typical tensile test specimens. Through-thickness slit cracks were created either in the center or edge of the plate. The center crack meshes were 20 mm \times 20 mm \times 1 mm, with a 2 mm long crack, and the edge crack meshes were 10 mm \times 20 mm \times 1 mm, with a 1 mm long crack (Figure 3.1). All cracks thus had a characteristic crack length of 1 mm (Janssen et al. 2002).

Uniaxial or biaxial tensile stretch was applied by displacing the edge nodes. Biaxial stretch was chosen because it is a standard test procedure for multiaxially loaded tissue (Sacks and Sun 2003; Bass et al. 2004; O'Connell et al. 2012). Thus, three combinations of crack location and loading were examined: center crack biaxial (CCB), center crack uniaxial (CCU), and uniaxially

loaded single edge notch (SENT) (Figure 3.1).

In all cases, the stretch ratio in the fiber direction was set to 1.14. The CCB case was stretched equibiaxially in the x - y plane. The uniaxially loaded cases were stretched parallel to the fiber axis, and the fiber-perpendicular axis was free to contract. This stretch ratio was chosen to fully load the simulated fibers, such that the resulting stress (~ 70 MPa) would be the same order of magnitude as fibrous tissue strength (LaCroix et al. 2013; Green et al. 1993; Skaggs et al. 1994b; Holzapfel et al. 2005; Ebara et al. 1996; Tissakht and Ahmed 1995).

3.2.2 Crack-fiber angle

For each configuration, the crack angle was varied relative to the fibers from 0° (parallel to the fiber axis) to 90° (perpendicular to the fiber axis). This variation was done in 15° increments. There is one exception: the SENT specimen has no 0° SENT case, as in that case the crack line and specimen edge would coincide.

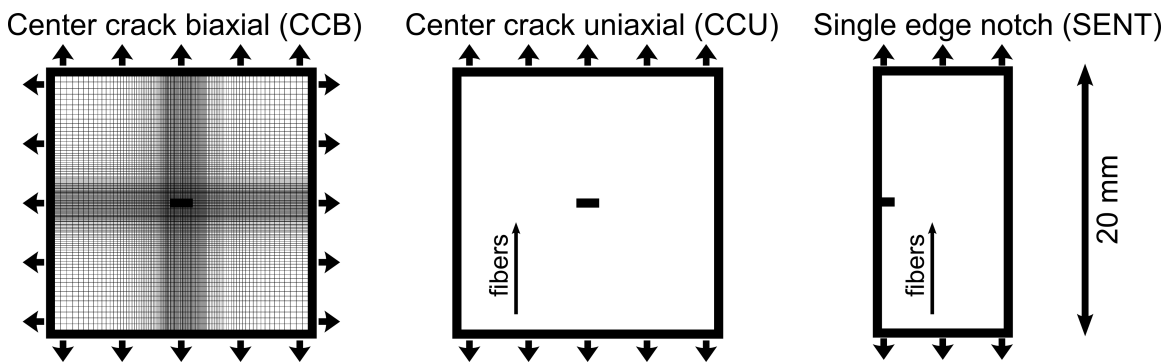


Figure 3.1: Test configurations. Three configurations were compared: center crack biaxial (CCB), center crack uniaxial (CCU), and single edge notch (SENT). Each is illustrated here for a crack perpendicular to the fibers. The crack angle was varied in each case.

3.2.3 Mesh construction

Meshes were created using 8-node trilinear brick elements. A primary goal of the meshing procedure was to ensure that differences in outcome between cases were not caused by differences in mesh geometry. Consequently, we explicitly defined the size and position of each element relative to the crack such that where large deformation gradients existed (i.e., near the crack tip) elements were sized and positioned the same for every load case. The mesh contained five layers of elements in the out-of-plane direction. Since the strain gradients were expected to be greatest at the crack tip, the element size was log-biased, with the smallest elements at the crack tip (Figure 3.1). The crack tip element size was parameterized, and all other element sizes were relative to this minimum element size. All elements touching the crack face were set to the minimum element size. In some of the center crack cases, regions containing large stress gradients extended further from the crack than in the SENT cases; consequently, for the center crack cases all elements within 1 mm of the crack were set to the minimum element size.

The effect of element size on the computed stress field was investigated by varying the minimum element size (the size of the elements near the crack tip). Three sizes were examined: 50 μm , 100 μm , and 200 μm . For all analysis other than the convergence study, the 50 μm mesh was used.

3.2.4 Constitutive model and material properties

Fibrous tissue mechanics were represented by a mixture model with matrix and fiber terms. The matrix was represented by the (isotropic) Holmes-Mow strain energy function (Holmes

and Mow 1990; Jacobs et al. 2014; Jacobs et al. 2013)

$$\Psi_m(I_1, I_2, J) = \frac{1}{2} \frac{\lambda + 2\mu}{2\beta} \left\{ e^{\frac{\beta}{\lambda+2\mu} ((2\mu-\lambda)(I_1-3) + \lambda(I_2-3) - (\lambda+2\mu) \ln J^2)} - 1 \right\}. \quad (3.1)$$

The fibers were represented by the exponential-power strain energy function

$$\Psi_f = \frac{\xi}{c_1 c_2} (\exp [c_1 (I_n - 1)^{c_2}] - 1). \quad (3.2)$$

The total strain energy is the sum of Ψ_m and Ψ_f . The λ and μ parameters are calculated from E and ν using $\lambda = \frac{E}{(1+\nu)(1-2\nu)}$ and $\mu = \frac{E}{2(1+\nu)}$. The material parameters were $E = 75.8$ kPa, $\nu = 0.2205$, $\beta = 0.9438$, $c_1 = 65$, $c_2 = 2$, and $\xi = 296$ kPa. These parameters were previously obtained and validated for annulus fibrosus in the context of organ-scale intervertebral disc FEA (Jacobs et al. 2013; Jacobs et al. 2014). They are qualitatively similar to meniscus fibrocartilage, which is sufficient for the aims of this study.

3.2.5 Stress components

Due to the composite structure of fibrous soft tissue, crack extension can occur by multiple mechanisms: fiber rupture (fiber-parallel stress), matrix rupture (fiber-perpendicular stress), and fiber sliding (fiber shear stress). Therefore, Cauchy stress (σ) tensors were expressed in a fiber-aligned coordinate system, defined as follows: axis 1 is parallel to the fibers, axis 2 is perpendicular to the fibers (in the specimen plane), and axis 3 is normal to the specimen plane. Fiber rupture risk was assessed using fiber-parallel stress (σ_{11}), matrix rupture risk was assessed using fiber-perpendicular stress (σ_{22}), and fiber shear risk was assessed using fiber shear stress

(σ_{12}). Fracture risk was ranked separately for each failure mechanism.

3.2.6 Fracture risk analysis

Fracture risk was compared between cases (CCB, CCU, and SENT, each with varied crack-fiber angles) using the peak stress, which indicates the severity of the stress concentration (Sano et al. 2006). Greater stress was considered to indicate greater risk of fracture. The peak stress was calculated using two methods: (1) fitting a stress profile to obtain the crack tip stress and (2) calculating the stress at each element centroid and taking the maximum.

The stress profile fit was used because an FEA solution does not directly specify crack tip stress. To obtain the stress profile, stress was sampled at evenly spaced points on a line (in the reference configuration) extending from the crack tip, in the mid-z plane, in the same direction as the crack (Figure 3.2a). Interpolation within an element was done using a sub-element formed by its Gauss points. To obtain the stress at the crack tip, the near-tip part of this stress profile was fit with an exponential function (Figure 3.2b). This stress profile method was used for the fiber-parallel stress component.

For the fiber-perpendicular stress and fiber shear stress profiles, the stress profiles tended to be near-constant (e.g. Figure S1) or oscillatory (e.g. Figure S2). The fiber-perpendicular and fiber shear stress concentrations did not follow a conventional crack tip centered pattern (see results section 3.3.1), so in these cases the profile line did not sample the most relevant regions. The maximum element-wise stress was used as a workaround for these cases.

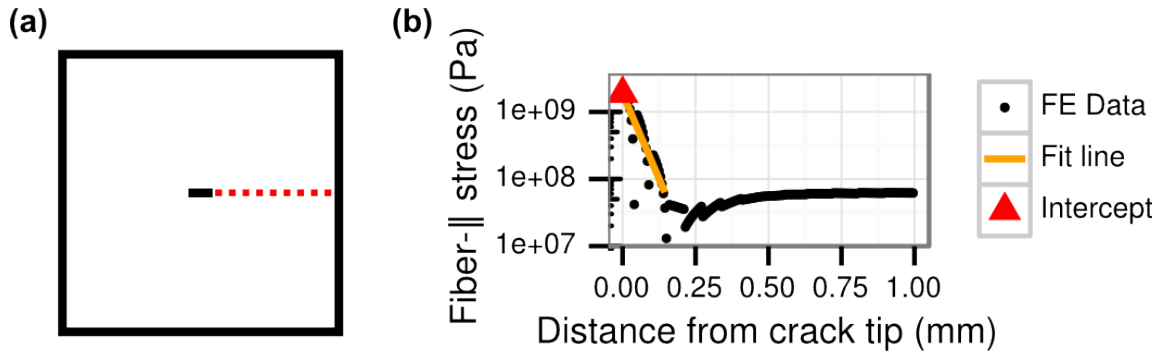


Figure 3.2: Quantification of crack tip stress. (a) Stress was sampled along a line (in the reference configuration) extending from the crack tip to the edge of the mesh. (b) To find the stress at the crack tip, the stress profile was fit with an exponential function and extrapolated to 0 mm distance. This example shows the fit for the 45° CCB case with 50 μm elements.

3.3 Results

3.3.1 Stress fields

Each stress component (fiber-parallel stress, fiber-perpendicular stress, and fiber shear stress) had a different spatial distribution. Fiber-parallel stress concentrations in all three test configurations were centered on the crack tip (Figure 3.3). The fiber-parallel stress concentrations extended far in the fiber direction, but hardly at all perpendicular to the fibers. Acutely oriented center cracks (Figure 3.3a,b) created more intense fiber-parallel stress bands than the other cases. Center cracks 90° to the fibers (Figure 3.3d,e) produced stress fields similar to SENT cracks of any orientation (Figure 3.3c,f).

Fiber-perpendicular stress concentrations were also centered on the crack tip (Figure 3.4). Acutely oriented center cracks produced fiber-perpendicular stress concentrations that extended for a short distance perpendicular to the crack, gradually curving to follow the fibers (Figure 3.4a,b). Regions of great tensile or compressive stress were also evident along the crack faces.

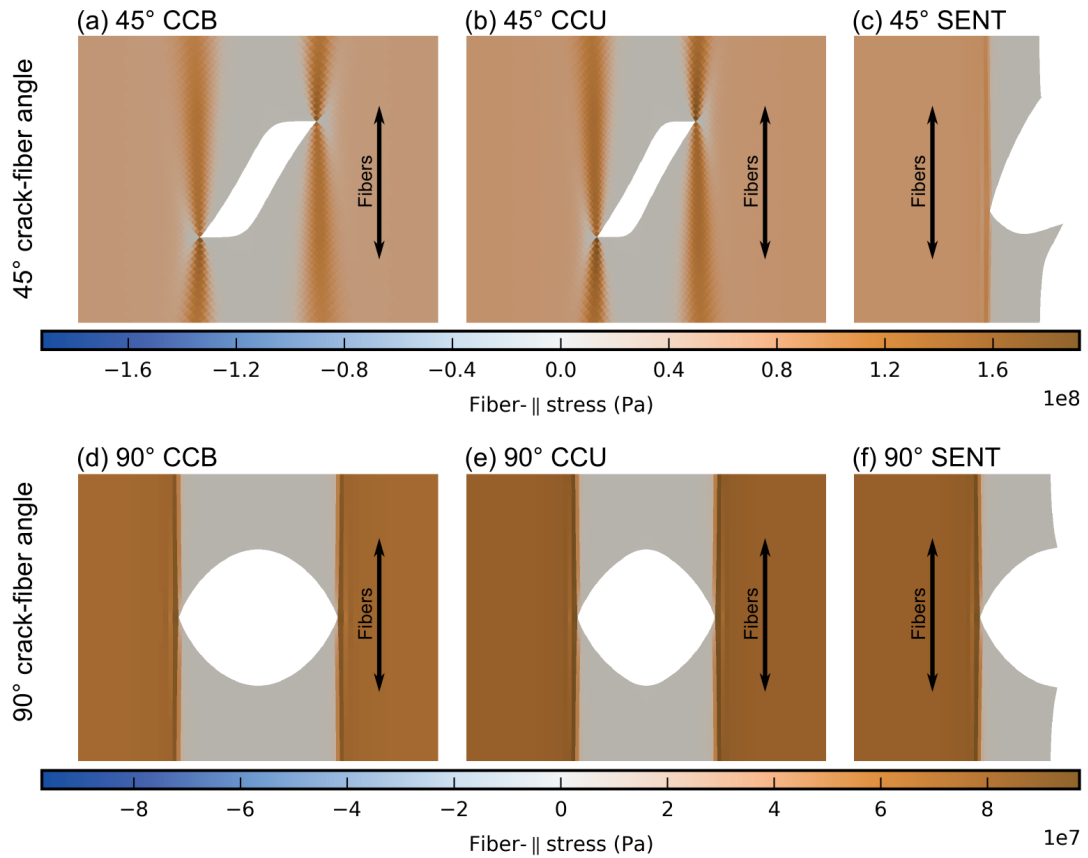


Figure 3.3: Fiber-parallel stress fields. (a) 45° CCB, (b) 45° CCU, (c) 45° SENT, (d) 90° CCB, (e) 90° CCU, and (e) 90° SENT. Each panel shows a 3.2 mm tall subregion of the specimen.

In contrast, the fiber-perpendicular stress concentrations produced by 90° center cracks, or any of the SENT cracks, were very local to the crack tip (Figure 3.4c–f).

Fiber shear stress concentrations for acutely angled center cracks were distributed in fiber-aligned bands above and below the crack faces (Figure 3.5a,b). The crack tip stress did not always dominate the fiber shear stress field; stresses similar in magnitude to the crack tip stress occurred ~ 1 mm away from the crack tip (asterisks in Figure 3.5a,b). However, 90° center cracks produced more conventional fiber shear stress concentrations that were tightly centered on the crack tip and elongated along the fiber axis (Figure 3.5d,e). The fiber shear stress in the

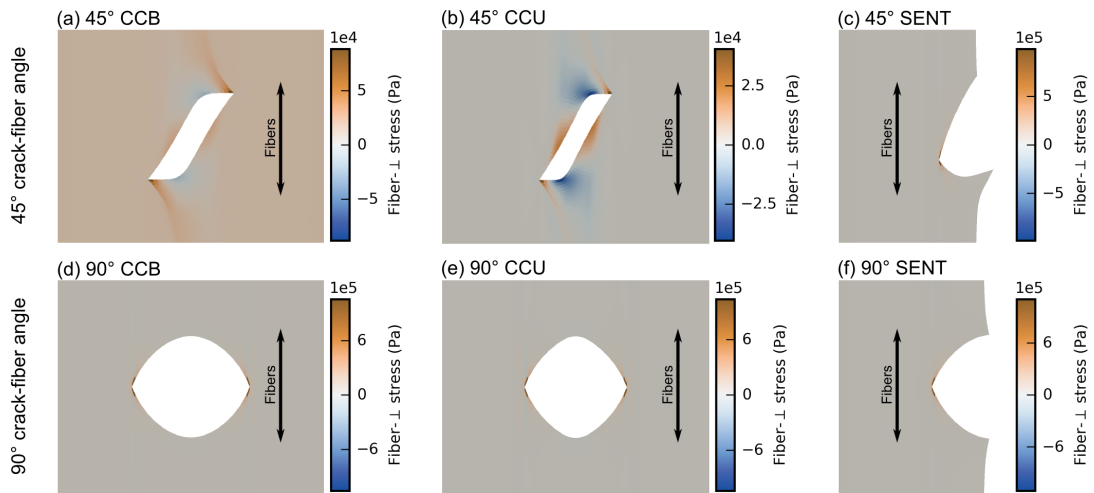


Figure 3.4: Fiber-perpendicular stress fields. (a) 45° CCB, (b) 45° CCU, (c) 45° SENT, (d) 90° CCB, (e) 90° CCU, and (e) 90° SENT. Each panel shows a 3.2 mm tall subregion of the specimen.

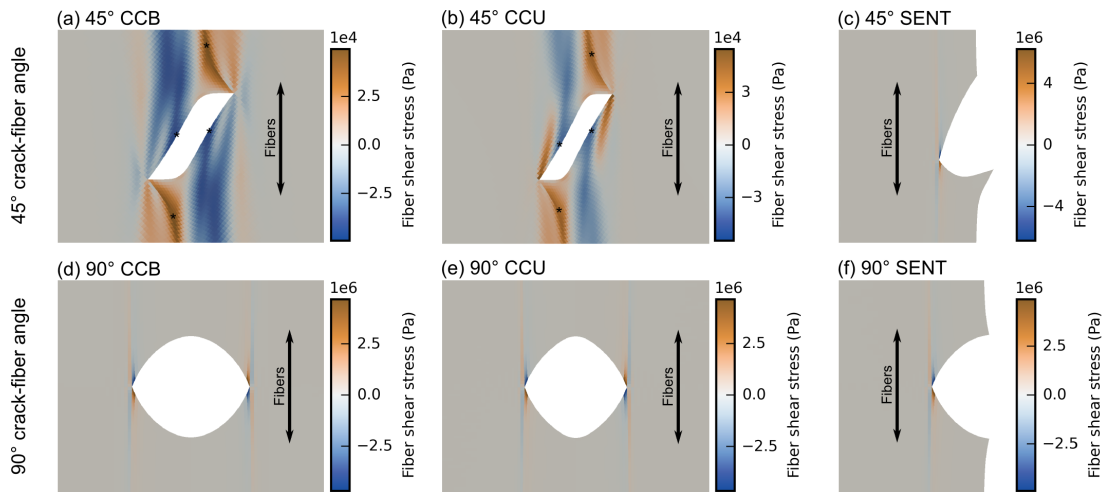


Figure 3.5: Fiber shear stress fields. (a) 45° CCB, (b) 45° CCU, (c) 45° SENT, (d) 90° CCB, (e) 90° CCU, and (e) 90° SENT. In panels a and b, asterisks mark locations with stress magnitudes similar to the crack tip stress, yet distant from the crack tip. Each panel shows a 3.2 mm tall subregion of the specimen.

90° center crack case, like the other stress components, was similar to the SENT cases (Figure 3.5c–f).

3.3.2 Relative stress concentration severity

The fiber stress at the crack tip, as quantified by stress profile fitting (section 3.2.6), was greatest for center-crack cases with oblique cracks (Figure 3.6). The CCB and CCU configurations were essentially identical. In contrast, the crack tip fiber stress for obliquely oriented SENT cracks were much less severe. Cracks oriented 90° to the fibers exhibited the same crack tip fiber stress for all three configurations. Cracks oriented 0° to the fibers did not increase the fiber stress relative to the crack-free condition.

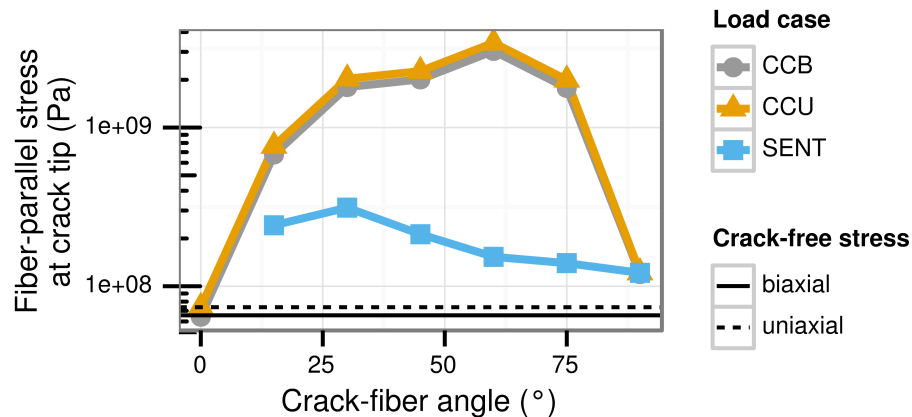


Figure 3.6: Fiber-parallel stress calculated by the stress profile fitting method. Center-cracked specimens with acutely angled cracks have greater fiber stress compared to edge-cracked specimens. 0° = crack parallel to fiber axis; 90° = crack perpendicular to fiber axis.

Since the matrix stress and fiber shear stress at the crack tip could not be obtained by fitting stress profiles (see section 3.2.6), they were instead quantified by the maximum element-wise stress (Figure 3.7). Fiber-perpendicular stress was equal between 90° CCB, CCU, and SENT

cases, but was greatly lessened for the center crack cases with crack-fiber angles $< 90^\circ$ (Figure 3.7b). Fiber-perpendicular stress for SENT specimens remained essentially constant regardless of crack-fiber angle. Similarly, fiber shear stress was equal for 90° CCB, CCU, and SENT cases, and decreased greatly for center crack cases with crack-fiber angles $< 90^\circ$ (Figure 3.7c). However, fiber shear stress for SENT specimens increased slightly as crack-fiber angle decreased.

As a consistency check, the maximum element-wise stress was also computed for the fiber-parallel stress. Trends in fiber-parallel stress measured by the maximum stress method are essentially the same as measured by the stress profile fits (compare Figure 3.7a to Figure 3.6).

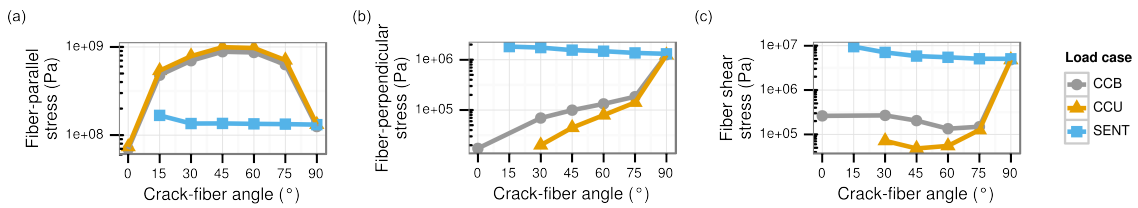


Figure 3.7: Maximum element-wise stress for (a) fiber-parallel stress, (b) fiber-perpendicular stress, and (c) fiber shear stress components. For fiber stress, Figure 3.6 uses a more robust metric. The 15° CCB and CCU cases are excluded from panels b and c because these cases nearly inverted some elements near the crack tip (shown in Figure S3), producing spurious values for fiber-perpendicular stress and fiber shear stress. The 0° CCU case has approximately zero fiber-perpendicular stress and fiber shear stress, so it is not shown in panels b or c. 0° = crack parallel to fiber axis; 90° = crack perpendicular to fiber axis.

3.3.3 Element size sensitivity

The crack tip fiber stress obtained from the stress profile fits was sensitive to the mesh size (Figure 3.8). Stress approximately doubled for each halving of the element size, with no apparent convergence to a limit.

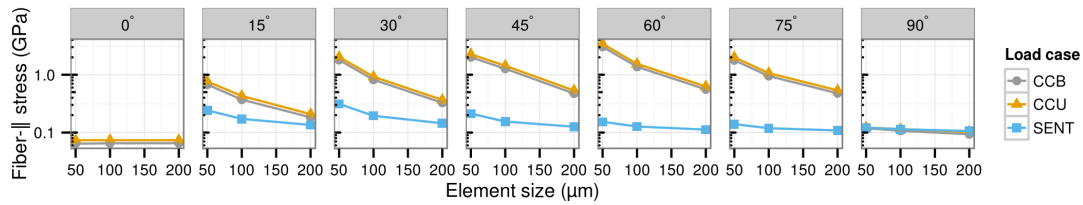


Figure 3.8: Effect of mesh element size on crack tip fiber stress. Each panel plots data from specimens with the indicated crack-fiber angle. For all acutely oriented cracks, smaller elements caused increases in stress. Specimens with a crack-fiber angle of 90° are much less sensitive to mesh size. Since specimens with cracks 0° to the fibers have no fiber stress concentration, they are insensitive to mesh size. 0° = crack parallel to fiber axis; 90° = crack perpendicular to fiber axis.

3.4 Discussion

3.4.1 Implications for physical crack extension testing

This study's primary purpose was to identify load configurations that are likely to cause crack extension and are thus good candidates for physical fracture testing. This was successful. Fiber rupture is most likely in center crack specimens with oblique crack-fiber angles, regardless of uniaxial or biaxial loading (Figure 3.6). Matrix rupture (perpendicular to the fibers) and fiber shear, however, are most likely in edge crack specimens or 90° center crack specimens (Figure 3.7b,c). Based on these results, the commonly used SENT configuration is a reasonable choice for tests of matrix rupture and fiber shear. Experiments instead meant to produce fiber rupture should include center-crack specimens with oblique crack-fiber angles.

When choosing a test configuration, the crack extension path must also be considered. Although the simulated SENT specimens did produce a relatively severe fiber-perpendicular stress and fiber shear stress concentrations, these stress components promote failure along the inter-

fiber boundary. For any crack not parallel to the fibers, extension (in the original direction of the crack) requires fiber rupture, which is promoted by fiber-parallel stress. Since the SENT configuration produces relatively weak fiber-parallel stress concentrations, it makes sense that crack extension has not been observed in experiments using this configuration. The strong fiber-perpendicular and fiber shear stress concentrations in the SENT configuration instead increase the likelihood of crack deflection or the creation of secondary cracks between fibers. Secondary cracks of this type, extending perpendicular to the main crack, are visible in Purslow et al.'s Figure 5 (Purslow 1985). In future work, it may be useful to systematically report secondary crack formation.

Crack extension by matrix rupture can be specifically studied using specimens with the loading axis perpendicular to both the fiber axis and the crack axis. This test configuration was not included in the present work because it leaves the fibers unloaded, but it has been previously applied to spine ligament, tissue engineered cartilage, deep zone articular cartilage, and temporomandibular joint disc (Von Forell et al. 2014; Koombua et al. 2006; Oyen-Tiesma and Cook 2001). Cracks did not extend in spine ligament (Von Forell et al. 2014), did extend in tissue engineered cartilage (Oyen-Tiesma and Cook 2001), and also extended in a subset of articular cartilage specimens (Chin-Purcell and Lewis 1996; Taylor et al. 2012). It was ambiguous whether the temporomandibular joint disc failed by fracture (Koombua et al. 2006; Taylor et al. 2012). This test configuration thus has a fair chance of producing crack extension, depending on the tissue.

Lastly, similar fiber stress between the CCB and CCU specimens (Figures 3.3a,b,d,e and

3.6) indicates that CCU specimens may be useful as a proxy for CCB specimens. Fiber-perpendicular stress and fiber shear stress are also similar, but less so (Figures 3.7b,c, 3.4a,b,d,e, and 3.5a,b,d,e). Uniaxial fracture testing for fibrous soft tissue is much easier than biaxial fracture testing, so the ability to substitute one for the other would be convenient.

3.4.2 Crack blunting and plastic deformation

The cracks changed shape dramatically during the simulation due to the high degree of material anisotropy and the large deformation. Cracks in the 0° and 90° center crack cases and all the edge crack cases opened extremely widely. Large elastic crack opening such as this blunts the crack and reduces the crack tip opening stress (Hui et al. 2003). In comparison, the oblique ($15\text{--}75^\circ$) center crack cases twisted into a tilde-like shape that maintained the sharpness of the crack tip and better concentrated the crack tip opening stress (Figure 3.3).

In a real material, plastic deformation will further contribute to crack blunting. Wide opening and blunting of edge cracks, with no crack extension, has been previously observed in physical testing of tissue and scaffolds (Stok and Oloyede 2003; Koh et al. 2013; Von Forell et al. 2014). Plastic inter-fibril sliding occurs in tendon (Szczesny and Elliott 2014b). SENT tests of ligament with fibers 45° to the loading axis showed blunting that was slanted along the fiber axis, consistent with fiber shear (Von Forell et al. 2014). The severity and kind of plastic blunting in the cases examined herein are not yet known.

3.4.3 Calculation of crack tip stresses and mesh sensitivity

We calculated crack tip stress by a fitting procedure (Figure 3.2) in an attempt to improve upon the use of maximum element-wise stresses. In elements with extreme stress gradients, such as those near the crack tip, small changes in sampling location cause large changes in the sampled stress value. Computation of maximum element-wise stresses uses the element centroids as sampling locations; thus, the sampling position is determined solely by the mesh geometry. This can be an unwanted source of variability. Additionally, the maximum is not a robust statistic; it only takes a single misbehaving element to distort the result. The crack tip stress obtained by fitting the stress profile corrects these disadvantages by using a specific sampling point and incorporating data from multiple elements. However, it is limited in that the stress profile must be sufficiently regular to suggest a fit. Thus, the stress profile method cannot supersede the maximum stress measure in all cases.

Note that the stress profile method is still sensitive to the element size in the mesh (Figure 3.8). This is because the underlying FEA solution is an approximation using a piecewise discontinuous linear strain field. Making the elements smaller improves the approximation; however, the true crack tip stress for a sharp crack (in an elastic material) is singular. Refinement of the solution therefore cannot cause the crack tip stress to converge to a finite value.

Comparison of the crack tip stress in the present study is really a comparison of the strength of the stress concentration, and the values only have meaning in terms of their relative rank. Extreme caution should be used when comparing stress values between studies, as the meshes are unlikely to have been prepared in the same way. Development of a metric for stress concen-

tration severity that is mesh-independent, and so can be compared between independent studies or used for prediction of in vivo failure, is a high priority for future work in biomechanics.

3.4.4 Limitations

This study has several limitations that should be considered when interpreting the results. The use of elastic models in this study means that damage and plastic deformation are not represented. Plasticity and damage may greatly affect the stress field in real specimens, most likely by reducing the stress concentration magnitude and spreading it over a larger region. Nonetheless, specimens with greater elastic stress concentrations should surpass the threshold for damage and plastic deformation before those with lesser elastic stress concentrations, so the elastic stress based ranking, albeit imperfect, is still useful.

Second, stress profiles could not be fit to the fiber-perpendicular and fiber shear stress fields, requiring that the fracture risk associated with these components be assessed using maximum element-wise stress. This measure is less robust than the crack tip stress fit used for the fiber-parallel stress. This lesser robustness is of greater concern when combined with severely deformed elements. Consequently, accurate maximum values for fiber-perpendicular stress and fiber shear stress could not be obtained for the 15° CCB and CCU cases (Figure 3.7b,c). Despite this, the crack tip stress obtained by stress profile fitting and the maximum element-wise stress had consistent trends for the fiber-parallel stress component (Figures 3.6 and 3.7a). This consistency increases our confidence in the use of maximum element-wise stress to compare the fiber-perpendicular and fiber shear stress concentrations.

Due to these limitations, we considered only the relative risk of failure modes between test configurations. Furthermore, since small differences are more likely to be artifactual or irrelevant, we interpreted only large (≥ 0.5 orders of magnitude) differences as meaningful.

3.5 Conclusion

The goal of this work was to identify good test configurations for producing crack extension in fracture tests of fibrocartilage. Center-cracked specimens with the crack 30° to 60° relative to the fibers were predicted to stress the fibers much more than commonly-used SENT specimens, and are therefore most likely to produce crack extension by fiber rupture. However, SENT specimens produce equal or greater fiber-perpendicular and fiber shear stress compared to center crack specimens. Consequently, SENT specimens are a good choice for investigating failure by matrix rupture and fiber sliding, although care must be taken to choose a test setup in which these kinds of failure can produce crack extension. These results will guide our choice of test configurations for future fracture testing of fibrous tissue.

CHAPTER 4: QUANTIFICATION OF MENISCUS TENSILE MECHANICS AND SELECTION OF SPECIMEN SHAPE

4.1 Introduction

The meniscus performs the critical function of distributing knee loads over articular cartilage and protecting it from overload. Meniscus damage impairs this function and may necessitate meniscectomy to resolve pain or mechanical symptoms, greatly increasing the risk of osteoarthritis. Due to the consequences of a mechanically compromised meniscus, there is great interest in developing methods to repair or replace damaged meniscus (Stapleton et al. 2008; Rodkey et al. 1999; Nerurkar et al. 2011; Fisher et al. 2015; Mauck and Burdick 2015). These efforts depend on accurate quantification of normal meniscus mechanics, damage, and failure. Mechanical property measurements must be reliable and functionally relevant, and procedural factors which affect the outcome of mechanical tests must be identified and controlled. These challenges merit careful attention; they have not been entirely solved for fibrous soft tissue in general or meniscus specifically. The specific objectives of this study are to quantify the meniscus' nonlinear mechanics, in the process resolving several issues pertaining to their quantification, and to determine the benefits and disadvantages of several popular specimen shapes for tensile testing.

The meniscus, like all fibrous soft tissues, has a nonlinear stress–strain curve in tension. It is

also anisotropic, necessitating testing in multiple loading directions. The meniscus is compliant at low strain (the toe region of the stress–strain curve), stiffens as strain increases (this region is often called the linear region), undergoes a loss of stiffness (strain softening), and finally ruptures. The strain stiffening is attributed to the incremental recruitment of collagen fibers (Mow et al. 2005). The nonlinearity of the stress–strain curve, which affects the toe region in particular, is usually left unparameterized, making it difficult to carry out tasks such as predicting the meniscus' in situ mechanical response. Some studies have modeled the nonlinear mechanics of the meniscus using an exponential or a piecewise quadratic and linear formulation (Stabile et al. 2010; Mow et al. 2005; Upton et al. 2006; Párraga Quiroga et al. 2014; Tissakht and Ahmed 1995). These phenomenological models, although they make mechanical predictions possible, are difficult to interpret in terms of meniscus structure or pathology. In this study, we quantify the stress–strain curve up to the strain softening regime using a structural model based on the concept of sequential fiber recruitment (Szczesny et al. 2012).

Meniscus mechanics are also quantified using non-model parameters. Historically, these have only included elastic modulus (slope of the stress–strain curve), peak strain (ultimate tensile strain), and peak stress (ultimate tensile strength) (Sweigart and Athanasiou 2005; Tissakht and Ahmed 1995; Kelly et al. 1990; Bullough et al. 1970; Lechner et al. 2000; Bursac et al. 2009; Stapleton et al. 2008; Tanaka et al. 2014; Proctor et al. 1989; Whipple et al. 1985; Stabile et al. 2010; Skaggs et al. 1994a). These metrics are useful and, compared to model-based approaches, are simple to measure. However, the elastic modulus is difficult to define due to the nonlinear stress–strain response of the meniscus. It is usually calculated using a linear re-

gression fit of the quasi-linear region where strain stiffening appears fully developed (Proctor et al. 1989; Viidik 1972; Anderson et al. 1993; Lechner et al. 2000; Tissakht and Ahmed 1995; Freutel et al. 2015; Bursac et al. 2009; Tanaka et al. 2014; Stabile et al. 2010), but there is no part of the stress–strain curve that is truly linear. The assignment of a linear region is thus rather arbitrary and so varies from study to study. The criteria used for assignment are often left unspecified, and human judgment on a case-by-case basis appears to tacitly be the most common procedure. Studies which reproducibly define the yield point do so using a strain or stress range relative to the peak value. While this solution is practical, it makes the linear region covariate with the peak point rather than specific to the stress–strain curve’s shape. The chosen range must be tweaked from study to study to ensure it corresponds to a region with quasi-linear behavior. The meaning of an elastic modulus obtained by fitting the linear region thus also varies. A related problem is identification of the transition from strain-stiffening to strain-softening; i.e., the yield point. This transition is a potentially important transition in function. The yield point has not yet been reported for meniscus. In this study we implement a procedure for measuring the meniscus’ elastic modulus and yield point based on the stress–strain curve’s shape, which should prove more robust than existing methods.

In an ideal tensile test, the specimen ruptures in the middle of the gauge region, away from the grips. This is called midsubstance rupture. It is desirable because the grips create local stresses by applying clamping force and restricting specimen deformation (Jacobs et al. 2013; Sun et al. 2005; Polzer et al. 2013). Rupture at or near the grip line thus occurs under different conditions than midsubstance rupture and measures a potentially different failure process. The

local grip stresses are complex and difficult to quantify, so tissue tests resulting in rupture of the gripped region are usually discarded (Lechner et al. 2000; Sweigart and Athanasiou 2005; Proctor et al. 1989). However, few studies report the rupture location; those that do so only report that midsubstance ruptures were used, and do not specify the rules by which midsubstance ruptures were identified. As a practical matter, classification of a rupture in a tissue specimen as a midsubstance or gripped region rupture is seldom clear. Tissue specimens are usually small, and ruptures can involve a large part of the specimen length. Many ruptures involve both the midsubstance and gripped regions (Anderson et al. 1993; Lechner et al. 2000). To help resolve uncertainty regarding how rupture locations should be identified, in this study we classified rupture locations in detail with illustrated definitions so that these classifications can be reproduced in future work. To help determine which rupture types should be considered valid test outcomes, we also compared mechanical test outcomes between rupture types.

Dogbone (DB)-shaped (also known as dumbbell-shaped) specimens are used to compensate for local grip-induced stresses by reducing the cross-sectional area in the specimen midsubstance, thus increasing its stress and the likelihood of midsubstance rupture. If the rupture is sufficiently far from the grip line that the local grip stresses have diffused into a uniform stress field, the midsubstance rupture is expected to be independent of grip effects (i.e., Saint-Venant's principle). Thus, dogbones in principle provide results unconfounded by grip effects and have been incorporated into test standards for many industrial materials (e.g., metal, plastic, leather) (*ASTM D638-14* 2014; *ASTM D2209-00* 2015; *ASTM E8/E8M-15a* 2015). They accordingly are the de facto standard for tensile tests of meniscus and other fibrous soft tissues (Skaggs et al.

1994a; Bowser et al. 2011; Lechner et al. 2000; Whipple et al. 1985; Proctor et al. 1989; Freutel et al. 2015). Rectangular specimens are also used, though, and may be preferable when specimens are only a few mm long (Villegas et al. 2007; Bursac et al. 2009; Sweigart and Athanasiou 2005; LeRoux and Setton 2002). However, for fibrous soft tissues, it is not clear whether the dogbone shape actually prevents grip effects from influencing test outcomes. Abatement of local grip stresses from the grips to the midsubstance region is unlikely in the (by necessity) short length of most tissue specimens (Reese et al. 2013; Skaggs et al. 1994b; Sun et al. 2005). To resolve the question of which specimen shape is preferable for meniscus testing, we compared dogbone specimens with rectangular specimens. Strain fields were measured to elucidate the role of grip-associated local stresses and other local stress sources.

The meniscus, due to the arc of its circumferential fibers, poses an additional complication: the inner side and outer corners of standard fiber-aligned circumferential dogbone (DB) specimens and rectangle (R) specimens have fibers that insert into only one grip. Therefore, we also compared these specimen shapes to a non-standard expanded tab (ET) shape (Tanaka et al. 2014). The ET shape has elongated grip-region tabs that follow the arc of the meniscus fibers and are meant to ensure that all fibers which cross the grip line have sufficient length inside the grips to be securely clamped. Quantitatively, the ET specimens are hypothesized to have a greater proportion of fibers loaded by the tensile test and thus greater apparent stiffness and strength.

In summary, the objective of this study was to comprehensively quantify the nonlinear mechanical properties of the meniscus in uniaxial tension and resolve several experimental issues

regarding quantification procedure, rupture location, and specimen shape. Since the meniscus bears multiaxial loads, tensile tests were done in both the circumferential and radial directions. The mechanical properties reported in this study, as well as the advances made regarding (i) structure-based modeling of the nonlinear toe-region, (ii) yield and modulus quantification, (iii) rupture location classification, (iv) local strain field heterogeneity, and (v) choice of specimen shape are each a significant step forward for meniscus research and, importantly, are applicable to fibrous soft tissues in general.

4.2 Methods

4.2.1 Specimen preparation and tensile test protocol

Meniscus specimens were prepared for uniaxial tensile testing in both the circumferential and radial directions (Figure 4.1). Bovine menisci were purchased from Animal Technologies, Inc. (TX) and stored at $-20\text{ }^{\circ}\text{C}$. Both medial and lateral menisci were used. The source animals were all greater than 3 years old. Specimens were cut from the center (mid-circumferential, mid-radial, and mid-axial region) of the meniscus. While whole, the meniscus was measured and the placement of the specimen boundary planned. Both sides of the meniscus were then planed using a cryomicrotome to obtain the desired specimen thickness. The specimen's curved edges were cut with a biopsy punch and the straight edges were cut with a 130 mm histology trimming knife or, for tight work, a #15 scalpel. The target dimensions were adapted on a specimen-specific basis to accommodate anatomic variation between animals such that the same

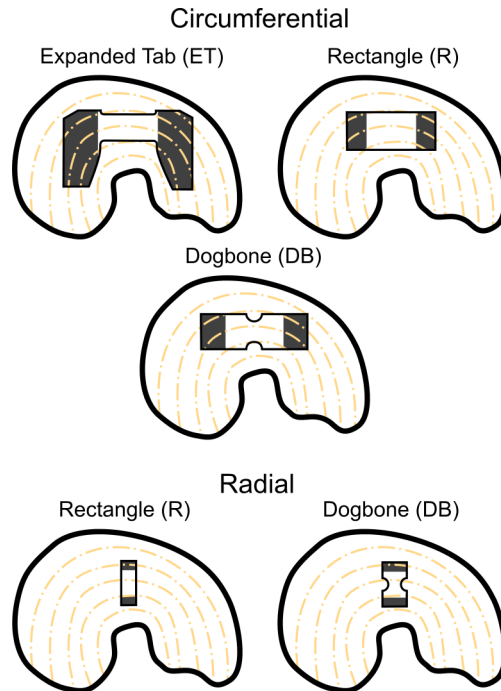


Figure 4.1: Meniscus specimen shapes used in this study and their dissection locations. The specimen and meniscus outlines are printed at 1:2 scale. The specimen outlines match the median dimensions used in this study. The gray shaded regions of the specimen were clamped by the grips. The dashed lines schematically illustrate the curved path of the meniscus' fibers.

anatomic region was sampled in all cases. For example, in an especially narrow meniscus, the width of a circumferential specimen or the length of a radial specimen was reduced to avoid the inner or outer regions. In a meniscus with a short anterior-posterior distance, and hence sharp fiber arcing, circumferential specimens were cut with reduced length to preserve grip-to-grip fiber continuity. Specimen cross-sectional area (i.e., thickness and width) was measured with a scanning laser displacement sensor (factory-specified z accuracy < 16 μm and x and y accuracy < 11 μm) (Szczesny et al. 2012; Favata 2006).

Circumferential tests used expanded tab (ET), rectangle (R), and dogbone (DB) shaped specimens (Figure 4.1). The ET shape was meant to improve grip-to-grip fiber continuity in

circumferential specimens by elongating the gripped tabs on the inner side of the meniscus, accommodating the arc of the circumferential fibers into the grips. Circumferential specimen dimensions were as follows. Specimen thickness was 1.3 ± 0.4 mm. ET specimens were 37 ± 2 mm long and 7.1 ± 2.5 mm wide in the midsubstance, with 1.5 mm radius fillets. The uniform-width midsection was 12.2 ± 1.8 mm long and the grip-to-grip length was 17.1 ± 2.4 mm. R specimens were 28 ± 4 mm long, 7.7 ± 1.4 mm wide, and the grip-to-grip length was 14.8 ± 3.6 mm. DB specimens were 28 ± 4 mm long and 8.8 ± 1.5 mm wide, with a 4.3 ± 1 mm wide midsubstance and 2 mm radius semicircular cutouts. Their grip-to-grip length was 15.4 ± 3.2 mm.

Radial tests used R and DB specimens (Figure 4.1). Radial specimen dimensions were as follows. Specimen thickness was 1.7 ± 0.2 mm. R specimens were 12.4 ± 2.6 mm long, 5.5 ± 1.0 mm wide, and had 7.8 ± 1.6 mm grip-to-grip length. DB specimens were 11.9 ± 1.6 mm long and 6.8 ± 0.8 mm wide, with a 3.8 ± 1.1 mm wide midsubstance. They had a grip-to-grip length of 8.3 ± 0.8 mm.

Prepared specimens were mounted in aluminum grips with 0.031 in tall 60° serrated teeth. A double layer of 400 grit cloth sandpaper was used to protect the specimen from the grips' teeth. The grips were tightened via bolts (2 per grip) to a standardized torque (8 in-lb; 4-40 thread) (Swank et al. 2014; Schechtman and Bader 1997). The grips were kept aligned by a rigid guide while the specimen was mounted and the grips tightened. The grips were then left to sit for ten minutes and tightened again to the target torque. The torque dropped to about 2 in-lb during this 10 min time. The surface of each specimen was speckle coated with Verhoeff's stain before it

was mounted on the mechanical tester to facilitate digital image correlation for strain analysis. The grips were then removed from the rigid guide and attached to an Instron 5943 tensile tester. Up to this point, the specimen was kept under gauze moistened with phosphate-buffered saline (PBS) except while being manipulated.

The specimen was loaded with a 20 kPa preload; the specimen length at this load was considered the undeformed length. Ten cycles of preconditioning to 4% strain were applied, followed by a displacement-controlled ramp to rupture. The displacement rate was 0.5 mm/s (quasistatic) for all tests. Video was recorded for each test at ~15 fps with a field of view of 1280×960 px and a scale of ~30 px/mm. The total testing time from removal of the damp gauze, through preconditioning and rupture was approximately 5 minutes. Circumferentially loaded ET specimens were tested in either air (5 in the final dataset) or PBS (14 in the final dataset). Other shapes were tested in air alone, except for 1 circumferentially loaded R specimen tested in PBS. Both test environments produced nearly identical stress–strain responses with no significant difference with respect to any measured parameters (Figure 4.2 and Table 4.1). Furthermore, the magnitude of the (non-significant) differences between tests in air and PBS were small relative to the differences observed between specimen shapes (compare Table 4.1 to Figure 4.7 or Table 4.3). Since there was no effect of test environment on the mechanical response, at least for this < 5 minute test duration, results from tests in air and PBS were pooled.

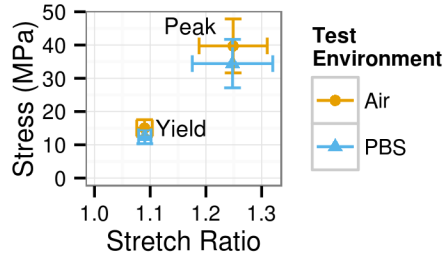


Figure 4.2: Mean and standard deviation of yield and peak points for circumferential ET specimens by test environment. The stress–strain response of specimens tested in air and PBS did not differ with respect to these points or any other measured parameter (see Table 4.1 for other parameters).

Table 4.1: Mechanical parameters compared between circumferential ET specimens tested in air and PBS. There was no significant difference with respect to any parameter and the 95% confidence intervals for potential differences are small.

	Air (Mean \pm SD)	PBS (Mean \pm SD)	Difference (95% CI)
λ_c	1.033 \pm 0.010	1.04 \pm 0.01	–0.017 to 0.008
λ_c^{SD}	0.016 \pm 0.004	0.020 \pm 0.004	–0.008 to 0.001
k_f (MPa)	264 \pm 35	238 \pm 48	–19 to 71
Yield Strain	0.09 \pm 0.02	0.09 \pm 0.01	–0.02 to 0.02
Yield Stress (MPa)	15 \pm 3	12 \pm 2	–0.43 to 5.66
Modulus (MPa)	271 \pm 41	231 \pm 43	–9.36 to 91.20
Peak Strain	0.28 \pm 0.08	0.28 \pm 0.09	–0.10 to 0.10
Peak Stress (MPa)	40 \pm 8	34 \pm 7	–4.58 to 15.22

4.2.2 Specimen characteristics and specimen exclusion

Sixty-seven bovine menisci were used for this study. From these menisci, 95 specimens were cut and tested. Specimens ruptured in a variety of ways, so ruptures were classified according to the following definitions (illustrated in Figure 4.3):

Midsubstance rupture The line of rupture did not cross or touch either grip line.

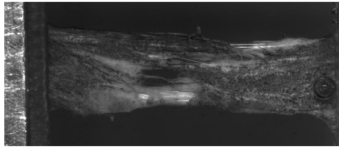
Mixed rupture The line of rupture touched or crossed a grip line, but did not qualify as any of the following rupture types. A mixed rupture can be thought of as a mix of midsubstance

Table 4.2: Specimen counts by rupture type, test axis, and specimen shape before and after excluding invalid ruptures and duplicate specimens from the same meniscus.

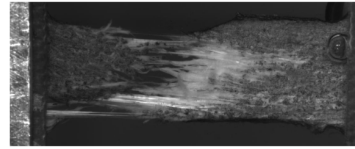
	Circumferential				Radial			
	ET	R	DB	DB	R	R	R	DB
Valid Failures								
Midsubstance rupture	6 (25%)	0 (0%)	1 (9%)	6 (24%)	5 (42%)			
Mixed rupture	10 (42%)	11 (48%)	4 (36%)	4 (16%)	2 (17%)			
Grip line rupture	4 (17%)	5 (22%)	2 (18%)	14 (56%)	4 (33%)			
Total	20 (83%)	16 (70%)	7 (64%)	24 (96%)	11 (92%)			
Excluded Failures								
Gripped region failure	4 (17%)	5 (22%)	4 (36%)	0 (0%)	0 (0%)			
Longitudinal split	0 (0%)	2 (9%)	0 (0%)	0 (0%)	0 (0%)			
No rupture	0 (0%)	0 (0%)	0 (0%)	1 (4%)	1 (4%)			
Total	4 (17%)	7 (30%)	4 (36%)	1 (4%)	1 (8%)			
Both	24 (100%)	23 (100%)	11 (100%)	25 (100%)	12 (100%)			
Discarded Duplicates	Total	1	4	2	16	3		
Final Dataset	Total	19	12	5	8	8		

(A) Circumferential specimen rupture types

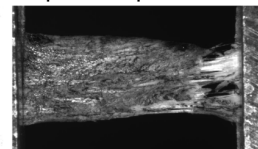
Midsubstance rupture



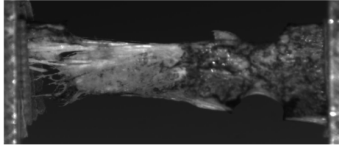
Mixed rupture



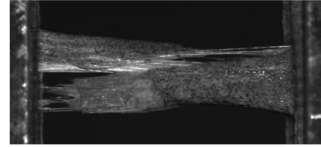
Grip line rupture



Gripped region failure

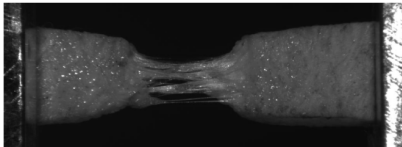


Longitudinal split

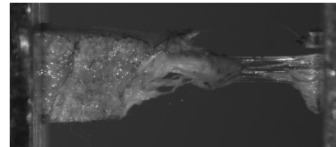


(B) Radial specimen rupture types

Midsubstance rupture



Mixed rupture



Grip line rupture

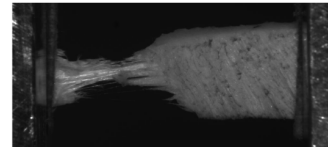


Figure 4.3: Classification scheme for types of specimen rupture. Circumferential specimens (A) ruptured in two more ways than radial specimens (B). Gripped region failures and longitudinal splits were considered invalid and excluded from mechanical analysis.

rupture and grip-related related rupture.

Grip line rupture The line of rupture was entirely within ~1 mm of the grip line, but did not enter the gripped region.

Gripped region rupture Rupture occurred inside the grips, and the rupture did not qualify as a longitudinal split.

Longitudinal split The line of rupture bisected the specimen lengthwise.

Counts of tests ending in each rupture type are given in Table 4.2 for each specimen shape and loading direction. Images of individual specimens are listed in Appendix A. Gripped region ruptures were excluded from further analysis because the stress field within the grips is unknown. Similarly, tests ending in longitudinal splits were excluded because the stress across the

rupture surface is unknown. Counts of tests ending with valid and excluded rupture types are given in Table 4.2.

After these exclusions, the sample set still included some duplicate specimens of the same shape cut from the same meniscus. (These duplicates were originally prepared with the aim of doing paired tests, but fair paired comparisons were not possible due to the variety of rupture outcomes.) To avoid considering within-meniscus covariance in the analysis, these duplicates were excluded first by dropping grip line ruptures, then at random, until each remaining specimen in each shape category came from a unique meniscus (Table 4.2). The final specimen counts used in each group for analysis, after all exclusion criteria were applied, are given in the last row of Table 4.2. The circumferential DB specimen count is low because, as the experiment proceeded, many issues with this shape became apparent (see Section 4.4.8). We consequently phased out the use of DB specimens.

4.2.3 Data analysis

Strain was measured using grip-to-grip displacement (grip strain) and reported in the form of the stretch ratio ($\lambda = l/l_0$, where l is the current length and l_0 is the undeformed length) or Lagrange strain ($E_{xx} = 1/2[\lambda^2 - 1]$). Stress was calculated using the initial cross-sectional area of the narrowest region of the specimen. The stress–strain curve was quantified by fitting it to a fiber recruitment model developed to represent the toe region (see Section 4.2.4) and by measuring yield strain, yield stress, tangent modulus at yield, strain at peak stress (peak strain), and peak stress (Figure 4.4, top half). The yield point was defined as the first inflection point

in the stress strain curve (Goh et al. 2012), which was identified by fitting a cubic smoothing spline (using the `smooth.spline` function in R 3.2 (Team 2015) with `spar = 1.0`) to the pre-peak stress–strain curve and taking its first derivative to obtain a smooth tangent modulus curve (Figure 4.4, bottom half). This procedure equates yield with the inflection point.

Strain fields were measured from video records of each test by digital image correlation using Vic-2D 2009 (Correlated Solutions). The parameters used in the digital image correlation are documented in Appendix B. An image taken between the preconditioning and ramp to failure steps was used as the zero-strain reference point. The correlation window was $0.7 \text{ mm} \times 0.7 \text{ mm}$. All strain fields were plotted in the reference space.

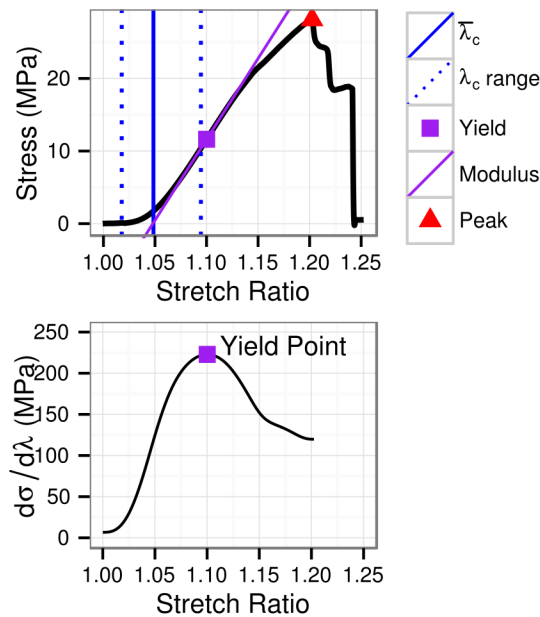


Figure 4.4: A representative stress–strain curve for circumferential ET specimens with the fiber recruitment range (the 0.025 and 0.975 quantiles of λ_c), mean fiber recruitment stretch ($\bar{\lambda}_c$), yield point, and peak point marked. The lower plot shows the point-wise tangent modulus curve (the first derivative of the stress–strain curve), the first local maximum of which was identified as the yield point. Both plots share the same x-axis.

4.2.4 Fiber recruitment model

The nonlinear stress–strain response of circumferentially loaded specimens was quantified using a fiber recruitment model (Szczesny et al. 2012; Sacks 2003; Lanir 1983). The model represents the tissue as an assembly of linear stiffness fibers aligned with the loading axis. Since radial specimens have fibers primarily perpendicular to the loading direction, the model was not applied to these tests. Sequential recruitment of fibers is represented by making the stretch at which each fiber starts to bear load, λ_c , a randomly distributed variable. Here, λ_c is called the fiber recruitment stretch. In other work, it is usually called the uncrimping stretch, but in this work we interpret λ_c as representing fiber reorientation into the loading direction as well as fiber uncrimping. Although the fibers are linear, the randomly distributed recruitment causes a nonlinear response.

Fibers are assumed to have linear stiffness k_f and bear no load in compression, such that the stress in the fibers is

$$\sigma_f = \begin{cases} k_f \epsilon_f & \epsilon_f \geq 0 \\ 0 & \epsilon_f < 0 \end{cases} \quad (4.1)$$

where ϵ_f is the fiber strain. The fiber stiffness k_f is assumed to be the same across all fibers.

The fiber strain is related to the fiber recruitment stretch λ_c and the tissue stretch λ by

$$\epsilon_f = \frac{1}{2} \left(\frac{\lambda^2}{\lambda_c^2} - 1 \right). \quad (4.2)$$

The variation in fiber recruitment stretch (i.e., fiber initial state) is given by the probability

density function

$$G(\lambda_c) = (\lambda_c - 1)^{\alpha-1} \frac{e^{-(\lambda_c-1)/\beta}}{\beta^\alpha \Gamma(\alpha)} \quad (4.3)$$

which is a gamma distribution with shape parameter α , location parameter = 1, and scale parameter β (Γ is the gamma function). The mean recruitment stretch ($\bar{\lambda}_c$) and the square root of the variance of the recruitment stretch (λ_c^{SD}) were calculated to make the physical meaning of the model clearer. They are related to the distribution parameters by

$$\bar{\lambda}_c = \alpha\beta + 1 \quad (4.4)$$

and

$$\lambda_c^{SD} = \sqrt{\alpha\beta^2}. \quad (4.5)$$

The overall tissue stress σ is given by integration over the fiber population.

$$\sigma = \frac{k_f}{2} \int_1^\lambda G(\lambda_c) \left(\frac{\lambda^2}{\lambda_c^2} - 1 \right) d\lambda_c \quad (4.6)$$

This fiber recruitment model was fit to the pre-yield stress–strain curve (the model is purely elastic) using the Levenberg-Marquardt algorithm implemented in SciPy (Jones et al. 2001).

The variables $\bar{\lambda}_c$, λ_c^{SD} , and k_f were used to report the model fit and compare specimen shapes.

4.2.5 Statistics and inference

Comparisons between the specimen shapes were done separately for circumferential and radial tests using the fiber recruitment model variables (for circumferential specimens only) and the five stress–strain curve summary statistics (for both radial and circumferential specimens). Circumferential tests of ET, R, and DB specimens were compared by ANOVA, followed by Tukey’s HSD post-hoc tests if indicated. Fiber recruitment model parameters were compared between ET and R specimens using Mann-Whitney-Wilcoxon tests. Radial tests of R and DB specimens were compared by two-sided Welch t-tests. The significance threshold was set at $p = 0.05$ for all comparisons. Boxplots show median (bar), first/third quartile (box), and min/max (whiskers) values. Unless otherwise noted, summary statistics are mean \pm s.d.

4.3 Results

4.3.1 Stress–strain curves, yield, and rupture

Stress–strain curves are plotted by failure type and specimen shape in Figure 4.5. The stress–strain curves display the nonlinear response typical of fibrous soft tissues. Subjective visual interpretation would place the yield point at about 3/4 of the peak stress, which is the point at which the loss of stiffness has caused visual deflection of the curve. However, the objectively measured yield point (the inflection point of the stress–strain curve) is placed at about 1/3 of the peak stress, within the subjectively linear region. This placement is precisely at the point of transition from strain-stiffening to strain-softening (e.g., Figure 4.4). This definition of yield

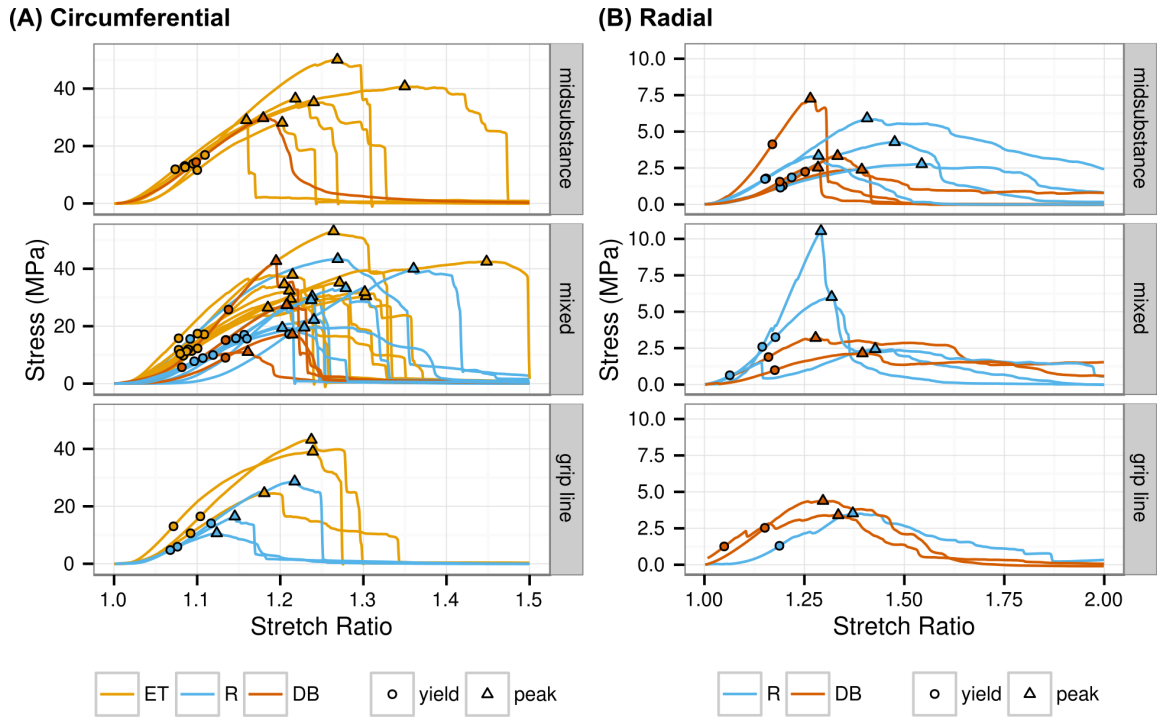


Figure 4.5: Stress–strain curves for circumferential and radial specimens by rupture type and specimen shape. The yield and peak stress points are marked.

has structural significance in that the tangent modulus at yield was nearly identical to the fiber modulus k_f from the fiber recruitment model (Figure 4.6). Yield therefore represents the point at which the model predicts complete fiber recruitment.

Most circumferentially loaded specimens ruptured with an abrupt, near-total release of stress, which was preceded by strain softening (Figure 4.5A). Qualitatively, there were no differences in the stress–strain curves between midsubstance, mixed, and grip line ruptures. In terms of rupture morphology, circumferentially loaded ET specimens failed mostly by mixed and midsubstance rupture (2/3 of all tests run), with the remainder split between grip line ruptures and gripped region ruptures (Table 4.2). In contrast, no circumferentially loaded R specimens failed by midsubstance rupture. About half failed by mixed rupture, 20% by grip line rupture, and 30%

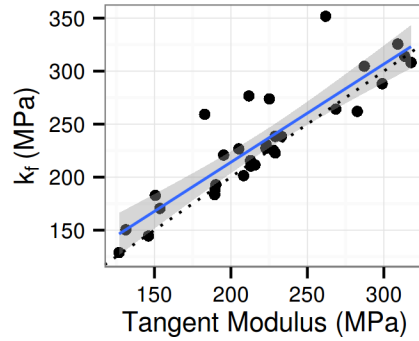


Figure 4.6: Fiber modulus (k_f) was strongly correlated with tangent modulus at yield (r [95% CI] = 0.77–0.94 by Pearson correlation). The solid blue line and shaded region is the best-fit line and its 95% confidence interval. The dotted black line illustrates a 1:1 relationship (slope = 1, intercept = 0).

by gripped region failure or longitudinal splitting. DB specimens showed a distribution of rupture types similar to the R specimens. Note that these ratios of rupture type by specimen shape are calculated from the total number of tests (i.e., with no exclusions). The mechanical analyses use the subset of specimens with valid ruptures and cut from different menisci (Section 4.2.2).

Radially loaded specimens, in contrast to circumferentially loaded specimens, ruptured with a gradual post-peak decrease in stress (Figure 4.5B). Radial specimens, as expected from their fiber orientation, were much less stiff and strong than the circumferential specimens (compare Figure 4.5A to 4.5B). Similar to circumferential specimens, the stress–strain curves of radial specimens did not differ by rupture type. Midsubstance, mixed, and grip line ruptures were all common.

4.3.2 Effect of specimen shape on mechanical properties

The fiber recruitment model produced excellent fits for all of the ET specimens (RMS error = 0.03 ± 0.02 MPa). Fits of ET specimen data were also physically plausible, with fiber recruit-

ment starting in the toe region and ending before the yield point (Figure 4.4)]. The rectangle specimens also had good model fits in a purely numeric sense (RMS error = 0.05 ± 0.02 MPa), but five (out of twelve) had fiber recruitment ranges extending below zero strain and above the yield point. The DB specimens all exhibited similarly wide fiber recruitment ranges or, in two (out of five) cases, did not even have a unique solution. Due to the low fit quality for DB specimens, they were dropped from the model-based analysis. Both the mean recruitment stretch ($\bar{\lambda}_c$) and the square root of the variance of the recruitment stretch (λ_c^{SD}) were significantly less in ET specimens than in R specimens (Figure 4.7). The model's fiber modulus (k_f) was not significantly different between the two shapes. The more rapid fiber recruitment and superior model fits evidenced by the ET specimens supports our hypothesis that the ET shape is more effective at ensuring fiber loading.

The yield and peak points from circumferential tests were also significantly affected by specimen shape. ET specimens had 0.04 lesser yield stretch, 50 MPa greater tangent modulus, and 9 MPa greater peak stress than R specimens, as well as narrower distributions for the yield stretch and yield stress (Figure 4.7). Yield points for ET specimens consequently form a tight cluster on the stress–strain plots, visibly separate from the yield points for the other shapes (Figure 4.5A). The peak points were broadly distributed for all specimen shapes. The stress–strain curve metrics for circumferential DB specimens were not significantly different from the ET or R specimens, but were qualitatively similar to the R specimens and dissimilar to the ET specimens. Radially loaded specimens had no significant differences in yield or peak points between specimen shapes (Figure 4.8). Nor did the radial stress–strain curves display any qualitative

differences between specimen shapes (Figure 4.5B). Differences between specimen shapes are summarized in Table 4.3.

Table 4.3: Fiber recruitment model and stress–strain results by loading direction and specimen shape.

	Circumferential			Radial	
	ET	R	DB	R	DB
$\bar{\lambda}_c$	$1.04 \pm 0.01^*$	$1.07 \pm 0.03^*$			
λ_c^{SD}	$0.019 \pm 0.004^*$	$0.04 \pm 0.02^*$			
k_f (MPa)	245 ± 45	215 ± 65			
Modulus (MPa)	$241 \pm 45^*$	$189 \pm 48^*$	215 ± 86	21 ± 13	19 ± 10
Yield Strain	$0.09 \pm 0.01^*$	$0.13 \pm 0.05^*$	0.12 ± 0.03	0.17 ± 0.05	0.18 ± 0.07
Yield Stress (MPa)	13 ± 2	12 ± 5	14 ± 8	1.79 ± 0.83	2.0 ± 1.0
Peak Strain	0.28 ± 0.09	0.26 ± 0.08	0.21 ± 0.03	0.47 ± 0.13	0.38 ± 0.07
Peak Stress (MPa)	$36 \pm 8^*$	$27 \pm 10^*$	26 ± 12	4.9 ± 2.7	3.6 ± 1.6

* This value is significantly different between tests of circumferential ET and R specimens.

4.3.3 Strain fields

Circumferential tests resulted in inhomogeneous strain fields for each strain component. Longitudinal strain (E_{xx}) fields, shown at the yield point in Figure 4.9, had spot-like regions (about 0.5 mm in diameter) of greater than average strain. In many cases (but not a majority), longitudinal strain was unevenly distributed over the scale of the whole specimen; e.g., one end of the specimen might have greater strain than the other (Figure 4.9A).

Shear strain (E_{xy}) fields for circumferentially loaded specimens were also inhomogeneous, with longitudinal bands (about 0.5 mm wide) of alternating positive and negative shear strain that resembled the pattern of fascicles on the specimen surface (Figure 4.10A and C). These shear bands sometimes extended from one grip to the other, but usually ended partway across

the specimen.

Transverse strain (E_{yy}) fields from circumferentially loaded specimens had pockets of concentrated strain similar to the E_{xx} strain concentrations, but more elongated (Figure 4.10B). These pockets were sometimes so elongated that they resembled the bands in the E_{xy} field. The transverse strain fields always included regions of tensile strain; these tensile strain concentrations were usually of similar magnitude to the compressive strain and could cover up to half the specimen area.

Qualitatively, there were no differences between ET and R strain fields under circumferential loading, but the margins of the DB specimens' flared ends had lesser longitudinal strain compared to the central region (Figure 4.9). This lack of stress and strain redistribution was confirmed by specifically labeling the part of the specimen with potential grip-to-grip fiber continuity (dotted outline in Figure 4.9C) and comparing strain in this region (the "loaded region") to that in the margins of the flared ends (the "shielded regions"). In all cases, median strain in the shielded regions was less than in the loaded region, with divergence occurring early in the test (< 5% grip strain). A representative case is shown in Figure 4.11. At the point of peak stress, longitudinal strain in the shielded region was about half of that in the loaded region. The E_{xy} and E_{yy} fields did not show a strain shielding effect; rather, the boundary between the shielded and loaded regions tended to develop large E_{xy} and E_{yy} strains.

Radially loaded specimens, whether R or DB, had smoother E_{xx} fields than the circumferentially loaded specimens, but often had large, irregularly shaped strain concentrations (Figure 4.12). The E_{xy} fields were organized into large regions of somewhat homogeneous positive

and negative shear. They did not exhibit the banding evident in circumferentially loaded specimens. The E_{yy} fields were almost entirely compressive, with small strain concentrations like those seen in the E_{xx} fields of circumferentially stretched specimens. The radially loaded DB specimens did not exhibit the strain shielding effect that was present in the circumferentially loaded DB specimens (compare Figure 4.9C to Figure 4.12A).

4.4 Discussion

4.4.1 Overview

This study met its objective of providing a more complete quantification of the meniscus' uniaxial tensile mechanics than was previously available. The pre-yield stress–strain response was quantified using a fiber recruitment model, which performed very well, justifying attribution of the meniscus' nonlinearity in circumferential tension to sequential fiber recruitment. The yield point was measured for the first time, and the modulus was quantified using a new procedure that is objective and reproducible. Circumferential specimens showed striking bands of shear strain and transverse tension that appeared to follow fascicle boundaries, supporting the notion that rupture occurs along these boundaries. These strain field inhomogeneities traverse the midsubstance and near-grip regions, indicating that the complex loads on the gripped ends of the specimen do not redistribute into homogeneous midsubstance loading. Nor does a narrow central region ensure midsubstance rupture, as evidenced by the ubiquitous involvement of the near-grip region in ruptures of DB and ET specimens. Our hypothesis that expanded

tab (ET) specimens would more effectively grip and load fibers than specimens with narrower tabs was confirmed. ET specimens showed enhanced stiffness and strength in circumferential stretch, as well as earlier and more rapid fiber recruitment. They are therefore recommended for circumferential tension tests of meniscus.

4.4.2 Fiber recruitment model and stress–strain nonlinearity

A fiber recruitment model was used to parameterize the meniscus' nonlinear stress–strain curve for fiber-aligned (circumferential) tension up to the yield point. The nonlinearity of the stress–strain curve is represented by sequential recruitment of linear fibers. A fiber is recruited when it starts to bear load due to uncrimping, rotation into the loading direction, or some other reason. The model showed excellent fits for ET and R specimens, with residuals two orders of magnitude less than the fitted data. DB specimens could not be fit; this and other issues associated with DB specimens are discussed in Section 4.4.8. The good fits for ET and R specimens indicate that the meniscus' circumferential tensile response is consistent with an assembly of linear fibers.

The fiber recruitment model was also consistent with key functional aspects of the meniscus' stress–strain curve. In the circumferential ET specimens, which most effectively load the meniscus fibers, the yield point consistently coincided with the point at which almost all the fiber were recruited. The tangent modulus at yield was, on average, the same as the fiber modulus k_f (Figure 4.6), further supporting the interpretation that yield occurs at the point of maximum fiber recruitment. The data also show that both the pre-yield stress–strain curve and its derivative are nonlinear (Figure 4.4); the model reflects both nonlinearities. The fiber recruitment

model thus has a strong structural interpretation that is consistent with non-model metrics for the stress–strain curve, and it is a good option for modeling the uniaxial tensile mechanics of meniscus.

4.4.3 Yield point

The yield point was defined in this study as the first inflection point of the stress–strain curve. There is no standard or rigorous definition of yield for fibrous soft tissues. Colloquially, it refers to the onset of strain–softening (i.e., the inflection point) or the onset of plastic strain. In quantification of standard engineering materials, the yield point refers to both the inflection point and the onset of obvious plastic deformation, but this association has not yet been demonstrated for fibrous soft tissue. Here, the yield point is a phenomenological quantification of the onset of strain-softening.

Quantitatively, yield in tissue has previously been defined as the point of first divergence from the linear region (Viinikainen et al. 2007; Palmer et al. 2009; Smith et al. 2008), the point at which the slope subjectively decreases (Espejo-Baena et al. 2006; Veres et al. 2013), or the intersection of a line parallel to the linear region but offset by a certain strain or displacement (Jones et al. 2014; Danso et al. 2014; Barber et al. 2011). Defining the yield point relative to the linear region poses the problem of how to identify the linear region of a curve which is nonlinear from beginning to end. Defining the yield point instead as the first inflection point of the stress–strain curve is objective, reproducible, and consistent with the commonly held meaning of yield. The use of a smoothing spline interpolant makes the method robust to noise

and variations in sampling rate. Calculation of derivatives by finite differences is also an option, but is less robust to these effects. The yield point obtained by the inflection point method occurs at lesser strain and stress than would probably be determined by eye (for example, a subjectively estimated yield point in Figure 4.4 would probably be 3/4 up the curve). The definition used here marks a clear transition from strain-stiffening to strain-softening (Figure 4.4).

The mechanisms that cause loss of stiffness (strain-softening) subsequent to the stress–strain inflection point are not yet clear. The inflection point may indicate the onset of damage and/or plasticity, perhaps by the onset of inter-fibrillar sliding (Szczesny and Elliott 2014b). In ligament, the onset of structural damage occurs at about 5% strain, prior to any observed strain-softening or plasticity (Provenzano et al. 2002b). On the other hand, tendon fascicles show elongation without increase in stress at about 4% strain, with detailed analysis indicating involvement of plastic inter-fibril shear (Szczesny and Elliott 2014b; Szczesny and Elliott 2014a). These thresholds are somewhat lower than the yield strain observed here for meniscus, but tendon fibers are quite well aligned with the tensile axis from the start of the test. Meniscus fibers have more orientational dispersion and may require more tissue strain before they are recruited and stretched to this putative damage threshold. More study is necessary to test the hypothesis that the stress–strain inflection point for fibrous soft tissue represents the onset of damage or plasticity.

4.4.4 Radial specimens and tie fibers

A few radial specimens had much greater peak stress and a more abrupt reduction in stress post-peak than the others (Figure 4.5). These sharp stress peaks may indicate the presence of radial tie fibers. The meniscus contains radially oriented tie fibers that increase its radial tensile strength and stiffness (Andrews et al. 2014; Skaggs et al. 1994a). Since these fibers are randomly distributed with mm-scale separation and are not necessarily parallel to the specimen plane, only a few specimens in this study would be expected to contain tie fibers. This is consistent with the low number of radial tests with sharply peaked stress–strain curves. The peak stress values from these sharply peaked curves are in the range previously observed in tests of radial meniscus specimens containing radial tie fibers (Skaggs et al. 1994a).

4.4.5 Comparison with prior work

Mechanical properties of meniscus from the literature are given in Table 4.4 for circumferential specimens and Table 4.5 for radial specimens. For the sake of comparison, we listed only properties from the center part of the meniscus (the location we tested). Few studies report a complete set of mechanical properties; only modulus is consistently reported. There is great variation in reported values. Since there is great diversity between studies regarding species, medial/lateral side, specimen thickness, method for quantifying modulus, method for measuring strain, and specimen shape, a large degree of variation is to be expected. Mechanical properties may vary with the side of the knee (medial/lateral) and anterior/posterior position, although reports conflict between studies (Kelly et al. 1990; Bursac et al. 2009; Tissakht and Ahmed

1995; Proctor et al. 1989). Of these studies, Tissakht et al. (Tissakht and Ahmed 1995) had the greatest statistical power and found no statistical anterior/posterior or medial/lateral effect for circumferential specimens. We verified (by 2-way ANOVA with specimen shape & medial/lateral side as factors) that there was no confounding medial/lateral effect in our present work. Modulus has been reported to be greater for thinner specimens, but the authors attributed this to specimen selection effects (Lechner et al. 2000). Bursac et al. (Bursac et al. 2009) use twice the thickness of Tissakht et al. (Tissakht and Ahmed 1995), but obtained similar modulus values for human meniscus. We verified (by linear regression) that the limited range of thickness variation in our present work did not impact our measurements.

Some of the variation in modulus is caused by variation in modulus definitions. For example, our modulus definition produces values 16 ± 16 MPa greater than Lechner et al.'s (Lechner et al. 2000) for circumferential tests, and 2 ± 4 MPa greater for radial tests. Note that the distributions of these differences are skewed positive because some stress–strain curves are not even quasilinear in Lechner et al.'s chosen stress range. One of the advantages of measuring the tangent modulus at yield is that it handles highly nonlinear curves well.

Peak stress from circumferentially tested specimens from large quadrupeds was greater for sheep ET specimens (Tanaka et al. 2014) than sheep DB specimens (Anderson et al. 1993) (Table 4.4). This is consistent with the specimen shape effects observed in our present work. Peak strain values have large ranges of variation, but are generally consistent within both circumferential (Table 4.4) and radial studies (Table 4.5), with a few outliers. The lesser peak strain reported by Anderson et al. (Anderson et al. 1993) for circumferential tests and Skaggs et al.

(Skaggs et al. 1994a) for radial tests may be due to calculation of strain using gauge lines rather than grip-to-grip displacement. Variation in peak strain may also be caused by the difficulty of standardizing the zero strain point, as strain is sensitive to the choice of preload. Strain can also be applied inadvertently during specimen mounting. Stress values are more consistent.

Human specimens show lesser modulus and peak stress than non-human animals in circumferential testing, regardless of specimen shape (Table 4.4). Age-related deterioration in the human meniscus specimens could reasonably be suspected as an explanation for this effect, but Tissakht et al. (Tissakht and Ahmed 1995) used specimens aged 29–45 years and reported near-identical values to Tanaka et al. (Tanaka et al. 2014), who used specimens aged 67–84 years. Despite this, the lesser modulus and peak stress in human specimens could still be caused by age-related deterioration if it occurs prior to the fourth decade of life. This would not be unprecedented; aspects of intervertebral disc degeneration are well underway by the fourth decade (Vernon-Roberts et al. 2007; Haefeli et al. 2006). Alternatively, humans may simply possess less stiff meniscus tissue.

4.4.6 Rupture location

A midsubstance rupture is considered desirable because it implies that the test result is unaffected by local grip-associated stresses. In this study, most specimens did not fail by midsubstance rupture (Table 4.2), but the stress–strain curves of midsubstance ruptures were not clearly different from the mixed or grip line ruptures (Figure 4.5). Even the gripped region failures and longitudinal splits, which were excluded from formal analysis, did not have qualitatively differ-

Reference	Species	Side	Shape	Modulus (MPa)	Peak Strain (%) ¹	Peak Stress (MPa)	Environment	Strain Measurement
Present Study	Cow	Both	ET	241 ± 43	25 ± 7	36 ± 8	Mixed	Grip displacement
Present Study	Cow	Both	R	190 ± 49	23 ± 6	27 ± 10	Air	Grip displacement
Present Study	Cow	Both	DB	215 ± 86	19 ± 2	26 ± 12	Air	Grip displacement
Proctor 1989 Proctor et al. 1989 ²	Cow	Medial	DB	140 ± 80	NA	NA	Bath	Gauge lines
Anderson 1993 Anderson et al. 1993 ²	Sheep	Medial	DB	239 ± 97	12 ± 3	24 ± 3	Bath	Gauge lines
Tanaka 2014 Tanaka et al. 2014 ³	Sheep	Medial	ET	187 ± 32	36 ± 2	36 ± 5	Mist	Grip displacement
Stabile 2010 Stabile et al. 2010	Sheep	Medial	Unknown	67 ± 30	NA	NA	Air	Gauge markers
Tanaka 2014 Tanaka et al. 2014	Pig	Medial	ET	209 ± 35	30 ± 5	38 ± 8	Mist	Grip displacement
LeRoux 2002 LeRoux and Setton 2002	Dog	Medial	R	68 ± 28	NA	NA	Bath	Optical
Sweigart 2005 Sweigart and Athanasiou 2005	Rabbit	Medial	R	157 ± 49	NA	22 ± 7	Mist	Grip displacement
Fithian 1990 Fithian et al. 1990 ⁴	Human	Both	DB	161 ± 37	NA	NA	Unknown	Gauge lines
Tissakht 1995 Tissakht and Ahmed 1995 ⁴	Human	Both	R	63 ± 11	27 ± 7	12 ± 2	Humid chamber	Grip displacement
Lechner 2000 Lechner et al. 2000	Human	Medial	DB	84 ± 24	NA	NA	Bath	Gauge lines
Tanaka 2014 Tanaka et al. 2014	Human	Medial	ET	98 ± 22	22 ± 4	12 ± 2	Mist	Grip displacement
Bursac 2009 Bursac et al. 2009 ⁴	Human	Both	R	73 ± 15	NA	NA	Bath	Grip displacement

¹ Cauchy (engineering) strain.

² Average of reported anterior and posterior values.

³ Skeletally immature animals.

⁴ Average of reported medial and lateral values.

Table 4.4: Comparison of current and prior circumferential uniaxial tensile tests. Values are listed for the center region (anterior-posterior axis) unless otherwise indicated.

Reference	Species	Side	Shape	Modulus (MPa)	Peak strain (%) ¹	Peak stress (MPa)	Environment	Strain Measurement
Present study	Cow	Both	R	21 ± 14	39 ± 9	5 ± 3	Air	Grip displacement
Proctor 1989	Cow	Both	DB	17 ± 11	32 ± 5	4 ± 2	Air	Grip displacement
Proctor et al. 1989 ²	Cow	Medial	DB	5 ± 2	NA	NA	Bath	Gauge lines
Skaggs 1994	Cow	Medial	DB	35 ± 20	17 ± 6	3 ± 2	Bath	Gauge lines
LeRoux 2002	Dog	Lateral	R	11 ± 4	NA	NA	Bath	Optical
LeRoux and Setton 2002	Human	Both	R	6 ± 2	44 ± 25	2 ± 1	Humid chamber	Grip displacement
Tissakht 1995	Ahmed 1995 ³							

¹ Cauchy (engineering) strain.

² Average of anterior and posterior values.

³ Average of reported medial and lateral values.

Table 4.5: Comparison of current and prior radial uniaxial tensile tests. Values are listed for the center region (anterior-posterior axis) unless otherwise indicated.

ent stress–strain curves, despite the ruptures extending *inside* the gripped region. Previously, comparison between at-grip and midsubstance ruptures in tendon has also shown no difference (Ng et al. 2005). It is not clear why at-grip and midsubstance ruptures do not appear mechanically different. In the present study, grip-associated strain inhomogeneities do extend to the midsubstance (discussed further in Section 4.4.7), so all ruptures may have been affected by the grips to some degree.

4.4.7 Strain field inhomogeneity, grip effects, and damage

The observed strain fields were extremely heterogeneous. Circumferential specimens developed intense shear bands that followed a pattern similar to the fascicles (Figure 4.10). We interpret these shear strain bands as caused by sliding between adjacent fascicles. Meniscus failure in uniaxial tension tends to occur by shear along a fascicle boundary (Kelly et al. 1990), consistent with the interdigitating fiber pull-out observed here (Figure 4.3A). Circumferential-radial shear has also been hypothesized to be important in the development of vertical meniscus tears (Kelly et al. 1990; Smillie 1978). Future work is required to definitively relate patterns of strain field inhomogeneity to meniscus structure and damage mechanisms.

Some of these strain field inhomogeneities—in particular, bands of longitudinal strain (Figure 4.9B) and, more commonly, shear strain and transverse strain (Figure 4.10)—spanned the near-grip and midsubstance regions in tests of circumferential specimens. This is direct evidence that complex local stresses in the gripped region probably do not dissipate into an even stress field in the midsubstance; i.e., Saint-Venant’s principle does not apply. In anisotropic,

inhomogeneous materials such as the meniscus, the spatial extent of local stress effects, such as grip effects, is much greater than for isotropic, homogeneous materials (Reese et al. 2013; Skaggs et al. 1994b; Horgan and Simmonds 1994; Stronge and Kashtalyan 1997). Due to the limited size of the meniscus, it is probably not possible to cut a specimen long enough for the midsubstance to be free of grip effects. Local stress effects almost certainly apply in situ as well. The capability to treat the meniscus as a highly anisotropic, inhomogeneous material with complicated boundary conditions will be important to make useful predictions for in vivo mechanics.

One specific effect produced by the grips was to prevent transverse deformation at either end of the specimen. The ends of the specimen thus cannot contract along with the midsubstance; this creates local stresses at the grip line (Jacobs et al. 2013; Sun et al. 2005). Consequently, many circumferential specimens exhibited small ruptures, separate from the main rupture site, at one of the corners formed by the specimen and the grip face. For example, the patches of tensile strain visible in the transverse strain fields (Figures 4.10b and 4.12c) are probably caused by the grips preventing transverse contraction. Transverse tension produced by this effect could damage inter-fascicle interfaces required for longitudinal load transfer.

4.4.8 Choice of specimen shape

We hypothesized that expanded tab (ET) specimens would be more effective at gripping and loading fibers than specimens with narrower tabs. This hypothesis was confirmed. In circumferential tension, ET specimens showed fiber recruitment at lesser stretch ($\bar{\lambda}_c$) and over a smaller

stretch interval (λ_c^{SD}), lesser yield stretch, greater tangent modulus at yield, and greater peak stress than R specimens (Figure 4.7). Since the fiber recruitment model fit both the ET and R specimens well, fiber recruitment can be considered the dominant mechanical mechanism for both shapes. Lesser $\bar{\lambda}_c$ and λ_c^{SD} indicate that the ET specimens recruited fibers more rapidly. Since yield occurred at about the point of maximum fiber recruitment, more rapid fiber recruitment explains the lesser yield stretch. The combination of greater modulus and peak stress in the ET specimens, but similar peak strain, indicates that ET specimens recruited a greater number of fibers per unit area, thus increasing the apparent modulus, but that individual fibers ruptured at about the same tissue strain regardless of specimen shape. Strain has been previously hypothesized to be the key failure metric for fibrous soft tissue (Wren et al. 2003), with peak stress determined by the combination of modulus and peak strain (LaCroix et al. 2013; Skaggs et al. 1994b). The ET specimens are capable of recruiting more fibers because the expanded tabs allow curved fibers on the inner side of the specimen to extend deep into the grips and thus be securely gripped; the other specimen shapes sever these fibers or grip them insecurely. Severed fibers or insecurely gripped fibers are experimental artifacts, so the superior fiber recruitment and associated changes in stress–strain curve parameters exhibited by ET specimens better represent the intact meniscus.

It is likely that the same differences in modulus, yield strain, and peak stress between ET and R specimens also exist between ET and DB specimens, and were just not detected due to the sample's statistical power. For circumferential specimens, this study was powered to detect differences of 1.1 standard deviation (s.d.) for the ET-R comparison ($\beta = 0.8$), and this was about

the magnitude of the detected differences. The ET-DB comparison was powered to detect differences of only 1.5 s.d., and the R-DB comparison was powered to detect differences of 1.6 s.d. However, the close similarity between the distributions of variables for R and DB specimens (Figure 4.7) suggests that any undetected difference is small. This is true for the radial tests as well (Figure 4.8). The radial R-DB comparison was powered to detect differences of 1.5 s.d. It is reasonable to conclude that the R and DB specimens have similar yield point, modulus, and peak point, and the ET specimens differ from both by the same amount.

The purpose of the DB shape is to increase stress in the narrow part and thus ensure failure at that location; it did not achieve this (Table 4.2). Dogbones are known to be ineffective at ensuring midsubstance failure in tests of synthetic fiber-reinforced composites; rectangles are preferred (*ASTM D3479/D3479M* 2015; De Baere et al. 2011; Arumugam et al. 2010). The inability of the DB shape to ensure midsubstance failure in circumferential tests was probably in part because the grip line was unevenly loaded, with strain-shielded regions (Figure 4.9C). Skaggs et al. hypothesized the existence of this strain-shielding effect as the cause of at-grip failures in dogbone-shaped specimens of annulus fibrosus (Skaggs et al. 1994b). The location of failure may also be controlled by inhomogeneous tissue strength, which could be exacerbated by severing of internal structures while cutting the specimen. Still, the juxtaposition of strain-shielded and loaded regions creates severe shear and transverse strain. The addition of these deformations is probably why the fiber recruitment model could not fit the DB specimen stress–strain response. Although no other specimen shape ensured midsubstance failure either, the strain-shielded regions in the DB specimens are disadvantageous.

The DB specimen shape has an additional disadvantage regarding the calculation of cross-sectional area: the width of a DB specimen varies. Since ruptures may occur anywhere along the specimen length (Figure 4.3), it is not obvious which cross-sectional area to use for stress calculations. We used the central minimum width, which in circumferential specimens is the width of the loaded region (Figure 4.9) and so is reasonably accurate for this case. However, using the minimum width for radially stretched DB specimens may have caused some overestimation of stress. The other specimen shapes have equal cross-sectional area throughout the inter-grip length and so do not pose this ambiguity.

Changing the dogbone specimen shape and the way it is mounted can mitigate its disadvantages. A dogbone specimen with a long, parallel-sided gauge region may function similarly to a rectangle if the flared ends are wholly within the grips, as in (Freutel et al. 2015). The parallel sides eliminate cross-sectional area variation, and placing the flared ends inside the grips prevents them from causing strain-shielded regions.

In general, circumferential testing of meniscus is best done using ET specimens because they sever fewer fibers and more securely grip fibers, producing enhanced fiber recruitment and increased apparent strength that better represents the intact meniscus. The principle value of the ET specimen shape lies in accommodating the meniscus' fiber curvature. Unlike a dogbone specimen, its wide tabs are almost entirely inside the grips, and the gauge region consequently is similar to that of a rectangle specimen (Figure 4.1). In materials without curved fibers, rectangles would probably produce identical results. The ET specimen shape does consume more tissue area than a plain rectangle, making it difficult to cut multiple specimens from the same

meniscus or test small subregions. However, it readily accommodates different inner/outer and distal/proximal locations. Anterior/posterior variation is more limited; only the mid-anterior, center, and mid-posterior regions are amenable. For testing of the extreme anterior or posterior locations, we suggest gripping the bony insertion as in (Villegas et al. 2007) and using an expanded tab on the opposite end. In radial testing of meniscus, fiber curvature is not relevant, so rectangles are the best choice.

4.4.9 Choice of strain measurement

Grip strain was used for the stress–strain curves rather than optical strain. There are several prior examples of this (Párraga Quiroga et al. 2014; Szczesny et al. 2012). Although optical strain is in principle preferable to grip strain because it measures actual tissue deformation, the extreme heterogeneity of the strain fields (Figures 4.9, 4.10, and 4.12) makes it difficult to convert the strain fields to a single summary strain value. The range of optical strain values broadens greatly as the test progresses (Figure 4.13). Strain concentrations and shear discontinuities in particular are major difficulties; should the entire strain field be used, or just the part that coincides with the site of rupture? If the site of rupture is used, its extent is not obvious. Strain concentrations can also locally change the appearance of the specimen surface sufficiently to cause the digital image correlation to fail in that region. In this study, since we discarded all tests with observed grip slip, the grip strain is a fair summary of the overall tissue strain (Figure 4.13), and has the advantages of clarity and reproducibility. However, the optical strain fields are a rich source of information and methods should be developed to unlock their potential.

4.5 Conclusion

This study represented the sub-yield uniaxial tensile response of the meniscus with a fiber recruitment model, providing a quantitative link between the meniscus' fiber structure and its nonlinear stress–strain response. The elastic modulus was quantified using a new procedure that measures a consistent functional region of the stress–strain curve and is simple enough to be used routinely in soft tissue testing. This method is more robust to variation in mechanical behavior than a linear fit of a chosen stress or strain range. Through this procedure, we quantified the meniscus' (previously unreported) yield point. We also quantified peak stress and strain. Together, these metrics are useful as functional targets for meniscus replacements or repair procedures, to compare disease states, or as diagnostic markers. Strain fields revealed significant heterogeneity in the strain response, which grew as the test progressed. Most interestingly, bands of shear strain and transverse strain occurred in the same pattern as the fascicles, suggesting inter-fascicle shear as an important deformation and damage mechanism. Local stresses (e.g., grip effects) and non-midsubstance ruptures appear endemic to fibrous soft tissue testing, and dogbone specimens do not resolve these issues. Due to fiber curvature in the meniscus, it is recommended to use expanded tab specimens for circumferential tension tests. The tabs ensure that as many fibers as possible are securely gripped, producing more rapid and complete fiber recruitment, lesser yield strain, and greater peak stress. Rectangular specimens are suitable for radial tension tests. Although this study makes significant strides in measurement of the meniscus' mechanics, more work needs to be done to develop procedures for fibrous soft tissue testing and to quantify processes of damage and failure.

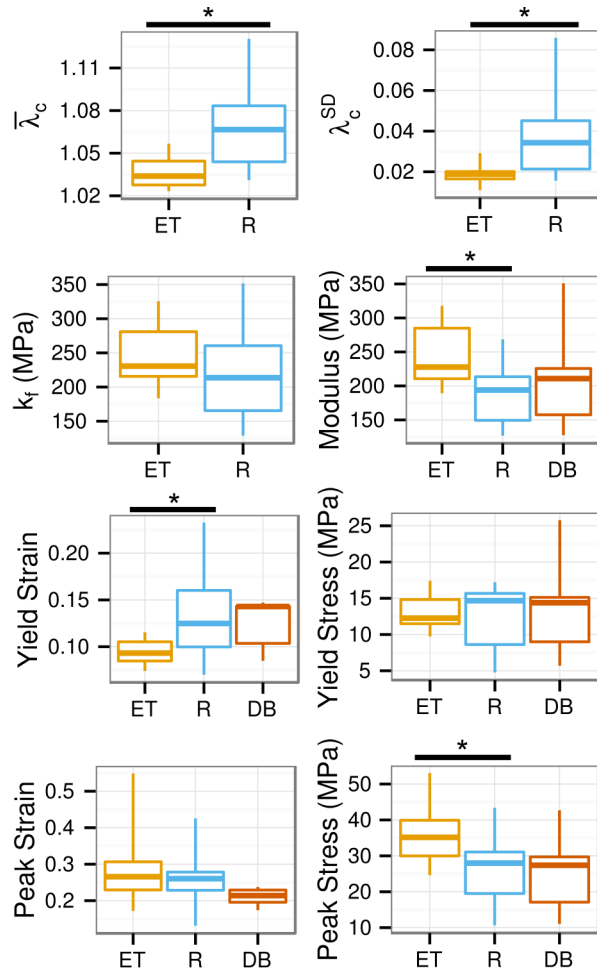


Figure 4.7: Fiber recruitment model and stress–strain results for circumferentially stretched expanded tab (ET), rectangle (R), and dogbone (DB) specimens. Significant differences between specimen shapes are marked with a bar and asterisk. The ET specimens showed differences indicating more complete and rapid fiber recruitment.

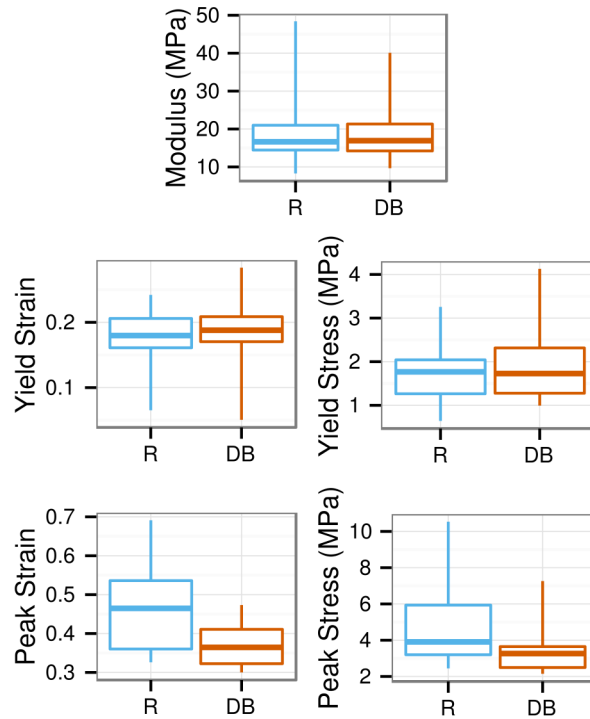


Figure 4.8: Stress–strain results for radially stretched rectangle (R) and dogbone (DB) specimens. There were no significant differences between specimen shapes.

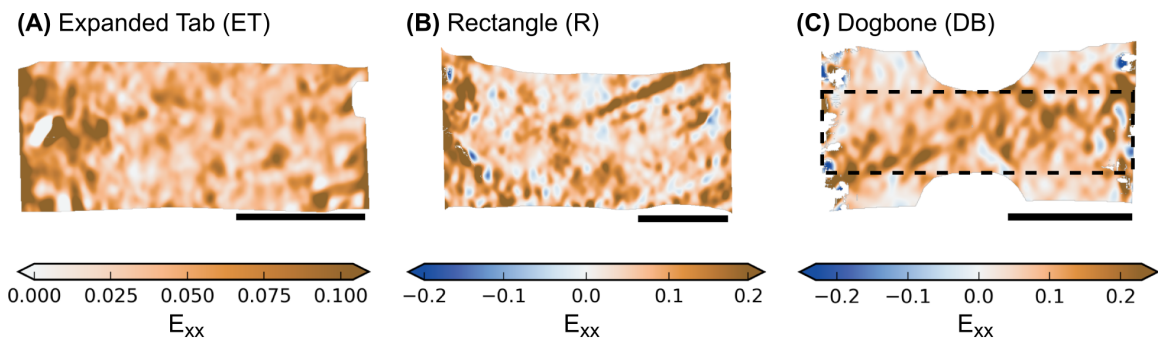


Figure 4.9: Representative longitudinal strain (E_{xx}) fields at yield for circumferentially loaded specimens. In subfigure C, the dashed outline over the dogbone’s strain field indicates the “loaded region”, which has potential grip-to-grip fiber continuity. The flared margins outside this outline are the “shielded region”, which has no grip-to-grip continuous fibers and exhibits less longitudinal strain than the loaded region. Color scales are truncated at the 0.05 and 0.95 quantiles. The scale bars are 5 mm long.

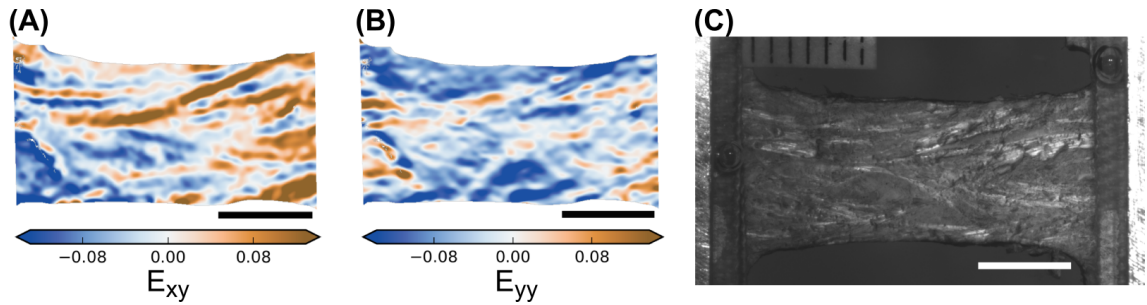


Figure 4.10: Representative (A) shear strain (E_{xy}) and (B) transverse strain (E_{yy}) field at yield for circumferential specimens with (C) the corresponding camera image of the specimen. An ET specimen is shown. The bands in the E_{xy} field qualitatively match the fascicle boundaries visible in the camera image. The color scales are truncated at the 0.05 and 0.95 quantiles. The scale bars are 5 mm long.

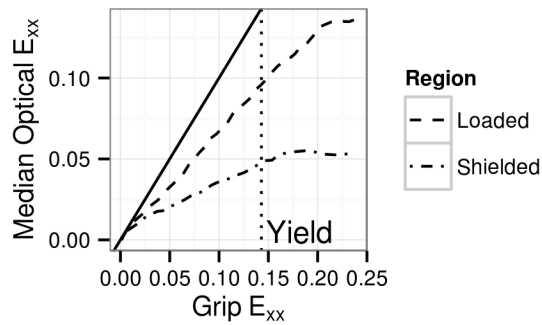


Figure 4.11: Representative plot of longitudinal strain (E_{xx}) in a DB specimen measured optically (y-axis) and by grip displacement (x-axis). The median optical strain in the central region (the “loaded region”), which has grip-to-grip fiber continuity, is much greater than in the flared ends of the specimen (the “shielded region”), which contain severed fibers. See Figure 4.9C for a diagram of these regions. The line of 1:1 correspondence between optical and grip strain is marked by a solid black line. Optical strain is approximately linearly correlated with grip strain up to and a little past the yield point.

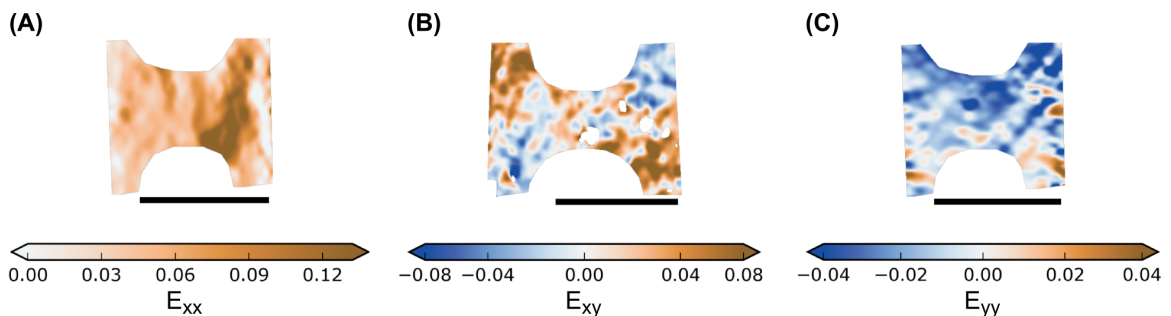


Figure 4.12: Representative longitudinal (E_{xx}), shear (E_{xy}), and transverse (E_{yy}) strain fields for radially stretched DB specimens at yield. The strain fields for radially stretched R specimens are similar. The scale bars are 5 mm long.

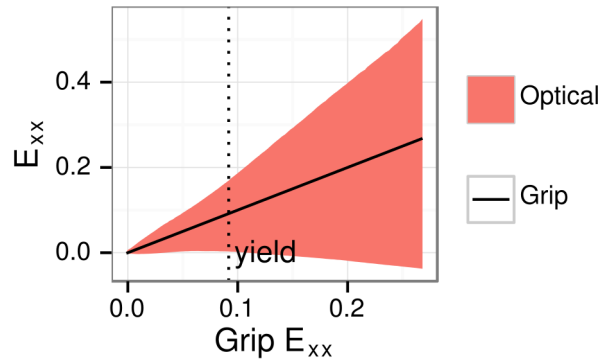


Figure 4.13: Optical longitudinal strain 0.05/0.95 inter-quantile range (red shaded region) compared with grip strain (solid black line). The optical strain range broadens in proportion to the applied grip strain. This is a representative example; in other cases, the optical strain range may broaden nonlinearly. The plot shows data up to the peak point.

CHAPTER 5: UNIAXIAL TENSILE TESTING OF CRACKED MENISCUS AND ITS FAILURE MECHANISMS

5.1 Introduction

Meniscus cracks (tears) are harmful because they cause joint pain and mechanical deficiency and increase the risk of osteoarthritis (Englund et al. 2012; Øiestad et al. 2009; Cohen et al. 2007; Englund et al. 2008). The most straightforward treatment for a crack—partial or total meniscectomy—greatly increases the risk of osteoarthritis (Magnussen et al. 2009; Shelbourne and Gray 2000; Feucht et al. 2015; Anetzberger et al. 2014; Petty and Lubowitz 2011), and repair, especially of the inner avascular region, is not always feasible (Arnoczky and Warren 1983; Englund et al. 2012). To make decisions regarding whether and how to treat a crack, it is important to be able to answer questions like: Will a crack grow for a given level of physical activity? Will a repair stop a crack from growing? Answering these questions requires quantitative knowledge of how the meniscus fails. This study addresses one possible mechanism for meniscus failure via crack growth: fracture.

Fracture is a failure mechanism associated with stress-concentrating defects such as cracks, which includes meniscus tears. A crack, in principle, creates a stress concentration at its tip. Because the stress at the crack tip is greater than elsewhere in the material, the material near the tip fails first. The crack grows and the stress concentration migrates to fresh material that fails

in turn. The crack thus cascades through the material at loads that would have been safe were the crack and its stress concentration not present. Fracture thus decreases the effective strength of a material and must be accounted for when predicting failure.

Since cracks in the meniscus grow, fracture is expected to be a relevant failure mechanism. Accordingly, the energy of crack propagation (fracture toughness) through meniscus scar tissue has been measured using peel tests (Sonoda et al. 2000; Roeddecker et al. 1994). However, if the zone of failure at the crack tip is large enough that the entire uncracked cross-section fails together (facilitated, e.g., by plasticity), fracture does not occur and there is no decrease in effective strength. This mechanism of failure is common in ductile materials and so is called ductile rupture. In this study, it will be subsequently referred to as bulk rupture out of uncertainty regarding whether ductility is the predominant mechanism in fibrous soft tissue. Accurate prediction of failure requires that fracture and bulk rupture be distinguished, but the conditions under which each occur in the meniscus are not yet known. Nor is much known about how meniscus cracks grow or what effects they have on meniscus mechanics.

In fact, few fracture studies have been performed for any type of fibrous soft tissue, and progress in this area has been slow. Reproducing physiologic crack propagation in controlled laboratory tests has proven difficult, and fracture studies of fibrous soft tissues have produced ambiguous results (Taylor et al. 2012). A fracture toughness value can be measured from any propagating crack, but it is only valid for predicting fracture if the specimen from which it is measured actually failed by fracture. A fracture toughness value measured from a non-fracture failure has no predictive capability. Crack propagation is necessary but not sufficient for failure

by fracture; a non-fracture failure can look like a growing crack. If a crack (crack-like defect) does not cause a decrease in the material's effective strength, fracture is not responsible for its failure and the material's ultimate strength is the appropriate failure predictor. Even though cracks grow in the meniscus in vivo, the expectation that fracture is responsible for that growth is not necessarily true, or may only be true for specific conditions.

Since it is usually equivocal whether a straightforward tensile test of cracked fibrous soft tissue resulted in fracture, the occurrence of fracture for a particular tissue and test configuration must be confirmed prior to quantifying fracture-related properties such as fracture toughness. The priority for investigating meniscus fracture is to identify a test configuration in which failure demonstrably occurs by fracture.

This strategy of verifying failure by fracture has been employed in tests of porcine Achilles tendon, showing that edge cracks in tendon loaded parallel, perpendicular, or 45° to the fiber direction do not decrease the tendon's strength (Von Forell et al. 2014). Studies of partial transection of tendon, although not designed as fracture studies, also suggest that cracks in tendon do not cause fracture (Kondratko et al. 2012; Kondratko-Mittnacht et al. 2015; Mazzocca et al. 2008; Hariharan et al. 1997; McCarthy et al. 1995; Tan et al. 2003). However, several factors mean that the meniscus is more likely to suffer from fracture. Cracks are not a major pathology in tendon, but they are the primary pathology in meniscus. The meniscus' structure and properties are also more conducive to failure by fracture. Tendons such as the Achilles are highly aligned, with few or no transverse fibers (Kahn et al. 2013). The weakness of the interfascicular matrix in tendon limits load transfer between fascicles, which likely prevents crack propaga-

tion and fracture. In contrast, the meniscus has a branched network of fibers interpenetrated by numerous circumferential collagen fascicles. Consequently, meniscus is relatively stiffer in its radial direction than tendon is in its transverse direction. Porcine Achilles tendon has a transverse stiffness of about 0.1 MPa and a longitudinal stiffness of about 80 MPa (Von Forell et al. 2014). The meniscus, in contrast, has a radial stiffness is between 5 MPa and 40 MPa and a circumferential modulus between 70 MPa and 240 MPa (Peloquin et al. 2016; Proctor et al. 1989; Skaggs et al. 1994a). Fracture has also been observed in superficial zone articular cartilage and possibly in temporomandibular joint disc (Chin-Purcell and Lewis 1996; Koombua et al. 2006), both of which are similar to meniscus fibrocartilage. The meniscus (1) exhibits extensive pathology involving cracks, (2) its structure should inhibit fracture to a lesser degree than tendon, and (3) fracture has been identified in tissue similar in structure and composite to meniscus, so fracture is a likely failure mechanism in the meniscus.

Even if a crack does not cause failure by fracture, it may still create a stress concentration near the crack tip and so promote local sub-failure damage. Roeddecker et al. (1994) observed a decrease in tearing energy near the tip of a naturally occurring meniscus crack compared to a uncracked contralateral control. Crack-induced sub-failure damage could adversely affect meniscus function by injuring cells or promoting long-term failure mechanisms such as creep or fatigue.

Since cracks are the central aspect of meniscus pathology and the role of fracture in meniscus crack propagation is unknown, this study was designed to achieve the following objectives: (1) test the hypothesis that cracks in meniscus cause failure by fracture, (2) test the hypothe-

sis that meniscus cracks increase strain near their tips, and (3) determine if crack propagation occurs in meniscus in uniaxial tension. To accomplish the first objective, this study compares strength between cracked and crack-free specimens (Von Forell et al. 2014). An innovation in the present work is the use of center crack specimens with the cracks oriented obliquely to the fiber direction. Prior FEA has predicted that, compared to edge cracks, this configuration enhances fiber-aligned stress near the crack tip (Chapter 3; Peloquin and Elliott 2016). This test configuration should increase the chances of fracture occurring across fibers. The remaining two objectives address important aspects of crack behavior irrespective of whether fracture occurs. Crack-associated local strain concentrations are a sign of crack-associated stress concentrations and, if present, promote damage or inelastic deformation. Finally, determining if cracks grow under the chosen uniaxial tensile conditions will help establish protocols for investigation of meniscus tears in non-fracture contexts (e.g., repair).

5.2 Methods

5.2.1 Specimen preparation

Table 5.1: Specimen counts for cracked and control specimens in each test group.

Group	Control/Cracked	n
circumferential 45° center crack	control	11
circumferential 45° center crack	cracked	12
circumferential 90° edge crack	control	11
circumferential 90° edge crack	cracked	13
radial 90° edge crack	control	26
radial 90° edge crack	cracked	16

Tensile test specimens were prepared from adult (age > 30 months) bovine meniscus. Menisci were purchased from Animal Technologies, Inc. (Tyler, TX) and stored frozen (-20°C) until specimen preparation. To prepare a specimen, a histology trimming knife was used to cut the meniscus to a size ~ 5 mm larger than the intended specimen size. The specimen was then planed to a target thickness of 1.0 mm to 1.5 mm thickness using a Leica SM2400 sledge microtome equipped with a freezing stage so that its proximal and distal surfaces were flat and normal to the anatomic proximal–distal axis. During planing, thickness was estimated using plastic shims, aiming for 1.0 to 1.5 mm thickness. The specimen was then trimmed to its final in-plane dimensions using a razor blade, #15 scalpel, and (to create fillets) a 3 mm diameter biopsy punch. Specimen outlines relative to the intact meniscus are shown in Figure 5.1a.

Specimens with cracks were prepared in three test configurations: (1) circumferential tension with a 90° edge crack, (2) circumferential tension with a 45° center crack, and (3) radial tension with a 90° edge crack (Figure 5.1b). Each cracked test configuration had a corresponding crack-free control. Final specimen counts are given in Table 5.1. Circumferential specimens were cut into dogbone shapes and the radial specimens were cut into rectangles in accordance with prior work (Peloquin et al. 2016). Edge cracks were cut with fresh #11 scalpel blades. Center cracks were cut with razor blade fragments that were broken to the target crack length of 3 mm. The actual cutting of the crack was done immediately before gripping the specimen (see below). Specimen dimensions are reported in Table 5.2. The reported width is from the midsubstance and is not reduced by the crack length. The circumferential specimens, except for the controls for the 90° edge crack case, were cut according to the pattern labeled “normal”

in Figure 5.1a. Since the meniscus' inner and outer regions have different composition, control specimens for the circumferential 90° edge crack case were cut so that their width was the same as the cracked specimens' intact width. Tests of cracked specimens and their crack-free controls thus loaded the same anatomic region.

The cross-sectional area of each prepared specimen was measured by scanning across its width with a laser displacement sensor (Szczyński et al. 2012; Favata 2006). The specimen was speckle coated with Verhoeff's stain using an airbrush to facilitate digital image correlation following the test. During the aforementioned preparation, specimens were kept covered under PBS-dampened gauze as much as possible to minimize dehydration.

5.2.2 Tensile test protocol

Screw-down clamps were used to grip the specimens for tensile testing. The same grips and tightening procedure were used as in (Peloquin et al. 2016). Specimens assigned to cracked groups had their cracks cut at this point. Two layers of 400 grit cloth sandpaper were used to protect the specimens from the grips' teeth while still maintaining clamping friction. The grips were tightened to 8 in-lb torque, left alone for 10 minutes for the specimen to relax, and retightened to the same torque. The gripped specimens were then transferred to the tensile tester.

The tensile test protocol consisted of applying a 20 kPa preload, which was used to establish the undeformed specimen length. Ten cycles of preconditioning to 4% grip-to-grip strain were then applied, followed by a ramp to failure. The applied displacement rate was 0.5 mm/s (quasi-static). Video was recorded during the test at 15 fps with frame dimensions of 1280 pixels by

Table 5.2: Specimen dimensions (mean \pm sd)

Group	Control/Cracked	Width (mm)	Grip-to-grip length (mm)	Thickness (mm)	Crack length (mm)
circumferential 45° center crack	control	7.7 \pm 2.9	35.8 \pm 1.8	1.2 \pm 0.3	
	cracked	10.1 \pm 2.0	35.9 \pm 2.3	1.2 \pm 0.3	3.2 \pm 0.3
circumferential 90° edge crack	control	6.9 \pm 1.6	37.3 \pm 2.4	1.07 \pm 0.14	
	cracked	9.1 \pm 2.4	37.6 \pm 1.8	1.02 \pm 0.25	2.9 \pm 0.4
radial 90° edge crack	control	5.6 \pm 1.0	12.1 \pm 2.3	1.6 \pm 0.3	
	cracked	5.8 \pm 1.7	12.7 \pm 2.0	1.5 \pm 0.3	1.9 \pm 0.5

960 pixels. The image scale was about 40 pixels/mm for circumferential specimens and about 60 pixels/mm for radial specimens.

Tested specimens were classified as terminating in midsubstance rupture, mixed rupture, grip line rupture, gripped region failure, or no rupture according to published definitions (Pelouquin et al. 2016; Chapter 4). As in this previous study, tests terminating in longitudinal split, gripped region failure, or no rupture were excluded from all analysis as stress cannot be reliably calculated for these failures. The final counts used for analysis are given by analysis group in Table 5.1, as previously mentioned. The full counts of each test terminus are presented in Table 5.3 to provide accurate marginal distributions for failure location by crack type. Images of ruptures for individual specimens are listed in Appendix C.

Table 5.3: Specimen counts by rupture type

Group	Rupture Type	Included	Control	Cracked	Sum
Circumferential 45° center crack	Midsubstance rupture	Yes	3	3	6
	Mixed rupture	Yes	6	7	13
	Grip line rupture	Yes	2	2	4
	Gripped region failure	No	1	4	5
	Longitudinal split	No	0	0	0
	No rupture	No	4	3	7
	Sum			16	19
Circumferential 90° edge crack	Midsubstance rupture	Yes	3	3	6
	Mixed rupture	Yes	5	10	15
	Grip line rupture	Yes	3	0	3
	Gripped region failure	No	4	5	9
	Longitudinal split	No	0	2	2
	No rupture	No	1	1	2
	Sum			16	21
Radial 90° edge crack	Midsubstance rupture	Yes	8	11	19
	Mixed rupture	Yes	3	3	6
	Grip line rupture	Yes	15	2	17
	Gripped region failure	No	0	1	1
	Longitudinal split	No	0	0	0
	No rupture	No	1	3	4
	Sum			27	20

5.2.3 Stress and strain data processing

The stress–strain curves resulting from the tensile tests were summarized using the yield point (yield strain and yield stress), tangent modulus at the yield point, and the peak point (peak strain and peak stress). Strain was calculated using the current grip-to-grip length l and the initial grip-to-grip length l_0 and reported as stretch ratio ($\lambda = l/l_0$) or Lagrange strain ($E_{xx} = 1/2[\lambda^2 - 1]$). Yield was identified as the inflection point in the stress–strain curve following the methodology in (Peloquin et al. 2016). For cracked specimens, the cross-sectional area in the stress calculations was reduced by a factor equal to the proportional width severed by the crack. The calculated stress is thus the average stress in the narrow part of the specimen left untransected by the crack.

Optical Lagrange strain fields were computed across the specimen surface from the video recordings using digital image correlation. The software used was Vic-2D 2009 (Correlated Solutions, Columbia, SC). Settings were the same as in Chapter 4. The correlation window (subset size) was $0.7 \text{ mm} \times 0.7 \text{ mm}$. Exhaustive search, low pass filtering, and incremental correlation were enabled. Strain post-processing used a 15 px exponential decay filter. Trial runs during the study development showed that the subset size setting had the strongest effect on the appearance of the resulting strain field. The particular choice of $0.7 \text{ mm} \times 0.7 \text{ mm}$ is a compromise between minimizing spurious correlations (which favors a large correlation window) and retaining spatial fidelity to identify strain concentrations and inter-fascicle sliding (which favors a small correlation window). The chosen Vic-2D settings are discussed in detail in Appendix B, including a sensitivity analysis for subset size and filter size.

In cracked specimens, the region of interest for strain analysis was drawn so that no correlation window spanned the crack. Otherwise, large spurious strains would result as the crack opened. Longitudinal strain (E_{xx}), shear strain (E_{xy}), and transverse strain (E_{yy}) were measured individually. In cracked specimens, the optical strain field was partitioned into near-tip and away-from-tip regions (Figure 5.2) to check for strain concentrations near the crack tip. Since center crack specimens have two each of near-tip and away-from tip regions, the pairs were combined into one region for analysis.

Average optical strain vs. time plots were constructed by choosing a set of evenly spaced ~100 interpolation points along the grip strain axis. For each interpolation point and for each specimen, the image frame with grip strain most closely approximating the interpolation point was selected. The median optical strain in each region (near-tip and away-from-tip) was calculated for each of these frames, then the median and quantiles were calculated across all specimens.

5.2.4 Statistics and inference

The hypothesis that cracks weaken the meniscus was tested by comparing stress–strain statistics between cracked and crack-free specimens for each of the three test cases (circumferential loading and 90° edge cracks, circumferential loading and 45° center cracks, and radial loading and 90° edge cracks). Comparisons were made using unpaired two-sided Welch t-tests. The type I error rate for this (and all other) statistical tests was set at 0.05. In this set of comparisons, peak stress had principal importance—lesser peak stress in cracked specimens would mean that the

crack weakened the meniscus tissue.

The hypothesis that cracks generate strain concentrations near their tips was tested by comparing optical strain in the near-tip region (Figure 5.2) to that in the away-from-tip region. Comparisons were made using optical strain from the image frame at 70% of the peak stress. This stress level was chosen for comparison because by that point in the stress–strain curve all sub-rupture strain concentrations were fully developed, but rupture was mostly absent. Rupture interferes with digital image correlation because it changes the appearance of the specimen surface. The difference between the median away-from-tip region strain and the median near-tip region strain was computed for each specimen and the existence of a nonzero difference was tested using a one-sided Welch t-test.

The hypothesis that cracks propagate in meniscus tissue was tested by qualitative evaluation. The occurrence of clean crack propagation would have warranted measuring changes in crack length over time, but, as will be evident in Section 5.3.2, qualitative inspection was best suited to record the tissue’s actual behavior.

5.3 Results

5.3.1 Effects of cracks on stress–strain curves and strain fields

Comparison of stress–strain parameters between cracked specimens and their corresponding controls showed few differences, and no cracked case showed a decrease in peak stress. For both circumferential 90° edge cracks and circumferential 45° center cracks there was no difference

in yield stretch, yield stress, tangent modulus, peak stretch, or peak stress between cracked specimens and their controls (Figure 5.3). The circumferential stress–strain curves are shown in Figure 5.5. For radial 90° edge crack specimens, yield stretch, peak stretch, and peak stress were not different between cracked specimens and their controls (Figure 5.4). However, radial 90° edge crack specimens showed greater yield stress ($p = 0.02$) and tangent modulus ($p = 0.04$) than their controls. The increased yield stress and tangent modulus can also be seen in the radial stress–strain curves (Figure 5.6).

Although the presence of a crack only affected the grip-to-grip stress–strain curve parameters for the radial 90° edge crack group, every group showed a strain concentration near the crack tip. Circumferentially loaded specimens, both 45° center crack and circumferential 90° edge crack, had statistically greater longitudinal strain and shear strain near the tip than away from it (Figure 5.7). Transverse strain was not statistically different between the near-tip and away-from-tip regions. Radial 90° edge crack specimens had statistically greater longitudinal and shear strain near the crack tip, and statistically larger transverse compressive strain (Figure 5.7). Statistics are provided in Table 5.4. Although these comparisons were made at 70% of peak stress to satisfy statistical requirements, the near-tip strain concentrations appeared to begin around the yield point and to grow in severity up to the peak point (Figure 5.8).

Strain fields in circumferential tension had a mottled pattern for the E_{xx} component and strong longitudinal banding in the E_{xy} and E_{yy} components (Figure 5.9). The E_{xy} and E_{yy} bands follow the fascicle arcs and are continuous for about half the specimen length. The circumferential 45° center crack specimens and the circumferential 90° edge crack specimens exhibited

Table 5.4: Statistics for comparison of near-tip strain to away-from tip strain at 70% of peak stress. Values are mean \pm s.d. (across tests). The p value is from a paired Welch t-test.

Group	Strain	Near-tip	Away-from-tip	Near - Away	95% CI	p	p < 0.05
circumferential 90° edge	E_{xx}	0.11 ± 0.056	0.07 ± 0.02	0.04 ± 0.04	0.01 to 0.06	0.006	*
circumferential 90° edge	E_{xy}	0.08 ± 0.07	0.02 ± 0.02	0.06 ± 0.07	0.1 to 0.07	0.006	*
circumferential 90° edge	E_{yy}	-0.009 ± 0.073	-0.02 ± 0.02	0.01 ± 0.08	-0.04 to 0.06	0.7	
circumferential 45° center	E_{xx}	0.11 ± 0.038	0.076 ± 0.024	0.03 ± 0.04	0.01 to 0.05	0.012	*
circumferential 45° center	E_{xy}	0.07 ± 0.04	0.03 ± 0.02	0.05 ± 0.04	0.02 to 0.07	0.001	*
circumferential 45° center	E_{yy}	-0.02 ± 0.05	-0.03 ± 0.03	0.01 ± 0.05	-0.03 to 0.04	0.6	
radial 90° edge	E_{xx}	0.19 ± 0.13	0.14 ± 0.08	0.05 ± 0.07	0.01 to 0.09	0.012	*
radial 90° edge	E_{xy}	0.04 ± 0.03	0.02 ± 0.02	0.03 ± 0.02	0.01 to 0.04	0.0001	*
radial 90° edge	E_{yy}	-0.08 ± 0.04	-0.05 ± 0.04	-0.03 ± 0.03	-0.04 to 0.01	0.006	*

different strain patterns near the crack. In the circumferential 90° edge crack specimens, the regions to the side of the crack were strain-shielded. The edge of the strain-shielded region appeared to follow the arc of the neighboring fascicles. The near-tip E_{xy} and E_{yy} strain concentrations in the circumferential 90° edge crack specimens tended to be qualitatively greater in magnitude than the E_{xy} and E_{yy} concentrations elsewhere in the specimen; this was less evident in the circumferential 45° center crack specimens. The circumferential strain fields, except for the crack-related perturbations, were similar to the uncracked controls and the uncracked specimens used in (Chapter 4; Peloquin et al. 2016).

The radial 90° edge crack specimens exhibited a smoother E_{xx} field than the circumferential specimens. There were a handful of blob-shaped regions with elevated E_{xx} (Figure 5.9). The crack tip E_{xx} and E_{xy} concentrations were clearly evident in most radial 90° edge crack specimens, but other regions could exhibit strain with similar magnitude. The crack tip compressive E_{yy} concentrations were usually not very obvious; regions with similar or greater magnitudes of transverse compression existed elsewhere. Like the circumferential specimens, the radial specimens' strain fields were similar to those in Chapter 4 (Peloquin et al. 2016) except for the perturbations caused by the crack.

5.3.2 Qualitative rupture patterns and crack behavior

Rupture in the circumferential 90° edge crack specimens proceeded predominantly by interfascicle sliding, creating broad, irregular tears with many bridging fibers (for example, see Figure 5.10). In 12 of the 13 specimens, the region near the crack tip was the first to display visible

rupture. Eight of these near-tip ruptures initially grew by inter-fascicle shear perpendicular to the original crack direction. The other four near-tip ruptures initially grew in the original crack direction. However, the ruptures broadened as they grew, with fully developed ruptures forming a ragged tear with ~2 mm of frayed tissue on either side. Large, easily visible ruptures almost always occurred post-peak. Furthermore, inter-fascicle sliding occurred throughout the specimen, with individual shear bands spanning the whole specimen length. The rupture zone often shifted location longitudinally via a band of inter-fascicle shear. Secondary ruptures also occurred separate from the initial rupture, either merging with the initial rupture or remaining separate and incomplete.

A common site of secondary rupture (6 cases observed) was where the anatomic outer edge of the specimen (opposite the crack side) crossed the grip line; this is in contrast to the intersection of the inner edge with the grip line, where secondary ruptures did not occur. The manner in which ruptures developed was qualitatively similar between crack and control specimens. Overall, although the crack tip was the preferential location for initial rupture, the formation of shear bands, the large extent of the rupture region, and the formation of secondary rupture sites in the circumferential 90° edge crack specimens means that even if the crack initially propagated, it rapidly transformed into a failure that was not at all crack-like.

Ruptures in the circumferential 45° edge crack specimens had the same broad, irregular morphology as in the other circumferentially stretched specimens, but the association of initial rupture with the crack tips was less obvious. Small ruptures still occurred at the crack tips in the early stages of rupture, but in parallel with early rupture formation at the grip line (6 out

of 12 cases) or at the specimen edge (6 out of 12 cases). The primary rupture usually (8 out of 12 cases) grew to cross the crack (Figure 5.12). (The other four cases include 3 grip line ruptures and 1 rupture independent of both the crack and the grip line.) Shear rupture between fascicles, qualitatively, did not affect rupture progression as strongly as in the circumferential 90° edge crack specimens. It was still ubiquitous, however, and in two cases shear bands of sufficient strength developed at the crack tips to cause a z-patterned rupture (Figure 5.13). With rupture usually originating away from the crack, there is little evidence for crack growth in the circumferential 45° center crack specimens.

Radial specimens, unlike circumferential specimens, did show some examples of crack growth via incremental, local rupture at the crack tip (Figure 5.14). Out of 16 cases, 9 showed crack growth. Ruptures sometimes developed separate from the crack, so only 4 cases exhibited crack growth across the entire specimen with no other rupture sites. The 7 (out of 16) cases without crack growth failed by necking and simultaneous rupture across the entire uncracked width, i.e., bulk rupture. In 3 of the non-crack growth cases, bulk rupture occurred adjacent to the crack (Figure 5.15). The remainder of the non-crack growth cases failed at the grip line (3 cases) or halfway between the crack and the grip (1 case). Radial crack-free controls failed by bulk rupture. Ruptures in radial specimens, whether by crack growth or bulk rupture, were much cleaner than in circumferential specimens. Though some small fibers still bridged the rupture, only tissue within ~0.5 mm of the rupture appeared affected by it (Figures 5.14 and 5.15). The radial test configuration thus appears more amenable to crack growth than the circumferential configuration, but crack growth in the radial specimens is still a minority failure mode.

5.3.3 Rupture location

Rupture location varied considerably from one specimen to another, with numerous examples of both pure midsubstance ruptures and ruptures that in some way involved the grip line. Complete counts of each type of rupture are given in Table 5.3, including rupture types that warranted exclusion from mechanical analysis. Circumferential specimens most commonly failed by mixed rupture (involving both the midsubstance and the grip line). Radial specimens most commonly failed by midsubstance rupture, followed closely by grip line rupture. In no group did the majority of specimens fail by a single type of rupture.

Considering only the specimens that actually ruptured and were included in the mechanical analysis, circumferential 90° edge crack specimens were more likely than their corresponding controls to fail by mixed rupture, and less likely to fail by grip line rupture or midsubstance rupture ($p = 0.03$, chi-squared test). Circumferential 45° center crack specimens showed no difference in rupture type compared to their controls. Radial 90° edge crack specimens that ruptured were more likely than their controls to fail by midsubstance rupture and less likely to fail by grip line rupture ($p = 0.01$, chi-squared test).

5.4 Discussion

5.4.1 No fracture observed

This study detected no difference in strength (peak stress) between cracked and crack-free meniscus specimens loaded in either circumferential or radial uniaxial tension, implying that the

cracked specimens did not fail by fracture. Considering potential undetected effects, the available data rule out, at the 95% confidence level, a reduction in strength for any circumferential specimen group > 50% and a reduction in strength for the radial 90° edge crack group > 40%. If an undetected effect of this size existed, it would decrease the mean strength of cracked specimens to about the level of the 1st quartile strength of crack-free specimens (see Figures 5.3 and 5.4). An undetected effect of this size would not be an especially useful predictor for the strength of any individual meniscus. The data in this study thus are sufficient to conclude that cracked meniscus specimens rupture at stresses functionally similar to their crack-free counterparts.

The conclusion that circumferential specimens did not fail by fracture is also strongly supported by the video recordings of each test, which show broad ruptures with extensive interdigitating fiber sliding (Figure 5.10). Crack growth, a necessary component of fracture, was not observed in circumferential specimens. Nor did the presence of the crack change the stress at failure. This evidence indicates that the circumferential specimens did not fail by fracture.

Radial specimens were more equivocal, with roughly half showing progressive failure by crack growth (Figure 5.14). Crack growth is consistent with fracture, but it alone is not sufficient to conclude that failure was by fracture. Cracked radial specimens had similar peak stress to their controls and so did not demonstrably fail by fracture. Fracture may have been partially involved in radial specimen failure, but not enough to change the nominal stress at failure. A valid, predictive measurement of fracture toughness cannot be made from this data.

5.4.2 Fracture test configurations

To contextualize the finding that the failure of the cracked specimens did not occur by fracture, it is necessary to consider the ability of the test setup to elicit crack propagation. This can be done to some degree by analogy to standard engineering materials, with the caveat that the meniscus' anisotropy, nonlinearity, heterogeneity, fluid flow, and viscoelasticity make these comparisons imprecise. If the meniscus tissue in the 90° edge crack test configuration, which is a single edge notch (SENT) configuration, was substituted with aluminum, titanium, or most steels, the particular specimen shape and size used here would have produced fracture at loads 50% to 15% less than the ultimate tensile strength. These estimates were made with the formula $K_I = \sigma\sqrt{\pi a}f(a/W)$ with $f(a/W) = 1.6$, where K_I is the stress intensity, σ is the remote stress, and a is the crack length (Tada et al. 2000). SENT tests are not a particularly demanding test of fracture toughness.

Alternatives such as compact tension or single edge notched bend tests can generate stress intensity values ~4 times greater than SENT. Chin-Purcell and Lewis (1996) tested compact tension specimens of patellar cartilage, using the subchondral bone for gripping and as part of the crack; this test configuration may have produced fracture and a valid measurement of fracture toughness (Taylor et al. 2012). However, the temporomandibular joint disc has also been tested in compact tension, and did not produce a crack-induced decrease in strength (Koombua et al. 2006; Taylor et al. 2012). It may be possible to use compact tension or single edge notched bend tests for soft tissue like the meniscus, or otherwise devise a test configuration that produces greater stress intensity than SENT, but this must be left to future studies.

The 45° center crack configuration was used in the present study as an ostensibly more severe inducer of meniscus fracture, as it was previously predicted by FEA of fiber-reinforced soft tissue to produce ~10× greater near-tip fiber-aligned stresses (Peloquin and Elliott 2016) (Chapter 3). However, the 45° center crack configuration did not cause crack extension or a reduction in specimen strength. The extent to which the FEA prediction from (Chapter 3) was valid is uncertain. The meniscus' fracture toughness may be so great that a 10-fold stress increase relative to the stress concentration in SENT specimens is still insufficient to cause fracture. Inter-fascicle sliding was a major component of failure and the FEA model does not represent this. Additionally, the crack most likely interacts with fascicles as discrete units, rather than a continuum as employed in the model. Further work is necessary to add the characteristic features of meniscus failure to the model.

5.4.3 Crack-induced changes in radial specimen yield stress and tangent modulus

The stress-strain curve statistics for radial specimens produced the unexpected result that, compared to crack-free controls, the cracked specimens had greater yield stress and tangent modulus. Inspection of the stress-strain curves confirmed that the cracked radial specimens had steeper stress-strain curves, at least up to the peak (Figure 5.6). The reason is not clear. The cracked radial specimens were more likely than their crack-free controls to fail in the midsubstance, but the cracked specimens' midsubstance ruptures also had greater yield stress (not significant; $p > 0.05$), so there is some other effect at work besides a change in failure location. The test endpoint (type of rupture) does not explain this effect.

5.4.4 Morphology of ruptures and functional failure

Nearly all large ruptures in circumferential specimens developed post-peak. Fibers that bridged the rupture continued to connect the two halves of the specimen even when all load-bearing capacity had been lost post-peak. For example, the circumferential specimen rupture illustrated in Figure 5.10 is bearing ~0 MPa stress and 100% strain at the time the image was taken; its strain at peak load was 42%. This is a typical outcome. Small fiber connections were frequently maintained past 100% strain. A ruptured specimen that still has fibers bridging the rupture resembles a degenerative tear (for example, Figure 2D in McDermott 2006).

The stress–strain curves for both circumferential (Figure 5.5) and radial (Figure 5.6) specimens show residual load bearing for about as much strain past the peak point as there was before the peak point. However, the maintenance of tissue strength once the peak point has been exceeded is precarious; any fixed-load boundary condition would result in complete failure. However, a prescribed-displacement boundary condition would preserve the meniscus' remaining structural integrity. As the meniscus shares the role of knee stabilization with the various knee ligaments and the joint capsule (Pedersen 2006; Peltier et al. 2015; Greis et al. 2002), a post-peak, a partially ruptured meniscus in vivo may not be stretched to the point where dissociates into two pieces. Even if the tissue appears to be still in one piece (in, e.g., MRI), near-complete mechanical failure may exist.

5.4.5 Significance of increased strain near the crack tip

Longitudinal and shear strain in all test groups was greater near the crack tip than away from it. Radial cracked specimens additionally had greater transverse strain near the crack tip. The increase in longitudinal strain in the circumferential specimens (i.e., fiber-aligned strain) was between 0.01 and 0.06 (95% CI), which could cause adverse events near the crack tip even under normal physiologic deformation. In a study of rat medial collateral ligament, longitudinal strain > 0.05 causes permanent deformation, which was interpreted as structural damage (Provenzano et al. 2002b). Other work reports a permanent deformation threshold of 0.06 strain in porcine flexor tendon (Duenwald-Kuehl et al. 2012). Sverdlik and Lanir (2002) consider the damage threshold of tendon to be 0.08 strain. FEA of intact meniscus under physiologic loads has predicted strains between 0.01 and 0.04 (albeit with limited constitutive models and geometry) (Aspden 1985; Spilker et al. 1992). Compression of porcine menisci with $2 \times$ body weight results in radial and circumferential stretches of $\sim 1\%$ and compressive stretch of -12% , as measured by MR image correlation (Freutel et al. 2014). The excess strain near the crack tip is thus very likely to exceed the strain at which permanent deformation occurs. The notion that increased near-tip strain causes early near-tip damage is supported, in the present study, by the prevalence of initial rupture at the crack tip. Although the increase in near-tip strain was not sufficiently severe to decrease yield stress or peak stress in a single loading cycle, repeated loading cycles may cause cumulative damage with consequent compromised meniscus function.

In addition to structural damage, increased strain near the crack tip may cause local cell death. In ligament, cell death is linearly proportional to applied strain (Provenzano et al. 2002b).

Although healthy tissue presumably has some capacity for self-renewal, greater near-tip strain increases the risk of exceeding this capacity. Necrotic cells also release proteases, increasing the risk of structural degradation. Similar to mechanical damage, cell damage may accumulate over time via repeated loading and cause dysfunction.

The meniscus' fibrous structure guides local rupture along fascicle boundaries, deflecting crack growth so that the near-tip strain concentration does not extend across the width of a tensile test specimen. However, although crack deflection can prevent transverse rupture, it can also increase the size of the strain concentration associated with the crack tip by spreading it along the length of the neighboring fascicles. Greater strain may promote damage, so a larger strain concentration region may not be desirable. In circumferential tests, shear strain concentrations extended from the crack tip all the way to the grips, and were probably caused by inter-fascicle shear. These inter-fascicle strain concentrations could cause problems in vivo by promoting the growth of circumferential, bucket handle, vertical, and horizontal tears (Aspden 1985; Fithian et al. 1990; Kelly et al. 1990; Smillie 1978).

5.4.6 Permanent deformation

Although detecting the onset and severity of permanent deformation and damage was not a study objective, non-recoverable inter-fascicle sliding (shear strain) is clearly visible in the test videos. Fascicles accrue relative slip of several mm and this slip does not recover upon rupture. The onset of damage and permanent deformation deserves further investigation. The yield point is a good candidate for the onset of damage or plasticity. However, the permanent deformation

threshold in tendon is about 0.05 strain (Provenzano et al. 2002b; Duenwald-Kuehl et al. 2012), which is half of the meniscus' yield strain. Measurements of post-rupture strain recovery from the present study's data are uncertain due to the difficulty of digital image correlation past the rupture point, but the onset of damage and permanent deformation deserves future study.

5.4.7 Comparison of meniscus failure to that of other tissues

This interdigitating rupture pattern in circumferential meniscus specimens is reminiscent of the “mop-head” or frayed failure pattern typical of tendon (Schechtman and Bader 1997; Von Forell et al. 2014; Von Forell and Bowden 2014), but the extent of interdigitating fiber pull-out is smaller in the meniscus. Accordingly, the crack blunting observed in the present study's meniscus specimens was less severe, and crack-associated increases in near-tip strain (all test groups) and crack propagation (albeit only in the radial 90° edge crack group) was observed. The meniscus cracks also exhibited much less blunting than did cracks in bovine articular cartilage, in which the entire uncracked width undergoes rupture by necking (Stok and Oloyede 2007). Cultured cartilage hydrogels, in contrast, displayed sharp crack propagation (Oyen-Tiesma and Cook 2001), although post-publication analysis shows that the crack may not have reduced the hydrogel's strength (Taylor et al. 2012). The two fibrous tissues in which fracture was observed with some certainty, stratum corneum (Wu et al. 2006b) and bone-attached superficial zone cartilage (Chin-Purcell and Lewis 1996), unfortunately do not have published images of their rupture morphology. Rupture of edge-cracked cooked muscle somewhat resembles the rupture of edge-cracked meniscus, although the muscle did not exhibit much fascicle sliding (Purslow

1985). Meniscus is somewhere between tendon and articular cartilage in structure and properties, so the general lack of fracture in tendon and the inconsistent observation of fracture in fracture studies of articular cartilage implies that fracture in the meniscus is either irrelevant (like tendon) or limited to particular circumstances (like articular cartilage).

Biomimetic materials may be a better subject than native fibrous material for future crack-related studies, as the consistency and adjustability of manufactured materials should allow more flexible and efficient study designs. Fracture—both sharp crack propagation and decreased strength—has been observed in tensile tests of edge-cracked gelatin scaffolds, but neither in PCL electrospun scaffolds nor in nonwoven fabric (Koh et al. 2013). Scanning electron microscopy of the cracks in gelatin showed a sharp μm -scale crack extending from the macroscopic crack tip. The gelatin fibers are only $\sim 0.1 \mu\text{m}$ in diameter and randomly aligned, which allows for sharp crack growth. The nonwoven fabric, with fibers a thousandfold larger, exhibits crack blunting and inter-fiber shear like the meniscus. A biomimetic material based on nonwoven fabric may be useful as a surrogate material for failure studies in meniscus and other fibrous soft tissues, such as annulus fibrosus, that have crack-related pathologies.

5.4.8 Differences between loading axes

The fascicle structure of the meniscus appears to have a strong influence on how cracks in the meniscus do and do not propagate. Circumferential specimens appeared to preferentially rupture along fascicle boundaries, typically by inter-fascicle shear. In circumferential tension this results in deflection of the crack to proceed parallel to the fascicles (as opposed to its original di-

rection perpendicular to the fibers). Consequently, insufficient fascicle stress develops to cause fascicle rupture. Instead, ruptures propagate across the specimen by inter-fascicle shear, causing fascicles to slide past each other in an interdigitating pattern over a large area. Specimens tested in radial tension instead have their fascicles oriented perpendicular to the tensile axis. The interfaces between fascicles provide a propagation path for a 90° edge crack that guides the crack to extend in its original direction—this is likely why crack extension was actually observed in radial specimens.

The meniscus contains sparsely distributed radial tie fibers (Andrews et al. 2014; Rattner et al. 2011). These tie fibers, when present, increase the stiffness and strength of radial specimens (Skaggs et al. 1994a). The extent to which radial tie fibers were present in the present study's specimens is unclear. Skaggs and Mow (1990) observed about even proportions of specimens with full grip-to-grip tie fibers, partial tie fibers, and no tie fibers in their study of radial-axial specimens, but specimens cut in the radial-circumferential plane (as used in the present study) are less likely to contain tie fibers. Qualitative examination of radial specimens in the present study revealed no examples of radial tie fibers spanning the site of rupture. The radial stress–strain curves (Figure 5.6) appear to be clustered into a high stiffness and low stiffness group, but this pattern is subjective. The effect of radial tie fibers on crack behavior, if any, is unknown and may be addressed in future work.

5.4.9 Potential for fracture in vivo

Although none of the test configurations used in this study—circumferential 90° edge crack (SENT), circumferential 45° center crack, and radial 90° edge crack (Figure 5.1)—produced fracture, this is not conclusive evidence that fracture does not occur under in vivo conditions. There are many differences between the ex vivo test and in vivo conditions that could inhibit fracture in the ex vivo test and promote it in vivo.

In vivo, the meniscus is thought, largely based on FEA models, to be subjected to biaxial tension in the circumferential-radial plane combined with axial compression and shear (Kawamura et al. 2003; Fithian et al. 1990; Mononen et al. 2013). FEA simulations have predicted heterogeneous internal strain and stress, with both negative and positive magnitudes for the same component depending on the region (Aspden 1985; Spilker et al. 1992; Párraga Quiroga et al. 2014; Atmaca et al. 2013). Although the FEA models may not have perfect fidelity, they suffice to demonstrate that the meniscus has a complex internal deformation field under normal activity. The existence of heterogeneous internal strains has also been verified by MR image correlation (Freutel et al. 2014). Tests with boundary conditions and internal deformations more representative of in vivo conditions may produce fracture.

Based on the observed failure morphology in the present study, inter-fascicle sliding appeared to be the primary deformation mechanism limiting crack propagation in circumferential specimens. Inter-fascicle sliding both deflected the crack towards the grips and caused a large process zone (or possibly plastic zone) to develop. A process zone of similar size to the uncracked width can inhibit fracture and cause a shift to a different failure mechanism (Taylor et

al. 2012), such as bulk rupture. Inter-fascicle sliding may have been promoted by the creation of fascicle free ends at the specimen surface while microtoming. Deflection of the crack towards the grips also caused the grip line stress concentration to have a major role in the specimen's rupture. Also, inter-fascicle sliding allowed individual fascicles to slip out of the gripped region. In vivo, the effect of inter-fascicle sliding may be more limited because (1) there are fewer free fascicle ends, (2) the whole meniscus allows more space for a process zone to exist away from the meniscus boundaries, and (3) the meniscus' bony insertions presumably cause less of a stress concentration than metal tensile grips. In tests of radial specimens, necking at the crack location, facilitated by fiber reorientation, appeared to be the principal inhibitor of fracture. In vivo, necking via reorientation of circumferential fibers would be limited because these fibers would be under tension. Eliminating or limiting inter-fascicle sliding and fiber reorientation would increase the crack tip stress concentration and keep the process zone local to the crack tip, promoting fracture.

Loading rate and crack length are also worth investigating as factors that may promote fracture. Meniscus tears often occur in the context of sports, implying involvement of high rate loading (Drosos and Pozo 2004; Feucht et al. 2015), and ex vivo impact testing has produced meniscus tears (Isaac et al. 2010; Isaac et al. 2008). Tests of longer cracks would also be beneficial, although this is somewhat limited by the possible specimen dimensions. Tears in vivo that are of concern are often have length in the 5 mm to 25 mm range (Stärke et al. 2009; Roeddecker et al. 1994; Lento and Akuthota 2000; Seil et al. 2009). Large tears begin as small tears, though, so examining the entire range would be ideal.

5.5 Conclusion

In this study, circumferential and radial cracked meniscus specimens were loaded to failure in uniaxial tension to determine whether they fail by fracture. This determination was made by comparing the peak stress of cracked specimens to crack-free controls. Cracks did not significantly change the peak stress. Fracture therefore did not occur or had a non-significant impact on meniscus strength. Any potential undetected fracture effect was similar to the magnitude of inter-individual variation. Therefore, the presence of a crack says nothing useful about the meniscus's effective strength, only that the cross-sectional area (and thus the maximum safe load) is reduced. Inter-fascicle sliding produced ubiquitous crack deflection and large rupture zones in circumferentially stretched specimens, with no sign of crack growth except for local rupture extending ~ 0.5 mm from the crack tip early in the failure process. In radial tension, about 50% of specimens failed with crack growth. Despite the lack of fracture and, generally, crack growth, cracks did cause increased local strain near their tips. Cracked circumferential and radial specimens had increased longitudinal (fiber-aligned) and shear strain near the crack tip. Cracked radial specimens in addition had greater transverse compressive strain near the crack tip. Increased near-tip strain may cause local damage, such as collagen denaturation or cell death, and, in vivo, meniscus dysfunction. Increased crack tip strain may also facilitate crack growth under cyclic loading. These findings are a step towards accurately predicting the (non-)propagation of meniscus tears in vivo, which will aid to clinical treatment planning. The methods employed can also be applied to materials used for meniscus repair or regeneration to test whether they have fracture resistance comparable to native meniscus.

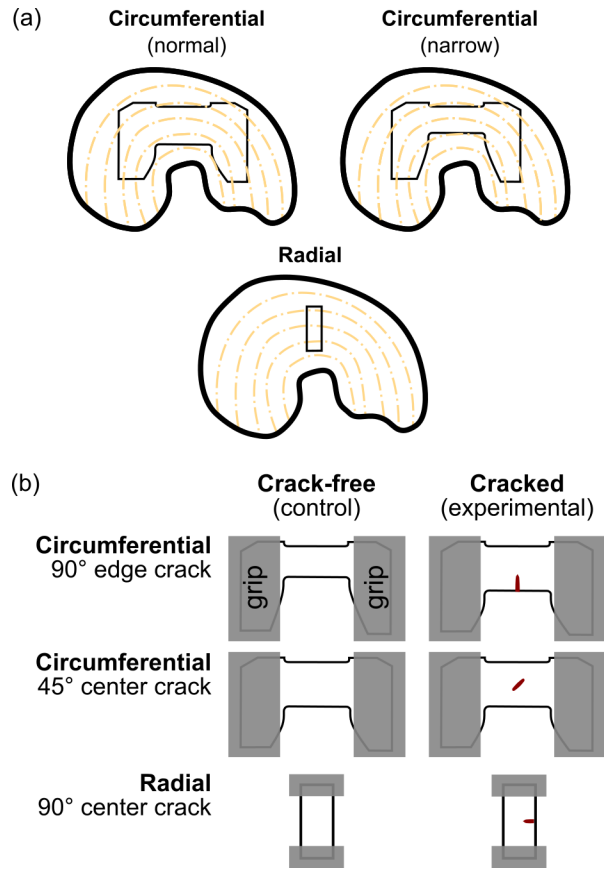


Figure 5.1: Specimen schematics. (a) Anatomic origin of specimens with respect to the whole meniscus. This example shows a lateral meniscus. The narrow circumferential specimens are cut so that they have the same width and come from the same region as the uncracked width in a normal specimen with a 90° edge crack. (b) Specimen shapes for each of this study's analysis groups (circumferential 90° edge crack, circumferential 45° center crack, and radial 90° center crack) and their corresponding crack-free controls. The narrow specimens are used as controls for the 90° edge crack specimens so that they have similar cross-sectional area and come from the same region.

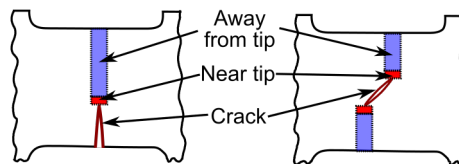


Figure 5.2: Near-tip and away-from-tip regions defined for identifying possible near-tip strain concentrations. Both regions extended 0.5 mm to the left and right of the crack. The near-tip region extended 0.5 mm from the crack tip. All other tissue in the 1 mm wide band extending from the crack tip was assigned to the away-from-tip region.

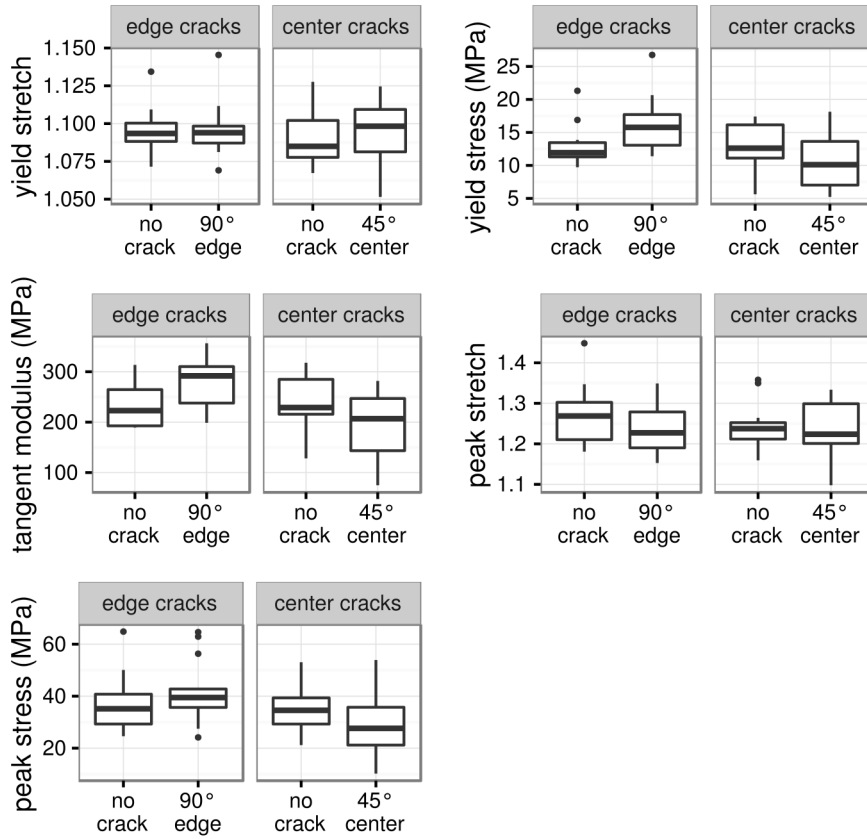


Figure 5.3: Comparison of stress–strain curve parameters between circumferentially stretched cracked specimens and their corresponding controls. The boxplots follow Tukey’s style.

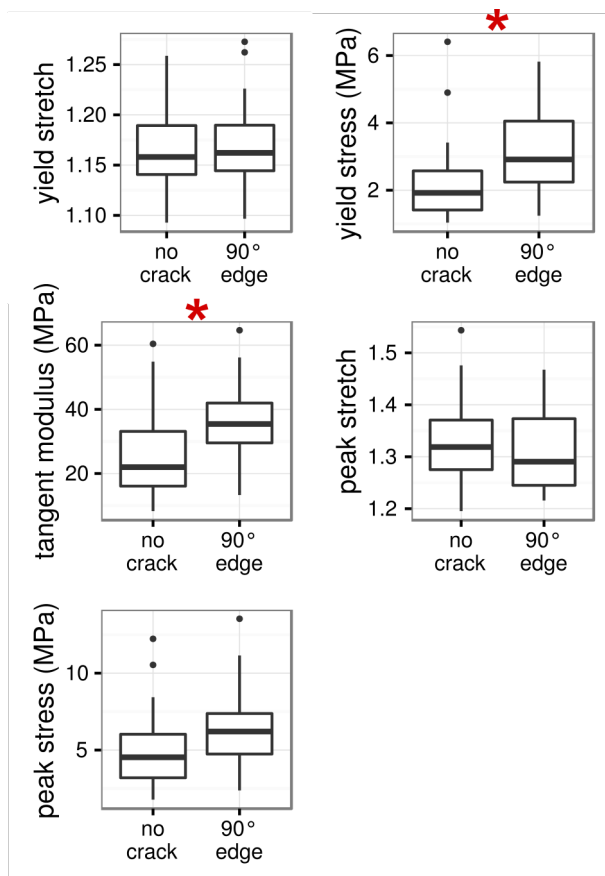


Figure 5.4: Comparison of stress–strain curve parameters between radially stretched cracked specimens and their corresponding controls. The boxplots follow Tukey’s style. * indicates $p < 0.05$, no crack vs. 90° edge.

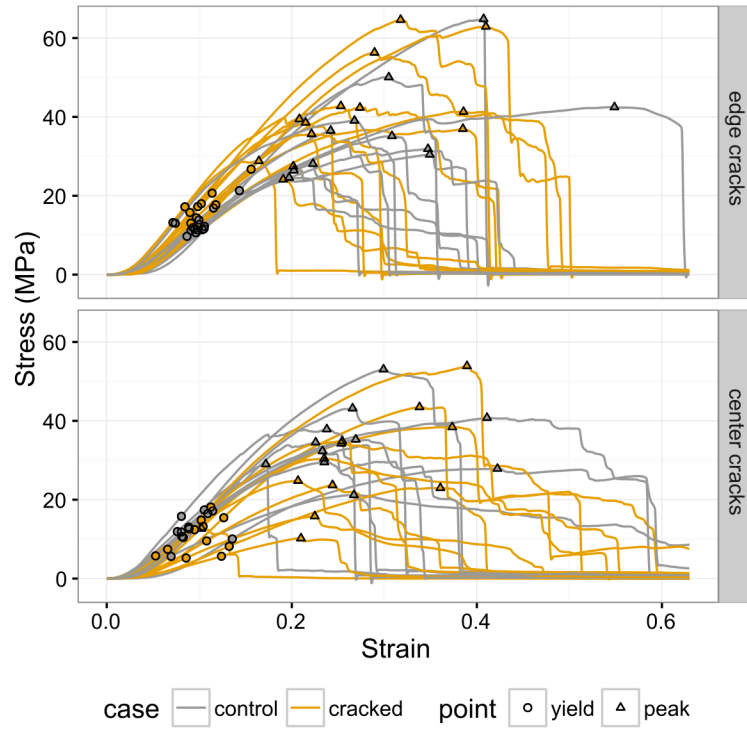


Figure 5.5: Stress–strain curves for circumferential 90° edge crack and 45° center crack specimens and their controls.

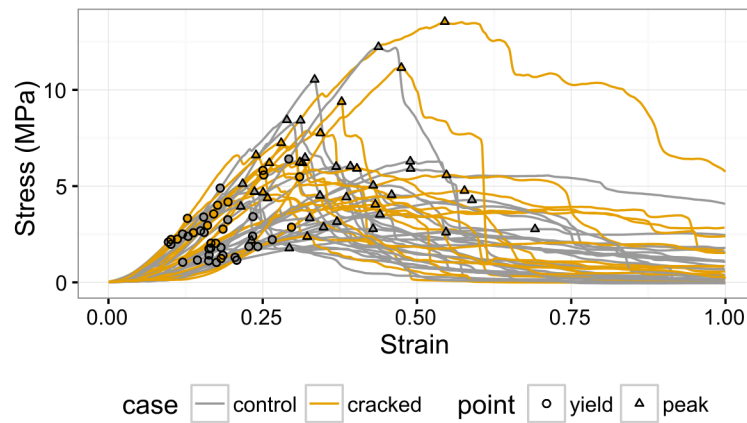


Figure 5.6: Stress–strain curves for radial 90° edge crack specimens and their controls.

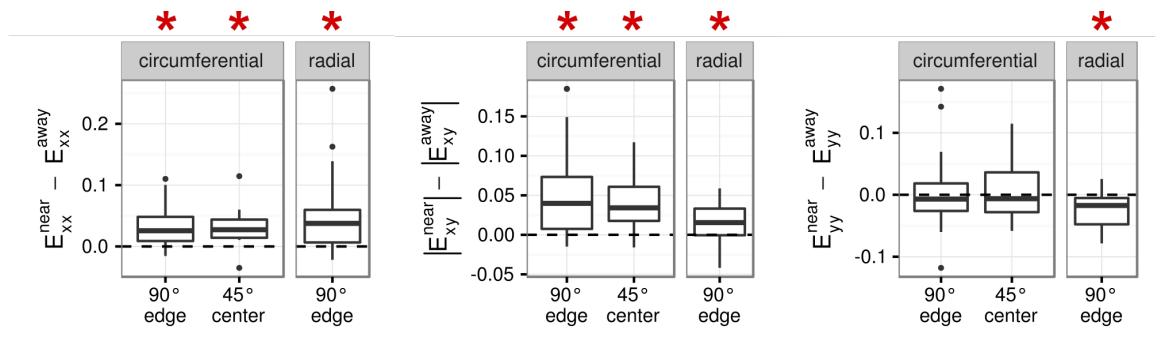


Figure 5.7: Optical strain compared pairwise between near-tip and away-from tip regions. * indicates $p < 0.05$, paired near-tip vs. away-from-tip.

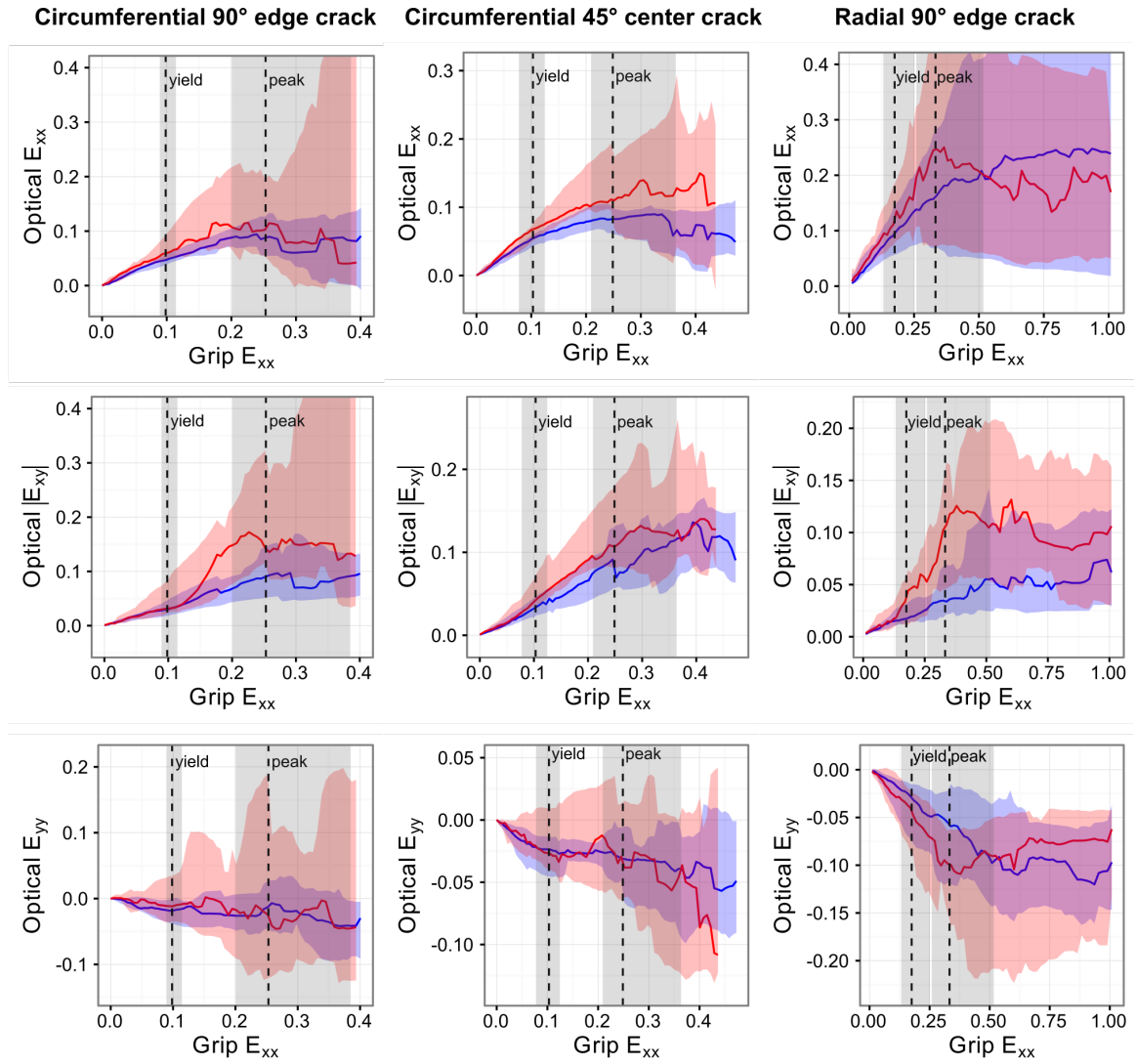
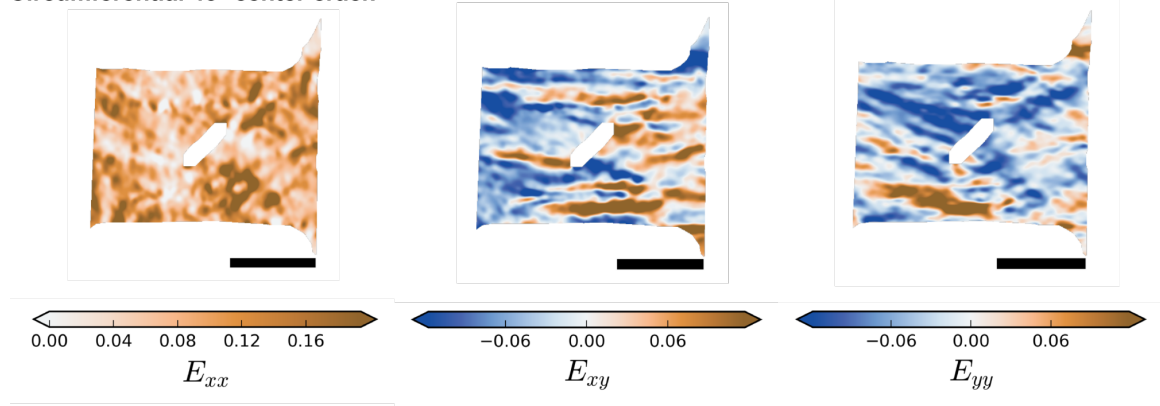
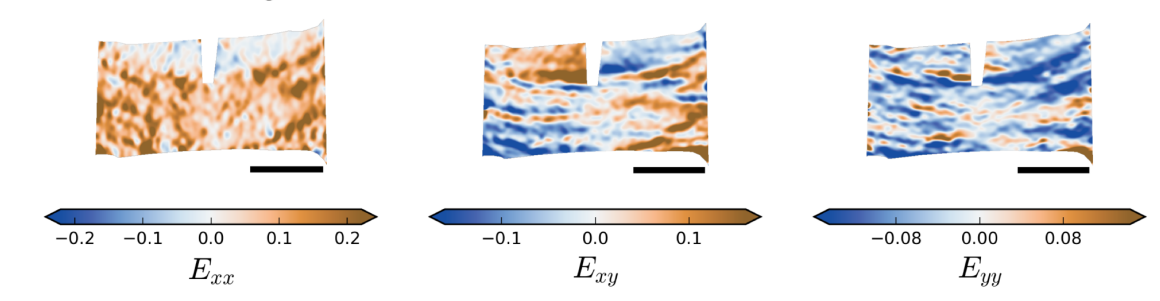


Figure 5.8: Optical strain near and away from the crack tip. Solid or dashed line = median; shaded band = 0.16 and 0.84 quantiles; blue = away from tip; red = near tip. The yield strain and peak strain for the tests shown in each plot are marked with vertical dashed lines. The plotted values were computed from the pooled median strain values for each region for each test.

Circumferential 45° center crack



Circumferential 90° edge crack



Radial 90° edge crack

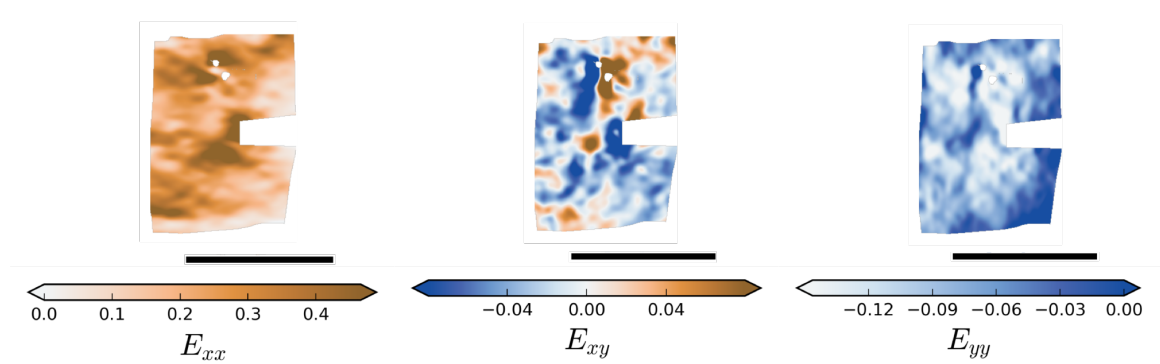


Figure 5.9: Representative strain fields for cracked specimens in each analysis group loaded to 70% of peak stress.

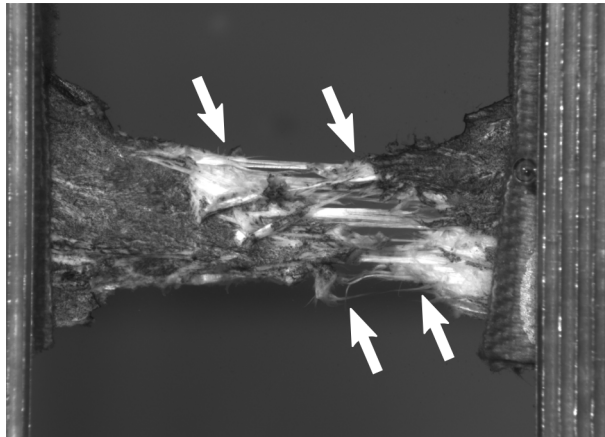


Figure 5.10: Representative example of circumferential specimen rupture (bracketed by arrows). Ruptures were consistently broad, spanning ~5 mm of specimen length and were bridged by fascicles and smaller fibers.

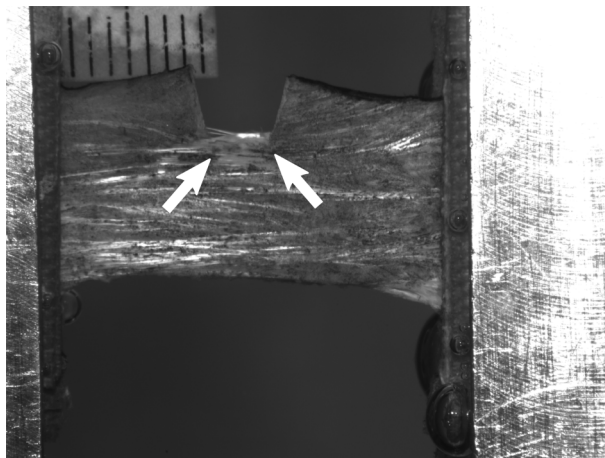


Figure 5.11: Example of near-crack-tip rupture (bracketed by arrows) and crack tip opening in a circumferential 90° edge crack specimen.

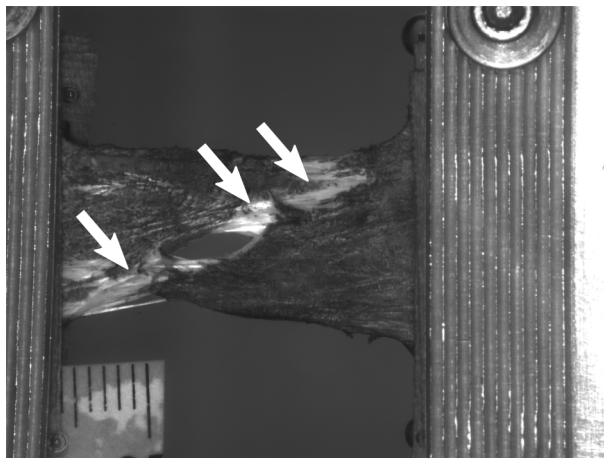


Figure 5.12: Representative example of rupture (arrows) in a circumferential 45° center crack specimen.

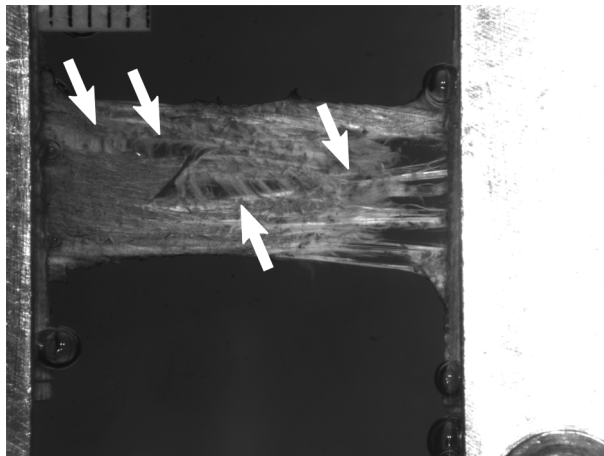


Figure 5.13: An unusual z-shaped rupture (arrows) in a circumferential 45° center crack specimen.

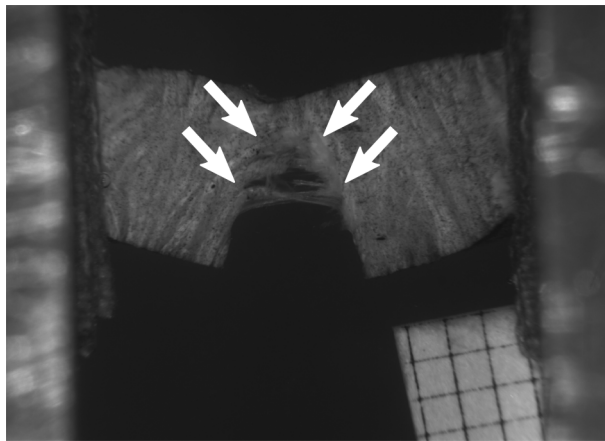


Figure 5.14: Example of crack growth (bracketed by arrows) in a radial 90° edge crack specimen.



Figure 5.15: Example of rupture (bracketed by arrows) in a radial 90° edge crack specimen by necking and simultaneous rupture across the entire uncracked width. This failure mode is in contrast to crack growth.

CHAPTER 6: CONCLUSION AND FUTURE DIRECTIONS

6.1 Summary

The overall objective of this work was to investigate meniscus mechanics and failure in the context of meniscus cracks, with specific attention to failure mechanisms and local strain concentrations. Despite the predominant role cracks have in meniscus pathology, and their role in the etiology of osteoarthritis, very little is known about the mechanics of cracked meniscus. This lack of information means that clinical decisions must be made on the basis of accumulated experience and rules of thumb, without recourse to quantitative predictions of crack propagation and mechanical deficiency. This study was undertaken to begin filling this gap in knowledge regarding the behavior of meniscus cracks. To support this goal, key nonlinear mechanical properties of the meniscus were quantified in uniaxial tension for both crack-free and cracked specimens and several experimental issues regarding stress–strain curve quantification, rupture location, and specimen shape were examined. FEA was used to assist experimental design by identifying test cases with the greatest risk of fracture or crack growth; these test cases were selected for physical *ex vivo* testing. Since the meniscus bears both circumferential and radial tension *in vivo*, and tension causes crack opening and, potentially, propagation, tensile properties were quantified in both the circumferential and radial directions for cracked and crack-free specimens. The cracked specimen configurations employed represented *in vivo* tears of the ra-

dial, oblique, and circumferential or bucket-handle types, which are considered to generally be caused by acute (traumatic) injury rather than progressive degeneration. This study provides new measurements of sub-failure meniscus mechanics, including a fiber recruitment model and yield point (inflection point) measurements, recommends an elongated tab specimen shape for more accurate quantification of fiber-aligned meniscus tensile mechanics, and demonstrates that, even though fracture was not observed, cracks cause increased strain near the crack tip prior to failure.

The goal of Chapter 3 was to identify test configurations for cracked meniscus specimens that would produce large stress concentrations and thus inure the likelihood that subsequent tensile testing would observe failure by fracture or, at least, crack extension. This was accomplished using finite element analysis with a previously validated hyperelastic continuum model originally established in work on intervertebral disc annulus fibrosus. The model had a matrix term and an oriented exponential fiber term. Center-cracked specimens with cracks angled 45° relative to the prevailing fiber direction were predicted to produce the greatest fiber stress concentration at the crack tip, much greater than in commonly used edge crack specimens. The 45° center crack specimen configuration was therefore considered a possible solution to the lack of crack propagation and fracture observed in previous fracture tests of fibrous soft tissue. However, 90° edge crack specimens were predicted to produce equal or greater fiber-perpendicular and fiber shear stress compared to center crack specimens. Consequently, 90° edge crack specimens were considered to be a good choice for investigating failure by matrix rupture and fiber sliding.

The goal of the work in Chapter 4 was to quantify the nonlinear mechanical properties of the meniscus in uniaxial tension and resolve several experimental issues regarding stress–strain curve quantification, rupture location, and specimen shape. Since the meniscus must support both circumferential and radial tension in vivo, tensile tests were done in both the circumferential and radial directions. A structural model based on fiber recruitment was introduced and successfully fit to experimental data. This model provides a quantitative link between the meniscus' fiber structure and its toe region stress–strain response. The yield point was quantified for the first time in meniscus using a method that defines its position in terms of the stress–strain curve's shape, rather than subjective measurement or an arbitrary threshold crossing. This method defines the yield point as the inflection point of the stress–strain curve. As an additional benefit, measurement of the yield point in this manner allows the modulus to be defined as the tangent modulus at yield. Previously, the modulus was defined using a linear fit to an arbitrary stress or strain range. The yield strain was found to closely match the strain at which fiber recruitment in the aforementioned fiber recruitment model reached ~100%. Together, the model and these stress–strain metrics are useful as functional targets for meniscus replacements or repair procedures, to compare disease states, or as diagnostic markers.

In an effort to control failure location and ensure midsubstance failure, dogbone-shaped specimens were compared with rectangular specimens. For circumferential tension tests, an expanded tab shape was introduced that has wide, asymmetric flarings in the gripped region to better accommodate the arc of the meniscus' fascicles. Failure location—midsubstance, mixed between midsubstance and grip line, and at the grip line—was classified and found to be highly

variable, but did not significantly affect the stress–strain or model parameters. Although the various specimen shapes were not effective at ensuring midsubstance rupture, the expanded tab specimens were found to securely grip the meniscus’ fibers much more effectively than either of the other two shapes. The expanded tab specimens had more rapid and complete fiber recruitment, lesser yield strain, and greater peak stress. Among the specimen shapes tested, expanded tab specimens are best for circumferential tensile testing and rectangular specimens are best for radial testing.

Strain fields measured by digital image correlation revealed significant heterogeneity in the strain response, which grew as the test progressed. Bands of shear strain, apparently developing along fascicle boundaries, were the predominant feature, suggesting inter-fascicle shear as an important deformation and damage mechanism. The shear bands extended from the midsubstance into the gripped region.

Chapter 5 describes the results of uniaxial tensile tests of cracked circumferential and radial meniscus specimens, with the goal of determining whether failure occurred by fracture or bulk rupture. Based on the results from Chapter 3, circumferential 45° center crack specimens, circumferential 90° edge crack specimens, and radial 90° edge crack specimens were used in an effort to maximize the chances of obtaining strong stress concentrations, crack propagation, and fracture. Based on the results from Chapter 4, the circumferential specimens were cut to an expanded tab shape and radial specimens were cut to a rectangle shape. Whether fracture occurred was determined by comparing the peak stress of cracked specimens to crack-free controls. It was found that cracks did not significantly change the peak stress, and failure did not

occur by fracture. A crack—at least in a uniaxial tensile test—reduces the cross-sectional area and thus reduces the maximum load the specimen can support, but does not significantly change the expected strength of the uncracked material.

Despite the lack of fracture, cracks created strain concentrations at their tips. Longitudinal (fiber-aligned) strain and shear strain (inter-fascicle shear) were significantly greater near the crack tip in circumferential specimens. In radial specimens, longitudinal (fiber-perpendicular) strain, shear strain, and transverse compression were significantly greater near the crack tip. These strain concentrations are likely to cause structural damage and cell death near the crack tip at lesser strains than would otherwise be expected. This local damage may cause crack growth under repeated loading. With the monotonic ramp loading used in the present work, circumferential cracks only propagated for a very short (< 1 mm) distance before being deflected along fascicle boundaries or spreading out into broad regions of interdigitating fascicle pull-out. About 1/2 of radial specimens displayed qualitative crack growth, but the unchanged peak stress indicated that fracture still did not occur or at most had a minor effect.

6.2 Path forward for studying crack propagation in meniscus

Tear propagation is the central aspect of meniscus pathology and requires further study. How best to proceed, however, is a difficult question. The role of fracture in meniscus failure remains uncertain. Although the present work did not demonstrate fracture, it is not ruled out as an in vivo failure mechanism. A test with a different loading rate, multiaxial loading, hydration (preload), crack geometry, heterogeneous loading, fascicle anchoring (native bony insertion vs.

screw-down clamps), specimen geometry, and other factors could produce fracture. Unlike the meniscus, other materials such as metals show a clear dichotomy between fracture and ductile rupture, with the applicable failure mechanism clearly apparent based on the failure morphology. Fracture is failure by crack propagation; ductile rupture is failure by necking and shear. Interpretation of meniscus tears is more difficult. Meniscus cracks (tears), in vivo, clearly initiate, grow, and stop growing. This process looks like fracture, but qualitative crack propagation is not proof of fracture. The actual underlying mechanisms controlling tear initiation, growth, and arrest remain to be identified. Several competing (but not necessarily exclusive) hypotheses for how meniscus tears form and grow can be formulated:

1. Acute (traumatic; single loading cycle) meniscus tear growth can occur by fracture. It did not occur in the present study because the test conditions did not produce a sufficiently severe stress concentration relative to the tissue toughness or produced a too large process or plastic zone relative to the specimen dimensions. Other sets of conditions exist that would produce a greater stress concentration and cause fracture; furthermore, such conditions occur in vivo.
2. Acute meniscus tear growth can be caused by fracture, but requires pre-existing alterations in the meniscus' properties caused by accumulated damage, disease, or aging.
3. Acute meniscus tears occur by a non fracture process involving heterogeneous loading, but this heterogeneity is not caused by the tear itself and so the tear does not self-propagate. For example, loading the inner meniscus in circumferential tension and the outer meniscus in circumferential compression would only cause failure in the inner

meniscus. The result when examined after the fact would be a radial tear. Under this hypothesis, abnormal knee motion may be required to create acute meniscus tears.

4. Meniscus tears initiate and grow due to heterogeneous material strength. The resulting partial ruptures look like tear propagation because the tear starts growing in weaker regions and grows into stronger regions. Fracture is not involved.
5. Meniscus tears grow over time as material near the tear progressively accumulates damage under repeated loading. Proteolytic degradation may assist in this process.

The snapping or popping sensation that often accompanies acute meniscus injury in young people (Lento and Akuthota 2000; Wagemakers et al. 2008) suggests sudden tear initiation and growth, favoring hypotheses 1, 2, 3, or 4. This kind of failure, from an engineering perspective, is associated with a risk of fracture, weakly favoring hypotheses 1 or 2. Tear growth in healthy rabbit meniscus can be produced by impact loading of the whole knee joint, favoring hypotheses 1, 3, or 4 (Isaac et al. 2010), but this requires the application of severe loading conditions: 13 J of energy via a dropped mass, generating 1100 N of force at impact, with the joint flexed at 90°. This impact both creates meniscus tears and ruptures the ACL. The present work's observation of tear propagation in only ~50% of radial specimens (Section 5.3.2), but no statistically significant loss of strength, is weak (inconclusive) evidence against hypothesis 1. Hypothesis 4 was suggested in a slightly different form by Kelly et al. (1990), who proposed that whether a tear propagates or not depends on the tissue architecture near its tip.

Degenerative tears, in contrast, can seldom be traced to specific loading events (Lento and Akuthota 2000; Drosos and Pozo 2004), suggesting tear growth over time (hypothesis 5). This

hypothesis can be true or false independently of the others. It is conceivable that a degenerative tear could have originated as an asymptomatic acute tear, but degenerative tears tend to have different morphology (horizontal cleavage, flap, or complex) than acute tears (Drosos and Pozo 2004). Development of symptoms also implies some degree of tear propagation or remodeling since the tear's origination. Tear propagation by multiple loading cycles over a long time period is most likely a separate process from acute tear formation. Chapter 5 shows that a crack, under single-cycle monotonic loading, causes a strain concentration near its tip. If this local increase in strain causes damage, repeated cycles may cause progressive accumulation of damage near the crack tip, potentially causing local failure and growth of the crack. A pre-existing crack or other stress concentrating defect under repeated loading may therefore cause development of a degenerative tear.

Testing these hypotheses is not straightforward, as an assertion that fracture occurs in at least one loading condition (as in hypotheses 1 and 2) cannot be directly disproved without exploring all possible variant loading configurations. Such a plan is thoroughly impractical; relevant factors include: loading rate, multiaxiality, hydration, crack length, orientation, and position, heterogeneous boundary conditions, contact loading, grip type, specimen geometry, and others. A more practical approach is to pick a test configuration estimated to be likely to produce fracture based on meniscus tear epidemiology, the limited number of fibrous soft tissue fracture studies, and by analogy with other materials. The expected utility of this approach varies with one's subjective estimate of the likelihood that fracture will occur. Discussion later in this Chapter will present compact tension specimens and rapid, physiologically representative

loading of whole meniscus that is still attached to the knee as good candidates. Regardless of the approach chosen, any test must be designed to distinguish between failure by fracture and failure without fracture; for example, by measuring crack-induced weakness or lack thereof, as was done in Chapter 5. This task is discussed in Section 6.5.

An alternative approach, and the one employed in the present work, is model-based experimental design. In the present work, FEA using existing mechanical models was used to rank readily available test designs to identify the one with the greatest chance of producing fracture (Chapter 3). The best case, circumferential uniaxial tension with a 45° center crack, was evaluated in Chapter 5 alongside established standards. Although none of the trialed configurations produced fracture in the end, the resulting data can be used to train more accurate mechanical models that incorporate effects such as structural heterogeneity and damage. The improved model can then be used to design the next round of fracture tests. Requirements for the model are discussed further in Section 6.5. Importantly, as the model converges with reality over repeated iterations, it becomes a useful research product in its own right.

6.3 Role of meniscus fascicle structure and anisotropy

The meniscus' fascicle structure is an important factor in its mechanics. The meniscus is known to be much stiffer and stronger in circumferential tension (parallel to the prevailing fascicle orientation) than in radial tension. The fascicle structure also appeared in the present work to be responsible for significant strain field heterogeneity and may have been responsible for the lack of observed fracture in uniaxial tension (related to hypothesis 1 in Section 6.2).

Strain fields in circumferential tensile tests (Chapters 4 and 5) showed bands of elevated shear strain and transverse strain that appeared to follow fascicle boundaries. The failure pattern in circumferential tension—broad ruptures with extensive interdigitating fiber sliding—suggests that failure of the inter-fascicle matrix was the critical step in determining when the entire specimen failed. The circumferential specimens used in this study were prepared so that failure by fracture required crack growth across the specimen and thus required fascicle rupture. These test cases were chosen based on the results of Chapter 3, which suggested the 45° center crack as a test case for achieving novel crack propagation and fracture in fibrous soft tissue. However, failure of the inter-fascicle matrix by inter-fascicle sliding caused crack deflection towards the grip line, diverting the crack from its original path. Widespread inter-fascicle sliding across much of the specimen width served to dissipate any crack-induced stress concentrations, limiting fascicle tension. The crack diversion and stress dissipation caused by inter-fascicle sliding may have prevented fracture from occurring.

Inter-fascicle matrix sliding also appeared to limit stress transfer from loaded fascicles to unloaded fascicles. For example, in Chapter 4 fascicles severed by the dogbone cutouts were observed to be strain shielded and hence largely unloaded; stress did not apparently redistribute across fascicle boundaries between grip-to-grip continuous fascicles in the narrow central region and the severed fascicles in the flared ends. Similarly, in the cracked specimens (Chapter 5) it is likely that the fascicles severed by the crack remained largely unloaded and the specimen behaved like it was made only of the region containing intact fascicles, reducing the effect of the crack. Since near-tip strain concentrations were observed (Section 5.3.1), crack-induced

stress concentration were still present, but it is likely that they were severely reduced compared to a homogeneous meniscus-like material without fascicle interfaces.

Factors which limit inter-fascicle sliding may in turn limit crack diversion, produce a more confined and more intense stress concentration, and increase inter-fascicle stress transfer. These changes would increase fascicle tension and make crack growth and/or fracture more likely. If the inter-fascicle matrix is viscoelastic, greater strain rate (more closely mimicking injurious overload in vivo) may achieve this. If inter-fascicle stress transfer is frictional, a reduction in fluid content such as by compression and hence tighter fascicle packing might also reduce inter-fascicle sliding. The properties of the inter-fascicle connections may also change with age or disease, potentially affecting crack propagation and fracture risk.

Although mechanical models for the meniscus such as those in Chapter 3 typically include anisotropy, the fascicles are represented as a homogeneous continuum rather than as discrete structural units with interfaces that slip, accrue damage, and fail. Consequently, current models do not reproduce the heterogeneous strain patterns observed in this work and cannot be used to predict how inter-fascicle sliding may limit fracture in favor of bulk rupture. Models have been developed to explain tissue mechanics by stress transfer between fibers inter-fiber shear and slip (Skaggs et al. 1994b; Szczesny and Elliott 2014b; Szczesny and Elliott 2014a; Ahmadzadeh et al. 2015; Gao et al. 2008), but this concept has not yet been translated to cm-scale simulations with individual fascicles explicitly represented. Implementing and validating a model for meniscus that incorporates inter-fascicle shear and slip would be an important step forward, enabling further simulations to more accurately predict crack-induced stress concentrations and

identify test cases that may produce crack growth.

For radial specimens, specimens that exhibited crack propagation did so by growth of the crack along inter-fascicle boundaries. Other radial specimens failed by necking and bulk rupture. These specimens exhibited large amounts of fiber reorientation into the loading axis, which may have been responsible for changes in the apparent yield strength and tangent modulus. For radial specimens, the role of the inter-fascicle matrix as the first structure to fail provides a crack propagation path straight across the specimen. Strain fields in radial specimen did not exhibit patterns associated with the fascicle boundaries. Accurate representation of local fiber rotation and the single inter-fascicle interface coincident with the crack is most likely sufficient to represent radial specimen failure.

It is important to note that this study focused on crack growth by opening stress (mode I fracture). Crack growth can also occur by in-plane shear (mode II) and out-of-plane shear (mode III) failure. For an anisotropic material such as meniscus, the propagation modes are expected to have different mechanical behavior depending on their orientation relative to the material axes (i.e., parallel or perpendicular to the prevailing fascicle direction). As discussed above, inter-fascicle slip interferes with mode I crack growth in circumferential tension, causing diversion of cracks towards the grip line. However, alternative test configurations could be designed to prioritize quantification of crack growth by inter-fascicle slip (circumferential, mode II) or inter-fascicle peeling (circumferential, mode III). The apparent fracture toughness of meniscus scar tissue has been measured using peel tests (Sonoda et al. 2000; Roeddecker et al. 1994), but there is not yet verification that the measured values can predict fracture in other

test cases. There is some indication that longitudinal tears in the intact meniscus are loaded predominantly by shear rather than opening stress (Richards et al. 2008; Stärke et al. 2009). These prior findings, combined with the ubiquity of inter-fascicle slip observed in the present work, justify investigation of the potential involvement of mode II and mode III fracture in meniscus failure.

6.4 Boundary conditions and grips

In Chapters 4 and 5, the grips appeared to create non-physiologic boundary conditions, with grip line failures and more fascicle slip than expected. In circumferential specimens, the corner where the outer (radial axis) side of the meniscus intersected the grip line was a common site of secondary failure. This corner combined a grip-induced stress concentration with an oblique local fascicle angle, creating tensile stress across the inter-fascicle boundaries. Clamps or sandpaper tabs are known to produce stress concentrations in the corners in biaxial testing, and sutures or hooks are preferred (Jacobs et al. 2011; Sun et al. 2005; Waldman et al. 2002; Polzer et al. 2013; Bursa and Zemanek 2008). The goal of switching to sutures or hooks would be to eliminate (or, at least, reduce) the influence of the grip stress concentrations on the test outcome. However, influence of the grips on the test results may be impossible to eliminate. If the tissue is considered a material with discrete fiber and matrix phases, an aspect ratio of 40:1 may be necessary for boundary effects to subside (Reese et al. 2013). A specimen with that aspect ratio is only possible when testing individual fascicles or fibrils. This is worth trying, but meniscus fascicles are difficult to isolate.

Another potential grip-related confounding factor is the ability of the grips to securely grip fibers. The observation of fiber sliding up to the grip line implies that the grips did not in fact prevent relative fascicle movement within the gripped region. Freeze grips are a potential solution. A comparison of serrated jaws, sandpaper, frozen ends, and dehydrated ends for gripping chicken deep digital flexor tendons revealed no differences between grips, but in all cases the majority of specimens failed at the grips (Ng et al. 2005). In tests of tendon grafts using suture, compression clamps, wire mesh, cement, and freeze grips, the freeze grips produced failure forces 4 times greater than the general compression clamp (Hangody et al. 2016). Failure tests of quadriceps tendon using freeze grips produce failure loads 12 times greater than using sutures (Liggins et al. 1992). In tests of muscle, freeze grips provide a doubling of measured strength relative to compression clamps or sutures (Schöttle et al. 2009). These results indicate that freeze grips most likely provided superior fiber anchoring compared to the other grips, more like the native insertion. In tendon testing, using freeze clamps on the origin end and clamping the bone on the insertion end, or using freeze grips on both ends, is a common and effective way to eliminate slip (Wren and Carter 1998; Riemersa and Schamhardt 1982; Bosch et al. 2010; Thorpe et al. 2012; Pring et al. 1985; Thermann et al. 2001; Miles et al. 1992; Powell et al. 1989; Jansen and Savelberg 1994; Sharkey et al. 1995; Villegas et al. 2007; Hauch et al. 2010; Abraham et al. 2011; Bowser et al. 2011; Swank et al. 2014). Plastination of tendon ends is also sometimes used (Hammer et al. 2012; Reese et al. 2013), and probably offers similar secure gripping of fibers. Based on these results, freeze grips seem efficacious and should be tried. Inhibition of fascicle sliding, which might be achieved by secure fiber anchoring better

mimicking native meniscus insertions, should limit crack deflection and make the process zone smaller, promoting fracture.

6.5 Discriminating between fracture and bulk rupture

Valid measurements of fracture toughness from mechanical tests requires both qualitative crack propagation and for fracture to be the active failure mechanism. In the context of fibrous soft tissue, the two methods to demonstrate that fracture occurs are to (1) measure a crack-induced reduction in effective strength (Von Forell et al. 2014) or (2) measure fracture toughness and verify that it accurately predicts failure for a variety of crack lengths (Taylor et al. 2012). The latter approach relies on demonstrating the expected $\sigma_f \propto 1/\sqrt{a}$ relationship between failure stress σ_f and crack half-length a in fracture. It is possible to produce crack propagation by the dropped mass method of Isaac et al. (2010), but some degree of control or at least measurement of the impact is necessary to obtain sufficient data to determine if fracture was the responsible mechanism. A high speed camera combined with a pressure plate to record the impact force vs. time profile may suffice to determine the crack propagation threshold, especially if combined with an FEA model. An electromechanical tensile tester could be substituted for dropped mass to attain a greater degree of control. Since this is a rare example of ex vivo mechanical testing of the meniscus that resulted in crack, a test employing similar rapid, multiaxial loading to the meniscus while it is still attached to the knee joint would be a good starting point for future fracture studies.

Using the resulting data from a test of the still-attached whole meniscus or a similar test

requires a well-developed constitutive model incorporating all relevant effects. This may include fluid flow (biphasic), solid viscoelasticity, plasticity, damage, and crack propagation. The model must also incorporate the geometry of the specimen, possibly including its structural heterogeneity. This requires a considerable amount of development work and so would be a long term plan. A good approach for simulating crack propagation in fibrous soft tissue within existing FEA frameworks is cohesive zone modeling (Grantab and Shenoy 2012; Grantab and Shenoy 2011; Hui et al. 2003; Yang et al. 2006). This approach has been applied to cracks in bone (Yang et al. 2006) and artery (Wang et al. 2014; Gasser and Holzapfel 2007).

Using failure stress as a way to distinguish between fracture and failure without fracture may not be ideal because of its intrinsically large variance, requiring large sample sizes. Some of this variance may be caused by cutting the specimen to a standard planar shape, but biological materials in general tend to have large variance. However, failure stress is at least easy to measure. Alternative measures that can be compared between model predictions and observed data include strain fields, whether a crack propagated, and energy release for a unit crack extension. These measures aren't necessarily better from a variance standpoint. Strain fields have tremendous spatial variation in both magnitude and pattern within and between specimens. Classifying a crack as propagating or not is somewhat subjective in borderline cases (e.g., the radial specimens in Chapter 5). Furthermore, mechanical models for fibrous soft tissue failure have not yet demonstrated the capability to precisely predict failure morphology (position and extent). Fracture in models that can be used in the near future probably will not look exactly like fracture in the actual tissue, as current models need approximations such as homogenization or represent a

large failure zone with a strip of cohesive zone elements. Assuming a test configuration is found that produces unambiguous crack propagation (in which the crack has a well defined length), using the energy of crack propagation as a discriminant between fracture and non-fracture failure may be a good option.

The energy of crack propagation may also be useful for discriminating between fracture and bulk rupture if it is used in conjunction with a model. The energy of crack propagation has been previously measured in studies of various fibrous soft tissues (Taylor et al. 2012; Purslow 1985; Purslow 1983a; Purslow 1983b; Chin-Purcell and Lewis 1996; Stok and Oloyede 2007; Oyentjesma and Cook 2001; Koombua et al. 2006; Wu et al. 2006b). Some of these studies used FEA to compute energy of crack propagation via the J integral method (Koombua et al. 2006; Wu et al. 2006b). The fracture toughness can also be computed from FEA directly by using finite differences to calculate the change in strain energy with respect to crack length (Anderson 2005). Chin-Purcell and Lewis (1996) and Wu et al. (2006b) and Wu et al. (2006a), who most likely did observe fracture (Taylor et al. 2012), report variance in crack propagation energy of ~20% (compared to ~200% for studies with ambiguous fracture). To distinguish between fracture (for which the energy of crack propagation determines failure) and bulk rupture (for which the material strength determines failure), it is only necessary to find a test case in which the fracture and bulk rupture parameters predict different outcomes.

The radial 90° edge crack specimens from Chapter 5 qualify to an extent as a fracture candidate because some of them failed with crack propagation, but this specimen group was not found to fail by fracture based on measured peak stress. However, the existence of failure resembling

crack propagation is promising. As discussed in Section 6.6, increasing the width of the radial specimen and the crack length may induce fracture, especially if the specimen was also loaded biaxially to keep the fibers in tension and thereby limit necking.

6.6 Adjustment of test geometry to promote crack propagation and fracture

Specimen size is a potential reason why fracture was not obtained in the present study (Chapter 5). Circumferentially oriented specimens were generally 7 mm to 10 mm wide and the cracks were ~3 mm. An edge cracked circumferential specimen thus only has about 4 mm to 7 mm of uncracked material between the crack tip and the opposite edge of the specimen. A center cracked circumferential specimen only has 3 mm to 4 mm of uncracked material between the crack tip and the edge of the specimen. Edge cracked radial specimens were 5 mm to 6 mm wide, with a crack length of about 2 mm. This also leaves only 3 mm to 4 mm of uncracked material between the crack tip and the opposite edge of the specimen.

If the process zone is longer than ~1 mm, fracture can barely develop before the process zone encompasses the entire remaining cross-sectional width of the specimen, at which point the failure process will shift to bulk rupture. The meniscus is highly extensible and has remarkable post-peak load bearing capacity (Figures 4.5, 5.5 and 5.6). About double the peak strain must be applied to obtain complete loss of stress-carrying capacity. To obtain failure by fracture, the near-tip tissue must stretch at least twice as much as the tissue on the far side of the specimen; otherwise the entire cross-section will be post-peak and failing simultaneously. The observed

near-tip longitudinal strain (E_{xx}) enhancement is only 25% to 50% relative to the the away-from-tip strain (Table 5.4), so the far side of the specimen will most likely reach peak strain before the near-tip region completely fails. As a result, the region of failure encompasses the entire specimen width, and no fracture occurs.

One solution to the process zone being larger than the specimen is wide is to use a bigger specimen. It is uncertain how large a specimen would be necessary. The data presented in Figure 5.7 only show that a difference between the near-tip and away-from tip region exists, not whether the difference is a step transition or a gradient. If the near-tip strain enhancement is confined to the near tip region and there is a step transition in strain from the near-tip region to the away-from-tip region, this step is probably determined by local structure (fascicle boundaries), and making the specimen wider is unlikely to change matters. Since the displacement applied by the grips is uniform across the specimen width, a structurally mediated step transition would mean that tissue away from the influence of the crack would have the same average strain regardless of how wide the specimen is. The strain field data in Chapter 5 might be sufficient to determine the strain distribution during tearing if a modified analysis is used. Since at the post-peak time points the specimen is tearing apart, and this disrupts the digital image correlation, the size of the process zone cannot be directly observed. However, the tear could be labeled manually in the post-peak frames and a virtual strain gauge placed across it, with each end of the virtual strain gauge in intact tissue. This modified procedure may still not suffice for circumferential specimens in which the region of failure spans most of the specimen length and touches the grip line. A more robust approach would be to develop a computational model that can predict the

size of the process zone; such a model must incorporate damage and most likely would need to also incorporate inter-fascicle sliding (due to both its importance as a failure mechanism and the similar length scale between fascicles and the crack tip).

Increasing the specimen width would have an indirect benefit in that the crack could be made longer. A longer crack should increase the near-tip stress concentration according to the $1/\sqrt{\text{crack length}}$ scaling, in turn increasing the near-tip strain. A longer crack could cause complete near-tip failure before the far edge of the specimen reaches peak stress. This suggests a worthwhile experiment: test whether the near-tip vs. away-from-tip strain enhancement correlates with crack length.

Testing the effect of crack length would also be useful clinically. Currently, full-thickness peripheral tears shorter than 5 mm and radial tears shorter than 5 mm are considered to not always require surgical repair (Lento and Akuthota 2000). A rule of thumb for medial meniscus vertical tears accompanying ACL tears is that tears greater than or equal to 10 mm in length require repair (Seil et al. 2009). Rules for optimal management of meniscus tears remain uncertain (Vermesan et al. 2014), and supporting them with mechanical data would be useful.

Unfortunately, the specimen size is limited by the size of the native meniscus. The circumferential specimens are about as large as they can be while having a rectangular midsubstance. The radial specimens could be made wider, but would cease to have a grip-to-grip distance greater than the specimen width. Specimens with non-standard shapes such as a crescent could be made larger, and a crescent stretched using the posterior and anterior attachments might serve as a compact tension test. As discussed in Section 5.4.2, compact tension tests are desirable be-

cause they should produce a greater stress concentration than single edge notch tension tests. Non-rectangular shapes would make the stress–strain curve parameters nonstandard, and data would have to be parameterized via mechanical models to be translated to different contexts. However, the low length:width ratio possible for meniscus specimens, the curvature of circumferential fascicles, the frequent occurrence of ruptures that interact with the grip line, and the ubiquity of inter-fascicle shear bands extending into the gripped regions makes it dubious that measured stress–strain curve parameters are generalizable even for standard specimen shapes. The use of mechanical models is thus beneficial regardless, so in the long term (as models mature) there is little reason to avoid non-rectangular specimen shapes.

6.7 Identifying mechanical and structural mechanisms of failure

The underlying microstructural failures and rearrangements involved in meniscus failure are of fundamental interest and, given the observed propensity for meniscus failure to proceed along fascicle boundaries (Sections 4.4.7 and 5.4.8), likely a key determinant of crack behavior. Identifying structural damage and failure mechanisms in the meniscus will provide qualitative answers for: (1) why meniscus tears adopt a particular morphology, (2) whether a tear might grow or not grow, (3) whether fracture is likely to apply or not, (4) whether a tear is repairable, (5) how tissue engineered scaffolds might be created with fracture toughness similar to the meniscus, and (6) whether the side effects of tears (such as the strain concentrations identified in Chapter 5) might cause changes in cell phenotype. Enumerating failure mechanisms will also provide

crucial guidance developing quantitative tools to predict failure. Failure mechanisms can be looked at from both mechanical and structural viewpoints. The mechanical perspective deals with tissue-scale stress and strain, with failure considered in terms of deleterious changes in mechanical function, such as an increase in friction coefficient or decreased load bearing capacity. The structural perspective deals with the sub-structural failures and rearrangements responsible for changes in meniscus shape or properties. Both perspectives are important and, ideally, are unified by quantification of structure–function relationships.

The mechanical perspective mainly classifies failure mechanisms by their effects. Several mechanisms contribute to meniscus mechanics: elasticity, poroelasticity (fluid flow), osmotic pressure, viscoelasticity, plasticity, and damage. Damage is used here to mean a permanent reduction in a functional property such as stiffness or strength, whereas plasticity is meant to indicate a change in the shape of a solid, with no loss of load-bearing capacity, that does not recover upon unloading. In the context of failure, damage is the most relevant mechanism, but other mechanisms may cause changes (such as strain-softening) that appear similar to damage. It is important to note that, from a clinical perspective, a meniscus may be considered to have functionally failed when its properties change sufficiently to cause pain, limited joint motion, cartilage overload, or other failures to fulfill normal functional requirements. Determining whether functional failure has occurred requires detailed quantification of the meniscus' mechanics and how they change with injurious overload, more so than simply determining when the meniscus will break. Although properties relevant to elasticity, poroelasticity, osmotic pressure, and viscoelasticity have been quantified for the meniscus to at least some extent, the effects

of damage and plasticity are still unknown.

From the structural perspective, the present work indicates the existence of at least three tissue-scale failure mechanisms: inter-fascicle sliding, inter-fascicle rupture, and fascicle rupture. Inter-fascicle sliding may enable crack propagation parallel to the fascicles by in-plane shear (mode II crack growth). Inter-fascicle rupture may also enable crack propagation parallel to the fascicles, but instead requires tension perpendicular to the fascicles (mode I crack growth). Inter-fascicle sliding and inter-fascicle rupture are likely mechanisms for the formation and growth of horizontal, longitudinal, bucket-handle, and oblique tears (Figure 2.2), which all involve tear growth along fascicle boundaries. Fascicle rupture by fascicle-parallel tension appears necessary only for radial tears. Complex (degenerative) tears may involve all three mechanisms.

In this study, inter-fascicle sliding was observed directly in the test videos, and slip of single fascicles often occurred as a prelude to general failure. The inter-fascicle sliding appeared non-recoverable in that it remained visible in the test videos following complete failure, but it is not known whether it would recover if left at zero load. Sliding that recovers is not damage but rather viscoelastic deformation. Sliding that does not recover might be damage or plasticity. Inter-fascicle sliding can be measured using stain lines to track relative fascicle displacement. This method is often used on the microscale with photobleached lines (Szczesny and Elliott 2014b; Motavalli et al. 2013; Cheng and Screen 2007), but ink lines on cm-scale specimens can be used the same way. Strain fields measured by digital image correlation, as in the present study, can be used only if the correlation window can be made smaller than a single fascicle

diameter (100 μm to 500 μm), which would require a higher resolution camera. An alternative is to reduce the field of view (increasing pixel/mm scale) so as to not encompass the whole specimen, but an incomplete video record hampers observation of rupture location and crack growth. Whether the sliding is recoverable can be determined by monitoring inter-fascicle slip throughout a test consisting of loading, unloading, and a recovery period (Thorpe et al. 2015b). Measuring the extent of inter-fascicle sliding may be useful in estimating the size of the process zone and/or plastic zone and establishing minimum criteria for specimen size in tissue fracture tests.

Inter-fascicle sliding likely interacts with the other two failure mechanisms. Fascicle sliding may occur due to fascicle rupture causing sudden unloading of the ruptured fascicle, causing it to recoil. This would constitute permanent damage to the fascicle but not necessarily the inter-fascicle connections. Fascicle sliding could also occur due to shear stress on the inter-fascicle connections causing their failure, which would constitute inter-fascicle matrix rupture. Inter-fascicle connections can also fail by tension, and this was observed in the present work. Video records of inter-fascicle rupture reveals fine fibers crossing between the fascicles (Figure 5.13). The fascicles are comprised of tightly packed 5 μm diameter bundles of collagen fibrils (Rattner et al. 2011), so it is possible that the fine fibers observed in the test video are simply fibril bundles that cross between fascicles. This could be verified directly by serial ultramicrotomy and electron microscopy (Szczesny et al. 2015). The dense packing of intact meniscus means it may be beneficial to partially rupture the specimen or treat it with a weak acid (Rattner et al. 2011) to open up the structure and make it easier to visualize. It is not currently known exactly

how stress is transmitted between adjacent fascicles; investigating the structure of inter-fascicle connections will assist in answering this question.

Fascicle rupture is important because fascicles are ultimately responsible for bearing the bulk of the tensile load applied to the meniscus. Given that radial and oblique tears exist, some tears must propagate across fascicles; this would presumably involve fascicle rupture. The present study prioritized modes of crack propagation that proceed by fascicle rupture. The use of the circumferential 45° center crack specimens, based on the results of Chapter 3, was intended to cause an increased fiber stress and hence increase the likelihood of fracture by fascicle rupture. The prediction of increased fiber stress in the 45° center crack specimens may have been accurate; the experimental tests only demonstrate that whatever the fiber stress concentration, it was insufficient to cause fracture. Fascicle rupture can be observed by quantifying uncrimping of fibers at overload (as broken fascicles recoil and re-crimp) and by direct observation of ruptures (Winkler et al. 2013; Winkler et al. 2011; Jester et al. 2010; Sereysky et al. 2010; Rezakhaniha et al. 2012). Experiments that minimize inter-fascicle sliding (Section 6.4) would be best for studying fascicle rupture.

Structural damage can also be measured in terms of collagen denaturation and cell death (Provenzano et al. 2002b; Provenzano et al. 2002a). Enzymatic collagen I and collagen II degradation can be measured using fluorescence microscopy using a Col 2 3/4C_{short} antibody (Thorpe et al. 2015a; Billingham et al. 1997). Collagen denaturation can be measured with fluorescence microscopy using collagen hybridizing peptide (Zitnay et al. 2016). Collagen fibril damage in the form of repeating kinks can be observed via SEM and enhanced with partial trypsin diges-

tion (Veres et al. 2014; Veres et al. 2013). Partial trypsin digestion can also be used as part of biochemical assay to measure the overall amount of denatured collagen (Veres et al. 2014).

It would be informative to measure structural damage in the vicinity of the crack tip and compare it to the rest of the specimen. The crack creates a different local stress state near its tip than away from it, which could change the mechanism of rupture. Visualizing structural damage in a torn human meniscus (obtained, e.g., from meniscectomy) and contrasting the results with the mechanisms observed in *ex vivo* tests would greatly assist efforts to achieve crack propagation in *ex vivo* testing and help ensure that the *ex vivo* tests produce relevant failure processes. Direct observation of structural damage could be used to measure the size of the process zone, which would aid calculation of specimen size requirements (Section 6.6).

6.8 Improvements to protocol efficiency

As discussed in Section 6.2, the path forward for meniscus failure research, and fracture research involves many unknown factors. Identifying the influence of many factors requires a correspondingly large number of specimens, particularly when factors interact with one another. For example, axial compression combined with circumferential tension may produce a different type of failure than when either is applied individually. Testing of factor levels in combination geometrically increases the number of specimens required. Meniscus failure is also intrinsically variable—5 distinct rupture types were observed (Section 4.2.2). Failure may occur at the crack or away from it and by crack propagation or not. To achieve specific predictions regarding failure types, a sufficient number of specimens need to be tested to obtain a

representative sample of each type of failure. This would enable subgroup analysis to identify the underlying causes for why different specimens rupture in different ways, and whether this variety has any functional consequence. Specimen count, and thus specimen preparation and test time, is a major obstacle for future progress in meniscus failure research.

Based on the present work, some opportunities for reducing specimen preparation and test time can be identified. Each test, assuming an experienced worker, ideal conditions, and no unexpected events, took about 3 hours (2 hours cutting, 30 minutes dimension measurement and speckle coating, and 30 minutes tensile test setup and the test itself). Although this test duration is not especially prohibitive compared to many protocols in use (Showalter et al. 2014; Szczesny et al. 2012; Yoder et al. 2014), the expenditure of 2 hours during the cutting step (in which a freezing stage sledge microtome is employed) is not intrinsically necessary and is a good target for optimization. A system in which specimens are cut at room temperature in a single pass would decrease test time by a little more than half.

The analysis protocol has another time-expensive part that is amenable to optimization: computing the strain fields. This procedure requires repeated computational runs with manual supervision to adjust point rejection thresholds to maximize the number of points tracked while eliminating tracking errors that alter the strain field topology and make it non-diffeomorphic (see B.1). Furthermore, the seed point that is used to initialize tracking in each image is sometimes lost when the specimen rearranges itself during failure. When this happens—almost always near the end of the test—the seed point location must be adjusted and the tracking restarted from the beginning. These adjustments require 1 to 2 hours of intermittent interaction with the software.

However, both adjustments could be handled automatically. Checking whether a strain field is diffeomorphic is, in principle, readily handled by software. Loss of tracking for the seed point could be dealt with by automatically switching to the pixel with the greatest correlation coefficient from the last tracked frame and continuing with the image correlation. Switching to an academic image correlation program developed for tissue analysis that has published source code, such as Boyle et al. (2014), and modifying it as necessary has the potential to completely automate the process.

Identifying meniscus failure mechanisms requires extensive further investigation by mechanical testing, and research into meniscus failure in its early stages. From this perspective, it is highly cost-effective to invest in developing efficient procedures to enable more rapid research iteration.

6.9 Conclusion

This work was designed to investigate meniscus failure mechanisms and strain concentrations in the context of meniscus cracks (tears). The meniscus is sufficiently tough that cracks did not propagate when loaded in (quasistatic) circumferential uniaxial tension with 45° center cracks or 90° edge cracks or in radial uniaxial tension with 90° edge cracks. Nor did the cracks reduce the effective strength of the meniscus. This work therefore demonstrated that, at least in quasistatic uniaxial tension, failure of the meniscus proceeds by bulk rupture rather than fracture. This toughness (resistance to fracture) is a desirable trait in an organ that undergoes millions of loading cycles over a person's lifetime. Materials meant as meniscus implants or regenerative

scaffolds may not be as resistant to fracture; this should be tested as part of establishing their safety and efficacy. Despite the meniscus' toughness, meniscus cracks do locally increase strain near their tips. These strain concentrations have the potential to cause structural damage, cell death, and other dysfunction, especially with repeated loading.

The morphology of meniscus failures gave scant indication of crack propagation in circumferential tension. About 50% of edge cracked radial specimens failed in a manner consistent with crack propagation, although as previously mentioned these failures did not proceed by fracture. Inter-fascicle sliding was observed to be a major failure mechanism and to deflect cracks from progressing across fascicles. Failure in circumferential specimens occurred via large rupture zones with extensive interdigitating fiber pull-out, blunting the crack and presumably reducing any crack-associated stress concentrations. Given the occurrence of crack growth in radial tension specimens and the predominance of inter-fascicle sliding, the boundary between fascicles may be a preferred crack propagation path *in vivo*. The mechanisms by which *in vivo* cracks propagate across fascicles remain unknown. This study is a major step towards reproducing *in ex vivo* testing the meniscus crack growth and failure that occurs *in vivo*, but further study is necessary to achieve this goal.

This work also quantified key nonlinear mechanical properties of the meniscus in both cracked and crack-free test configurations. The meniscus stress–strain curve was parameterized for the first time in terms of its inflection point (yield point) and the maximum tangent modulus. A fiber recruitment model was developed and fit to circumferential tension data with excellent fit quality. These metrics were used to compare tensile test specimen shapes, including

the uncommonly used expanded tab shape, which in circumferential tension was demonstrated to provide more rapid and complete fiber recruitment compared to dogbones or rectangles. The expanded tab specimen shape accommodates the curvature of the meniscus' fascicles, increasing fascicle continuity in the gripped region.

Meniscus specimens were observed to fail with a wide variety of rupture morphologies, and the strain fields revealed great spatial heterogeneity in the meniscus' mechanical behavior. Extensive inter-fascicle sliding meant that no tensile test specimen shape was effective at ensuring midsubstance rupture and hence independence from grip effects. Specimens often rupture at least partly at the grip line regardless of specimen shape. Further development of test protocols and grips is needed to determine the consequences of grip effects and how to ameliorate them.


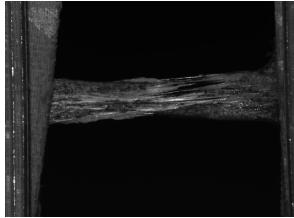
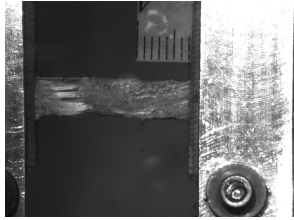
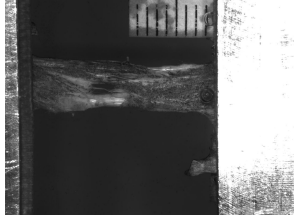
Finite element analysis was used as a predictive aid to experimental design, enabling the comparison of many cracked specimen configurations with different crack position (edge vs. center), boundary conditions (uniaxial vs. equibiaxial stretch), and crack-fiber angle (0° to 90°). The relative likelihood that each configuration would produce fracture was determined based on ranking the crack-associated stress magnitude. Specimens were ranked according to each in-plane stress component individually. Center cracked specimens with angled cracks were identified as producing large amounts of fiber stress, with similar stress fields for both uniaxial (fiber-aligned) and biaxial stretch. Edge cracked specimens and 90° center crack specimens were identified as producing the greatest inter-fiber shear stress and inter-fiber matrix stress. The test cases for the physical *ex vivo* tests described in the previous paragraphs were chosen based on these FEA results so that the experiments included test cases optimized for both fiber

rupture and inter-fiber sliding and matrix rupture. Further work is necessary to develop models to more accurately predict crack-induced stress concentrations, crack propagation, and failure of the meniscus. Model accuracy may be improved by incorporating the effects of discrete fascicle structure (i.e., non-continuum fascicle sliding) and sub-failure damage. Improved models will both aid in future joint modeling–experimental studies, and with continual improvement will eventually become an important tool for evaluating clinical pathology. Given the complexity introduced by in vivo geometry, multiaxial loading, and heterogeneity, models are a crucial component in translating the results of controlled ex vivo tests to the physiologic environment. The most clinically relevant questions are whether the meniscus will fail and, if failure is a multi-step process, how long the meniscus will retain function as it deteriorates. Mechanical quantification of meniscus failure will provide essential guidance for decisions regarding meniscus resection, repair, and regeneration.

APPENDIX A: ENDPOINTS FOR TESTS USED TO STUDY THE EFFECT OF SPECIMEN SHAPE

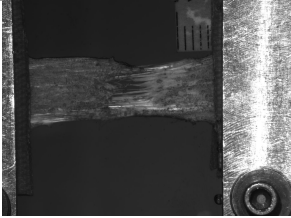
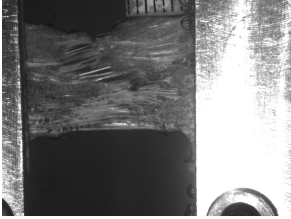
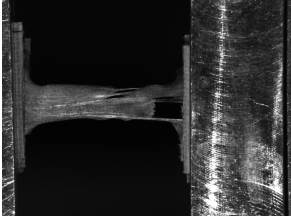
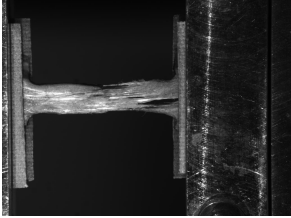
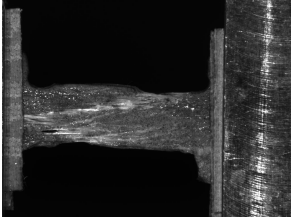
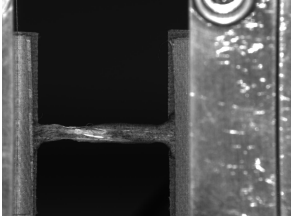
Table A.1 lists the endpoint of each test reported in Chapter 4. The image from each test best illustrating its endpoint is also shown. For endpoint definitions, see Section 4.2.2.

Table A.1: Test endpoints for specimens reported in Chapter 4.

Loading axis	Shape	Endpoint	Endpoint image
circumferential	ET	midsubstance rupture	
circumferential	ET	midsubstance rupture	
circumferential	ET	midsubstance rupture	
circumferential	ET	midsubstance rupture	

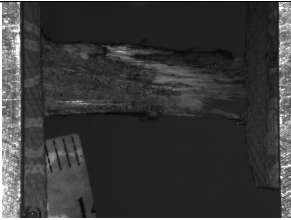
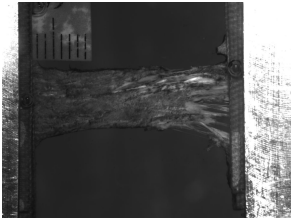
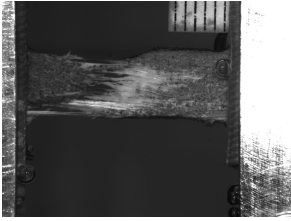
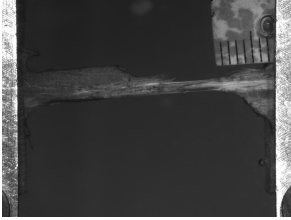
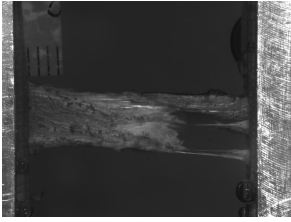

Continued on next page

Continued from previous page

Loading axis	Shape	Endpoint	Endpoint image
circumferential	ET	midsubstance rupture	
circumferential	ET	midsubstance rupture	
circumferential	ET	mixed rupture	
circumferential	ET	mixed rupture	
circumferential	ET	mixed rupture	
circumferential	ET	mixed rupture	

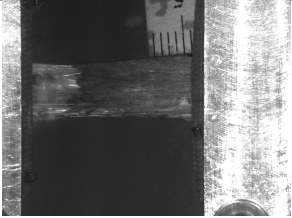
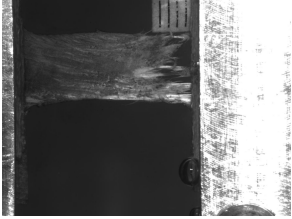
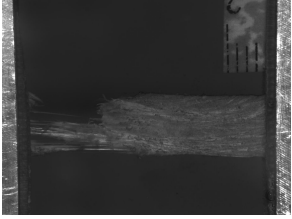
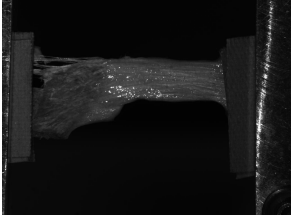
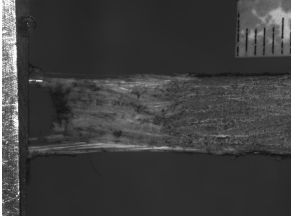
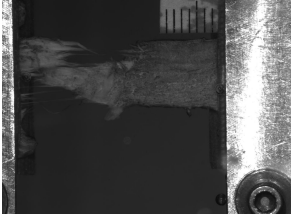
Continued on next page

Continued from previous page

Loading axis	Shape	Endpoint	Endpoint image
circumferential	ET	mixed rupture	
circumferential	ET	mixed rupture	
circumferential	ET	mixed rupture	
circumferential	ET	mixed rupture	
circumferential	ET	mixed rupture	
circumferential	ET	mixed rupture	

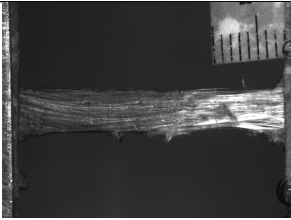
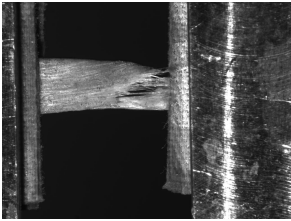
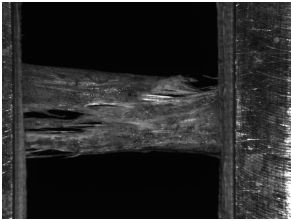
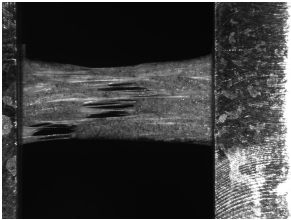
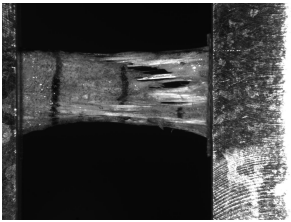
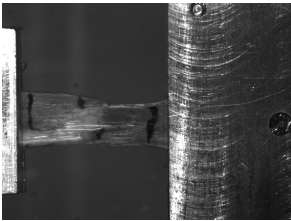
Continued on next page

Continued from previous page

Loading axis	Shape	Endpoint	Endpoint image
circumferential	ET	grip line rupture	
circumferential	ET	grip line rupture	
circumferential	ET	grip line rupture	
circumferential	ET	gripped region failure	
circumferential	ET	gripped region failure	
circumferential	ET	gripped region failure	

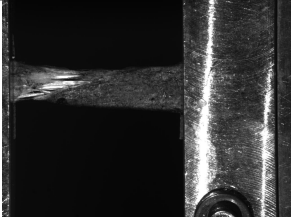
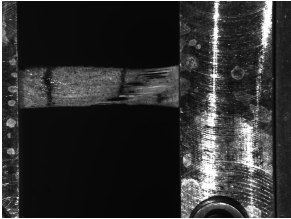
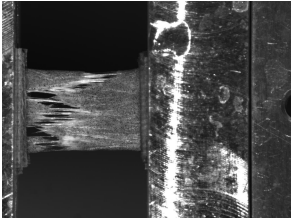
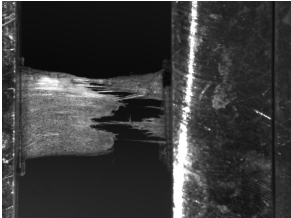
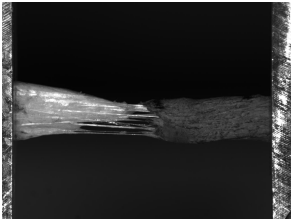
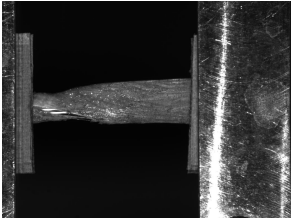
Continued on next page

Continued from previous page

Loading axis	Shape	Endpoint	Endpoint image
circumferential	ET	gripped region failure	
circumferential	R	mixed rupture	
circumferential	R	mixed rupture	
circumferential	R	mixed rupture	
circumferential	R	mixed rupture	
circumferential	R	mixed rupture	

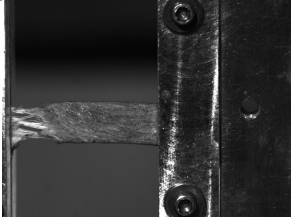

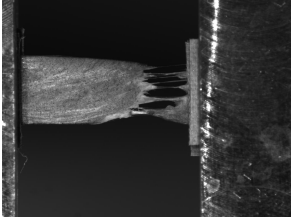
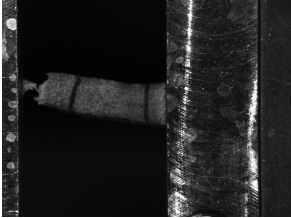
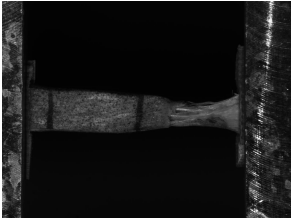
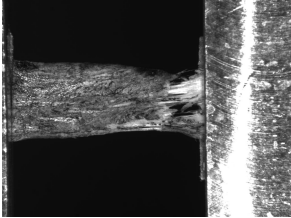
Continued on next page

Continued from previous page

Loading axis	Shape	Endpoint	Endpoint image
circumferential	R	mixed rupture	
circumferential	R	mixed rupture	
circumferential	R	mixed rupture	
circumferential	R	mixed rupture	
circumferential	R	mixed rupture	
circumferential	R	mixed rupture	

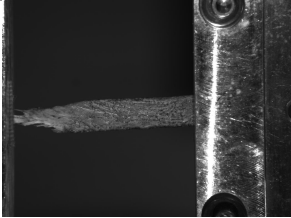
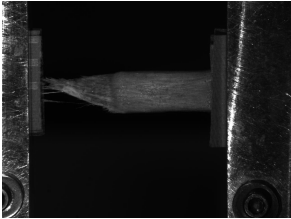
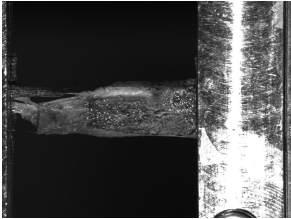
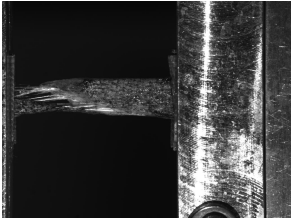
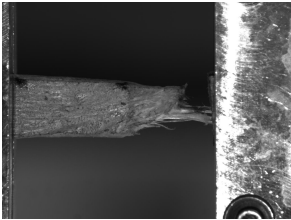
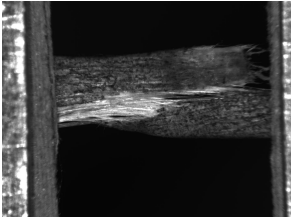
Continued on next page

Continued from previous page

Loading axis	Shape	Endpoint	Endpoint image
circumferential	R	grip line rupture	
circumferential	R	grip line rupture	
circumferential	R	grip line rupture	
circumferential	R	grip line rupture	
circumferential	R	grip line rupture	
circumferential	R	grip line rupture	

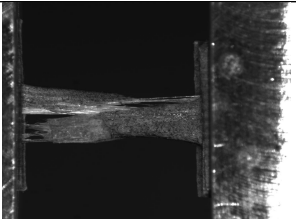
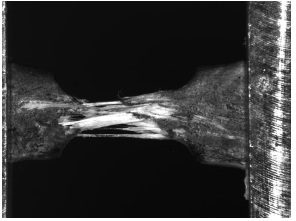
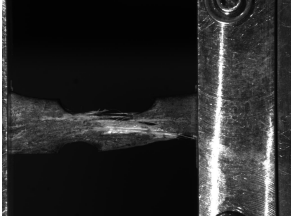
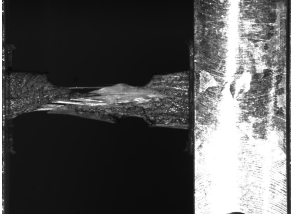
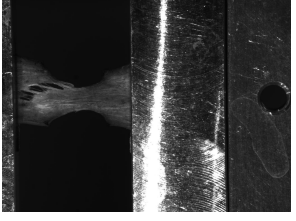
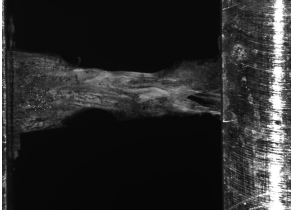
Continued on next page

Continued from previous page

Loading axis	Shape	Endpoint	Endpoint image
circumferential	R	gripped region failure	
circumferential	R	gripped region failure	
circumferential	R	gripped region failure	
circumferential	R	gripped region failure	
circumferential	R	gripped region failure	
circumferential	R	longitudinal split	

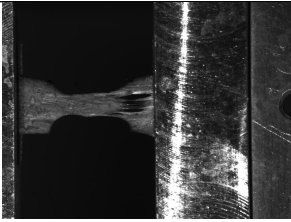
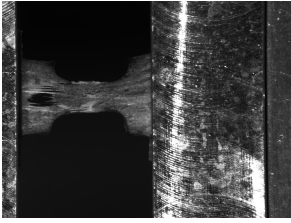
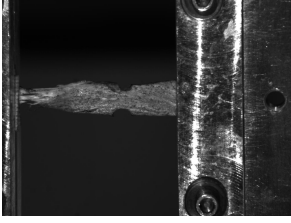

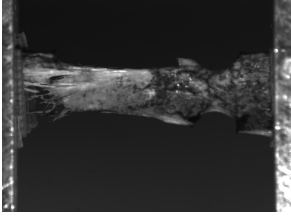
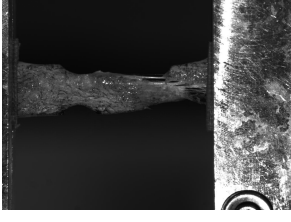
Continued on next page

Continued from previous page

Loading axis	Shape	Endpoint	Endpoint image
circumferential	R	longitudinal split	
circumferential	DB	midsubstance rupture	
circumferential	DB	mixed rupture	
circumferential	DB	mixed rupture	
circumferential	DB	mixed rupture	
circumferential	DB	mixed rupture	

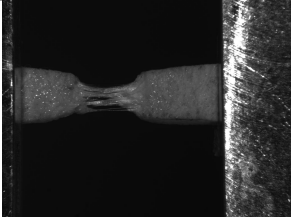
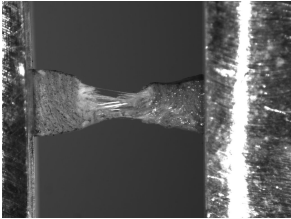
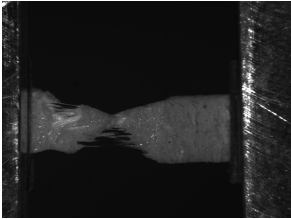

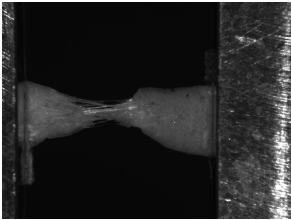
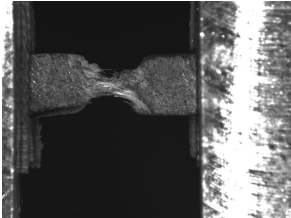
Continued on next page

Continued from previous page

Loading axis	Shape	Endpoint	Endpoint image
circumferential	DB	grip line rupture	
circumferential	DB	grip line rupture	
circumferential	DB	gripped region failure	
circumferential	DB	gripped region failure	
circumferential	DB	gripped region failure	
circumferential	DB	gripped region failure	

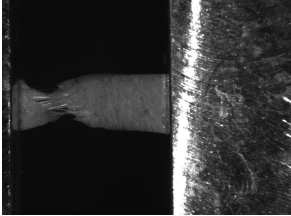
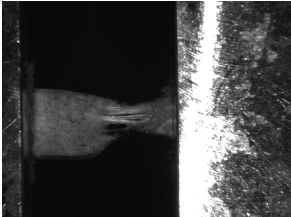
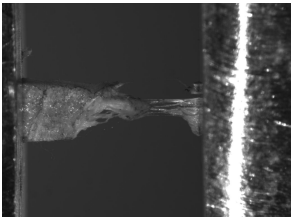
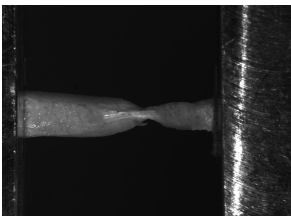
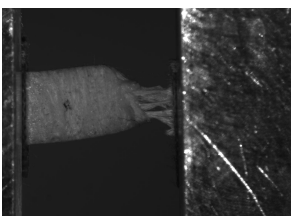
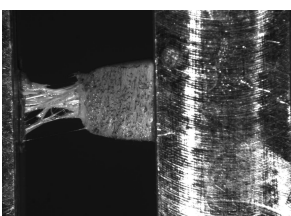
Continued on next page

Continued from previous page

Loading axis	Shape	Endpoint	Endpoint image
radial	R	midsubstance rupture	
radial	R	midsubstance rupture	
radial	R	midsubstance rupture	
radial	R	midsubstance rupture	
radial	R	midsubstance rupture	
radial	R	midsubstance rupture	

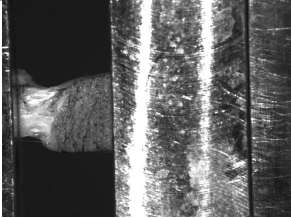
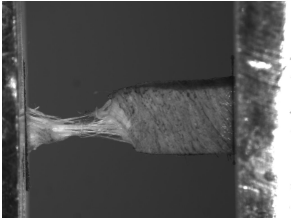
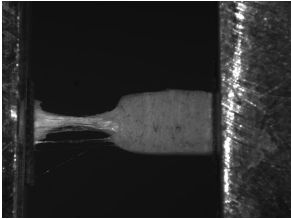
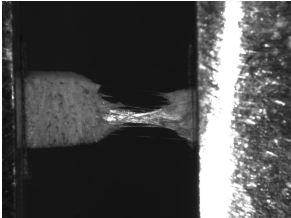
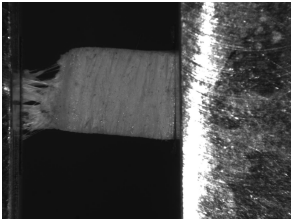
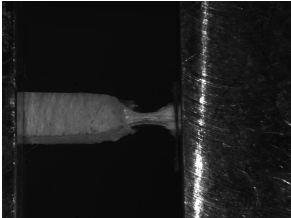
Continued on next page

Continued from previous page

Loading axis	Shape	Endpoint	Endpoint image
radial	R	mixed rupture	
radial	R	mixed rupture	
radial	R	mixed rupture	
radial	R	mixed rupture	
radial	R	grip line rupture	
radial	R	grip line rupture	

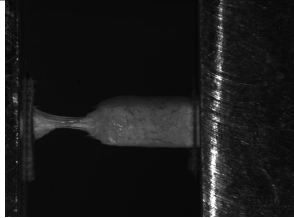
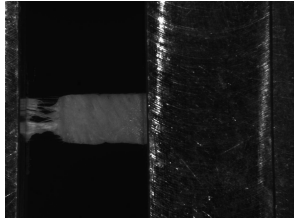
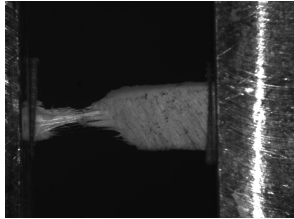
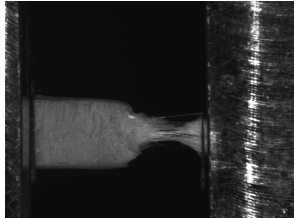
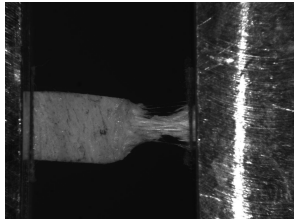
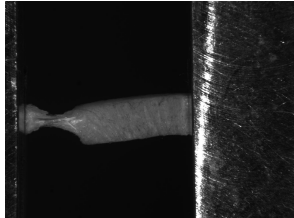
Continued on next page

Continued from previous page

Loading axis	Shape	Endpoint	Endpoint image
radial	R	grip line rupture	
radial	R	grip line rupture	
radial	R	grip line rupture	
radial	R	grip line rupture	
radial	R	grip line rupture	
radial	R	grip line rupture	

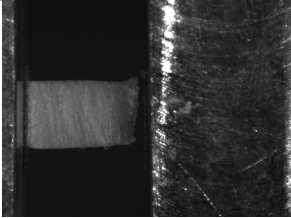
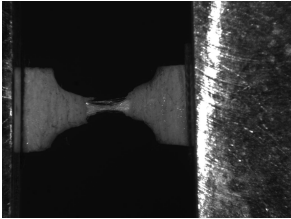
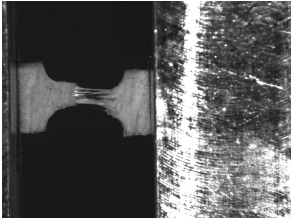
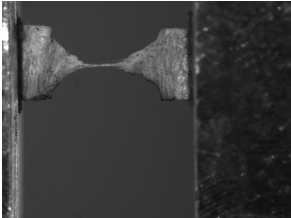
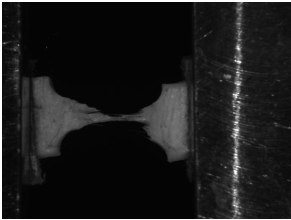
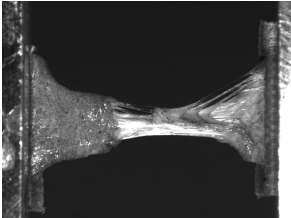
Continued on next page

Continued from previous page

Loading axis	Shape	Endpoint	Endpoint image
radial	R	grip line rupture	
radial	R	grip line rupture	
radial	R	grip line rupture	
radial	R	grip line rupture	
radial	R	grip line rupture	
radial	R	grip line rupture	

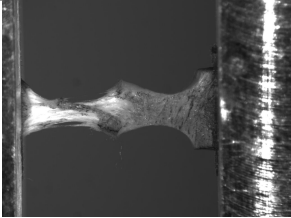
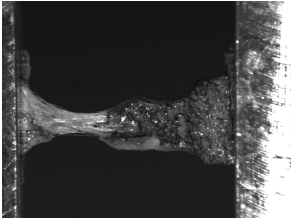
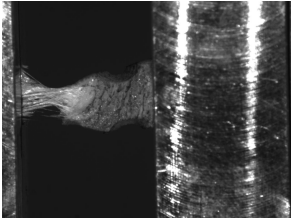
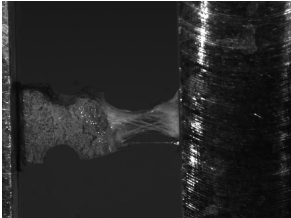
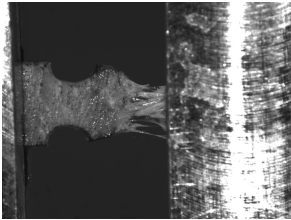
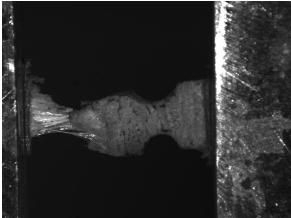
Continued on next page

Continued from previous page

Loading axis	Shape	Endpoint	Endpoint image
radial	R	no rupture	
radial	DB	midsubstance rupture	
radial	DB	midsubstance rupture	
radial	DB	midsubstance rupture	
radial	DB	midsubstance rupture	
radial	DB	midsubstance rupture	

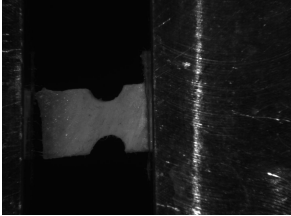
Continued on next page

Continued from previous page

Loading axis	Shape	Endpoint	Endpoint image
radial	DB	mixed rupture	
radial	DB	mixed rupture	
radial	DB	grip line rupture	
radial	DB	grip line rupture	
radial	DB	grip line rupture	
radial	DB	grip line rupture	

Continued on next page

Continued from previous page

Loading axis	Shape	Endpoint	Endpoint image
radial	DB	no rupture	

APPENDIX B: CHOICE OF VIC-2D PARAMETERS

B.1 Introduction

Strain fields in this study were computed from video records of each test using digital image correlation as implemented in the commercial software Vic-2D 2009 (Correlated Solutions, Columbia, SC). Vic-2D has numerous settings that may affect the resulting strain field. In this study, the following settings were used:

- Exhaustive search
- Low pass filtering
- Incremental correlation
- Optimized 8-tap interpolation
- Zero-normalized squared differences
- Gaussian weights
- Prediction margin = 0.101
- Confidence interval = 0.1 (adjusted for each specimen)
- Matchability = 0.1
- Subset size = 0.7 mm (converted to size in pixels on a per-specimen basis)
- Filter size = 15 px
- Exponential decay filter

The details of each parameter are specified in the Vic-2D manual, but the more important ones are discussed here. Incremental correlation is a particularly important setting. With it set, each image is correlated with the immediately preceding image, and the strain field for a particular image is calculated from the composition of every preceding correlation. Incremental correlation is essential for fibrous soft tissue because large deformations make a direct correlation between a deformed image and the reference image difficult; without it enabled, correlation is usually lost partway through the test. Exhaustive search, which expands the search radius for

spatial correlations, is also necessary to maintain the correlation throughout the test with large deformations. Using zero-normalized squared differences as the similarity metric for the correlation is recommended for meniscus because its reflectivity increases as collagen fibers are strained. Normalization compensates for this change in brightness.

The prediction margin, confidence interval, and matchability are thresholds for rejection of pixels with poor or possibly erroneous correlations. In the meniscus tests, the major correlation error was misregistration of points to a different region of the specimen. This kind of misregistration happens because large deformations or rupture greatly changes the appearance of the specimen. A region in the reference image that greatly changes appearance in the deformed image may be erroneously matched to a different region that coincidentally looks similar. An example is shown in Figure B.1.

In preliminary analysis, systematic variation of the prediction margin (0.05, 0.1, and 0.2), confidence interval (0.05, 0.1, 0.2), and matchability (0.025, 0.1, 0.4) showed no appreciable changes in the strain field values, so these parameters were chosen to prevent misregistration while preserving valid correlations. The prediction margin and matchability were set to 0.1. The confidence interval, which rejects points if their displacement is too dissimilar to neighboring points, was most effective at selectivity excluding misregistrations, so it was decreased on a per-specimen basis as necessary to exclude misregistrations while preserving valid correlations. It was never necessary to decrease the confidence interval parameter below 0.037, and usually a value ≥ 0.064 sufficed.

Subset size and filter size were found in preliminary investigations to affect the strain fields, so they were varied systematically in order to investigate this sensitivity and select appropriate values. Because these effects may be important when measuring local strain, such as strain near the crack tip, and observing fascicle-associated strains, the results of this sensitivity analysis are reported in detail in the following sections. Increases in subset size and filter size smoothed the strain field, with subset size having a much stronger effect. The final choices of subset size

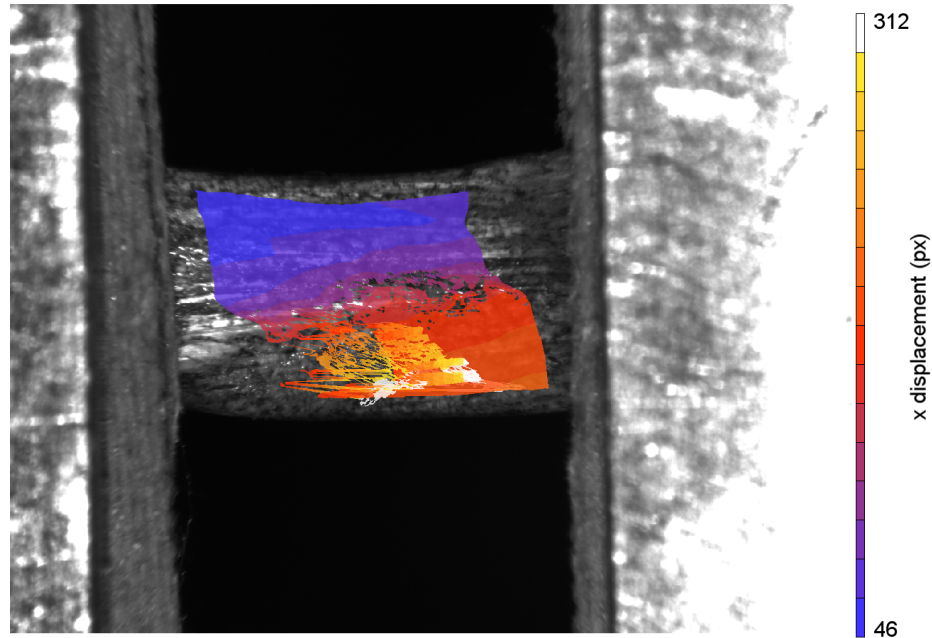


Figure B.1: An example of an erroneous image correlation. Points from the lower left are misclassified as displacing to the lower center, resulting in a displacement field that folds over itself, making it non-diffeomorphic.

and filter size were chosen to limit this smoothing effect, preserving large-scale patterns in the strain field while eliminating small-scale, apparently random variation.

B.2 Subset size sensitivity analysis

B.2.1 Subset size analysis setup

Four specimens were chosen with which to evaluate the effect of subset size: two circumferential and two radial (Figures B.2 and B.3). Since cracked specimens are likely to generate the most complex strain fields, and therefore represent the most challenging case, cracked specimens were used. These four specimens were considered to be sufficiently representative for a sensitivity analysis. The test protocol was the same as used in Chapter 5, except that the specimens were rectangular. Subset size was varied from 9 px to 55 px. For analysis of subset size effects, the

filter size was set to 15 px (the default value in Vic-2D). The other parameters were held fixed at the values listed in Section B.1.

To reduce the time required for Vic-2D processing, the image sequence was reduced to the reference image followed by one image every 1% strain, plus all the images within 0.01 strain of the rupture image. Sudden large deformations may occur just prior to rupture; a shorter interval between images in this part of the test makes it easier for the digital image correlation algorithm to track these deformations. The rupture image was chosen visually without reference to the strain curve. The visual criteria for rupture were (a) formation of a surface of discontinuity or (b) a sudden deformation suggesting fascicle failure.

The effect of varying the Vic-2D parameters was primarily evaluated by qualitative examination of the E_{xx} , E_{yy} , and E_{xy} (Lagrange) strain fields for an image frame immediately prior to specimen rupture. This is when the strain field is likely to be most complicated and the choice of subset size will have the greatest effect. In the strain field plots, the strain values were truncated at the 0.05 and 0.95 quantiles so that the local extrema would not overwhelm the color scale. Furthermore, most extreme strain values appeared to be caused by evolving ruptures (discontinuities), and so do not really represent strain as much as the spreading of a gap formed by rupture. In addition to plots of strain fields just prior to rupture, summary statistics (median and 0.05/0.95 quantiles) were calculated for strain fields from all images prior to the rupture image.

B.2.2 Effect of subset size on strain field appearance

Strain fields had a stippled pattern at small subset sizes that was eliminated as the subset size increased (Figures B.4, B.5, B.6, B.7, B.8, and B.9). The length scale of the stippling qualitatively matched that of the speckle coat, so the stippling is probably an artifact that occurs when the subset size is smaller or similar to the size of the speckle pattern spots. The random superposition of speckles with inter-fiber discontinuities causes aliasing; a larger subset includes more

speckles, reducing the aliasing artifact. For the circumferential samples, a subset size of 35 or 45 (depending on the strain component) was sufficient to eliminate the stippling (Figures B.4, B.5, and B.6). For the radial specimens, the stippling tended to be eliminated at subset sizes greater than 15 px or 25 px (Figures B.7, B.8, and B.9). The stippling was probably less of an issue in the radial specimens because of the lesser prominence of inter-fiber shear discontinuities, causing speckles to move with greater local homogeneity.

In circumferential specimens, the most prominent strain field features were bands of high strain, apparently between fascicles, in the shear and transverse strain fields. These shear and transverse strain bands were blurred when large subset sizes were used (Figures B.5 and B.6). Bands in the strain fields for circumferential specimen 1 merged with their surrounds at subset sizes > 35 px (for E_{xy} ; Figure B.5, top) or > 25 px (for E_{yy} ; Figure B.6, top). Similarly, a narrow shear band for circumferential specimen 2 to the upper left of the crack tip disappeared for subset sizes > 25 px (Figure B.5, bottom). Transverse strain bands in circumferential specimen 2 were obscured by stippling and point loss for subset sizes ≤ 25 px, and blurred to reduced prominence for subset sizes ≥ 45 px (Figure B.6, bottom). Unlike circumferential specimens, radial specimens had no shear or transverse strain bands that would be adversely affected by blurring with larger subset sizes.

From the perspective of measuring near-crack strain, a small subset size is better because all analyzed pixels must be at least half the subset size away from the specimen boundary. Since the region near the crack tip is of great interest, it is desirable to minimize the subset size as much as possible. Still, the appearance of the strain fields near the crack tips tended to be qualitatively similar regardless of subset size (Figures B.4, B.5, B.6, B.7, B.8, and B.9).

B.2.3 Effect of subset size on point tracking

Small subset sizes tended to cause more points be discarded during the image correlation process, particularly for specimens with lesser image quality. For example, droplets of water accumulated on the surface of circumferential specimen 2 as it contracted during the test (Figure B.2, bottom). The droplets appeared bright white due to reflected light, and the appearance of a droplet in a subset usually caused a sufficient change in local appearance to cause that subset to be discarded. A subset size of 9 px caused such severe point loss in specimen 2 that it was not useful for analysis. Larger subset sizes (especially 45 px and 55 px) allowed the retention of most of the points. A subset size of 35 px was sufficient to retain all points near the crack tip. (Note that most pixels were retained only up to the pre-rupture frame examined in this analysis; later images in the sequence lost more points as the specimen ruptured.) The risk of point loss at small subset sizes can offset the gain in analyzable area from being able to track points closer to the specimen's edges. Circumferential specimen 1 had more points near the crack tip with a 35 px subset size than with a 9 px subset size, even though the 9 px subset could track points within 4.5 px of the crack and the 35 px subset could only track points within 17.5 px of the crack. The improvement in point retention due to more robust tracking with increasing subset size seems to saturate at about 35 px to 45 px.

B.2.4 Effect of subset size on aggregate strain field statistics

Aggregate statistics for the strain fields were calculated and compared across between subset sizes (Figures B.10 and B.11). The median was generally insensitive to the subset size. Increasing the subset size moved the 0.05 and 0.95 quantiles towards the median. This was true for all frames collected from the start of the test to rupture, except when increases in the subset size caused fewer subsets to be discarded. For example, increasing the subset size for radial specimen 1 caused many more subsets from the middle of the sample to be included. The amount of

additional subsets was sufficient to skew the median (Figure B.11). In the case of radial specimen 2, increases in the subset size caused both sides of a rupture in the left of the specimen to be included in the same subsets, causing extreme strain values to be included in the summary statistics. This caused the 0.95 quantile to increase (Figure B.11), but the change in the number of points in this case was insufficient to skew the median. Therefore, aggregating statistics tend to benefit from larger subsets, as reducing the number of discarded points makes the statistic more representative, but this benefit is limited for robust statistics such as the median.

B.2.5 Subset size and image scale

The image scale (camera zoom) varied from sample to sample as necessary to fit the entire specimen in the field of view. Subset size affected the appearance of the stippling pattern and the inter-fascicle strain bands in circumferential specimens, which are both features related to physical characteristics. Stippling was considered to be related to the size of the speckle dots, whereas strain bands were considered to be related to fascicle interfaces. The specimen image scales are given in Table B.1. Circumferential specimen 1 had a lesser image magnification, so for specimen 1 a given subset size (in pixels) had a larger physical size. Accordingly, the strain fields for circumferential specimen 1 look smoother than those for circumferential specimen 2. It is therefore sensible to define the subset size in terms of the physical size of the specimen rather than purely by image dimensions so as to maintain a constant relationship between the subset size and the specimens' physical structure.

Table B.1: Image scale

Specimen	Scale (px/mm)	0.7 mm in px
Circumferential specimen 1	31.7	23
Circumferential specimen 2	44.3	31
Radial specimen 1	59.8	41
Radial specimen 1	53.1	37

B.2.6 Choice of subset size

The choice of subset size is subject to trade-offs. The need to include pixels near the crack tip and retain strain field bands favors smaller subsets. Larger subset sizes blur the strain field in all cases, so small subsets are needed to observe local details in the strain field. Large subset sizes can cause some features to be blurred into nonexistence. However, blurring can be beneficial in that it eliminates artifacts, such as the stippling effect. Large subset sizes also allow more points to be tracked, as larger subsets track larger features and so are more robust to local appearance changes. The benefits of larger subsets in terms of smoothing the stippling effect and decreasing point loss have a saturation threshold beyond which a larger subset offers little benefit; this threshold is an optimum choice for the subset size, and was chosen as the preferred setting. To ensure that the same physical features are captured, the subset size was scaled for each specimen to a constant physical dimension. The optimal choice, balancing these factors, appears to be a subset size of 35 px for an image with a scale of approximately 50 px/mm—in physical units, a subset size of 0.7 mm. The resulting subset size in pixels is given for each specimen in Table B.1. This choice means that strains cannot be measured within 0.35 mm of the crack. Fortunately, the near-crack strain field does not vary much with subset size; at least, the qualitative appearance of the strain field is similar. The choice of a 0.7 mm subset size is a good compromise between the competing priorities, retaining most local detail while decreasing point tracking loss and limiting artifacts, and consequently was used for the work presented in this dissertation.

B.3 Filter size sensitivity analysis

B.3.1 Filter size analysis setup

The effect of the Vic-2D filter size parameter was investigated in the same way as the subset size investigation, using the same specimens (Section B.2.1). The filter size is the radius from

which points in the displacement field are gathered to calculate strain at a given point. For this part of the sensitivity analysis, the subset size was set to 0.7 mm, as recommended in Section B.2.6. The filter size was varied across 5 px, 9 px, and 15 px (15 px is the default in Vic-2D). The primary question was whether the default filter size obscured important features, so larger filter sizes were not used. An exponential decay filter (the default) was used in all cases, as the alternative (a box filter) was considered to make local strain depend too much on far away points.

As in the subset size investigation, strain field plots were the primary analysis tool. The strain fields were plotted for a single image per specimen just prior to rupture—the same images as used in the subset size analysis. Since the plots of summary statistics vs. time did not change much for the subset size analysis and the aggregate statistics were unlikely to be very sensitive to filter size variation (since filtering only blurs the strain field), they were not used in the present analysis.

B.3.2 Effect of filter size

Larger filter sizes result in slight blurring of the strain field in circumferential specimens, but no features are obscured (Figures B.12 and B.13). The effect is much weaker than that found when varying the subset size. The filter size is less than the subset size, so it makes sense that the filter does not blur away any additional features. Overall, the blurring produced by the 15 px default filter is beneficial. Strain variation on a smaller scale than the speckle pattern is not believable, and a filter size of 15 px helps to eliminate this effect.

The radial samples had smoother strain fields than the circumferential specimens (Figures B.14 and B.15). The smoother strain fields are probably due to less independent fiber motion. At filter sizes of 5 px or 9 px, the radial strain fields had some blockiness, possibly arising from noise amplification by the displacement derivative used to calculate strain. A filter size

of 15 px eliminated this blockiness. This blockiness was likely obscured in the circumferential specimens by the large degree of variation in their strain fields.

B.3.3 Choice of filter size

Filter size has a small effect on the result, much less than the subset size. The default filter size of 15 px is beneficial in that it smooths small-scale, meaningless variation in the strain field without obscuring potentially important strain features. Therefore, a 15 px strain field was selected for the work presented in this dissertation.

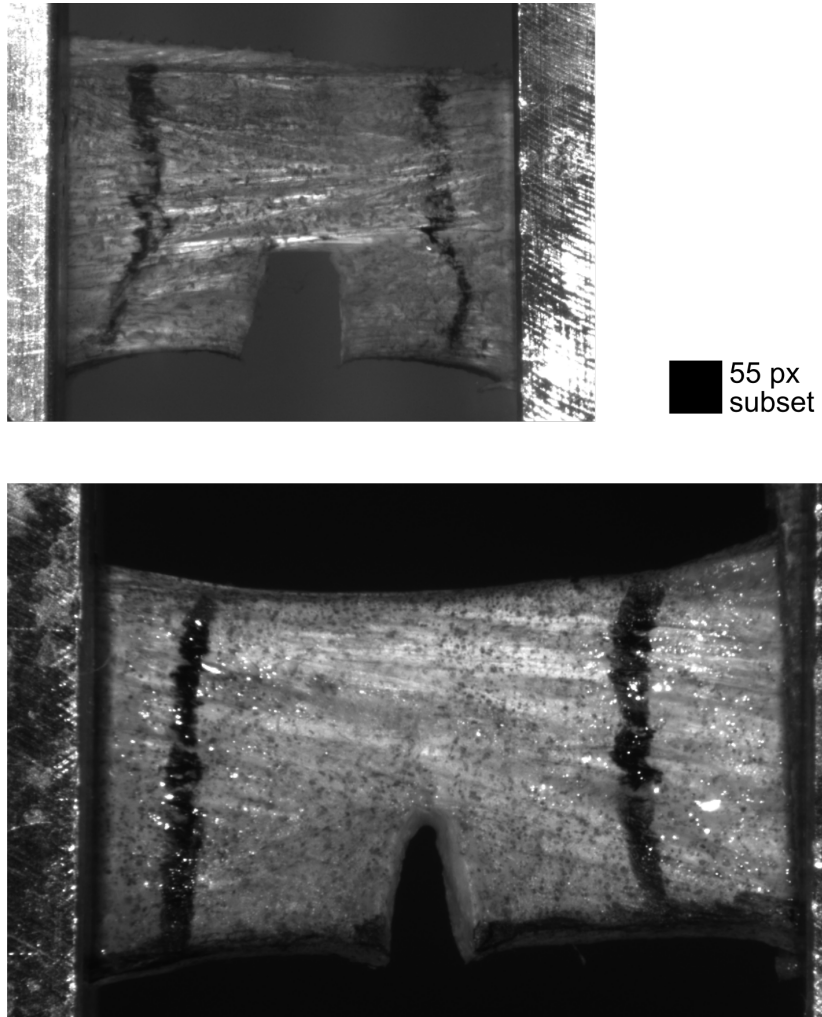
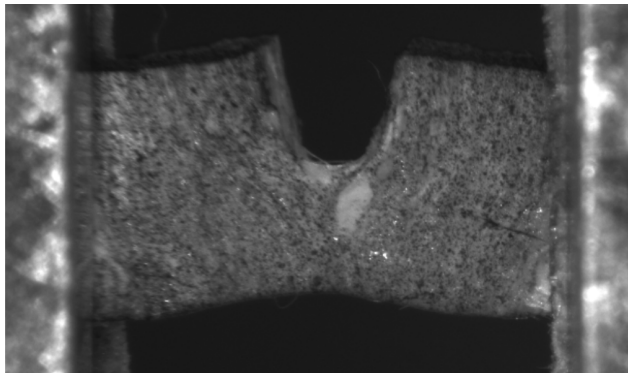


Figure B.2: The circumferential specimens used in the Vic-2D sensitivity analysis, shown immediately prior to rupture. The black square illustrates the size of a 55 px subset. The top specimen here is also the top specimen in the subsequent strain field figures. Top: Circumferential specimen 1. Bottom: Circumferential specimen 2.



55 px
subset

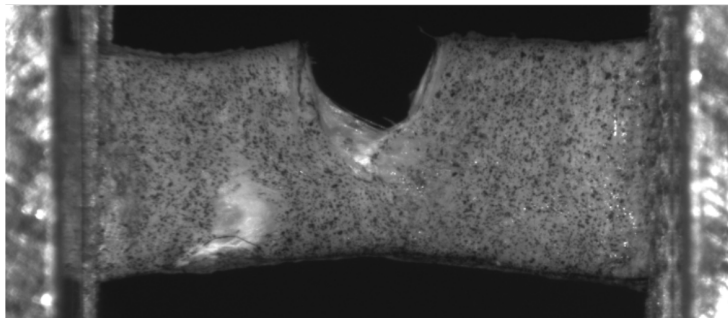


Figure B.3: The radial specimens used in the Vic-2D sensitivity analysis, shown immediately prior to rupture. The black square illustrates the size of a 55 px subset. The top specimen here is also the top specimen in the subsequent strain field figures. Top: Radial specimen 1. Bottom: Radial specimen 2.

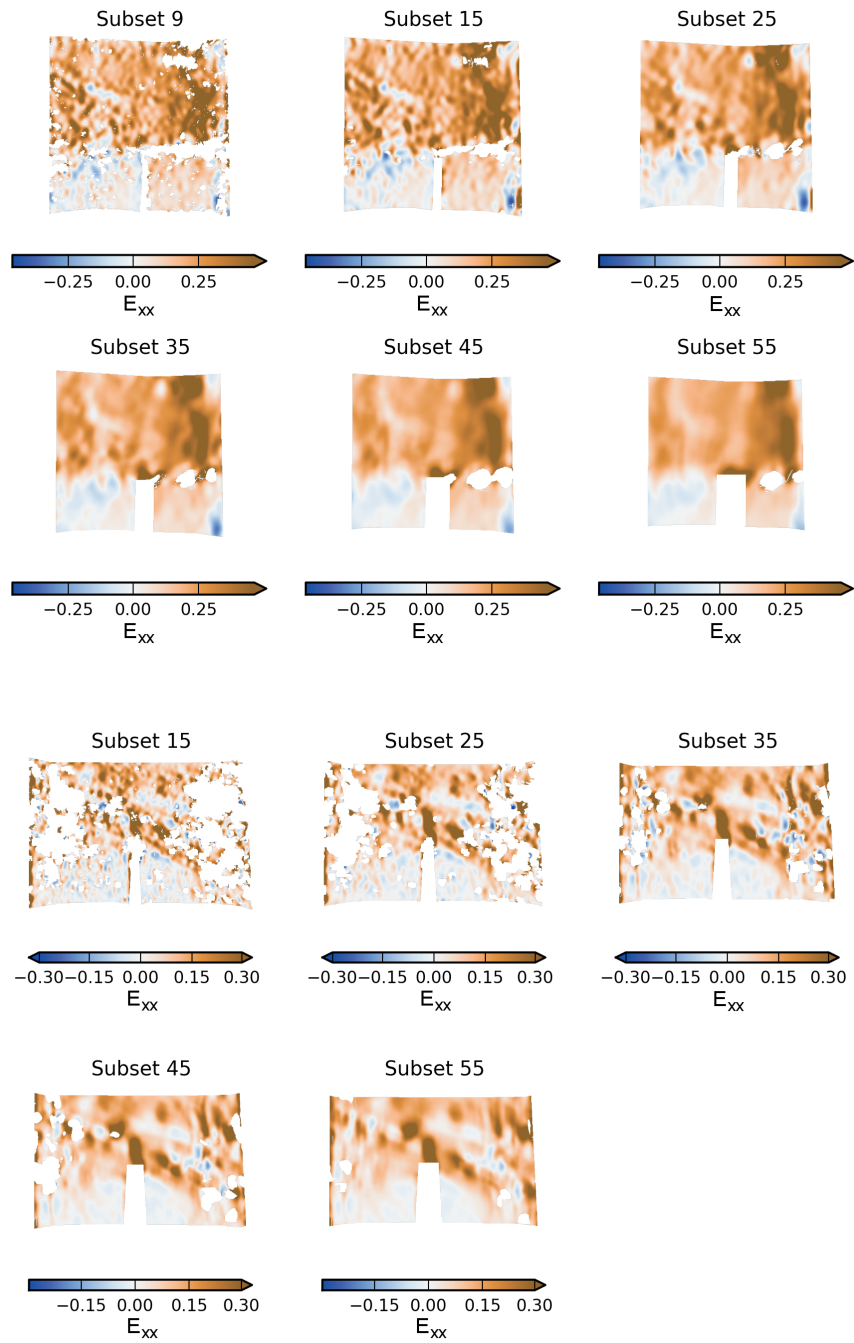


Figure B.4: Effect of Vic-2D subset size on the longitudinal (E_{xx}) strain field for circumferential specimens. Top: Circumferential specimen 1. Bottom: Circumferential specimen 2. Circumferential specimen 2 has no strain field for the 9 px subset size because too many points were lost in the digital image correlation.

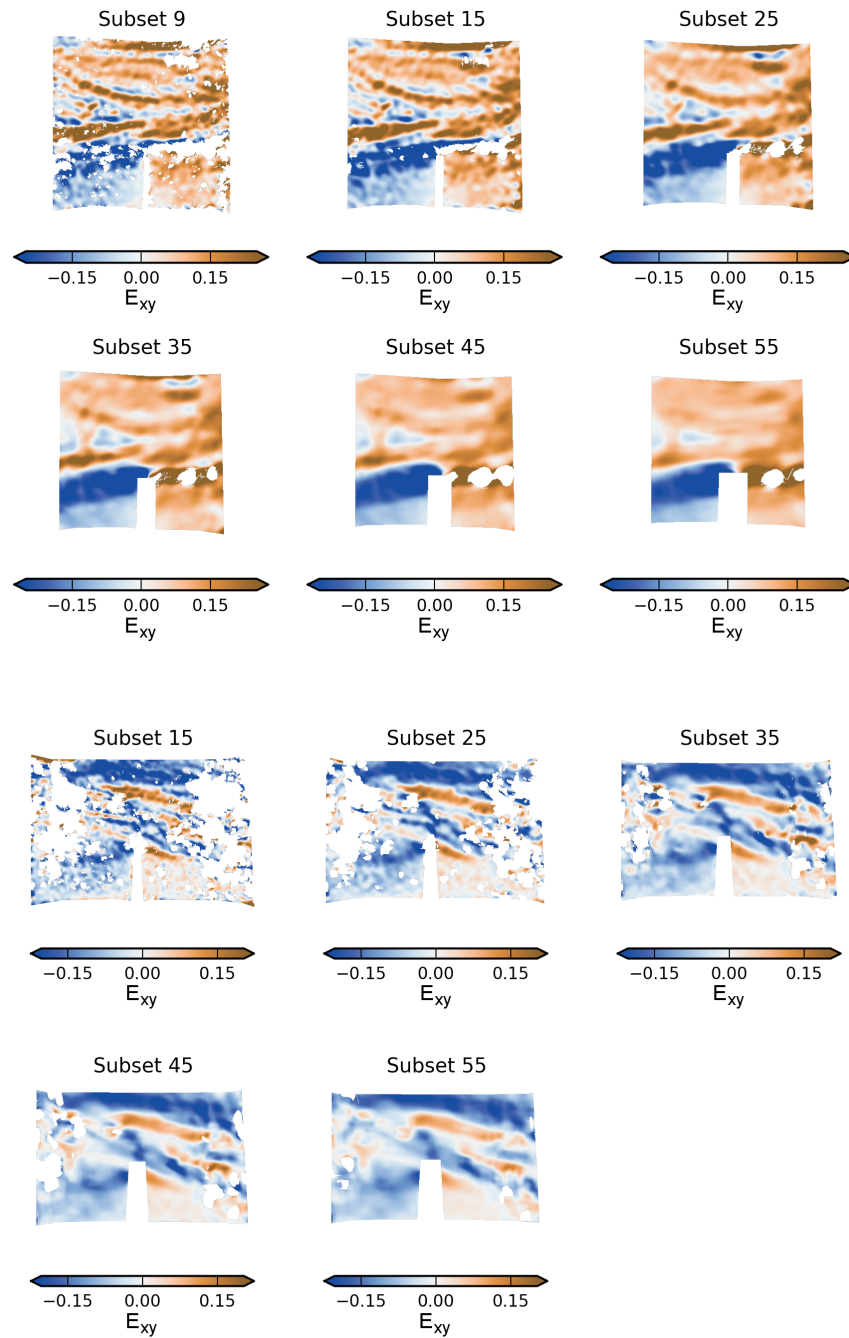


Figure B.5: Effect of Vic-2D subset size on the shear (E_{xy}) strain field for circumferential specimens. Top: Circumferential specimen 1. Bottom: Circumferential specimen 2. Circumferential specimen 2 has no strain field for the 9 px subset size because too many points were lost in the digital image correlation.

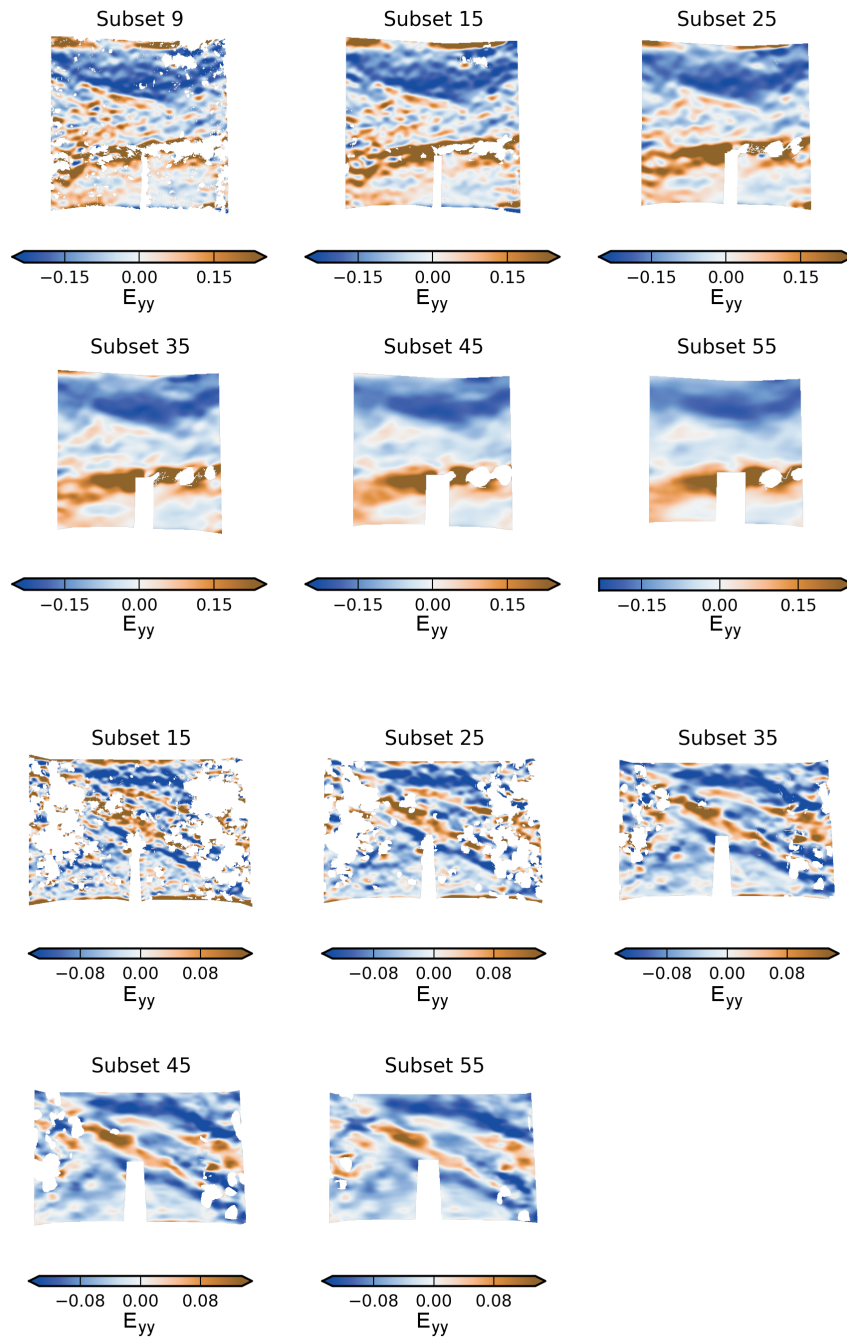


Figure B.6: Effect of Vic-2D subset size on the transverse (E_{yy}) strain field for circumferential specimens. Top: Circumferential specimen 1. Bottom: Circumferential specimen 2. Circumferential specimen 2 has no strain field for the 9 px subset size because too many points were lost in the digital image correlation.

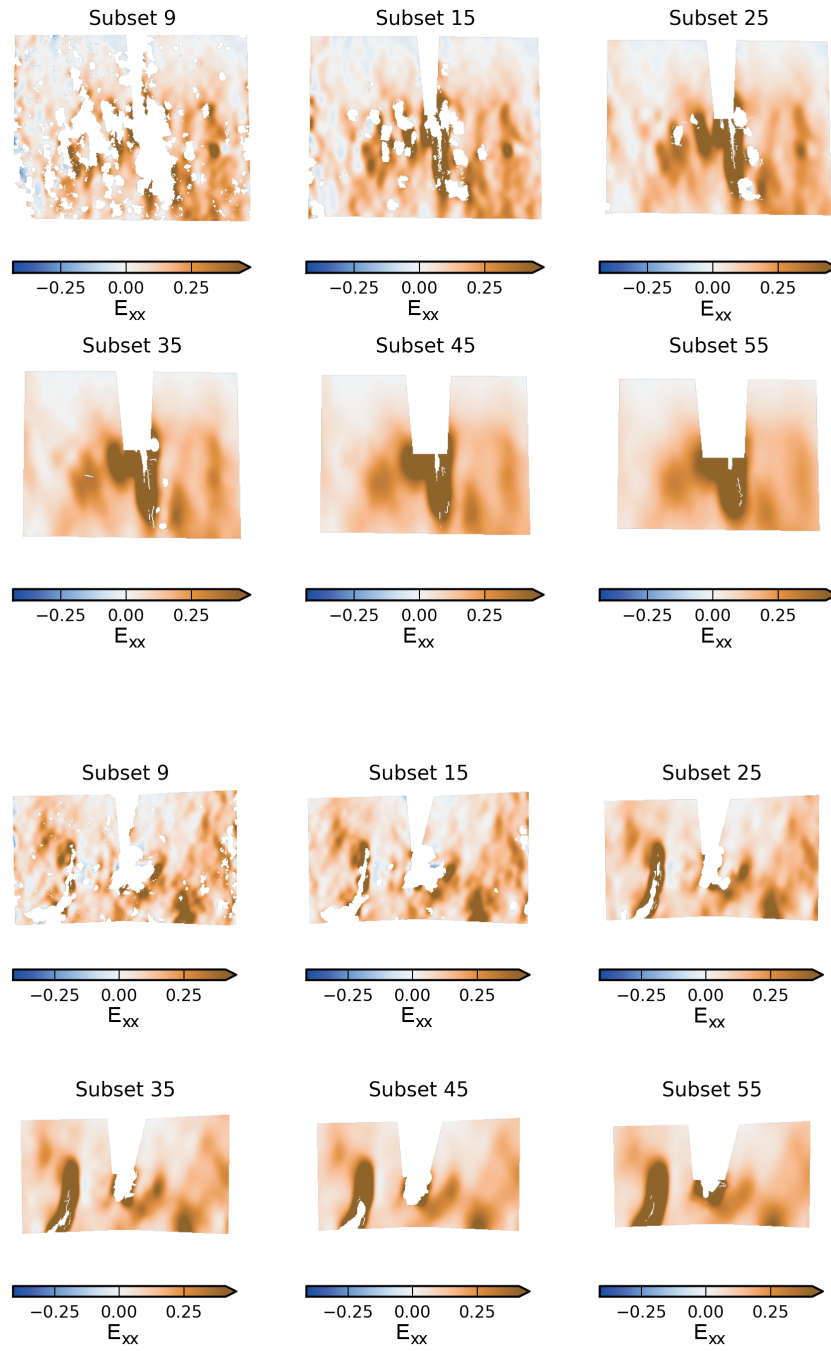


Figure B.7: Effect of Vic-2D subset size on the longitudinal (E_{xx}) strain field for radial specimens. Top: Radial specimen 1. Bottom: Radial specimen 2.

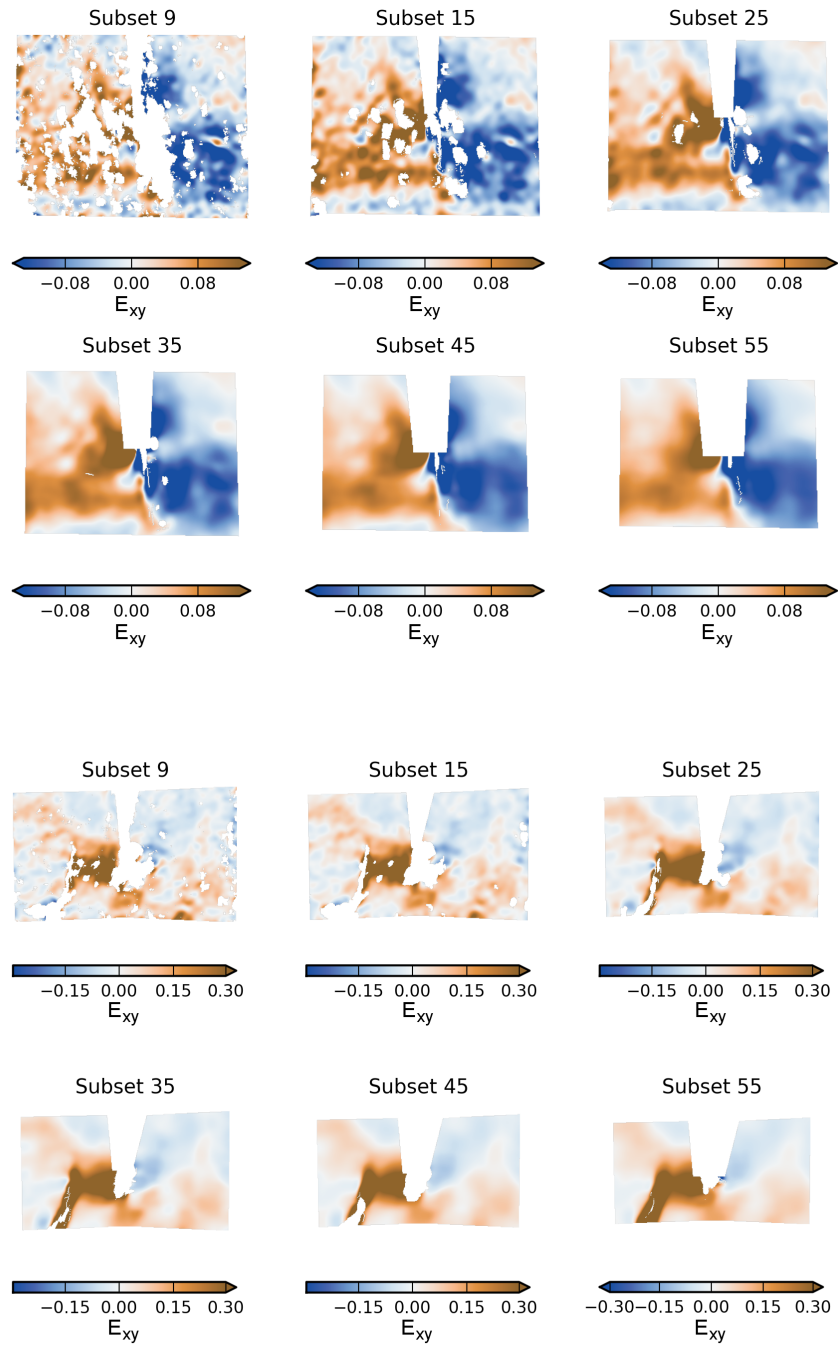


Figure B.8: Effect of Vic-2D subset size on the shear (E_{xy}) strain field for radial specimens. Top: Radial specimen 1. Bottom: Radial specimen 2.

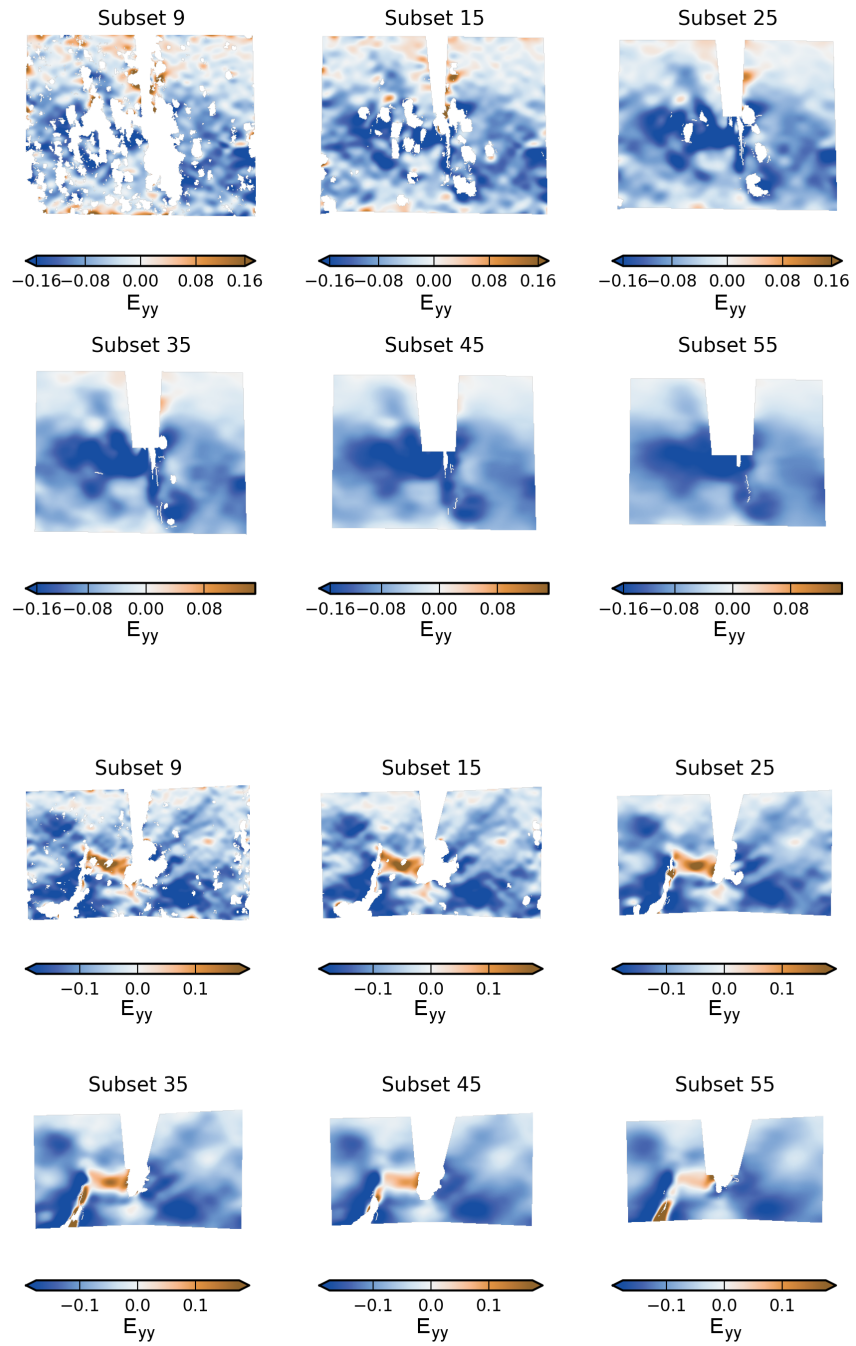
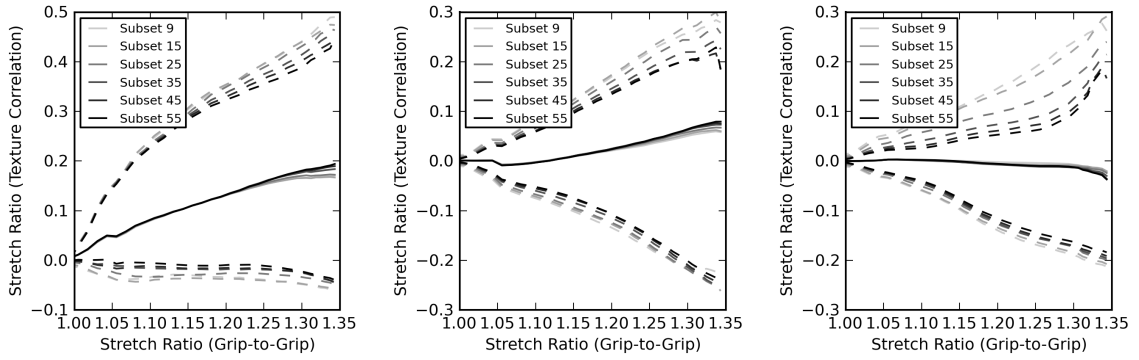
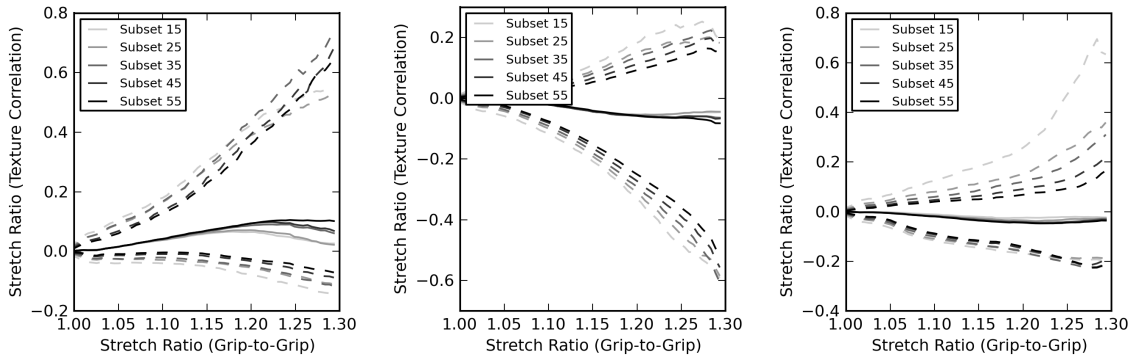


Figure B.9: Effect of Vic-2D subset size on the transverse (E_{yy}) strain field for radial specimens. Top: Radial specimen 1. Bottom: Radial specimen 2.



(a) E_{xx} , circumferential specimen 1 (b) E_{xy} , circumferential specimen 1 (c) E_{yy} , circumferential specimen 1



(d) E_{xx} , circumferential specimen 2 (e) E_{xy} , circumferential specimen 2 (f) E_{yy} , circumferential specimen 2

Figure B.10: Effect of subset size on median strain (solid line) and 0.05 and 0.95 quantiles (dashed lines) for circumferential specimens.

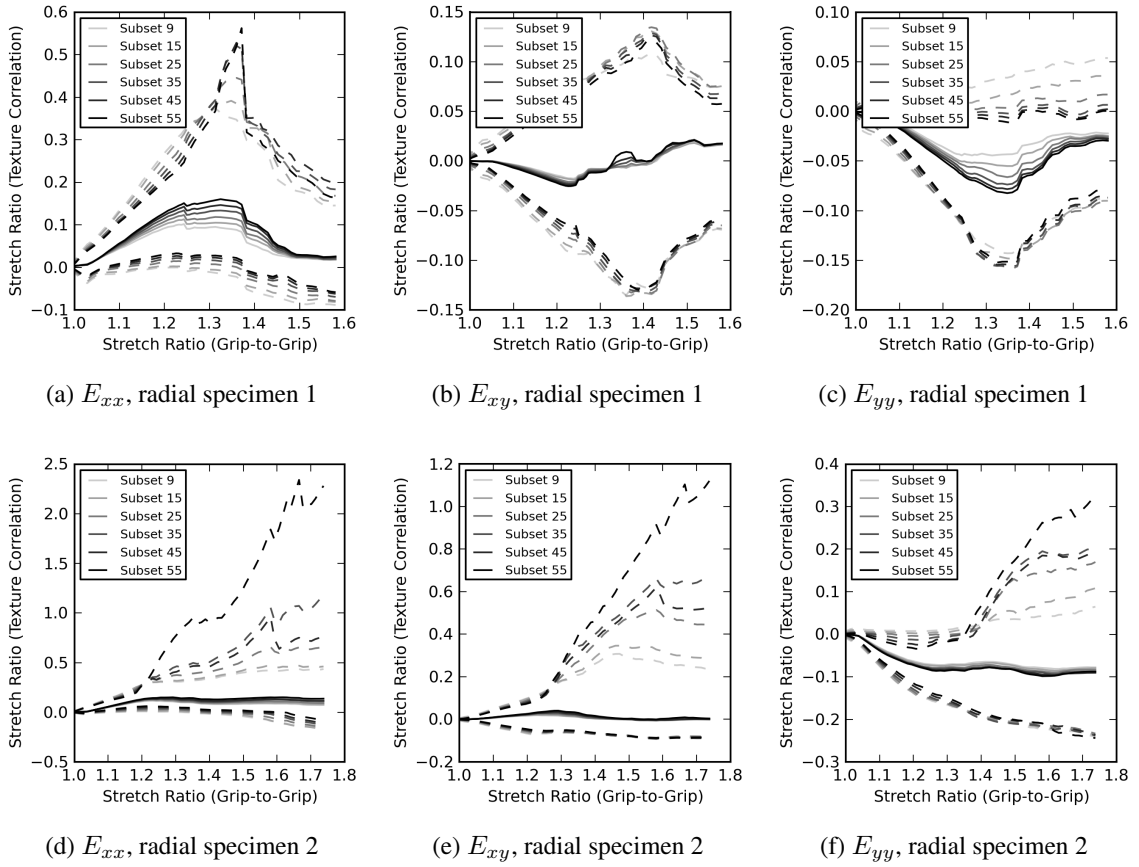


Figure B.11: Effect of subset size on median strain (solid line) and 0.05 and 0.95 quantiles (dashed lines) for radial specimens.

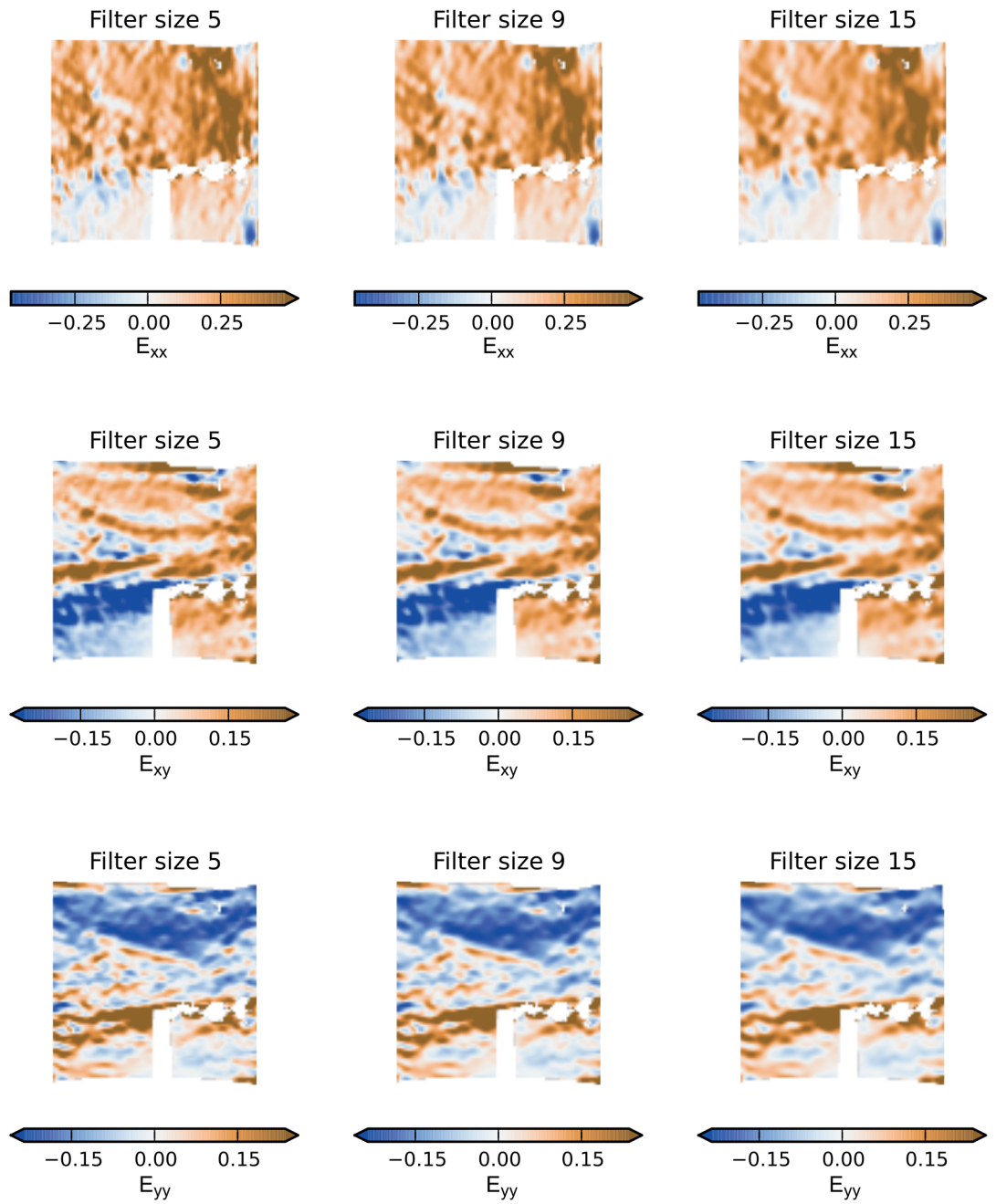


Figure B.12: Effect of filter size on the strain field for circumferential specimen 1.

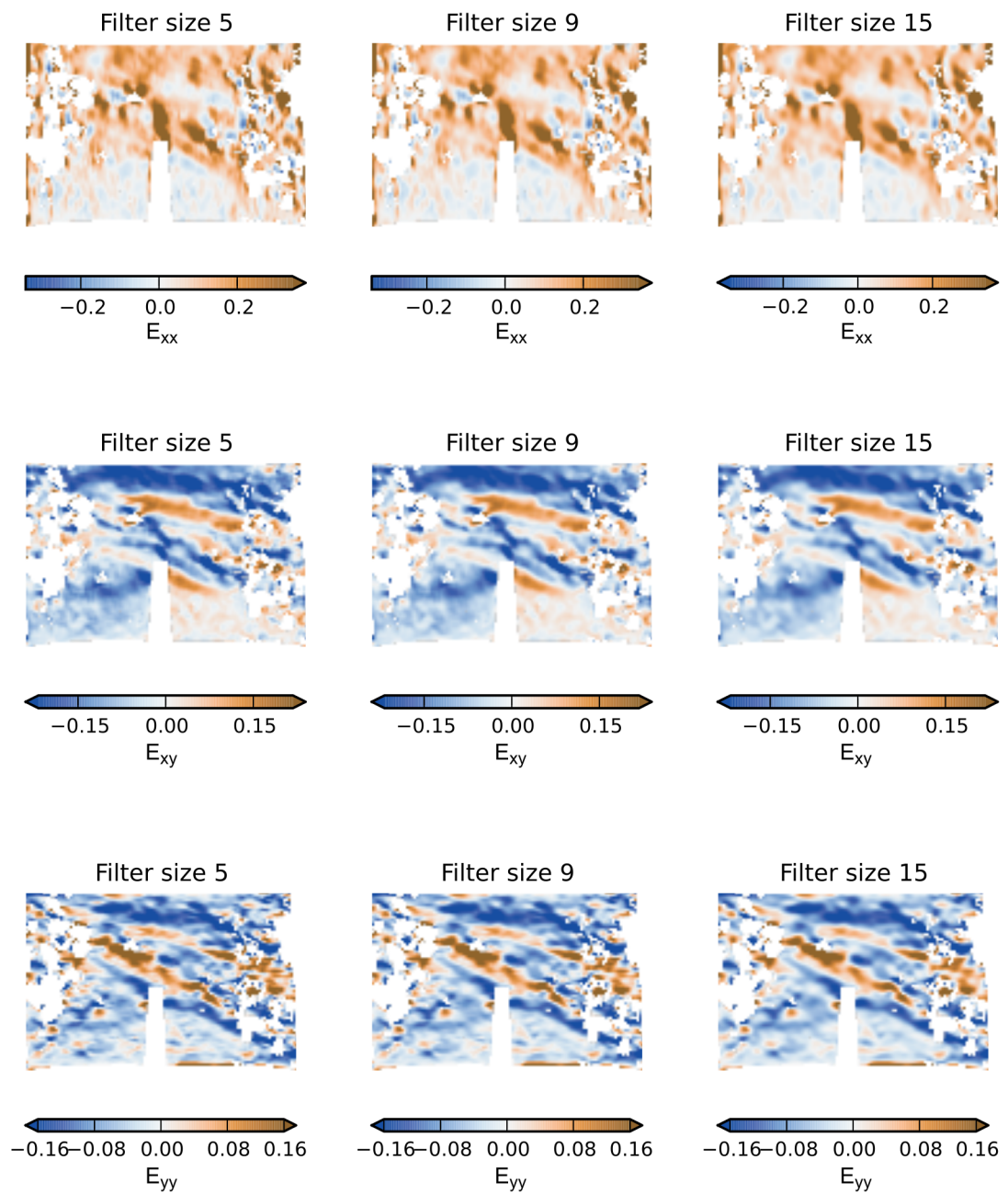


Figure B.13: Effect of filter size on the strain field for circumferential specimen 2.

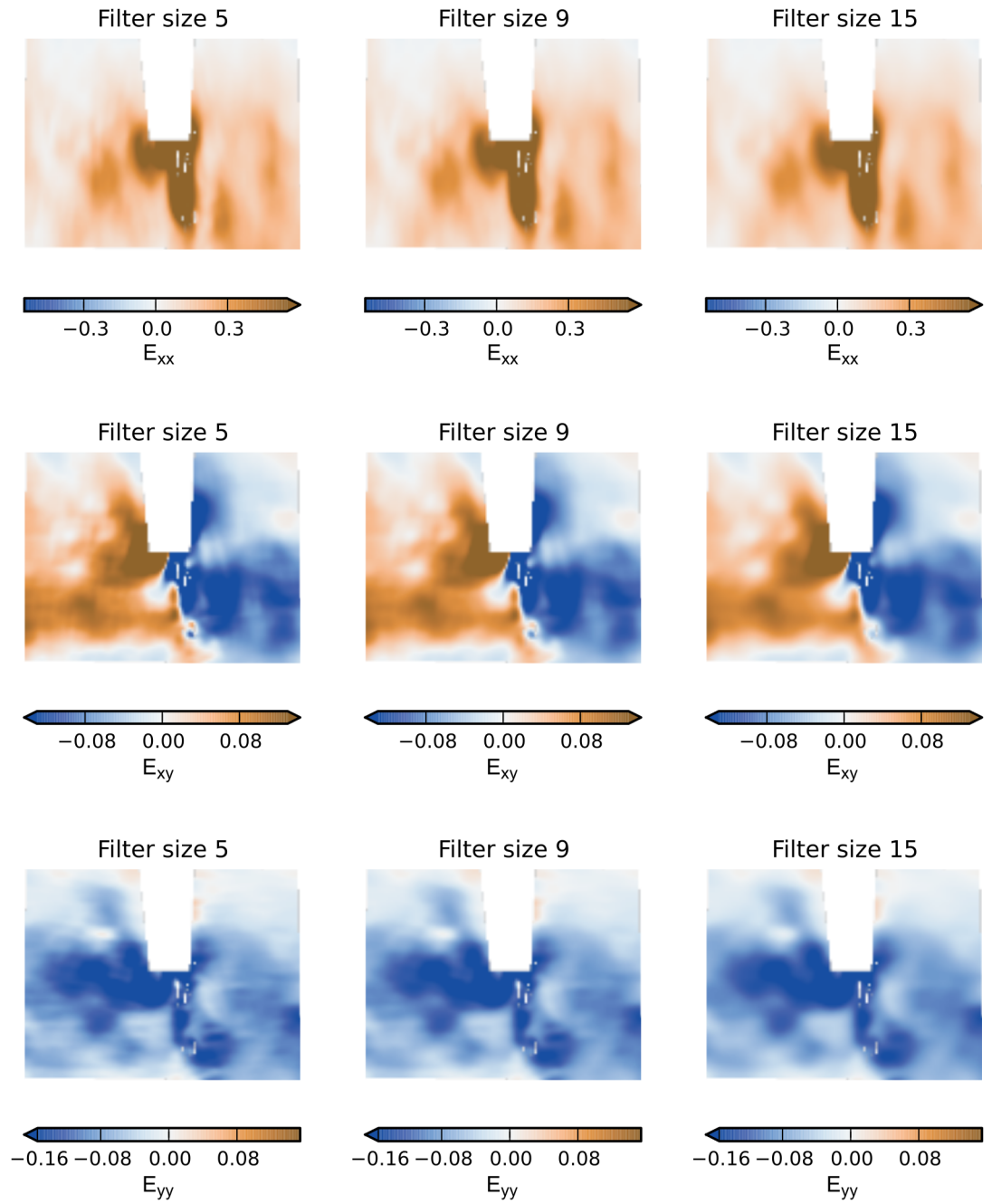


Figure B.14: Effect of filter size on the strain field for radial specimen 1.

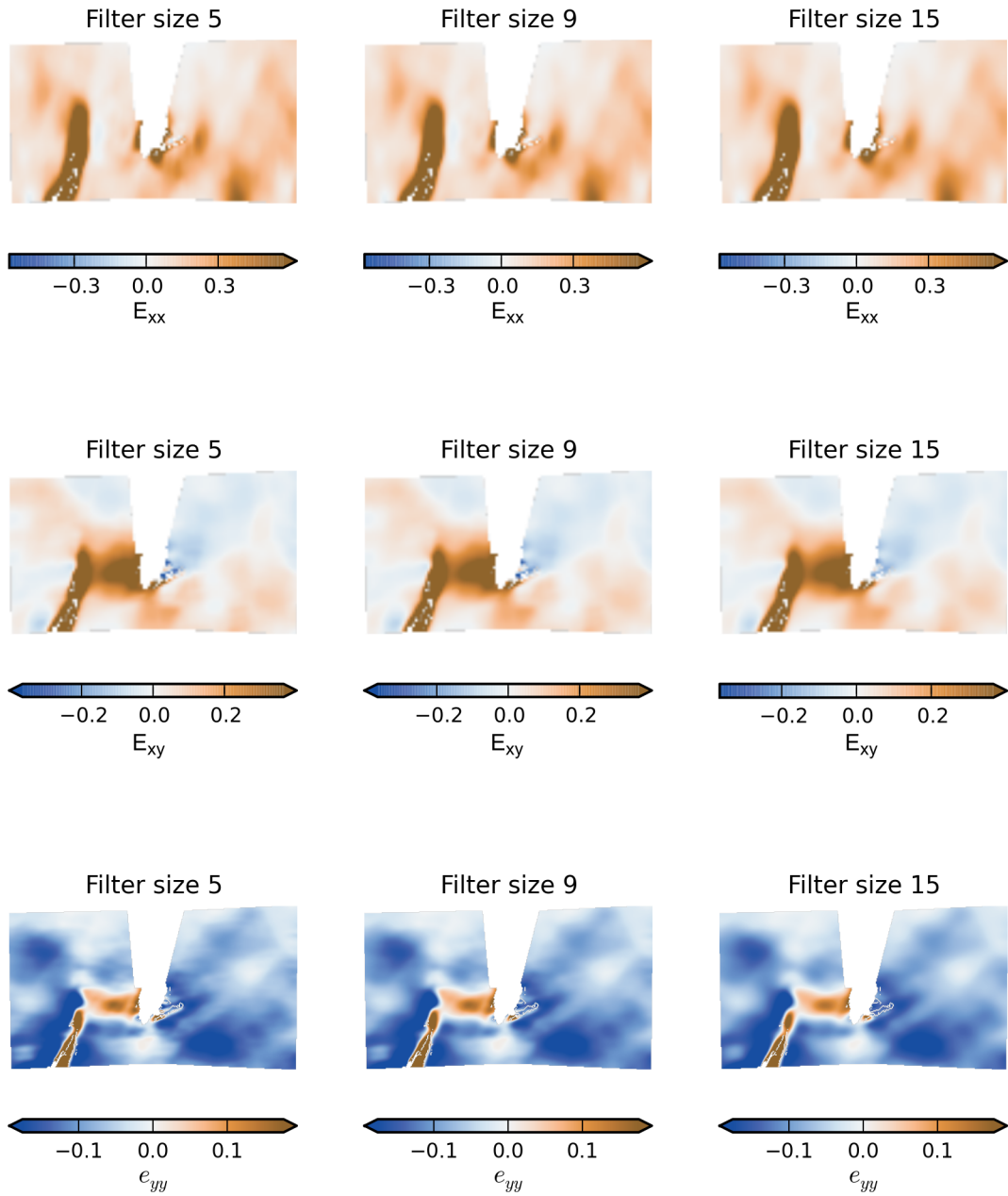

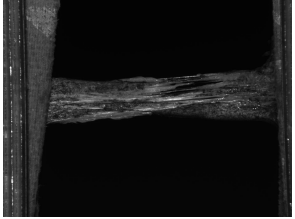
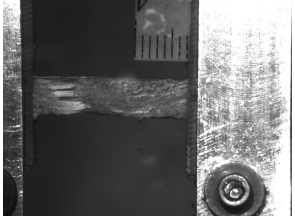
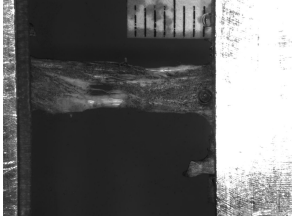


Figure B.15: Effect of filter size on the strain field for radial specimen 2.

APPENDIX C: ENDPOINTS FOR TESTS USED TO STUDY THE EFFECT OF CRACKS

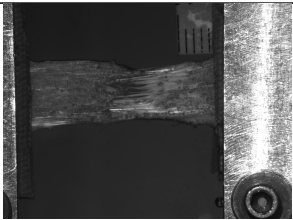
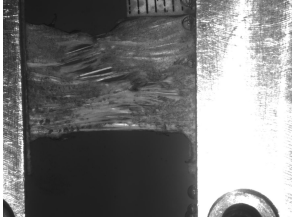
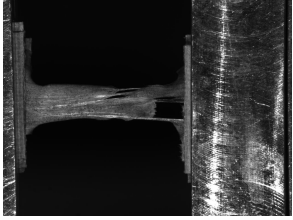
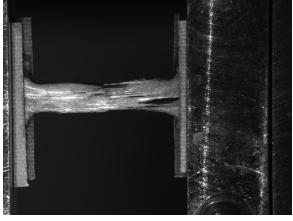
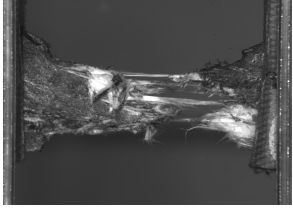

Table C.1 lists the endpoint of each test reported in Chapter 5. The image from each test best illustrating its endpoint is also shown. For endpoint definitions, see Section 4.2.2.

Table C.1: Test endpoints for specimens reported in Chapter 5.

Loading axis	Shape	Cracked	Endpoint	Endpoint image
circumferential	ET	control	midsubstance rupture	
circumferential	ET	control	midsubstance rupture	
circumferential	ET	control	midsubstance rupture	
circumferential	ET	control	midsubstance rupture	

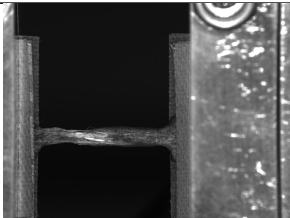
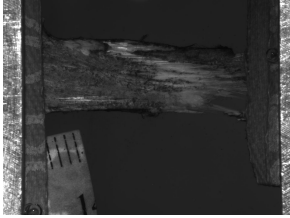
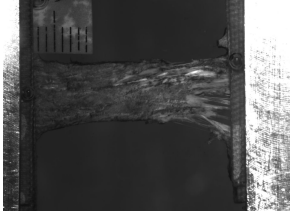



Continued on next page

Continued from previous page

Loading axis	Shape	Cracked	Endpoint	Endpoint image
circumferential	ET	control	midsubstance rupture	
circumferential	ET	control	midsubstance rupture	
circumferential	ET	control	mixed rupture	
circumferential	ET	control	mixed rupture	
circumferential	ET	control	mixed rupture	
circumferential	ET	control	mixed rupture	


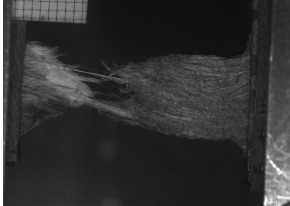

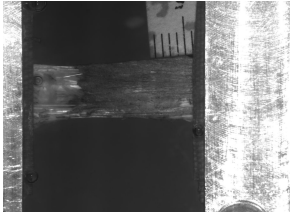
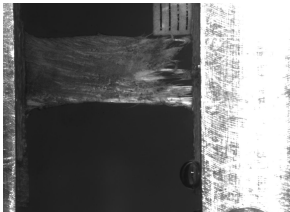
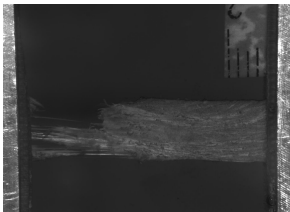
Continued on next page

Continued from previous page

Loading axis	Shape	Cracked	Endpoint	Endpoint image
circumferential	ET	control	mixed rupture	
circumferential	ET	control	mixed rupture	
circumferential	ET	control	mixed rupture	
circumferential	ET	control	mixed rupture	
circumferential	ET	control	mixed rupture	
circumferential	ET	control	mixed rupture	

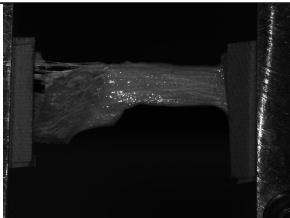
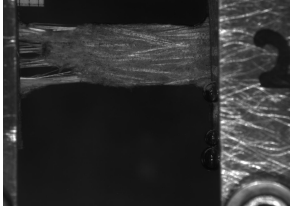
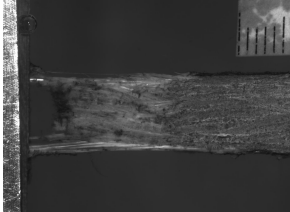
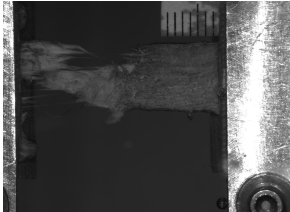
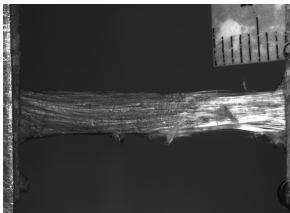

Continued on next page

Continued from previous page

Loading axis	Shape	Cracked	Endpoint	Endpoint image
circumferential	ET	control	mixed rupture	
circumferential	ET	control	grip line rupture	
circumferential	ET	control	grip line rupture	
circumferential	ET	control	grip line rupture	
circumferential	ET	control	grip line rupture	
circumferential	ET	control	grip line rupture	

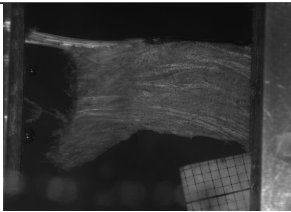
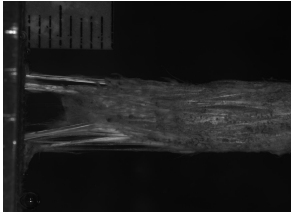
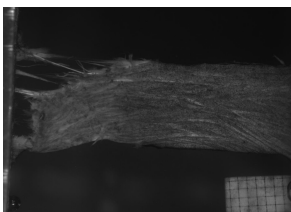
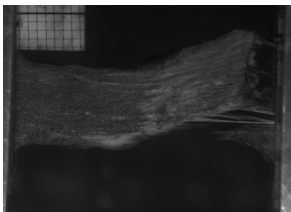
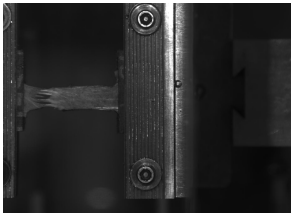
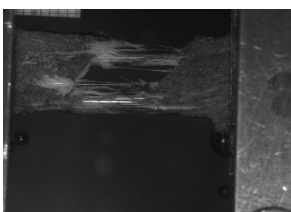
Continued on next page

Continued from previous page

Loading axis	Shape	Cracked	Endpoint	Endpoint image
circumferential	ET	control	gripped region failure	
circumferential	ET	control	gripped region failure	
circumferential	ET	control	gripped region failure	
circumferential	ET	control	gripped region failure	
circumferential	ET	control	gripped region failure	
circumferential	ET	control	no rupture	


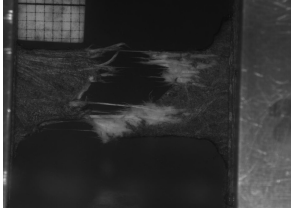
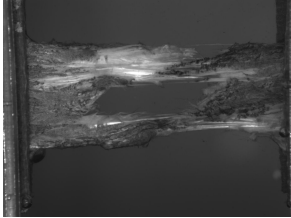
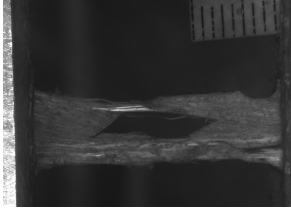
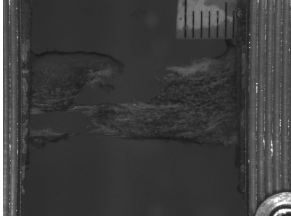
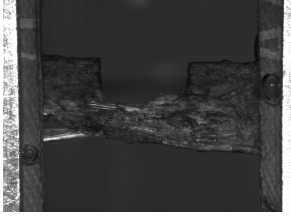
Continued on next page

Continued from previous page

Loading axis	Shape	Cracked	Endpoint	Endpoint image
circumferential	ET	control	no rupture	
circumferential	ET	control	no rupture	
circumferential	ET	control	no rupture	
circumferential	ET	control	no rupture	
circumferential	ET	cracked	midsubstance rupture	
circumferential	ET	cracked	midsubstance rupture	

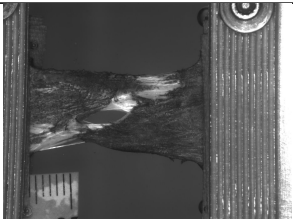


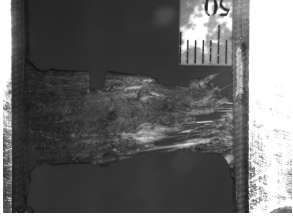
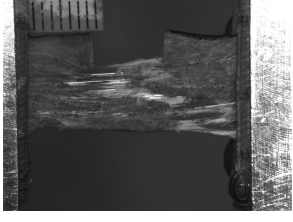
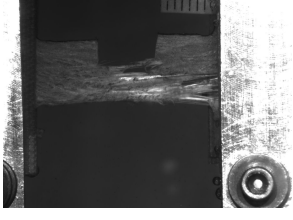
Continued on next page

Continued from previous page

Loading axis	Shape	Cracked	Endpoint	Endpoint image
circumferential	ET	cracked	midsubstance rupture	
circumferential	ET	cracked	midsubstance rupture	
circumferential	ET	cracked	mixed rupture	
circumferential	ET	cracked	mixed rupture	
circumferential	ET	cracked	mixed rupture	
circumferential	ET	cracked	mixed rupture	

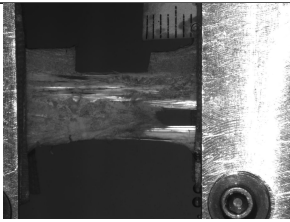
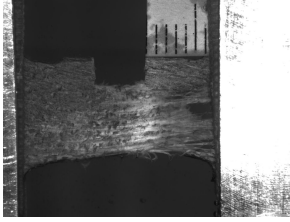
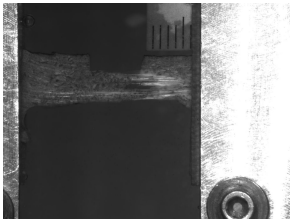
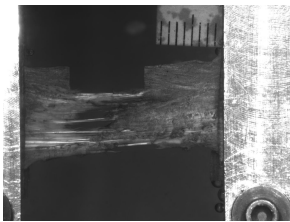

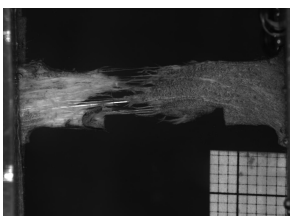
Continued on next page

Continued from previous page

Loading axis	Shape	Cracked	Endpoint	Endpoint image
circumferential	ET	cracked	mixed rupture	
circumferential	ET	cracked	mixed rupture	
circumferential	ET	cracked	mixed rupture	
circumferential	ET	cracked	mixed rupture	
circumferential	ET	cracked	mixed rupture	
circumferential	ET	cracked	mixed rupture	

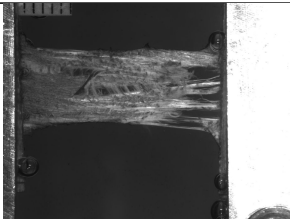
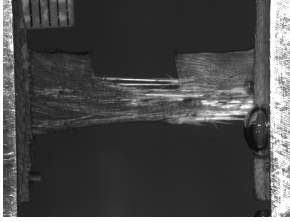
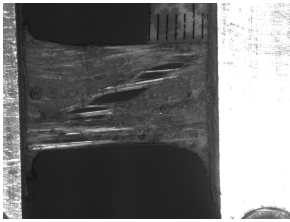
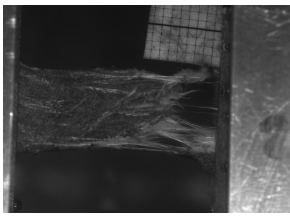
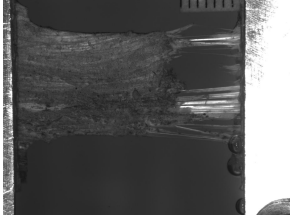

Continued on next page

Continued from previous page

Loading axis	Shape	Cracked	Endpoint	Endpoint image
circumferential	ET	cracked	mixed rupture	
circumferential	ET	cracked	mixed rupture	
circumferential	ET	cracked	mixed rupture	
circumferential	ET	cracked	mixed rupture	
circumferential	ET	cracked	mixed rupture	
circumferential	ET	cracked	mixed rupture	

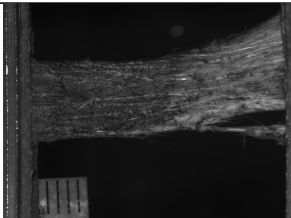

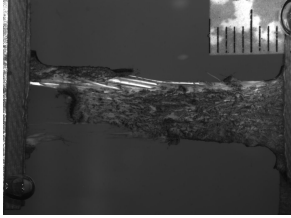
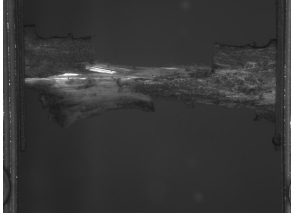
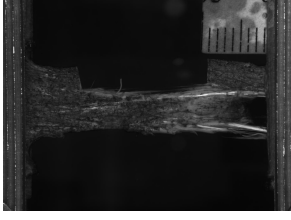
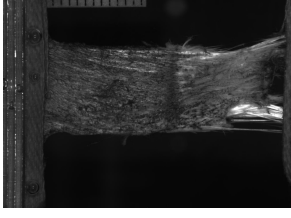
Continued on next page

Continued from previous page

Loading axis	Shape	Cracked	Endpoint	Endpoint image
circumferential	ET	cracked	mixed rupture	
circumferential	ET	cracked	mixed rupture	
circumferential	ET	cracked	mixed rupture	
circumferential	ET	cracked	grip line rupture	
circumferential	ET	cracked	grip line rupture	
circumferential	ET	cracked	gripped region failure	


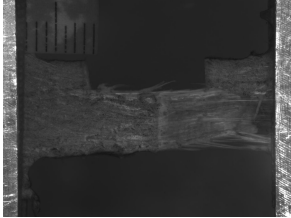
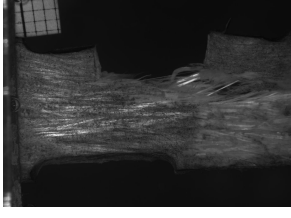
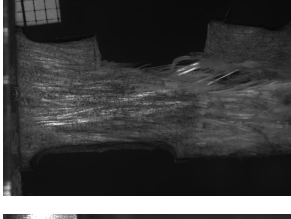
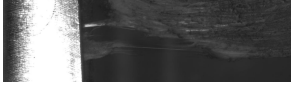
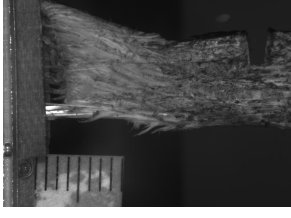
Continued on next page

Continued from previous page

Loading axis	Shape	Cracked	Endpoint	Endpoint image
circumferential	ET	cracked	gripped region failure	
circumferential	ET	cracked	gripped region failure	
circumferential	ET	cracked	gripped region failure	
circumferential	ET	cracked	gripped region failure	
circumferential	ET	cracked	gripped region failure	
circumferential	ET	cracked	gripped region failure	

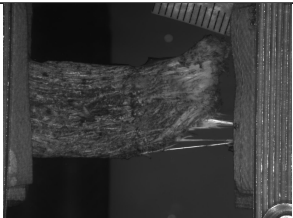
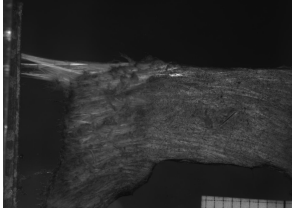
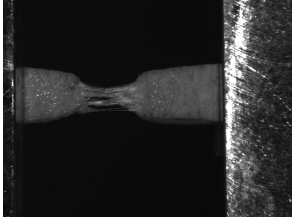
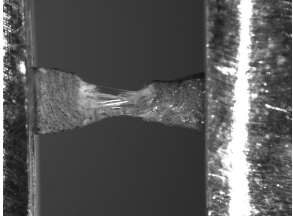

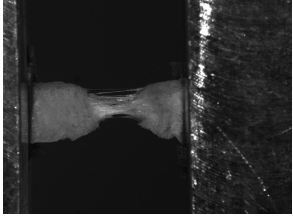
Continued on next page

Continued from previous page

Loading axis	Shape	Cracked	Endpoint	Endpoint image
circumferential	ET	cracked	gripped region failure	
circumferential	ET	cracked	gripped region failure	
circumferential	ET	cracked	longitudinal split	
circumferential	ET	cracked	longitudinal split	
circumferential	ET	cracked	no rupture	
circumferential	ET	cracked	no rupture	

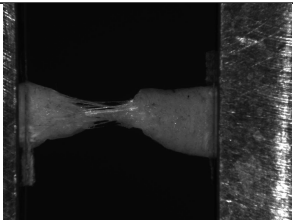
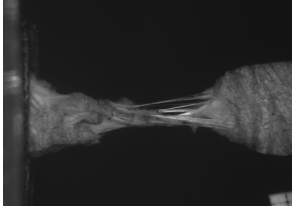
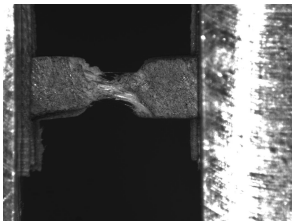
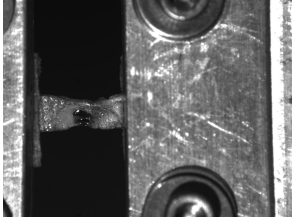
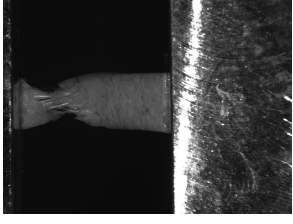

Continued on next page

Continued from previous page

Loading axis	Shape	Cracked	Endpoint	Endpoint image
circumferential	ET	cracked	no rupture	
circumferential	ET	cracked	no rupture	
radial	R	control	midsubstance rupture	
radial	R	control	midsubstance rupture	
radial	R	control	midsubstance rupture	
radial	R	control	midsubstance rupture	

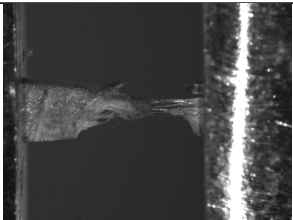
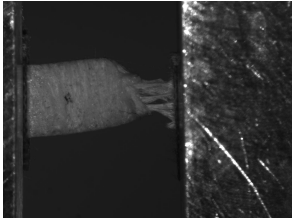
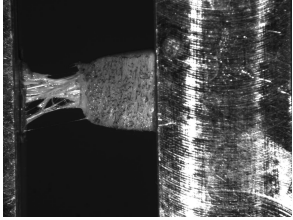
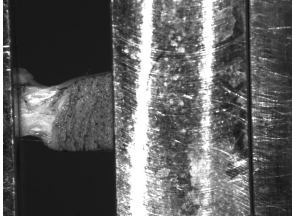
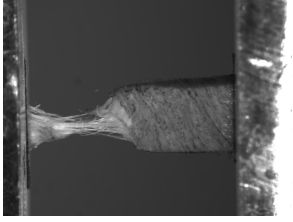
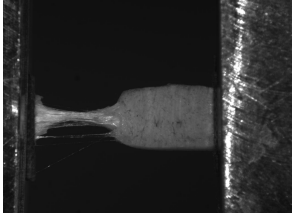
Continued on next page

Continued from previous page

Loading axis	Shape	Cracked	Endpoint	Endpoint image
radial	R	control	midsubstance rupture	
radial	R	control	midsubstance rupture	
radial	R	control	midsubstance rupture	
radial	R	control	midsubstance rupture	
radial	R	control	mixed rupture	
radial	R	control	mixed rupture	

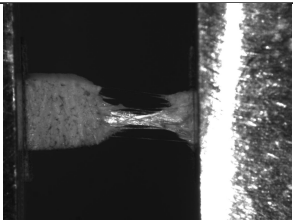
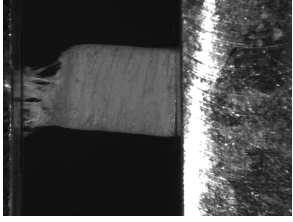
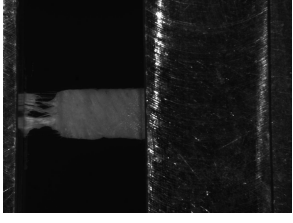
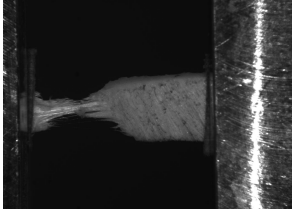
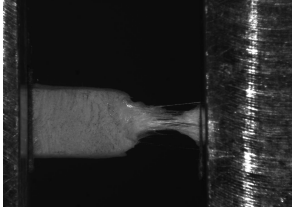
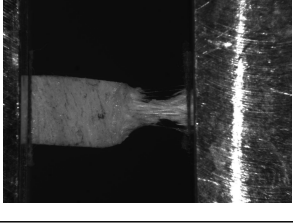
Continued on next page

Continued from previous page

Loading axis	Shape	Cracked	Endpoint	Endpoint image
radial	R	control	mixed rupture	
radial	R	control	grip line rupture	
radial	R	control	grip line rupture	
radial	R	control	grip line rupture	
radial	R	control	grip line rupture	
radial	R	control	grip line rupture	

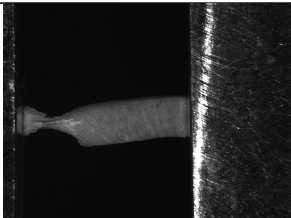
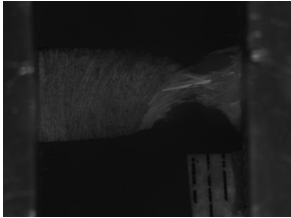

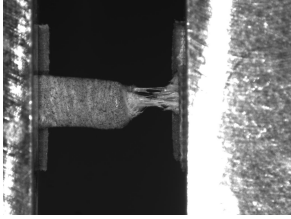
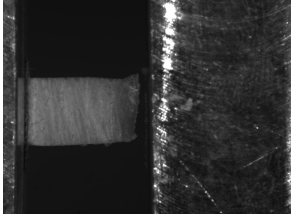
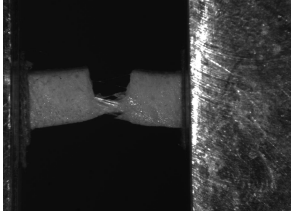
Continued on next page

Continued from previous page

Loading axis	Shape	Cracked	Endpoint	Endpoint image
radial	R	control	grip line rupture	
radial	R	control	grip line rupture	
radial	R	control	grip line rupture	
radial	R	control	grip line rupture	
radial	R	control	grip line rupture	
radial	R	control	grip line rupture	

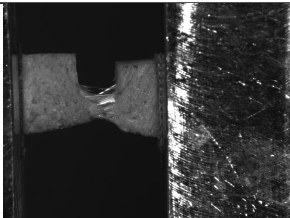
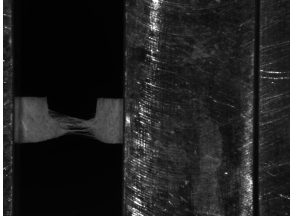


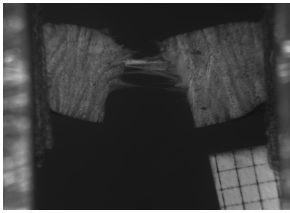
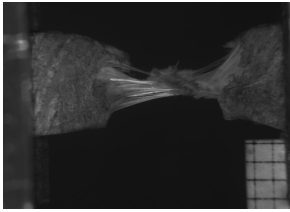
Continued on next page

Continued from previous page

Loading axis	Shape	Cracked	Endpoint	Endpoint image
radial	R	control	grip line rupture	
radial	R	control	grip line rupture	
radial	R	control	grip line rupture	
radial	R	control	grip line rupture	
radial	R	control	no rupture	
radial	R	cracked	midsubstance rupture	

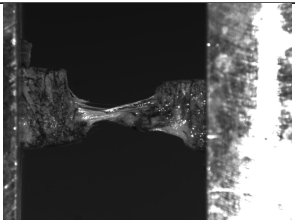
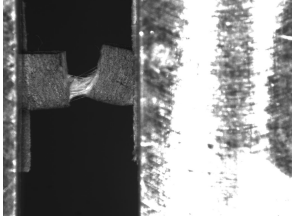

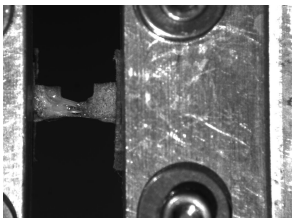
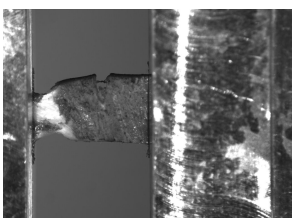

Continued on next page

Continued from previous page

Loading axis	Shape	Cracked	Endpoint	Endpoint image
radial	R	cracked	midsubstance rupture	
radial	R	cracked	midsubstance rupture	
radial	R	cracked	midsubstance rupture	
radial	R	cracked	midsubstance rupture	
radial	R	cracked	midsubstance rupture	
radial	R	cracked	midsubstance rupture	


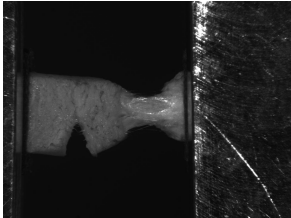
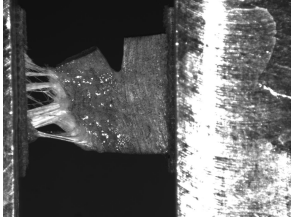
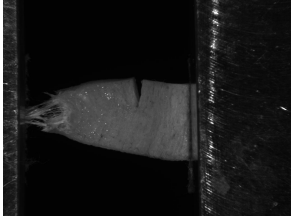

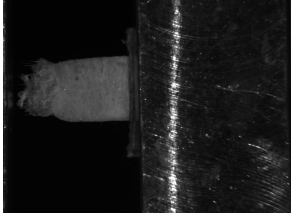
Continued on next page

Continued from previous page

Loading axis	Shape	Cracked	Endpoint	Endpoint image
radial	R	cracked	midsubstance rupture	
radial	R	cracked	midsubstance rupture	
radial	R	cracked	midsubstance rupture	
radial	R	cracked	midsubstance rupture	
radial	R	cracked	mixed rupture	
radial	R	cracked	mixed rupture	

Continued on next page

Continued from previous page

Loading axis	Shape	Cracked	Endpoint	Endpoint image
radial	R	cracked	mixed rupture	
radial	R	cracked	grip line rupture	
radial	R	cracked	grip line rupture	
radial	R	cracked	gripped region failure	
radial	R	cracked	no rupture	
radial	R	cracked	no rupture	

BIBLIOGRAPHY

- Abraham, Adam C., John T. Moyer, Diego F. Villegas, Gregory M. Odegard, and Tammy L. Haut Donahue (2011). “Hyperelastic properties of human meniscal attachments”. In: *Journal of Biomechanics* 44.3, pp. 413–418. DOI: 10.1016/j.jbiomech.2010.10.001.
- Ahmadzadeh, Hossein, Benjamin R. Freedman, Brianne K. Connizzo, Louis J. Soslowsky, and Vivek B. Shenoy (2015). “Micromechanical poroelastic finite element and shear-lag models of tendon predict large strain dependent Poisson’s ratios and fluid expulsion under tensile loading”. In: *Acta Biomaterialia* 22, pp. 83–91. DOI: 10.1016/j.actbio.2015.04.035.
- Ahmed, A M and D L Burke (1983). “In-vitro measurement of static pressure distribution in synovial joints—Part I: Tibial surface of the knee”. In: *Journal of Biomechanical Engineering* 105.3, pp. 216–225.
- Allen, C. R., E. K. Wong, G. A. Livesay, M. Sakane, F. H. Fu, and S. L. Woo (2000). “Importance of the medial meniscus in the anterior cruciate ligament-deficient knee”. In: *Journal of Orthopaedic Research* 18.1, pp. 109–115. DOI: 10.1002/jor.1100180116.
- Anderson, D. R., D. H. Gershuni, M. Nakhostine, and L. A. Danzig (1993). “The effects of non-weight-bearing and limited motion on the tensile properties of the meniscus”. In: *Arthroscopy: The Journal of Arthroscopic and Related Surgery* 9.4, pp. 440–445.
- Anderson, Ted L. (2005). *Fracture Mechanics: Fundamentals and Applications*. 3rd ed. Boca Raton, Florida: CRC Press.
- Andrews, Stephen H J, Jerome B Rattner, Ziad Abusara, Adetola Adesida, Nigel G Shrive, and Janet L Ronsky (2014). “Tie-fibre structure and organization in the knee menisci”. In: *Journal of Anatomy* 224.5, pp. 531–537. DOI: 10.1111/joa.12170.
- Andrews, Stephen HJ, Janet L Ronsky, Jerome B Rattner, Nigel G Shrive, and Heather A Jamiczky (2013). “An evaluation of meniscal collagenous structure using optical projection tomography”. In: *BMC Medical Imaging* 13.1, p. 21. DOI: 10.1186/1471-2342-13-21.
- Anetzberger, Hermann, Alexandra Mayer, Christian Glaser, Stephan Lorenz, Christof Birkenmaier, and Magdalena Müller-Gerbl (2014). “Meniscectomy leads to early changes in the mineralization distribution of subchondral bone plate”. In: *Knee Surgery, Sports Traumatology, Arthroscopy* 22.1, pp. 112–119. DOI: 10.1007/s00167-012-2297-7.
- Arno, Sally, Christopher P. Bell, Carlos Uquillas, Ilya Borukhov, and Peter S. Walker (2015). “Tibiofemoral contact mechanics following a horizontal cleavage lesion in the posterior horn of the medial meniscus”. In: *Journal of Orthopaedic Research* 33.4, pp. 584–590. DOI: 10.1002/jor.22809.
- Arno, Sally, Scott Hadley, Kirk A. Campbell, Christopher P. Bell, Michael Hall, Luis S. Beltran, Michael P. Recht, Orrin H. Sherman, and Peter S. Walker (2013). “The effect of arthroscopic

- partial medial meniscectomy on tibiofemoral stability”. In: *The American Journal of Sports Medicine* 41.1, pp. 73–79. DOI: 10.1177/0363546512464482.
- Arnoczky, S P and R F Warren (1983). “The microvasculature of the meniscus and its response to injury: an experimental study in the dog”. In: *The American Journal of Sports Medicine* 11.3, pp. 131–141.
- Arnoczky, Steven P. and Russell F. Warren (1982). “Microvasculature of the human meniscus”. In: *The American Journal of Sports Medicine* 10.2, pp. 90–95. DOI: 10.1177/036354658201000205.
- Arnold, J. A., T. P. Coker, L. M. Heaton, J. P. Park, and W. D. Harris (1979). “Natural history of anterior cruciate tears”. In: *The American Journal of Sports Medicine* 7.6, pp. 305–313.
- Arumugam, V., R. Naren Shankar, B. T. N. Sridhar, and A. Joseph Stanley (2010). “Ultimate strength prediction of carbon/epoxy tensile specimens from acoustic emission data”. In: *Journal of Materials Science & Technology* 26.8, pp. 725–729. DOI: 10.1016/S1005-0302(10)60114-4.
- Aspden, R M (1985). “A model for the function and failure of the meniscus”. In: *Engineering in medicine* 14.3, pp. 119–122.
- Atmaca, Halil, Cevdet Cumhur Kesemenli, Kaya Memişoğlu, Arif Özkan, and Yusuf Celik (2013). “Changes in the loading of tibial articular cartilage following medial meniscectomy: a finite element analysis study”. In: *Knee Surgery, Sports Traumatology, Arthroscopy* 21.12, pp. 2667–2673. DOI: 10.1007/s00167-012-2318-6.
- Baratz, Mark E., Freddie H. Fu, and Richard Mengato (1986). “Meniscal tears: The effect of meniscectomy and of repair on intraarticular contact areas and stress in the human knee A preliminary report”. In: *The American Journal of Sports Medicine* 14.4, pp. 270–275. DOI: 10.1177/036354658601400405.
- Barber, John G., Andrew M. Handorf, Tyler J. Allee, and Wan-Ju Li (2011). “Braided nanofibrous scaffold for tendon and ligament tissue engineering”. In: *Tissue Engineering Part A* 19.11-12, pp. 1265–1274. DOI: 10.1089/ten.tea.2010.0538.
- Baro, Vincent J, Edward D Bonnevie, Xiaohan Lai, Christopher Price, David L Burris, and Liyun Wang (2012). “Functional characterization of normal and degraded bovine meniscus: rate-dependent indentation and friction studies”. In: *Bone* 51.2, pp. 232–240. DOI: 10.1016/j.bone.2012.03.009.
- Bass, E. C., F. A. Ashford, M. R. Segal, and J. C. Lotz (2004). “Biaxial testing of human annulus fibrosus and its implications for a constitutive formulation”. In: *Annals of Biomedical Engineering* 32.9, pp. 1231–1242. DOI: 10.1114/B:ABME.0000039357.70905.94.
- Beatty, Mark W, Rebecca H Hohl, Jeffrey C Nickel, Laura R Iwasaki, and Ramana M Pidaparti (2008). “Mode I and Mode III fractures in intermediate zone of full-thickness porcine temporomandibular joint discs”. In: *Annals of Biomedical Engineering* 36.5, pp. 801–812. DOI: 10.1007/s10439-008-9436-9.
- Bedi, Asheesh, Natalie H Kelly, Michael Baad, Alice J S Fox, Robert H Brophy, Russell F Warren, and Suzanne A Maher (2010). “Dynamic contact mechanics of the medial meniscus as a function of radial tear, repair, and partial meniscectomy”. In: *The Journal of Bone and Joint Surgery* 92.6, pp. 1398–1408. DOI: 10.2106/JBJS.I.00539.

- Bellabarba, C., C. A. Bush-Joseph, and B. R. Bach (1997). "Patterns of meniscal injury in the anterior cruciate-deficient knee: a review of the literature". In: *American Journal of Orthopedics* 26.1, pp. 18–23.
- Berthiaume, M.-J., J.-P. Raynauld, J. Martel-Pelletier, F. Labonté, G. Beaudoin, D. A. Bloch, D. Choquette, B. Haraoui, R. D. Altman, M. Hochberg, J. M. Meyer, G. A. Cline, and J.-P. Pelletier (2005). "Meniscal tear and extrusion are strongly associated with progression of symptomatic knee osteoarthritis as assessed by quantitative magnetic resonance imaging". In: *Annals of the Rheumatic Diseases* 64.4, pp. 556–563. DOI: 10.1136/ard.2004.023796.
- Besier, T. F., D. G. Lloyd, J. L. Cochrane, and T. R. Ackland (2001). "External loading of the knee joint during running and cutting maneuvers". In: *Medicine and Science in Sports and Exercise* 33.7, pp. 1168–1175.
- Billinghurst, R. C., L. Dahlberg, M. Ionescu, A. Reiner, R. Bourne, C. Rorabeck, P. Mitchell, J. Hambor, O. Diekmann, H. Tschesche, J. Chen, H. Van Wart, and A. R. Poole (1997). "Enhanced cleavage of type II collagen by collagenases in osteoarthritic articular cartilage". In: *The Journal of Clinical Investigation* 99.7, pp. 1534–1545. DOI: 10.1172/JCI119316.
- Bosch, G, M C Lameris, A J M van den Belt, A Barneveld, and P R van Weeren (2010). "The propagation of induced tendon lesions in the equine superficial digital flexor tendon: an ex vivo study". In: *Equine Veterinary Journal* 42.5, pp. 407–411. DOI: 10.1111/j.2042-3306.2010.00099.x.
- Bowser, J. E., S. H. Elder, A. M. Rashmir-Raven, and C. E. Swiderski (2011). "A cryogenic clamping technique that facilitates ultimate tensile strength determinations in tendons and ligaments". In: *Veterinary and Comparative Orthopaedics and Traumatology* 24.5, pp. 370–373. DOI: 10.3415/VCOOT-10-09-0128.
- Boyle, John J., Maiko Kume, Matthew A. Wyczalkowski, Larry A. Taber, Robert B. Pless, Younan Xia, Guy M. Genin, and Stavros Thomopoulos (2014). "Simple and accurate methods for quantifying deformation, disruption, and development in biological tissues". In: *Journal of The Royal Society Interface* 11.100, p. 20140685. DOI: 10.1098/rsif.2014.0685.
- Bulgheroni, Erica, Alberto Grassi, Paolo Bulgheroni, Giulio Maria Marcheggiani Muccioli, Stefano Zaffagnini, and Maurilio Marcacci (2015). "Long-term outcomes of medial CMI implant versus partial medial meniscectomy in patients with concomitant ACL reconstruction". In: *Knee Surgery, Sports Traumatology, Arthroscopy* 23.11, pp. 3221–3227. DOI: 10.1007/s00167-014-3136-9.
- Bullough, P. G., L. Munuera, J. Murphy, and A. M. Weinstein (1970). "The strength of the menisci of the knee as it relates to their fine structure". In: *The Journal of Bone and Joint Surgery. British Volume* 52.3, pp. 564–567.
- Burk, D. L., M. K. Dalinka, E. Kanal, M. L. Schiebler, E. K. Cohen, R. J. Prorok, W. B. Gefter, and H. Y. Kressel (1988). "Meniscal and ganglion cysts of the knee: MR evaluation". In: *American Journal of Roentgenology* 150.2, pp. 331–336. DOI: 10.2214/ajr.150.2.331.

- Bursa, Jiri and Miroslav Zemanek (2008). "Evaluation of biaxial tension tests of soft tissues". In: *Studies in Health Technology and Informatics* 133, pp. 45–55.
- Bursac, Predrag, Amanda York, Paulette Kuznia, Lauren M Brown, and Steven P Arnoczky (2009). "Influence of donor age on the biomechanical and biochemical properties of human meniscal allografts". In: *The American Journal of Sports Medicine* 37.5, pp. 884–889. DOI: 10.1177/0363546508330140.
- Campbell, S E, T G Sanders, and W B Morrison (2001). "MR imaging of meniscal cysts: incidence, location, and clinical significance". In: *American Journal of Roentgenology* 177.2, pp. 409–413. DOI: 10.2214/ajr.177.2.1770409.
- Cheng, Vinton W. T. and Hazel R. C. Screen (2007). "The micro-structural strain response of tendon". In: *Journal of Materials Science* 42.21, pp. 8957–8965. DOI: 10.1007/s10853-007-1653-3.
- Cheung, H S (1987). "Distribution of type I, II, III and V in the pepsin solubilized collagens in bovine menisci". In: *Connective Tissue Research* 16.4, pp. 343–356.
- Chia, Helena N. and M. L. Hull (2008). "Compressive moduli of the human medial meniscus in the axial and radial directions at equilibrium and at a physiological strain rate". In: *Journal of Orthopaedic Research* 26.7, pp. 951–956. DOI: 10.1002/jor.20573.
- Chin-Purcell, Michele V. and Jack L. Lewis (1996). "Fracture of Articular Cartilage". In: *Journal of Biomechanical Engineering* 118.4, p. 545. DOI: 10.1115/1.2796042.
- Cohen, Moises, Joicemar Tarouco Amaro, Benno Ejnisman, Rogério Teixeira Carvalho, Kleber Kodi Nakano, Maria Stella Peccin, Rogério Teixeira, Cristiano F. S. Laurino, and Rene Jorge Abdalla (2007). "Anterior cruciate ligament reconstruction after 10 to 15 years: association between meniscectomy and osteoarthritis". In: *Arthroscopy: The Journal of Arthroscopic & Related Surgery* 23.6, pp. 629–634. DOI: 10.1016/j.arthro.2007.03.094.
- Cooper, D. E., S. P. Arnoczky, and R. F. Warren (1990). "Arthroscopic meniscal repair". In: *Clinics in Sports Medicine* 9.3, pp. 589–607.
- Corea, J. R., M. Moussa, and A. al Othman (1994). "McMurray's test tested". In: *Knee Surgery, Sports Traumatology, Arthroscopy* 2.2, pp. 70–72.
- Danso, E. K., J. T. J. Honkanen, S. Saarakkala, and R. K. Korhonen (2014). "Comparison of nonlinear mechanical properties of bovine articular cartilage and meniscus". In: *Journal of Biomechanics* 47.1, pp. 200–206. DOI: 10.1016/j.jbiomech.2013.09.015.
- De Baere, I., W. Van Paepegem, M. Quaresimin, and J. Degrieck (2011). "On the tension–tension fatigue behaviour of a carbon reinforced thermoplastic part I: limitations of the ASTM D3039/D3479 standard". In: *Polymer Testing* 30.6, pp. 625–632. DOI: 10.1016/j.polymertesting.2011.05.004.
- Drosos, G I and J L Pozo (2004). "The causes and mechanisms of meniscal injuries in the sporting and non-sporting environment in an unselected population". In: *The Knee* 11.2, pp. 143–149. DOI: 10.1016/S0968-0160(03)00105-4.
- Duchman, Kyle R., Robert W. Westermann, Kurt P. Spindler, Emily K. Reinke, Laura J. Huston, Annunziato Amendola, MOON Knee Group, and Brian R. Wolf (2015). "The fate of meniscus tears left in situ at the time of anterior cruciate ligament reconstruction: a 6-year

- follow-up study from the MOON cohort”. In: *The American Journal of Sports Medicine*. DOI: 10.1177/0363546515604622.
- Duenwald-Kuehl, Sarah, Jaclyn Kondratko, Roderic S Lakes, and Jr Vanderby Ray (2012). “Damage mechanics of porcine flexor tendon: mechanical evaluation and modeling”. In: *Annals of Biomedical Engineering* 40.8, pp. 1692–1707. DOI: 10.1007/s10439-012-0538-z.
- Dunn, Warren R., Brian R. Wolf, Annunziato Amendola, Jack T. Andrish, Christopher Kaeding, Robert G. Marx, Eric C. McCarty, Richard D. Parker, Rick W. Wright, and Kurt P. Spindler (2004). “Multirater agreement of arthroscopic meniscal lesions”. In: *The American Journal of Sports Medicine* 32.8, pp. 1937–1940.
- Ebara, S, J C Iatridis, L A Setton, R J Foster, V C Mow, and M Weidenbaum (1996). “Tensile properties of nondegenerate human lumbar annulus fibrosus”. In: *Spine* 21.4, pp. 452–461.
- Ellman, Michael B., Christopher M. LaPrade, Sean D. Smith, Matthew T. Rasmussen, Lars Engbretsen, Coen A. Wijdicks, and Robert F. LaPrade (2014). “Structural properties of the meniscal roots”. In: *The American Journal of Sports Medicine* 42.8, pp. 1881–1887. DOI: 10.1177/0363546514531730.
- Elsner, Jonathan J., Sigal Portnoy, Gal Zur, Farshid Guilak, Avi Shterling, and Eran Linder-Ganz (2010). “Design of a free-floating polycarbonate-urethane meniscal implant using finite element modeling and experimental validation”. In: *Journal of Biomechanical Engineering* 132.9, p. 095001. DOI: 10.1115/1.4001892.
- Englund, Martin, Ali Guermazi, Daniel Gale, David J Hunter, Piran Aliabadi, Margaret Clancy, and David T Felson (2008). “Incidental meniscal findings on knee MRI in middle-aged and elderly persons”. In: *The New England Journal of Medicine* 359.11, pp. 1108–1115. DOI: 10.1056/NEJMoa0800777.
- Englund, Martin, Frank W Roemer, Daichi Hayashi, Michel D Crema, and Ali Guermazi (2012). “Meniscus pathology, osteoarthritis and the treatment controversy”. In: *Nature Reviews Rheumatology* 8.7, pp. 412–419. DOI: 10.1038/nrrheum.2012.69.
- Espejo-Baena, Alejandro, Francisco Ezquerro, Ana Pérez de la Blanca, José Serrano-Fernandez, Fernando Nadal, and Elvira Montañez-Heredia (2006). “Comparison of initial mechanical properties of 4 hamstring graft femoral fixation systems using nonpermanent hardware for anterior cruciate ligament reconstruction: an in vitro animal study”. In: *Arthroscopy: The Journal of Arthroscopic & Related Surgery* 22.4, pp. 433–440. DOI: 10.1016/j.arthro.2005.09.021.
- Favata, Michele (2006). “Scarless healing in the fetus: Implications and strategies for postnatal tendon repair”. PhD thesis. University of Pennsylvania.
- Feucht, Matthias J, Sebastian Bigdon, Gerrit Bode, Gian M Salzmann, David Dovi-Akue, Norbert P Südkamp, and Philipp Niemeyer (2015). “Associated tears of the lateral meniscus in anterior cruciate ligament injuries: risk factors for different tear patterns”. In: *Journal of Orthopaedic Surgery and Research* 10.34. DOI: 10.1186/s13018-015-0184-x.
- Fisher, Matthew B., Elizabeth A. Henning, Nicole Söegaard, Marc Bostrom, John L. Esterhai, and Robert L. Mauck (2015). “Engineering meniscus structure and function via multi-

- layered mesenchymal stem cell-seeded nanofibrous scaffolds”. In: *Journal of Biomechanics* 48.8, pp. 1412–1419. DOI: 10.1016/j.jbiomech.2015.02.036.
- Fithian, D C, M A Kelly, and V C Mow (1990). “Material properties and structure–function relationships in the menisci”. In: *Clinical Orthopaedics and Related Research* 252, pp. 19–31.
- Fitzgibbons, R. E. and K. D. Shelbourne (1995). ““Aggressive” nontreatment of lateral meniscal tears seen during anterior cruciate ligament reconstruction”. In: *The American Journal of Sports Medicine* 23.2, pp. 156–159.
- Flachsmann, R., M. Kistler, A. Rentzios, and N. D. Broom (2006). “Influence of an initiating microsplit on the resistance to compression-induced rupture of the articular surface”. In: *Connective Tissue Research* 47.2, pp. 77–84. DOI: 10.1080/03008200600584090.
- Forkel, Philipp, Mirco Herbort, Frederike Sprenger, Sebastian Metzloff, Michael Raschke, and Wolf Petersen (2014). “The biomechanical effect of a lateral meniscus posterior root tear with and without damage to the meniscofemoral ligament: efficacy of different repair techniques”. In: *Arthroscopy: The Journal of Arthroscopic & Related Surgery* 30.7, pp. 833–840. DOI: 10.1016/j.arthro.2014.02.040.
- Fox, Alice J.S., Florian Wanivenhaus, Alissa J. Burge, Russell F. Warren, and Scott A. Rodeo (2015). “The human meniscus: A review of anatomy, function, injury, and advances in treatment”. In: *Clinical Anatomy* 28.2, pp. 269–287. DOI: 10.1002/ca.22456.
- Freutel, M., N. B. Scholz, A. M. Seitz, A. Ignatius, and Lutz Dürselen (2015). “Mechanical properties and morphological analysis of the transitional zone between meniscal body and ligamentous meniscal attachments”. In: *Journal of Biomechanics* 48.8, pp. 1350–1355. DOI: 10.1016/j.jbiomech.2015.03.003.
- Freutel, Maren, Andreas M. Seitz, Fabio Galbusera, Axel Bornstedt, Volker Rasche, Melissa L. Knothe Tate, Anita Ignatius, and Lutz Dürselen (2014). “Medial meniscal displacement and strain in three dimensions under compressive loads: MR assessment”. In: *Journal of Magnetic Resonance Imaging* 40.5, pp. 1181–1188. DOI: 10.1002/jmri.24461.
- Fukubayashi, T. and H. Kurosawa (1980). “The contact area and pressure distribution pattern of the knee. A study of normal and osteoarthrotic knee joints”. In: *Acta Orthopaedica Scandinavica* 51.6, pp. 871–879.
- Gao, Yingxin, Alan S. Wineman, and Anthony M. Waas (2008). “Mechanics of muscle injury induced by lengthening contraction”. In: *Annals of Biomedical Engineering* 36.10, p. 1615. DOI: 10.1007/s10439-008-9547-3.
- Gasser, T Christian and Gerhard A Holzapfel (2007). “Modeling plaque fissuring and dissection during balloon angioplasty intervention”. In: *Annals of Biomedical Engineering* 35.5, pp. 711–723. DOI: 10.1007/s10439-007-9258-1.
- Goh, K. L., D. F. Holmes, Y. Lu, P. P. Purslow, K. E. Kadler, D. Bechet, and T. J. Wess (2012). “Bimodal collagen fibril diameter distributions direct age-related variations in tendon resilience and resistance to rupture”. In: *Journal of Applied Physiology* 113.6, pp. 878–888. DOI: 10.1152/jappphysiol.00258.2012.

- Grantab, Rassin and Vivek B. Shenoy (2011). “Location- and orientation-dependent progressive crack propagation in cylindrical graphite electrode particles”. In: *Journal of the Electrochemical Society* 158.8, A948–A954. DOI: 10.1149/1.3601878.
- (2012). “Pressure-gradient dependent diffusion and crack propagation in lithiated silicon nanowires”. In: *Journal of the Electrochemical Society* 159.5, A584–A591. DOI: 10.1149/2.072205jes.
- Green, T P, M A Adams, and P Dolan (1993). “Tensile properties of the annulus fibrosus II. Ultimate tensile strength and fatigue life”. In: *European Spine Journal* 2.4, pp. 209–214.
- Greis, Patrick E., Davide D. Bardana, Michael C. Holmstrom, and Robert T. Burks (2002). “Meniscal injury I: basic science and evaluation”. In: *Journal of the American Academy of Orthopaedic Surgeons* 10.3, pp. 168–176.
- Haefeli, Mathias, Fabian Kalberer, Daniel Saegesser, Andreas G. Nerlich, Norbert Boos, and Günther Paesold (2006). “The course of macroscopic degeneration in the human lumbar intervertebral disc”. In: *Spine* 31.14, pp. 1522–1531. DOI: 10.1097/01.brs.0000222032.52336.8e.
- Hammer, Niels, Uwe Lingslebe, Gabriela Aust, Thomas L. Milani, Carsten Hädrich, and Hanno Steinke (2012). “Ultimate stress and age-dependent deformation characteristics of the iliotibial tract”. In: *Journal of the Mechanical Behavior of Biomedical Materials* 16, pp. 81–86. DOI: 10.1016/j.jmbbm.2012.04.025.
- Hangody, Gy, G. Pánics, G. Szebényi, R. Kiss, L. Hangody, and K. Pap (2016). “Pitfalls during biomechanical testing – evaluation of different fixation methods for measuring tendons endurance properties”. In: *Acta Physiologica Hungarica* 103.1, pp. 86–93. DOI: 10.1556/036.103.2016.1.8.
- Hardin, G. T., J. Farr, and B. R. Bach (1992). “Meniscal tears: diagnosis, evaluation, and treatment”. In: *Orthopaedic Review* 21.11, pp. 1311–1317.
- Hariharan, J S, E Diao, O Soejima, and J C Lotz (1997). “Partial lacerations of human digital flexor tendons: a biomechanical analysis”. In: *The Journal of Hand Surgery* 22.6, pp. 1011–1015. DOI: 10.1016/S0363-5023(97)80040-8.
- Hauch, Karen N, Diego F Villegas, and Tammy L Haut Donahue (2010). “Geometry, time-dependent and failure properties of human meniscal attachments”. In: *Journal of Biomechanics* 43.3, pp. 463–468. DOI: 10.1016/j.jbiomech.2009.09.043.
- Haughton, V. M., T. A. Schmidt, K. Keele, H. S. An, and T. H. Lim (2000). “Flexibility of lumbar spinal motion segments correlated to type of tears in the annulus fibrosus”. In: *Journal of Neurosurgery* 92.1 Suppl, pp. 81–86.
- Hellio Le Graverand, M. P., Y. Ou, T. Schield-Yee, L. Barclay, D. Hart, T. Natsume, and J. B. Rattner (2001). “The cells of the rabbit meniscus: their arrangement, interrelationship, morphological variations and cytoarchitecture”. In: *Journal of Anatomy* 198.Pt 5, pp. 525–535.
- Holmes, M.H. and V.C. Mow (1990). “The nonlinear characteristics of soft gels and hydrated connective tissues in ultrafiltration”. In: *Journal of Biomechanics* 23.11, pp. 1145–1156. DOI: 16/0021-9290(90)90007-P.

- Holzzapfel, G. A., C. A. J. Schulze-Bauer, G. Feigl, and P. Regitnig (2005). “Single lamellar mechanics of the human lumbar annulus fibrosus”. In: *Biomechanics and Modeling in Mechanobiology* 3.3, pp. 125–140. DOI: 10.1007/s10237-004-0053-8.
- Horgan, C. O. and J. G. Simmonds (1994). “Saint-Venant end effects in composite structures”. In: *Composites Engineering* 4.3, pp. 279–286.
- Hui, C.-Y., A. Jagota, S. J. Bennison, and J. D. Londono (2003). “Crack blunting and the strength of soft elastic solids”. In: *Proceedings of the Royal Society of London Series A* 459.2034, pp. 1489–1516. DOI: 10.1098/rspa.2002.1057.
- Isaac, Daniel I, Eric G Meyer, and Roger C Haut (2008). “Chondrocyte damage and contact pressures following impact on the rabbit tibiofemoral joint”. In: *Journal of Biomechanical Engineering* 130.4, p. 041018. DOI: 10.1115/1.2948403.
- (2010). “Development of a traumatic anterior cruciate ligament and meniscal rupture model with a pilot in vivo study”. In: *Journal of Biomechanical Engineering* 132.6, p. 064501. DOI: 10.1115/1.4001111.
- Jacobs, Nathan T., Daniel H. Cortes, John M. Peloquin, Edward J. Vresilovic, and Dawn M. Elliott (2014). “Validation and application of an intervertebral disc finite element model utilizing independently constructed tissue-level constitutive formulations that are nonlinear, anisotropic, and time-dependent”. In: *Journal of Biomechanics* 47.11, pp. 2540–2546. DOI: 10.1016/j.jbiomech.2014.06.008.
- Jacobs, Nathan T, Daniel H Cortes, Edward J Vresilovic, and Dawn M Elliott (2013). “Biaxial tension of fibrous tissue: using finite element methods to address experimental challenges arising from boundary conditions and anisotropy”. In: *Journal of Biomechanical Engineering* 135.2, p. 021004. DOI: 10.1115/1.4023503.
- Jacobs, Nathan T, Lachlan J Smith, Woojin M Han, Jeffrey Morelli, Jonathon H Yoder, and Dawn M Elliott (2011). “Effect of orientation and targeted extracellular matrix degradation on the shear mechanical properties of the annulus fibrosus”. In: *Journal of the Mechanical Behavior of Biomedical Materials* 4.8, pp. 1611–1619. DOI: 10.1016/j.jmbbm.2011.03.016.
- Jansen, Margot O. and H. H. C. M. Savelberg (1994). “Stress and strain of equine tendons of the forelimb at failure”. In: *Equine Veterinary Journal* 26.S17, pp. 57–60. DOI: 10.1111/j.2042-3306.1994.tb04875.x.
- Janssen, M., J. Zuidema, and R. J. H. Wanhill (2002). *Fracture Mechanics*. 2nd ed. Delft, The Netherlands: VSSD.
- Jester, James V., Moritz Winkler, Bryan E. Jester, Chyong Nien, Dongyul Chai, and Donald J. Brown (2010). “Evaluating corneal collagen organization using high-resolution nonlinear optical microscopy”. In: *Eye & Contact Lens* 36.5, pp. 260–264. DOI: 10.1097/ICL.0b013e3181ee8992.
- Jones, Eric, Travis Oliphant, Pearu Peterson, et al. (2001). *SciPy: open source scientific tools for Python*. <http://www.scipy.org/>.
- Jones, Matthew C., Frederick A. Rueggeberg, Hunter A. Faircloth, Aaron J. Cunningham, Carrie M. Bush, John D. Prosser, Jennifer L. Waller, Gregory N. Postma, and Paul M. Weinberger

- (2014). “Defining the biomechanical properties of the rabbit trachea”. In: *The Laryngoscope* 124.10, pp. 2352–2358. DOI: 10.1002/lary.24739.
- Jung, Kwang Am, Su Chan Lee, Seung Hyun Hwang, Ki Hyuk Yang, Dong Hoon Kim, Jin Hee Sohn, Su Jeong Song, and David John Hunter (2010). “High frequency of meniscal hypertrophy in persons with advanced varus knee osteoarthritis”. In: *Rheumatology International* 30.10, pp. 1325–1333. DOI: 10.1007/s00296-009-1153-7.
- Kahn, Cyril J F, Dominique Dumas, Elmira Arab-Tehrany, Vanessa Marie, Nguyen Tran, Xiong Wang, and Franck Cleymand (2013). “Structural and mechanical multi-scale characterization of white New-Zealand rabbit Achilles tendon”. In: *Journal of the Mechanical Behavior of Biomedical Materials* 26, pp. 81–89. DOI: 10.1016/j.jmbbm.2013.05.028.
- Kawamura, Sumito, Kristin Lotito, and Scott A. Rodeo (2003). “Biomechanics and healing response of the meniscus”. In: *Operative Techniques in Sports Medicine* 11.2, pp. 68–76. DOI: 10.1053/otsm.2003.35899.
- Kelly, M. A., D. C. Fithian, K. Y. Chern, and V. C. Mow (1990). “Structure and function of the meniscus: basic and clinical implications”. In: *Biomechanics of Diarthrodial Joints*. Ed. by Anthony Ratcliffe, Savio L.-Y. Woo, and Van C. Mow. Springer New York, pp. 191–211.
- Kettelkamp, Donald B. and Allen W. Jacobs (1972). “Tibiofemoral Contact Area-Determination and Implications”. In: *The Journal of Bone and Joint Surgery. American Volume* 54.2, pp. 349–356.
- Kim, Y (2000). “Prediction of peripheral tears in the anulus of the intervertebral disc”. In: *Spine* 25.14, pp. 1771–1774.
- Kisiday, John D, Eric J Vanderploeg, C Wayne McIlwraith, Alan J Grodzinsky, and David D Frisbie (2010). “Mechanical injury of explants from the articulating surface of the inner meniscus”. In: *Archives of Biochemistry and Biophysics* 494.2, pp. 138–144. DOI: 10.1016/j.abb.2009.11.022.
- Kluczynski, Melissa A., John M. Marzo, and Leslie J. Bisson (2013). “Factors associated with meniscal tears and chondral lesions in patients undergoing anterior cruciate ligament reconstruction: a prospective study”. In: *The American Journal of Sports Medicine* 41.12, pp. 2759–2765. DOI: 10.1177/0363546513503448.
- Koh, C.T., D.G.T. Strange, K. Tonsomboon, and M.L. Oyen (2013). “Failure mechanisms in fibrous scaffolds”. In: *Acta Biomaterialia* 9.7, pp. 7326–7334. DOI: 10.1016/j.actbio.2013.02.046.
- Kondratko, Jaclyn, Sarah Duenwald-Kuehl, Roderic Lakes, and Ray Vanderby (2012). “Mechanical compromise of partially lacerated flexor tendons”. In: *Journal of Biomechanical Engineering* 135.1, pp. 011001–011001. DOI: 10.1115/1.4023092.
- Kondratko-Mittnacht, Jaclyn, Sarah Duenwald-Kuehl, Roderic Lakes, and Ray Vanderby (2015). “Shear load transfer in high and low stress tendons”. In: *Journal of the Mechanical Behavior of Biomedical Materials* 45C, pp. 109–120. DOI: 10.1016/j.jmbbm.2015.01.021.
- Koombua, Kittisak, Ramana M Pidaparti, and Mark W Beatty (2006). “Fracture toughness estimation for the TMJ disc”. In: *Journal of Biomedical Materials Research Part A* 79.3, pp. 566–573. DOI: 10.1002/jbm.a.30807.

- Koop, Brendan E. and Jack L. Lewis (2003). "A model of fracture testing of soft viscoelastic tissues". In: *Journal of Biomechanics* 36.4, pp. 605–608. DOI: 10 . 1016 / S0021 – 9290 (02) 00435–9.
- Kurosawa, H, T Fukubayashi, and H Nakajima (1980). "Load-bearing mode of the knee joint: physical behavior of the knee joint with or without menisci". In: *Clinical Orthopaedics and Related Research* 149, pp. 283–290.
- Laberge, Marc A, Thomas Baum, Warapat Virayavanich, Lorenzo Nardo, M C Nevitt, J Lynch, C E McCulloch, and Thomas M Link (2012). "Obesity increases the prevalence and severity of focal knee abnormalities diagnosed using 3T MRI in middle-aged subjects—data from the Osteoarthritis Initiative". In: *Skeletal Radiology* 41.6, pp. 633–641. DOI: 10 . 1007 / s00256–011–1259–3.
- LaCroix, Andrew S., Sarah E. Duenwald-Kuehl, Roderic S. Lakes, and Ray Vanderby (2013). "Relationship between tendon stiffness and failure: a metaanalysis". In: *Journal of Applied Physiology* 115.1, pp. 43–51. DOI: 10 . 1152 / japplphysiol . 01449 . 2012.
- Lanir, Y (1983). "Constitutive equations for fibrous connective tissues". In: *Journal of biomechanics* 16.1, pp. 1–12.
- LaPrade, Christopher M., Kyle S. Jansson, Grant Dornan, Sean D. Smith, Coen A. Wijdicks, and Robert F. LaPrade (2014). "Altered tibiofemoral contact mechanics due to lateral meniscus posterior horn root avulsions and radial tears can be restored with in situ pull-out suture repairs". In: *The Journal of Bone and Joint Surgery. American Volume* 96.6, pp. 471–479. DOI: 10 . 2106 / JBJS . L . 01252.
- Lechner, K, M L Hull, and S M Howell (2000). "Is the circumferential tensile modulus within a human medial meniscus affected by the test sample location and cross-sectional area?" In: *Journal of Orthopaedic Research* 18.6, pp. 945–951. DOI: 10 . 1002 / jor . 1100180614.
- Lee, Sang-Heon, Richard Derby, Yung Chen, Kwan Sik Seo, and Mi Jung Kim (2004). "In vitro measurement of pressure in intervertebral discs and annulus fibrosus with and without annular tears during discography". In: *The Spine Journal* 4.6, pp. 614–618. DOI: 10 . 1016 / j . spinee . 2004 . 03 . 021.
- Lee, Stephen J, Kirk J Aadalén, Prasanna Malaviya, Eric P Lorenz, Jennifer K Hayden, Jack Farr, Richard W Kang, and Brian J Cole (2006). "Tibiofemoral contact mechanics after serial medial meniscectomies in the human cadaveric knee". In: *The American Journal of Sports Medicine* 34.8, pp. 1334–1344. DOI: 10 . 1177 / 0363546506286786.
- Lento, P H and V Akuthota (2000). "Meniscal injuries: A critical review". In: *Journal of back and musculoskeletal rehabilitation* 15.2, pp. 55–62.
- LeRoux, Michelle A and Lori A Setton (2002). "Experimental and biphasic FEM determinations of the material properties and hydraulic permeability of the meniscus in tension". In: *Journal of Biomechanical Engineering* 124.3, pp. 315–321.
- Levy, I. M., P. A. Torzilli, and R. F. Warren (1982). "The effect of medial meniscectomy on anterior-posterior motion of the knee". In: *The Journal of Bone and Joint Surgery. American Volume* 64.6, pp. 883–888.

- Liggins, A. B., R. Shemerluk, R. Hardie, and J. B. Finlay (1992). "Technique for the application of physiological loading to soft tissue in vitro". In: *Journal of Biomedical Engineering* 14.5, pp. 440–441.
- Lohmander, L. Stefan, P. Martin Englund, Ludvig L. Dahl, and Ewa M. Roos (2007). "The long-term consequence of anterior cruciate ligament and meniscus injuries: osteoarthritis". In: *The American Journal of Sports Medicine* 35.10, pp. 1756–1769. DOI: 10.1177/0363546507307396.
- Maffulli, Nicola, Umile Giuseppe Longo, Stefano Campi, and Vincenzo Denaro (2010). "Meniscal tears". In: *Open Access Journal of Sports Medicine* 1, pp. 45–54.
- Magnussen, Robert A., Alfred A. Mansour, James L. Carey, and Kurt P. Spindler (2009). "Meniscus status at anterior cruciate ligament reconstruction associated with radiographic signs of osteoarthritis at 5- to 10-year follow-up: a systematic review". In: *The Journal of Knee Surgery* 22.4, pp. 347–357.
- Makris, Eleftherios A., Pasha Hadidi, and Kyriacos A. Athanasiou (2011). "The knee meniscus: structure-function, pathophysiology, current repair techniques, and prospects for regeneration". In: *Biomaterials* 32.30, pp. 7411–7431. DOI: 10.1016/j.biomaterials.2011.06.037.
- Mauck, Robert L. and Jason A. Burdick (2015). "From repair to regeneration: biomaterials to reprogram the meniscus wound microenvironment". In: *Annals of Biomedical Engineering* 43.3, pp. 529–542. DOI: 10.1007/s10439-015-1249-z.
- Mazzocca, Augustus D, Lina M Rincon, Robert W O'Connor, Elifho Obopilwe, Matthew Andersen, Lauren Geaney, and Robert A Arciero (2008). "Intra-articular partial-thickness rotator cuff tears: analysis of injured and repaired strain behavior". In: *The American Journal of Sports Medicine* 36.1, pp. 110–116. DOI: 10.1177/0363546507307502.
- McCarthy, D M, D M Tramaglino, S S Chan, C C Schmidt, D G Sotereanos, and J H Herndon (1995). "Effect of partial laceration on the structural properties of the canine FDP tendon: an in vitro study". In: *The Journal of Hand Surgery* 20.5, pp. 795–800. DOI: 10.1016/S0363-5023(05)80434-4.
- McDermott, I. D. and A. A. Amis (2006). "The consequences of meniscectomy". In: *The Journal of Bone and Joint Surgery. British Volume* 88.12, pp. 1549–1556. DOI: 10.1302/0301-620X.88B12.18140.
- McDermott, Ian Douglas (2006). "Meniscal tears". In: *Current Orthopaedics* 20.2, pp. 85–94. DOI: 10.1016/j.cuor.2006.02.010.
- McNally, D. S. and M. A. Adams (1992). "Internal intervertebral disc mechanics as revealed by stress profilometry". In: *Spine* 17.1, pp. 66–73.
- Miles, J. W., W. A. Grana, D. Egle, K. W. Min, and J. Chitwood (1992). "The effect of anabolic steroids on the biomechanical and histological properties of rat tendon". In: *The Journal of Bone and Joint Surgery. American Volume* 74.3, pp. 411–422.
- Miller, Ross H., W. Brent Edwards, and Kevin J. Deluzio (2015). "Energy expended and knee joint load accumulated when walking, running, or standing for the same amount of time". In: *Gait & Posture* 41.1, pp. 326–328. DOI: 10.1016/j.gaitpost.2014.10.009.

- Mononen, Mika E., Jukka S. Jurvelin, and Rami K. Korhonen (2013). “Effects of radial tears and partial meniscectomy of lateral meniscus on the knee joint mechanics during the stance phase of the gait cycle—a 3D finite element study”. In: *Journal of Orthopaedic Research* 31.8, pp. 1208–1217. DOI: 10.1002/jor.22358.
- (2015). “Implementation of a gait cycle loading into healthy and meniscectomised knee joint models with fibril-reinforced articular cartilage”. In: *Computer Methods in Biomechanics and Biomedical Engineering* 18.2, pp. 141–152. DOI: 10.1080/10255842.2013.783575.
- Morrison, J. B. (1969). “Function of the knee joint in various activities”. In: *Biomedical Engineering* 4.12, pp. 573–580.
- Motavalli, Mostafa, G. Adam Whitney, James E. Dennis, and Joseph M. Mansour (2013). “Investigating a continuous shear strain function for depth-dependent properties of native and tissue engineering cartilage using pixel-size data”. In: *Journal of the Mechanical Behavior of Biomedical Materials* 28, pp. 62–70. DOI: 10.1016/j.jmbbm.2013.07.019.
- Mow, Van C, Wei Yong Gu, and Faye Hui Chen (2005). “Structure and function of articular cartilage and meniscus”. In: *Basic Orthopaedic Biomechanics & Mechano-Biology*. 3rd ed. Philadelphia: Lippincott Williams & Wilkins, pp. 181–258.
- Nerurkar, Nandan L., Woojin Han, Robert L. Mauck, and Dawn M. Elliott (2011). “Homologous structure-function relationships between native fibrocartilage and tissue engineered from MSC-seeded nanofibrous scaffolds”. In: *Biomaterials* 32.2, pp. 461–468. DOI: 10.1016/j.biomaterials.2010.09.015.
- Ng, B H, S M Chou, and V Krishna (2005). “The influence of gripping techniques on the tensile properties of tendons”. In: *Proceedings of the Institution of Mechanical Engineers. Part H, Journal of Engineering in Medicine* 219.5, pp. 349–354.
- Oberlander, MA and JA Pryde (1994). “Meniscal injuries”. In: *The Hughston Clinic Sports Medicine Book*. Ed. by CL Baker. Media, PA: Williams and Wilkins, pp. 465–472.
- O’Connell, Grace D, Sounok Sen, and Dawn M Elliott (2012). “Human annulus fibrosus material properties from biaxial testing and constitutive modeling are altered with degeneration”. In: *Biomechanics and Modeling in Mechanobiology* 11.3-4, pp. 493–503. DOI: 10.1007/s10237-011-0328-9.
- Ode, Gabriella E., Geoffrey S. Van Thiel, Samuel A. McArthur, Justin Dishkin-Paset, Sue E. Leurgans, Elizabeth F. Shewman, Vincent M. Wang, and Brian J. Cole (2012). “Effects of serial sectioning and repair of radial tears in the lateral meniscus”. In: *The American Journal of Sports Medicine* 40.8, pp. 1863–1870. DOI: 10.1177/0363546512453291.
- Øiestad, Britt Elin, Lars Engebretsen, Kjersti Storheim, and May Arna Risberg (2009). “Knee osteoarthritis after anterior cruciate ligament injury: a systematic review”. In: *The American Journal of Sports Medicine* 37.7, pp. 1434–1443. DOI: 10.1177/0363546509338827.
- O’Keefe, Regis J, Joshua J Jacobs, Constance R Chu, and Thomas A Einhorn (2013). *Orthopaedic Basic Science Foundations of Clinical Practice*. Rosemont, IL: American Academy of Orthopaedic Surgeons.
- Oliveira Silva, Danilo de, Ronaldo Valdir Briani, Marcella Ferraz Pazzinato, Deisi Ferrari, Fernando Amâncio Aragão, and Fábio Mícolis de Azevedo (2015). “Reduced knee flexion

- is a possible cause of increased loading rates in individuals with patellofemoral pain”. In: *Clinical Biomechanics* 30.9, pp. 971–975. DOI: 10.1016/j.clinbiomech.2015.06.021.
- Osti, O L, B Vernon-Roberts, R Moore, and R D Fraser (1992). “Annular tears and disc degeneration in the lumbar spine: a post-mortem study of 135 discs”. In: *The Journal of Bone and Joint Surgery. British Volume* 74.5, pp. 678–682.
- Oyen-Tiesma, M and R F Cook (2001). “Technique for estimating fracture resistance of cultured neocartilage”. In: *Journal of Materials Science. Materials in Medicine* 12.4, pp. 327–332.
- Palmer, M.P., E.L. Abreu, A. Mastrangelo, and M.M. Murray (2009). “Injection temperature significantly affects in vitro and in vivo performance of collagen-platelet scaffolds”. In: *Journal of Orthopaedic Research* 27.7, pp. 964–971. DOI: 10.1002/jor.20804.
- Papageorgiou, C. D., J. E. Gil, A. Kanamori, J. A. Fenwick, S. L. Woo, and F. H. Fu (2001). “The biomechanical interdependence between the anterior cruciate ligament replacement graft and the medial meniscus”. In: *The American Journal of Sports Medicine* 29.2, pp. 226–231.
- Párraga Quiroga, J. M., P. Emans, W. Wilson, K. Ito, and C. C. van Donkelaar (2014). “Should a native depth-dependent distribution of human meniscus constitutive components be considered in FEA-models of the knee joint?” In: *Journal of the Mechanical Behavior of Biomedical Materials* 38, pp. 242–250. DOI: 10.1016/j.jmbbm.2014.03.005.
- Paul, Jonathan J., Kurt P. Spindler, Jack T. Andrish, Richard D. Parker, Michelle Secic, and John A. Bergfeld (2003). “Jumping versus nonjumping anterior cruciate ligament injuries: a comparison of pathology”. In: *Clinical Journal of Sport Medicine* 13.1, pp. 1–5.
- Paxton, E. Scott, Michael V. Stock, and Robert H. Brophy (2011). “Meniscal repair versus partial meniscectomy: a systematic review comparing reoperation rates and clinical outcomes”. In: *Arthroscopy: The Journal of Arthroscopic & Related Surgery* 27.9, pp. 1275–1288. DOI: 10.1016/j.arthro.2011.03.088.
- Pedersen, Roar R. (2006). “Imaging of intratendinous distribution of glucocorticosteroid in the treatment of Achilles tendinopathy. Pilot study of low-field magnetic resonance imaging correlated with ultrasound”. In: *Clinical and Experimental Rheumatology* 24.6, pp. 664–669.
- Peloquin, John M. and Dawn M. Elliott (2016). “A comparison of stress in cracked fibrous tissue specimens with varied crack location, loading, and orientation using finite element analysis”. In: *Journal of the Mechanical Behavior of Biomedical Materials* 57, pp. 260–268. DOI: 10.1016/j.jmbbm.2015.12.004.
- Peloquin, John M., Michael H. Santare, and Dawn M. Elliott (2016). “Advances in quantification of meniscus tensile mechanics including nonlinearity, yield, and failure”. In: *Journal of Biomechanical Engineering* 138.2, p. 021002. DOI: 10.1115/1.4032354.
- Peltier, A., T. Lording, L. Maubisson, R. Ballis, P. Neyret, and S. Lustig (2015). “The role of the meniscotibial ligament in posteromedial rotational knee stability”. In: *Knee Surgery, Sports Traumatology, Arthroscopy* 23.10, pp. 2967–2973. DOI: 10.1007/s00167-015-3751-0.

- Peña, E., B. Calvo, M.A. Martínez, D. Palanca, and M. Doblaré (2005). “Finite element analysis of the effect of meniscal tears and meniscectomies on human knee biomechanics”. In: *Clinical Biomechanics* 20.5, pp. 498–507. DOI: 10.1016/j.clinbiomech.2005.01.009.
- Peng, B., W. Wu, S. Hou, P. Li, C. Zhang, and Y. Yang (2005). “The pathogenesis of discogenic low back pain”. In: *The Journal of Bone and Joint Surgery. British Volume* 87.1, pp. 62–67.
- Petersen, W and B Tillmann (1998). “Collagenous fibril texture of the human knee joint menisci”. In: *Anatomy and Embryology* 197.4, pp. 317–324.
- Petty, Catherine A. and James H. Lubowitz (2011). “Does arthroscopic partial meniscectomy result in knee osteoarthritis? A systematic review with a minimum of 8 years’ follow-up”. In: *Arthroscopy: The Journal of Arthroscopic & Related Surgery* 27.3, pp. 419–424. DOI: 10.1016/j.arthro.2010.08.016.
- Poehling, G G, D S Ruch, and S J Chabon (1990). “The landscape of meniscal injuries”. In: *Clinics in Sports Medicine* 9.3, pp. 539–549.
- Polzer, Stanislav, T. Christian Gasser, Jiri Bursa, Robert Staffa, Robert Vlachovsky, Vojtech Man, and Pavel Skacel (2013). “Importance of material model in wall stress prediction in abdominal aortic aneurysms”. In: *Medical Engineering & Physics* 35.9, pp. 1282–1289. DOI: 10.1016/j.medengphy.2013.01.008.
- Powell, E. S., I. A. Trail, and J. Noble (1989). “Non-suture repair of tendons”. In: *Journal of Biomedical Engineering* 11.3, pp. 215–218.
- Pring, D. J., A. A. Amis, and R. R. Coombs (1985). “The mechanical properties of human flexor tendons in relation to artificial tendons”. In: *Journal of Hand Surgery* 10.3, pp. 331–336.
- Proctor, C S, M B Schmidt, R R Whipple, M A Kelly, and V C Mow (1989). “Material properties of the normal medial bovine meniscus”. In: *Journal of Orthopaedic Research* 7.6, pp. 771–782. DOI: 10.1002/jor.1100070602.
- Provenzano, Paolo P, Kei Hayashi, David N Kunz, Mark D Markel, and Jr Vanderby Ray (2002a). “Healing of subfailure ligament injury: comparison between immature and mature ligaments in a rat model”. In: *Journal of Orthopaedic Research* 20.5, pp. 975–983. DOI: 10.1016/S0736-0266(02)00036-0.
- Provenzano, Paolo P, Dennis Heisey, Kei Hayashi, Roderic Lakes, and Jr Vanderby Ray (2002b). “Subfailure damage in ligament: a structural and cellular evaluation”. In: *Journal of Applied Physiology* 92.1, pp. 362–371.
- Pujol, Nicolas and Philippe Beaufile (2009). “Healing results of meniscal tears left in situ during anterior cruciate ligament reconstruction: a review of clinical studies”. In: *Knee surgery, sports traumatology, arthroscopy: official journal of the ESSKA* 17.4, pp. 396–401. DOI: 10.1007/s00167-008-0711-y.
- Purslow, P. P. (1983a). “Measurement of the fracture toughness of extensible connective tissues”. In: *Journal of Materials Science* 18.12, pp. 3591–3598. DOI: 10.1007/BF00540731.
- Purslow, Peter P. (1983b). “Positional variations in fracture toughness, stiffness and strength of descending thoracic pig aorta”. In: *Journal of Biomechanics* 16.11, pp. 947–953. DOI: 10.1016/0021-9290(83)90058-1.

- Purslow, Peter P. (1985). "The physical basis of meat texture: observations on the fracture behaviour of cooked bovine M. Semitendinosus". In: *Meat Science* 12.1, pp. 39–60. DOI: 10.1016/0309-1740(85)90024-5.
- Qasim, Muhammad, Raghu N Natarajan, Howard S An, and Gunnar B J Andersson (2012). "Initiation and progression of mechanical damage in the intervertebral disc under cyclic loading using continuum damage mechanics methodology: a finite element study". In: *Journal of Biomechanics*. DOI: 10.1016/j.jbiomech.2012.05.022.
- Qasim, Muhammad, Raghu N. Natarajan, Howard S. An, and Gunnar B. J. Andersson (2014). "Damage accumulation location under cyclic loading in the lumbar disc shifts from inner annulus lamellae to peripheral annulus with increasing disc degeneration". In: *Journal of Biomechanics* 47.1, pp. 24–31. DOI: 10.1016/j.jbiomech.2013.10.032.
- Quapp, K M and J A Weiss (1998). "Material characterization of human medial collateral ligament". In: *Journal of Biomechanical Engineering* 120.6, pp. 757–763.
- Rattner, J. B., J. R. Matyas, L. Barclay, S. Holowaychuk, P. Sciore, I. K. Y. Lo, N. G. Shrive, C. B. Frank, Y. Achari, and D. A. Hart (2011). "New understanding of the complex structure of knee menisci: implications for injury risk and repair potential for athletes". In: *Scandinavian Journal of Medicine & Science in Sports* 21.4, pp. 543–553. DOI: 10.1111/j.1600-0838.2009.01073.x.
- Reese, Shawn P., Benjamin J. Ellis, and Jeffrey A. Weiss (2013). "Micromechanical model of a surrogate for collagenous soft tissues: development, validation and analysis of mesoscale size effects". In: *Biomechanics and Modeling in Mechanobiology* 12.6, pp. 1195–1204. DOI: 10.1007/s10237-013-0475-2.
- Rezakhaniha, R, A Agianniotis, J T C Schrauwen, A Griffa, D Sage, C V C Bouten, F N van de Vosse, M Unser, and N Stergiopoulos (2012). "Experimental investigation of collagen waviness and orientation in the arterial adventitia using confocal laser scanning microscopy". In: *Biomechanics and Modeling in Mechanobiology* 11.3-4, pp. 461–473. DOI: 10.1007/s10237-011-0325-z.
- Richards, David P, F Alan Barber, and Morley A Herbert (2008). "Meniscal tear biomechanics: loads across meniscal tears in human cadaveric knees". In: *Orthopedics* 31.4, pp. 347–350.
- Riemersma, D J and H C Schamhardt (1982). "The cryo-jaw, a clamp designed for in vitro rheology studies of horse digital flexor tendons". In: *Journal of biomechanics* 15.8, pp. 619–620.
- Rivlin, R. S. and A. G. Thomas (1953). "Rupture of rubber. I. Characteristic energy for tearing". In: *Journal of Polymer Science* 10.3, pp. 291–318. DOI: 10.1002/pol.1953.120100303.
- Rodkey, W. G., J. R. Steadman, and S. T. Li (1999). "A clinical study of collagen meniscus implants to restore the injured meniscus". In: *Clinical Orthopaedics and Related Research* 367 Suppl, S281–292.
- Roeddecker, K., U. Muennich, and M. Nagelschmidt (1994). "Meniscal Healing: A Biomechanical Study". In: *Journal of Surgical Research* 56.1, pp. 20–27. DOI: 10.1006/jsre.1994.1004.

- Rongen, Jan J., Gerjon Hannink, Tony G. van Tienen, Judith van Luijk, and Carlijn R. Hooijmans (2015). “The protective effect of meniscus allograft transplantation on articular cartilage: a systematic review of animal studies”. In: *Osteoarthritis and Cartilage*. DOI: 10.1016/j.joca.2015.04.025.
- Roughley, P J and R J White (1992). “The dermatan sulfate proteoglycans of the adult human meniscus”. In: *Journal of Orthopaedic Research* 10.5, pp. 631–637. DOI: 10.1002/jor.1100100505.
- Sacks, Michael S (2003). “Incorporation of experimentally-derived fiber orientation into a structural constitutive model for planar collagenous tissues”. In: *Journal of Biomechanical Engineering* 125.2, pp. 280–287.
- Sacks, Michael S. and Wei Sun (2003). “Multiaxial mechanical behavior of biological materials”. In: *Annual Review of Biomedical Engineering* 5, pp. 251–284. DOI: 10.1146/annurev.bioeng.5.011303.120714.
- Sano, Hirotaka, Ikuko Wakabayashi, and Eiji Itoi (2006). “Stress distribution in the supraspinatus tendon with partial-thickness tears: an analysis using two-dimensional finite element model”. In: *Journal of Shoulder and Elbow Surgery* 15.1, pp. 100–105. DOI: 10.1016/j.jse.2005.04.003.
- Schechtman, H. and D.L. Bader (1997). “In vitro fatigue of human tendons”. In: *Journal of Biomechanics* 30.8, pp. 829–835. DOI: 10.1016/S0021-9290(97)00033-X.
- Schillhammer, Carl K., Frederick W. Werner, Matthew G. Scuderi, and John P. Cannizzaro (2012). “Repair of lateral meniscus posterior horn detachment lesions: a biomechanical evaluation”. In: *The American Journal of Sports Medicine* 40.11, pp. 2604–2609. DOI: 10.1177/0363546512458574.
- Schöttle, Philip, Ioannis Goudakos, Nikolaus Rosenstiel, Jan-Erik Hoffmann, William R. Taylor, Georg N. Duda, and Markus O. Heller (2009). “A comparison of techniques for fixation of the quadriceps muscle–tendon complex for in vitro biomechanical testing of the knee joint in sheep”. In: *Medical Engineering & Physics* 31.1, pp. 69–75. DOI: 10.1016/j.medengphy.2008.04.010.
- Seedhom, B. B. and D. J. Hargreaves (1979). “Transmission of the load in the knee joint with special reference to the role of the menisci part II: experimental results, discussion and conclusions”. In: *Engineering in Medicine* 8.4, pp. 220–228. DOI: 10.1243/EMED_JOUR_1979_008_051_02.
- Seil, R, N VanGiffen, and D Pape (2009). “Thirty years of arthroscopic meniscal suture: What’s left to be done?” In: *Orthopaedics & Traumatology: Surgery & Research* 95.8 Suppl 1, S85–96. DOI: 10.1016/j.otsr.2009.09.004.
- Sereysky, Jedd B., Nelly Andarawis-Puri, Stephen J. Ros, Karl J. Jepsen, and Evan L. Flatow (2010). “Automated image analysis method for quantifying damage accumulation in tendon”. In: *Journal of Biomechanics* 43.13, pp. 2641–2644. DOI: 10.1016/j.jbiomech.2010.04.043.
- Sharkey, N. A., T. S. Smith, and D. C. Lundmark (1995). “Freeze clamping musculo-tendinous junctions for in vitro simulation of joint mechanics”. In: *Journal of Biomechanics* 28.5, pp. 631–635.

- Shelbourne, K. D. and T. Gray (2000). “Results of anterior cruciate ligament reconstruction based on meniscus and articular cartilage status at the time of surgery: five- to fifteen-year evaluations”. In: *The American Journal of Sports Medicine* 28.4, pp. 446–452.
- Shelbourne, K. Donald and Michael D. Dersam (2004). “Comparison of partial meniscectomy versus meniscus repair for bucket-handle lateral meniscus tears in anterior cruciate ligament reconstructed knees”. In: *Arthroscopy: The Journal of Arthroscopic & Related Surgery* 20.6, pp. 581–585. DOI: 10.1016/j.arthro.2004.03.009.
- Shieh, Alvin, Tracey Bastrom, Joanna Roocroft, Eric W. Edmonds, and Andrew T. Pennock (2013). “Meniscus tear patterns in relation to skeletal immaturity: children versus adolescents”. In: *The American Journal of Sports Medicine* 41.12, pp. 2779–2783. DOI: 10.1177/0363546513504286.
- Showalter, Brent L., Neil R. Malhotra, Edward J. Vresilovic, and Dawn M. Elliott (2014). “Nucleotomy reduces the effects of cyclic compressive loading with unloaded recovery on human intervertebral discs”. In: *Journal of Biomechanics* 47.11, pp. 2633–2640. DOI: 10.1016/j.jbiomech.2014.05.018.
- Skaggs, D. L. and V.C. Mow (1990). “Function of radial tie fibers in the meniscus”. In: *Transactions of the Orthopaedic Research Society*. Vol. 15, p. 248.
- Skaggs, D L, W H Warden, and V C Mow (1994a). “Radial tie fibers influence the tensile properties of the bovine medial meniscus”. In: *Journal of Orthopaedic Research* 12.2, pp. 176–185. DOI: 10.1002/jor.1100120205.
- Skaggs, D L, M Weidenbaum, J C Iatridis, A Ratcliffe, and V C Mow (1994b). “Regional variation in tensile properties and biochemical composition of the human lumbar annulus fibrosus”. In: *Spine* 19.12, pp. 1310–1319.
- Smillie, Ian Scott (1978). *Injuries of the Knee Joint*. Edinburgh; New York; New York: Churchill Livingstone ; Distributed by Longman.
- Smith, Christopher D., Spyros Masouros, Adam M. Hill, Andrew L. Wallace, Andrew A. Amis, and Anthony M.J. Bull (2008). “Mechanical testing of intra-articular tissues. Relating experiments to physiological function”. In: *Current Orthopaedics* 22.5, pp. 341–348. DOI: 10.1016/j.cuor.2008.07.010.
- Snoeker, Barbara A. M., Eric W. P. Bakker, Cornelia A. T. Kegel, and Cees Lucas (2013). “Risk factors for meniscal tears: a systematic review including meta-analysis”. In: *The Journal of Orthopaedic and Sports Physical Therapy* 43.6, pp. 352–367. DOI: 10.2519/jospt.2013.4295.
- Song, Yongnam, Dennis R. Carter, and Nicholas J. Giori (2014). “Cartilage nominal strain correlates with shear modulus and glycosaminoglycans content in meniscectomized joints”. In: *Journal of Biomechanical Engineering* 136.6, p. 064503. DOI: 10.1115/1.4027298.
- Sonoda, Masaki, Frederick L. Harwood, Michael E. Amiel, Hideshige Moriya, Michele Temple, Douglas G. Chang, Lisa M. Lottman, Robert L. Sah, and David Amiel (2000). “The effects of hyaluronan on tissue healing after meniscus injury and repair in a rabbit model”. In: *The American Journal of Sports Medicine* 28.1, pp. 90–97.
- Spilker, R L, P S Donzelli, and V C Mow (1992). “A transversely isotropic biphasic finite element model of the meniscus”. In: *Journal of Biomechanics* 25.9, pp. 1027–1045.

- Stabile, Kathryn J., Devin Odom, Thomas L. Smith, Casey Northam, Patrick W. Whitlock, Beth P. Smith, Mark E. Van Dyke, and Cristin M. Ferguson (2010). “An acellular, allograft-derived meniscus scaffold in an ovine model”. In: *Arthroscopy: The Journal of Arthroscopic & Related Surgery* 26.7, pp. 936–948. DOI: 10.1016/j.arthro.2009.11.024.
- ASTM D638-14 (2014). *Standard test method for tensile properties of plastics*. Tech. rep. D638-14. ASTM.
- ASTM D2209-00 (2015). *Standard test method for tensile strength of leather*. Tech. rep. D2209-00. ASTM.
- ASTM D3479/D3479M (2015). *Standard test method for tension-tension fatigue of polymer matrix composite materials*. Tech. rep. D3479/D3479M. ASTM.
- ASTM E8/E8M-15a (2015). *Standard test methods for tension testing of metallic materials*. Tech. rep. E8/E8M-15a. ASTM, p. 29.
- Stapleton, Thomas W, Joanne Ingram, Jaynath Katta, Richard Knight, Sotirios Korossis, John Fisher, and Eileen Ingham (2008). “Development and characterization of an acellular porcine medial meniscus for use in tissue engineering”. In: *Tissue engineering. Part A* 14.4, pp. 505–518. DOI: 10.1089/tea.2007.0233.
- Stärke, Christian, Sebastian Kopf, Wolf Petersen, and Roland Becker (2009). “Meniscal repair”. In: *Arthroscopy: The Journal of Arthroscopic & Related Surgery* 25.9, pp. 1033–1044. DOI: 10.1016/j.arthro.2008.12.010.
- Stok, K. and A. Oloyede (2003). “A qualitative analysis of crack propagation in articular cartilage at varying rates of tensile loading”. In: *Connective Tissue Research* 44.2, pp. 109–120.
- (2007). “Conceptual fracture parameters for articular cartilage”. In: *Clinical Biomechanics* 22.6, pp. 725–735. DOI: 10.1016/j.clinbiomech.2007.03.005.
- Stronge, W. J. and M. Kashtalyan (1997). “Saint-Venant’s principle for two-dimensional anisotropic elasticity”. In: *Acta Mechanica* 124.1-4, pp. 213–218.
- Sun, Wei, Michael J Scott, and Michael S Sacks (2005). “Effects of boundary conditions on the estimation of the planar biaxial mechanical properties of soft tissues”. In: *Journal of Biomechanical Engineering* 127.4, pp. 709–715.
- Sverdlik, A. and Y. Lanir (2002). “Time-dependent mechanical behavior of sheep digital tendons, including the effects of preconditioning”. In: *Journal of Biomechanical Engineering* 124.1, pp. 78–84.
- Swank, Katherine R., Anthony W. Behn, and Jason L. Drago (2014). “The effect of donor age on structural and mechanical properties of allograft tendons”. In: *The American Journal of Sports Medicine*. DOI: 10.1177/0363546514557246.
- Sweigart, M A and K A Athanasiou (2005). “Tensile and compressive properties of the medial rabbit meniscus”. In: *Proceedings of the Institution of Mechanical Engineers. Part H, Journal of Engineering in Medicine* 219.5, pp. 337–347.
- Swenson, T. M. and C. D. Harner (1995). “Knee ligament and meniscal injuries: current concepts”. In: *The Orthopedic Clinics of North America* 26.3, pp. 529–546.

- Szczesny, Spencer E., Jeffrey L. Caplan, Pal Pedersen, and Dawn M. Elliott (2015). “Quantification of interfibrillar shear stress in aligned soft collagenous tissues via notch tension testing”. In: *Scientific Reports* 5, p. 14649. DOI: 10.1038/srep14649.
- Szczesny, Spencer E. and Dawn M. Elliott (2014a). “Incorporating plasticity of the interfibrillar matrix in shear lag models is necessary to replicate the multiscale mechanics of tendon fascicles”. In: *Journal of the Mechanical Behavior of Biomedical Materials* 40, pp. 325–338. DOI: 10.1016/j.jmbbm.2014.09.005.
- (2014b). “Interfibrillar shear stress is the loading mechanism of collagen fibrils in tendon”. In: *Acta Biomaterialia* 10.6, pp. 2582–2590. DOI: 10.1016/j.actbio.2014.01.032.
- Szczesny, Spencer E., John M. Peloquin, Daniel H. Cortes, Jennifer A. Kadlowec, Louis J. Soslowsky, and Dawn M. Elliott (2012). “Biaxial tensile testing and constitutive modeling of human supraspinatus tendon”. In: *Journal of Biomechanical Engineering* 134.2, p. 021004. DOI: 10.1115/1.4005852.
- Tada, Hiroshi, Paul C. Paris, and George R Irwin (2000). *Stress Analysis of Cracks Handbook*. 3rd Revised ed. edition. New York: ASME Press.
- Tan, J, B Wang, B Tan, Y Xu, and J B Tang (2003). “Changes in tendon strength after partial cut and effects of running peripheral sutures”. In: *Journal of Hand Surgery* 28.5, pp. 478–482.
- Tanaka, Martin L., Nikolaj Vest, Cristin M. Ferguson, and Paul Gatenholm (2014). “Comparison of biomechanical properties of native menisci and bacterial cellulose implant”. In: *International Journal of Polymeric Materials* 63.17, pp. 891–897. DOI: 10.1080/00914037.2014.886226.
- Taylor, David (2007). *The Theory of Critical Distances: A New Perspective in Fracture Mechanics*. 1st ed. Elsevier Science.
- Taylor, David, Niamh O’Mara, Eoin Ryan, Michael Takaza, and Ciaran Simms (2012). “The fracture toughness of soft tissues”. In: *Journal of the Mechanical Behavior of Biomedical Materials* 6, pp. 139–147. DOI: 10.1016/j.jmbbm.2011.09.018.
- Team, R Core (2015). *R: A Language and Environment for Statistical Computing*. Vienna, Austria: R Foundation for Statistical Computing.
- Thermann, H., O. Frerichs, A. Biewener, and C. Krettek (2001). “Healing of the Achilles tendon: an experimental study”. In: *Foot & Ankle International* 22.6, pp. 478–483.
- Thorpe, C. T., S. Chaudhry, I. I. Lei, A. Varone, G. P. Riley, H. L. Birch, P. D. Clegg, and H. R. C. Screen (2015a). “Tendon overload results in alterations in cell shape and increased markers of inflammation and matrix degradation”. In: *Scandinavian Journal of Medicine & Science in Sports*, n/a–n/a. DOI: 10.1111/sms.12333.
- Thorpe, Chavaunne T., Marta S. C. Godinho, Graham P. Riley, Helen L. Birch, Peter D. Clegg, and Hazel R. C. Screen (2015b). “The interfascicular matrix enables fascicle sliding and recovery in tendon, and behaves more elastically in energy storing tendons”. In: *Journal of the Mechanical Behavior of Biomedical Materials*. DOI: 10.1016/j.jmbbm.2015.04.009.
- Thorpe, Chavaunne T., Chineye P. Udeze, Helen L. Birch, Peter D. Clegg, and Hazel R. C. Screen (2012). “Specialization of tendon mechanical properties results from interfascicular

- differences”. In: *Journal of The Royal Society Interface*. DOI: 10.1098/rsif.2012.0362.
- Tissakht, M and A M Ahmed (1995). “Tensile stress-strain characteristics of the human meniscal material”. In: *Journal of Biomechanics* 28.4, pp. 411–422.
- Toman, Charles V., Warren R. Dunn, Kurt P. Spindler, Annunziata Amendola, Jack T. Andriash, John A. Bergfeld, David Flanigan, Morgan H. Jones, Christopher C. Kaeding, Robert G. Marx, Matthew J. Matava, Eric C. McCarty, Richard D. Parker, Michelle Wolcott, Armando Vidal, Brian R. Wolf, Laura J. Huston, Frank E. Harrell, and Rick W. Wright (2009). “Success of meniscal repair at anterior cruciate ligament reconstruction”. In: *The American Journal of Sports Medicine* 37.6, pp. 1111–1115. DOI: 10.1177/0363546509337010.
- Upton, Maureen L, Farshid Guilak, Tod A Laursen, and Lori A Setton (2006). “Finite element modeling predictions of region-specific cell-matrix mechanics in the meniscus”. In: *Biomechanics and Modeling in Mechanobiology* 5.2-3, pp. 140–149. DOI: 10.1007/s10237-006-0031-4.
- Veres, Samuel P., Julia M. Harrison, and J. Michael Lee (2013). “Cross-link stabilization does not affect the response of collagen molecules, fibrils, or tendons to tensile overload”. In: *Journal of Orthopaedic Research* 31.12, pp. 1907–1913. DOI: 10.1002/jor.22460.
- (2014). “Mechanically overloading collagen fibrils uncoils collagen molecules, placing them in a stable, denatured state”. In: *Matrix Biology* 33, pp. 54–59. DOI: 10.1016/j.matbio.2013.07.003.
- Vermesan, D, R Prejbeanu, S Laitin, V Georgianu, H Haragus, S Nitescu, M Tatullo, M Tatoli, M Caprio, and R Cagiano (2014). “Meniscal tears left in situ during anatomic single bundle anterior cruciate ligament reconstruction”. In: *European Review for Medical and Pharmacological Sciences* 18.2, pp. 252–256.
- Vernon-Roberts, Barrie, Robert J. Moore, and Robert D. Fraser (2007). “The natural history of age-related disc degeneration: the pathology and sequelae of tears”. In: *Spine* 32.25, pp. 2797–2804. DOI: 10.1097/BRS.0b013e31815b64d2.
- Videman, Tapio and Markku Nurminen (2004). “The occurrence of anular tears and their relation to lifetime back pain history: a cadaveric study using barium sulfate discography”. In: *Spine* 29.23, pp. 2668–2676. DOI: 10.1097/01.brs.0000146461.27105.2b.
- Viidik, A (1972). “Simultaneous mechanical and light microscopic studies of collagen fibers”. In: *Zeitschrift Für Anatomie Und Entwicklungsgeschichte* 136.2, pp. 204–212.
- Viinikainen, Anna, Harry Göransson, Katja Huovinen, Minna Kellomäki, Pertti Törmälä, and Pentti Rokkanen (2007). “The strength of the 6-strand modified Kessler repair performed with triple-stranded or triple-stranded bound suture in a porcine extensor tendon model: an ex vivo study”. In: *The Journal of Hand Surgery* 32.4, pp. 510–517. DOI: 10.1016/j.jhsa.2007.01.010.
- Villegas, Diego F., Jason A. Maes, Sarah D. Magee, and Tammy L. Haut Donahue (2007). “Failure properties and strain distribution analysis of meniscal attachments”. In: *Journal of Biomechanics* 40.12, pp. 2655–2662. DOI: 10.1016/j.jbiomech.2007.01.015.
- Voloshin, A. S. and J. Wosk (1983). “Shock absorption of meniscectomized and painful knees: a comparative in vivo study”. In: *Journal of Biomedical Engineering* 5.2, pp. 157–161.

- Von Forell, Gregory A. and Anton E. Bowden (2014). “A damage model for the percutaneous triple hemisection technique for tendo-achilles lengthening”. In: *Journal of Biomechanics*. DOI: 10.1016/j.jbiomech.2014.08.006.
- Von Forell, Gregory A, Peter S Hyung, and Anton E Bowden (2014). “Failure modes and fracture toughness in partially torn ligaments and tendons”. In: *Journal of the Mechanical Behavior of Biomedical Materials* 35C, pp. 77–84. DOI: 10.1016/j.jmbbm.2014.03.020.
- Vrancken, Anne Christiane Theodora, Pieter Buma, and Tony George van Tienen (2013). “Synthetic meniscus replacement: a review”. In: *International Orthopaedics* 37.2, pp. 291–299. DOI: 10.1007/s00264-012-1682-7.
- Wagemakers, Harry Pa, Edith M. Heintjes, Simone S. Boks, Marjolein Y. Berger, Jan An Verhaar, Bart W. Koes, and Sita Ma Bierma-Zeinstra (2008). “Diagnostic value of history-taking and physical examination for assessing meniscal tears of the knee in general practice”. In: *Clinical Journal of Sport Medicine* 18.1, pp. 24–30. DOI: 10.1097/JSM.0b013e31815887a7.
- Waldman, S. D., M. S. Sacks, and J. M. Lee (2002). “Boundary conditions during biaxial testing of planar connective tissues. Part 2: Fiber orientation”. In: *Journal of Materials Science Letters* 21.15, pp. 1215–1221. DOI: 10.1023/A:1016576603938.
- Wang, Y., J. A. Johnson, F. G. Spinale, M. A. Sutton, and S. M. Lessner (2014). “Quantitative measurement of dissection resistance in intimal and medial layers of human coronary arteries”. In: *Experimental Mechanics* 54.4, pp. 677–683. DOI: 10.1007/s11340-013-9836-0.
- Warren, R. F. and J. L. Marshall (1978). “Injuries of the anterior cruciate and medial collateral ligaments of the knee: a retrospective analysis of clinical records—part I”. In: *Clinical Orthopaedics and Related Research* 136, pp. 191–197.
- Waterman, Brian R., Nicholas Rensing, Kenneth L. Cameron, Brett D. Owens, and Mark Pallas (2016). “Survivorship of meniscal allograft transplantation in an athletic patient population”. In: *The American Journal of Sports Medicine*. DOI: 10.1177/0363546515626184.
- Whipple, RR, CR Wirth, and VC Mow (1985). “Anisotropic and zonal variations in the tensile properties of the meniscus”. In: *Transactions of the Orthopaedic Research Society*. Vol. 10, p. 367.
- Wilson, W., C. C. van Donkelaar, B. van Rietbergen, K. Ito, and R. Huiskes (2004). “Stresses in the local collagen network of articular cartilage: a poroviscoelastic fibril-reinforced finite element study”. In: *Journal of Biomechanics* 37.3, pp. 357–366.
- Winkler, Moritz, Dongyul Chai, Shelsea Kriling, Chyong Jy Nien, Donald J. Brown, Bryan Jester, Tibor Juhasz, and James V. Jester (2011). “Nonlinear optical macroscopic assessment of 3-D corneal collagen organization and axial biomechanics”. In: *Investigative Ophthalmology & Visual Science* 52.12, pp. 8818–8827. DOI: 10.1167/iovs.11-8070.
- Winkler, Moritz, Golroxan Shoa, Yilu Xie, Steven J Petsche, Peter M Pinsky, Tibor Juhasz, Donald J Brown, and James V Jester (2013). “Three-dimensional distribution of transverse collagen fibers in the anterior human corneal stroma”. In: *Investigative Ophthalmology & Visual Science* 54.12, pp. 7293–7301. DOI: 10.1167/iovs.13-13150.

- Wren, T A and D R Carter (1998). “A microstructural model for the tensile constitutive and failure behavior of soft skeletal connective tissues”. In: *Journal of Biomechanical Engineering* 120.1, pp. 55–61.
- Wren, Tishya A. L., Derek P. Lindsey, Gary S. Beaupré, and Dennis R. Carter (2003). “Effects of creep and cyclic loading on the mechanical properties and failure of human achilles tendons”. In: *Annals of Biomedical Engineering* 31.6, pp. 710–717. DOI: 10.1114/1.1569267.
- Wu, Kenneth S, William W van Osdol, and Reinhold H Dauskardt (2006a). “Mechanical properties of human stratum corneum: effects of temperature, hydration, and chemical treatment”. In: *Biomaterials* 27.5, pp. 785–795. DOI: 10.1016/j.biomaterials.2005.06.019.
- Wu, Kenneth S., Morgan M. Stefik, K. P. Ananthapadmanabhan, and Reinhold H. Dauskardt (2006b). “Graded delamination behavior of human stratum corneum”. In: *Biomaterials* 27.34, pp. 5861–5870. DOI: 10.1016/j.biomaterials.2006.08.008.
- Yang, Q.D., Brian N. Cox, Ravi K. Nalla, and R.O. Ritchie (2006). “Fracture length scales in human cortical bone: The necessity of nonlinear fracture models”. In: *Biomaterials* 27.9, pp. 2095–2113. DOI: 10.1016/j.biomaterials.2005.09.040.
- Yoder, Jonathon H., John M. Peloquin, Gang Song, Nick J. Tustison, Sung M. Moon, Alexander C. Wright, Edward J. Vresilovic, James C. Gee, and Dawn M. Elliott (2014). “Internal three-dimensional strains in human intervertebral discs under axial compression quantified noninvasively by magnetic resonance imaging and image registration”. In: *Journal of Biomechanical Engineering* 136.11. DOI: 10.1115/1.4028250.
- Zitnay, Jared L, Yang Li, S. Michael Yu, Shawn P. Reese, and Jeffrey A Weiss (2016). “Molecular level detection and localization of mechanical damage in collagen using collagen hybridizing peptides”. In: *Transactions of the Orthopaedic Research Society*.